CZECH TECHNICAL UNIVERSITY IN PRAGUE
Faculty of Nuclear Sciences and Physical Engineering
Department of Physics

DIPLOMA THESIS

Energetické ztráty jetů v relativistických srážkách těžkých iontů s modelováním realistického média

Jet energy loss in relativistic heavy-ion collisions with realistic medium modelling

Author: Bc. Josef Bobek
Supervisor: Iurii Karpenko, Ph.D.

Academic year: 2022/2023

ČESKÉ VYSOKÉ UČENÍ TECHNICKÉ V PRAZE
FAKULTA JADERNÁ A FYZIKÁLNĚ INŽENÝRSKÁ
PRAHA 1 - STARÉ MĚSTO, BŘEHOVÁ 7 - PSČ 115 19

Katedra: fyziky *Akademický rok:* 2021/2022

ZADÁNÍ DIPLOMOVÉ PRÁCE

Student: Bc. Josef Bobek

Studijní program: Jaderná a částicová fyzika

Název práce: (česky) Energetické ztráty jetů v relativistických srážkách těžkých iontů s modelováním realistického média

Název práce: (anglicky) Jet energy loss in relativistic heavy-ion collisions with realistic medium modeling

Pokyny pro vypracování:

1) Studium evoluce a modelování jetů v elementárních a proton-protonových stážkách bez efektů média a jejich rekonstrukce

2) Mechnismus kolizních a radiačních energetických ztrát partonů s vysokou energií v médiu

3) Nejmodernější modelování evoluce média v relativistických srážkách těžkých iontů

4) Praktické modelování průletu jetu skrze médium a jeho přidružené energetické ztráty

5) Extrakce příslušných pozorovatelných jako je jaderný modifikační faktor hadronů s vysokou příčnou hybností a rekonstruovaných jetů

Doporučená literatura:

[1] A. Buckley, et al.: General-Purpose Event Generators for LHC Physics, Physics Reports 504 5 145-233 (2011)

[2] K. C. Zapp: A Monte Carlo model for jet evolution with energy loss, PhD disertační práce, University of Heidelberg, 2008

[3] J. Aichelin, et al.: Gluon radiation by heavy quarks at intermediate energies. Physical Review D 89 7 074018 (2014)

[4] H. A. Andrews, et al.: Novel tools and observables for jet physics in heavy-ion collisions. arXiv:1808.03689 (2020)

[5] P. Romatschke and R. Ulrike: Relativistic Fluid Dynamics In and Out of Equilibrium - Ten Years of Progress in Theory and Numerical Simulations of Nuclear Collisions. arXiv:1712.05815 (2019)

Jméno a pracoviště vedoucího diplomové práce:

Iurii Karpenko, Ph.D., Katedra fyziky,
Fakulta jaderná a fyzikálně inženýrská ČVUT v Praze

Datum zadání diplomové práce: 20.10.2021

Termín odevzdání diplomové práce: 02.05.2022

Doba platnosti zadání je dva roky od data zadání.

.....
garant studijního programu

.....
vedoucí katedry

ČESKÉ VYSOKÉ UČENÍ TECHNICKÉ V PRAZE Fakulta jaderná a fyzikálně inženýrská - 1 -

.....
děkan

V Praze dne 20.10.2021

České vysoké učení technické v Praze

Fakulta jaderná a fyzikálně inženýrská

Břehová 7
115 19 Praha 1

Já, níže podepsaný

Jméno a příjmení studenta: Josef Bobek

Osobní číslo: 468015

Název studijního programu: Jaderná a částicová fyzika

prohlašuji, že jsem diplomovou práci s názvem:

Energetické ztráty jetů v relativistických srážkách těžkých iontů s modelováním realistického média

vypracoval samostatně a uvedl veškeré použité informační zdroje v souladu s Metodickým pokynem o dodržování etických principů při přípravě vysokoškolských závěrečných prací.

Nemám závažný důvod proti použití tohoto díla ve smyslu § 60 Zákona c. 121/1200 Sb., o právu autorském, o právech souvisejících s právem autorským a o změně některých zákonů (autorský zákon).

V Praze dne 5. ledna 2023

Bobek

.....
Josef Bobek

Acknowledgement

First of all, I would like to thank my supervisor Iurii Karpenko, Ph.D., for his guidance. I am enormously grateful to have a supervisor like he is. I respect his deep knowledge about the field that became my passion, thanks to him. I am thankful for the time he spent with our meetings, planning my research and with this thesis in general.

I would also like to thank my family and friends for their support. Everybody close to me created a perfect environment to be here and doing what I enjoy the most - physics. Special thanks belong to my parents, Mgr. Josef Bobek and Mgr. Zuzana Bobková.

Last but certainly not least, I would like to thank my girlfriend Mgr. Tereza Jiráková. It is impossible to thank her enough for what she does for me and how much she supports me throughout my life. I am very grateful to have such an amazing person next to me.

Poděkování

V první řadě bych rád poděkoval memu vecoucímu Iuriimu Karpenkovi, Ph.D. za jeho odborné vedení. Jsem nesmírně vděčný, že mám vedoucího jako je on. Hluboce respektuji jeho znalosti v oboru, který se stal mou vášní díky němu. Jsem vděčný za jeho čas, který strávil na našich schůzkách, plánováním mého výzkumu a obecně s touto diplomovou prací.

Dále bych rád poděkoval mé rodině a přátelům za jejich podporu. Každý, kdo je mi blízký, vytvořil perfektní prostředí k tomu, abych byl tady a dělal, co mě baví nejvíce - fyziku. Speciální poděkování patří mým rodičům, Mgr. Josefu Bobkovi a Mgr. Zuzaně Bobkové.

V neposlední řadě bych rád poděkoval mé partnerce Mgr. Tereze Jirákové. Je nemožné ji dostatečně poděkovat za to, co pro mě dělá a jak mě v mém životě podporuje. Jsem velmi vděčný, že mám tak úžasnou osobu vedle sebe.

Bc. Josef Bobek

Název práce:
Energetické ztráty jetů v relativistických srážkách těžkých iontů s modelováním realistického média

Autor: Bc. Josef Bobek

Studijní program: Jaderná a částicová fyzika

Druh práce: Diplomová práce

Vedoucí práce: Iurii Karpenko, Ph.D., Fakulta jaderná a fyzikálně inženýrská ČVUT v Praze

Abstrakt:
Jádro-jaderné srážky jsou nástrojem jak vytvořit extrémní stav hmoty nazývaný kvark-gluonové plazma. Kvark-gluonové plazma má vlastnosti kapaliny a jeho evoluce může být fenomenologicky nasimulovaná pomocí relativistické hydrodynamiky.

Tvrdé pozorovatelné jsou výborným nástrojem, jak zkoumat vlastnosti kvark-gluonového plazma. Jedna z těchto pozorovatelných je kolimovaná sprška hadronů nazývaných jet. Evoluce tohoto jetu může být simulována společně s médiem a je možné z této několika fázové simulace získat hadronové pozorovatelné jako je jaderný modifikační faktor.

Klíčová slova: QGP, relativistická hydrodynamika, jet, zhášení jetů

Title:
Jet energy loss in relativistic heavy-ion collisions with realistic medium modelling

Author: Bc. Josef Bobek

Abstract:
During the heavy-ion collision an extreme state of matter is created. This medium is called a quark-gluon plasma. The quark-gluon plasma has the properties of a fluid, and its evolution can be phenomenologically simulated with relativistic hydrodynamics.

Hard observables are great tools to investigate properties of the quark-gluon plasma. One of the observables is high transverse momentum p_{T} collimated shower of hadrons called jet. Evolution of the jet can be simulated along with the medium and it is possible to obtain hadronic observables such as nuclear modification factor from this multistage simulation.

Key words: QGP, relativistic hydrodynamics, jet, jet quenching

Contents

Chapter 1

Introduction

With relativistic heavy-ion collisions, we can create a matter that was in our universe approximately 10^{-10} s after the Big Bang. This matter is composed of quarks and gluons that can travel through the medium freely. Quarks and gluons cannot escape outside the hadrons under ordinary conditions; this is called colour confinement. Colour confinement is a consequence of the nature of strong interaction.

Gluons, as a strong force carrier, can interact with themselves. This is different from the photon γ for example, which does not carry an electric charge and thus, does not possess a self-interaction. Gluons carry colour charge and their self-interaction considerably complicates first-principles calculations for certain processes. The first principle physics of the colour charge is considered as quantum chromodynamics (QCD).

The main decisive factor whether something is calculable in QCD is the energy transferred during the process. Processes with high-energy transfer are known as hard processes and on the opposite side of the spectrum are soft processes. If the energy transferred between two particles is high enough, we can utilise a very powerful tool called perturbative quantum field theory (QFT). Perturbave theory is an approach to unfolding the process into a series. For some strong interaction phenomena, it is a relatively straightforward procedure. However, for soft processes perturbation series do not converge.

This, unfortunately, includes a lot of processes, such as quarks being bound inside the hadrons, quarks and gluons hadronising into hadrons, or even evolution of the hot and dense medium that is created during heavy-ion collision. To make the situation worse, processes that can be calculated from pertubative theory are accompanied by those that are not calculable.

For example, if two quarks violently collide and exchange a lot of energy, it can be calculated perturbatively. However, we cannot observe individual quarks due to the already mentioned confinement and process of hadronisation, where those quarks converted into hadrons is not calculable from first principles.

This thesis interconnects two topics in the field of heavy relativistic heavy-ion collisions. The first branch is the physics of the medium. When ions collide with each other, they deposit energy and, after some short evolution, quark-gluon plasma (QGP) is created. It was discovered that QGP has collective behaviour. This creates an opportunity to employ relativistic hydrody-

namics. The development of relativistic hydrodynamics showed that it is a powerful tool for describing measured observables such as hadronic p_T spectra or azimuthal harmonic coefficients. Nowadays, relativistic hydrodynamics is essential to our current understanding of the soft sector observables that come from the bulk properties of the QGP.

The second branch of high-energy physics that is studied in this thesis is the hard sector. One of the observables arising from the hard process at the beginning of the heavy-ion collision are high transverse momentum p_{T} colimated showers of hadrons called jets. The initial hard parton fragments into more partons, which lose energy inside the strongly interacting medium and then hadronizes.

In this thesis, you can find the results of simulations of the heavy-ion collision in form of observales. This is accompanied by rather deep theoretical review of almost each aspect of this simulation. The goal was to employ various frameworks (T$_{\mathrm{R}}$ENTo [1], `freestream-milne` [2], `MUSIC` [3], `iSS` [4], `SMASH` [5], `Pythia` [6], `MATTER` [7], `LBT` [8]) implemented in the Jetscape framework [9] and obtain experimentaly measurable quantities like nuclear modification factor.

Chapter 2

The Standard Model

The Standard Model is a theory of particle physics based on quantum field theory (QFT). This theory incorporates all known elementary particles of matter, three out of four fundamental forces that are carried out by 4+8 intermediate particles represented by Yang-Mills fields [10], and the final yet important four-component Higgs field, which with its Higgs potential is connected to spontaneous symmetry breaking.

The first of three forces is electromagnetism, and its QFT called quantum electrodynamics (QED) is well known for its very high accuracy in the late 1940s, after the renormalisation procedure was developed. This success accompanied the renormalizability of other theories, apart from QED.

A much more difficult path to renormalizability was laid out for the interaction observed in the β decay and later in the muon or pion decay. Currently, we call this interaction weak, and the label for its QFT is quantum flavourdynamics (QFD). The description of this interaction started as a parity-conserving vector 4-point fermion interaction, called Fermi theory. The vector current interaction (γ_μ) was inspired by QED, where the vertex factor of the photon is also vector-based.

However, Fermi theory could not explain the Gamow-Teller β decay, where the angular momentum of the nucleus is changed. Furthermore, the observation of the decay of the polarised ^{60}Co showed that the weak interaction does not preserve the parity symmetry. This experiment is called the Wu experiment [11], since it was conducted in 1956 by the Chinese-American physicist Chien-Shiung Wu.

The QFD was later constructed with all possible currents ($\mathbb{1}, \gamma_5, \gamma_\mu, \gamma_\mu\gamma_5, \sigma_{\mu\nu} = [\gamma_\mu, \gamma_\nu]$) that were later fixed by the experiments. This was called the V-A theory, since only the vector γ_μ and the axial vector $\gamma_\mu\gamma_5$ are preserved in the form of a current $\gamma_\mu(1-\gamma_5)$ between two elementary particles. This form of current gives the maximum-parity violation.

However, both four-point fermion effective theories were not renormalizable. This was caused by the dimension of the Fermi coupling constant $[G_\mathrm{F}] = M^{-2}$ given by the condition on the action dimension $[\mathcal{S}] = \hbar = 1$ and by the fact that the fermionic bispinor has dimension $[\psi] = M^{\frac{3}{2}}$. Since both theories are built on the four-fermion interaction $\sim G_\mathrm{F}\overline{\psi}\psi\overline{\psi}\psi$, coupling constant G_F must have dimension $[G_\mathrm{F}] = M^{-2}$.

This behaviour is due to the fact that the matrix element $\mathscr{M}$ in perturbation theory is a series of the coupling constant G as $\mathscr{M} \sim G + G^2\Lambda^2 + \cdots$, where Λ is a parameter of the perturbation theory for witch $\Lambda^2 \gg s$ (see A.5 for more information on Mandelstam variables). This series leads to non-renormalizability. The same issue has QFT of gravity with $[G_N] = M^{-2}$.

This led to the introduction of massive intermediate bosons $W^{\pm}$ with a suitable dimension of the coupling constant $[g] = 1$. However, this theory does not lead to renormalizability either because the matrix element $\mathscr{M}$ for Feynman tree diagram processes has an asymptotic leading behaviour as a positive integer power of the energy. This means that in the limit $s \to +\infty$ (see A.5 for more information on Mandelstam variables), $\mathscr{M}$ diverges quickly and the S-matrix becomes ununitary. The unitarity of the S-matrix is connected to the conservation of the probability current in quantum mechanics, and thus it is necessary to preserve this property. However, in terms of renormalisation, the logarithmic violation of unitarity is the highest-energy asymptotic behaviour of the partial-wave scattering amplitude that is acceptable.

This led to electroweak theory (EWT), which is based on the minimal group that cancels the leading asymptotic behaviours of tree-level diagrams. This group happens to be $\mathrm{SU}(2)_L \times \mathrm{U}(1)_Y$ with four vector gauge fields. The Abelian gauge field of subgroup $\mathrm{U}(1)_Y$ is called a weak hypercharge field, and three non-Abelian gauge fields of subgroup $\mathrm{SU}(2)_L$ are called weak isospin fields. These fields are a linear combination of the physical electroweak bosonic field. This theory based on compact, reductive Lie algebras is called the Yang-Mills theory, and the fields within this theory are called the Yang-Mills fields after Yang Chen-Ning and Robert Mills, who developed this approach [10] to fundamental interactions in early 1954.

The Yang-Mills theory of the electroweak unification interaction built on symmetry $\mathrm{SU}(2)_L \times \mathrm{U}(1)_Y$ still had two problems. First, there are still some residual energy divergences in the matrix elements of some tree-level diagrams caused by the longitudinal polarisation of massive weak bosons. Second, the mass terms in the Lagrangian density violate the $\mathrm{SU}(2)_L \times \mathrm{U}(1)_Y$ symmetry. Both issues were solved by the four-component Higgs scalar field and its potential. The potential has a symmetry of $\mathrm{O}(4)$. During spontaneous symmetry breaking of the Higgs potential, the three components of the Higgs field correspond to unphysical Goldstone bosons that are removed by a gauge-fixing condition called the U-gauge. As a consequence, for each Goldstone boson that disappears from the physical spectrum, the vector gauge field acquires a mass. This means that the three weak intermediate vector bosons become massive without terms violating the symmetry in the Lagrangian density. Furthermore, additional tree-level Feynman diagrams cancel the residual bad high-energy behaviour of the matrix elements, and the S-matrix becomes unitary. This is the renormalizable EWT of the Standard Model.

The last interaction described by the Standard Model is the strong interaction. This part of the Standard Model is also based on Yang-Mills theory [10]. This time, it is the group $\mathrm{SU}(3)_c$ that represents the symmetry of the strong interaction. In contrast to the EWT, there are eight Yang-Mills gauge fields (see A.4 for more details on the differences between the SU(2) and SU(3) Lie algebras).

The strong interaction is the crucial interaction in this thesis. A strong nuclear interaction dictates the properties of the medium created during heavy-ion collisions, and it also determines how the particles with high transverse momenta p_{T} are created in the primary collision, their interaction with the medium, and their overall evolution including hadronization. Therefore,

there is a dedicated Section 2.3 for QFT that describes the strong interaction, also called quantum chromodynamics (QCD).

2.1 Particles of the Standard Model

Particles of the Standard Model are classified into three main groups. First, we have the particles of matter that, among other things, build the world around us. Next, we have the force carriers that provide the interaction between the particles. Finally, the Higgs field generates masses of elementary particles.

The main distinguishable quantum property between these groups is spin. Spin is an intrinsic angular momentum of elementary particles and comes in half-integer or integer values. For all elementary particles of matter, the spin is $\frac{1}{2}$ and they are represented as the 4-dimensional reducible representation

$$\left(\frac{1}{2},0\right)\oplus\left(0,\frac{1}{2}\right)$$

that can be put in the form of a four-component Dirac spinor $\psi(x)$.

Then there are intermediate particles that are gauge vector bosons with spin equal to 1. These particles are called vector particles due to the possible representation of their wave function as the Lorentz four-vector A^μ (see A.2 for more information on four-vectors). Higgs field is also a boson, a scalar particle with spin 0. However, the Higgs field is also represented by four components, where three of them correspond to unphysical Goldstone bosons that disappear during the Higgs mechanism, and one component is a physical Higgs boson.

In addition to this pleasant categorisation, the spin of the particle consequently causes the particle to have different statistical behaviour. The other way around, quantum statistics of the particles are related to the value of spin.

2.1.1 Statistical behaviour

Statistics of elementary particles are introduced for two types of particles. The first family of particles is called fermions, and their most characteristic property is that they carry a half-integer spin. In contrast, the other group is called bosons, and they carry an integer spin.

Fermions

The fermions follow Fermi-Dirac statistics that were named after and introduced by Enrico Fermi [12, 13] and Paul Dirac [14] independently in 1926.

Fermions follow the law called the Pauli exclusion principle. This principle was introduced for electrons by Wolfgang Pauli in 1925 [15] and later in 1940 it was extended to all fermions. The Pauli exclusion principle states that no more than one identical particle can occupy the given quantum state simultaneously.

From this principle, it is possible to construct the grand canonical partition function for a grand

canonical ensemble for a system of identical fermions in thermodynamic equilibrium as

$$Z_G^{FD} = \prod_i \left[\sum_{n_i=0}^{1} \exp\left(n_i \frac{\mu - E_i}{T} \right) \right] = \prod_i \left[1 + \exp\left(\frac{\mu - E_i}{T} \right) \right],$$

where n_i is the number of particles occupying a given microstate, E_i is the energy of the microstate i, T is the temperature, and finally, μ is the chemical potential. It is possible to derive the grand potential Ω from the grand canonical partition function Z_G^{FD} as

$$\Omega^{FD} = -T \ln Z_G^{FD} = T \sum_i \ln\left(1 + \exp\left(\frac{\mu - E_i}{T} \right) \right).$$

Grand potential Ω can be used, amongst other things, to derive the mean number of fermions inside the thermodynamical system

$$\langle N^{FD} \rangle = \sum_i n_i = -\left(\frac{\partial \Omega^{FD}}{\partial \mu} \right)_{V,T} = \sum_i \frac{\exp\left(\frac{\mu - E_i}{T} \right)}{\exp\left(\frac{\mu - E_i}{T} \right) + 1}$$

There is a straightforward path from this result to obtain the average number of fermions in a single-particle state

$$n_i = \frac{1}{\exp\left(\frac{E_i - \mu}{T} \right) + 1}.$$

This formula is called the Fermi-Dirac distribution and is the basis for Fermi-Dirac statistics.

There are other properties of fermions. First, they follow the rule of half-integer spin. This means that fermions can have spin only $\frac{1}{2}, \frac{3}{2}, \frac{5}{2}$, etc. Next, the multiparticle wave function is antisymmetric. Finally, fermionic fields follow anticommutation relations

$$\{\psi, \psi\} = \{\overline{\psi}, \overline{\psi}\} = 0, \qquad \{\psi(\vec{x}, t), \overline{\psi}(\vec{y}, t))\} = \gamma^0 \delta(\vec{x} - \vec{y}),$$

where ψ and $\overline{\psi}$ are Dirac spinor and conjugated spinor with spin $\frac{1}{2}$. They are either Grassman-valued fields or field operators depending on whether one considers canonical quantisation or Grassmann path integral representation. This topic will be discussed in more detail in Section 2.2. Finally, γ^0 is a gamma matrix (see Appendix A.3).

Bosons

Bosons behave according to Bose-Einstein statistics. This statistical description was developed by Satyendra Nath Bose in 1924 [16]. Albert Einstein translated Bose's work from English to German and helped Bose publish his findings in the *Zeitschrift für Physik* journal. Einstein later collaborated with Bose on the further development of this theory.

Bosons, in contrast to fermions, do not follow the Pauli exclusion principle. This means that the occupancy number of the bosons n_i^γ is not limited and can be any positive integer. Again, it is possible to construct the grand canonical partition function for a grand canonical ensemble for a system of identical bosons in thermodynamic equilibrium

$$Z_G^{BE} = \sum_\gamma \exp\left(\sum_i n_i^\gamma \frac{\mu - E_i}{T} \right) = \prod_i \frac{1}{1 - \exp\left(\frac{\mu - E_i}{T} \right)},$$

where E_i is the energy of the microstate i, T is the temperature, and μ is the chemical potential. Same as for fermions, it is possible to derive the grand potential

$$\Omega^{BE} = -T\ln Z_G^{BE} = T\sum_i \ln\left(1-\exp\left(\frac{\mu - E_i}{T}\right)\right)$$

and the average number of bosons

$$\langle N^{BE}\rangle = -\left(\frac{\partial\Omega^{BE}}{\partial\mu}\right)_{V,T} = \sum_i \frac{\exp\left(\frac{\mu-E_i}{T}\right)}{1-\exp\left(\frac{\mu-E_i}{T}\right)}.$$

Finally, the expected number of particles in the energy state i will be

$$n_i = \frac{1}{\exp\left(\frac{E_i-\mu}{T}\right)-1}. \tag{2.1}$$

In contrast to the Fermi-Dirac distribution, the equation 2.1 is the basis for Bose-Einstein statistics.

To complete the description of bosons, their properties are in contrast to fermions. They have an integer spin (that is, $0,1,2,...$). Their multi-particle wave function is symmetric. Finally, bosonic fields follow the commutation relations

$$[\phi,\phi] = [\pi,\pi] = 0, \qquad [\phi(\vec{x},t),\pi(\vec{y},t)] = i\delta(\vec{x}-\vec{y}),$$

where $\phi(x)$ is the scalar field and $\pi(x)$ is its conjugate momentum. Similar relations would apply to vector fields A^μ since they are also bosons.

2.1.2 Classification of particles of matter

There are twelve particles of matter, all of which are fermions. The Standard Model presumes that all twelve particles of matter are Dirac fermions and that all twelve particles have their own antiparticle. In total, this involves twelve particles and twelve antiparticles of matter. However, regarding the number of particles and antiparticles of matter, some beyond the Standard Model (BSM) theories assume the Majorana nature of neutrinos. This would imply that neutrinos are antiparticles of themselves.

Leptons

Leptons come in three different flavours, called electron, muon, and tauon. The electron neutrino ν_e was theorised by Wolfgang Pauli in 1930 [17] due to seemingly violated energy conservation in decay β, and in 1956 it was discovered by Clyde Cowan and Frederick Reines [18]. The muon neutrino ν_μ was discovered by Leon M. Lederman, Melvin Schwartz, and Jack Steinberger in 1962 [19] in an experiment at Brookhaven National Laboratory (BNL). The tauon neutrino ν_τ was a direct implication of the existence of the third flavour of leptons [20]. However, direct observation of the tau neutrino ν_τ was performed in 2000 by the DONUT collaboration [21].

There is one phenomenon about neutrinos that the Standard Model cannot explain and that

is their mass. For all fermions, we can use chirality projection operators to obtain components with left-handed and right-handed helicity

$$\psi_L = \frac{1}{2}(1-\gamma_5)\psi, \qquad \psi_R = \frac{1}{2}(1+\gamma_5)\psi, \qquad \overline{\psi}_L = \overline{\psi}\frac{1}{2}(1+\gamma_5), \qquad \overline{\psi}_R = \overline{\psi}\frac{1}{2}(1-\gamma_5),$$

where ψ is the Dirac bispinor, $\overline{\psi} = \psi^\dagger\gamma_0$ is the adjoint bispinor and $\gamma_5 = i\gamma_0\gamma_1\gamma_2\gamma_3$ (see A.3 for more details on gamma matrices γ_μ). One can formulate the Lagrangian density mass term for neutrinos as

$$m_\nu\overline{\nu}\nu = m_\nu\overline{(\nu_L+\nu_R)}(\nu_L+\nu_R) = m_\nu\overline{\nu_L}\nu_R + m_\nu\overline{\nu_R}\nu_L.$$

However, since neither a right-handed neutrino nor a left-handed antineutrino was observed, both terms in the last expression would be zero.

In contrast, kinematic observations of muon and neutron decay energy spectra showed that neutrinos are not massless. One of the kinematic experiments is the Karlsruhe Tritium Neutrino (KATRIN) experiment, which was built to measure the mass of the neutrino on the sub-eV scale. The combined KATRIN runs from 2019 and 2021 resulted in the upper limit of neutrino mass $m_\nu < 0.8$ eV at 90% CL [22] and the experiment continues to improve statistical uncertainties.

Furthermore, Pontecorvo, Maki, Nakagawa, and Sakata proposed the neutrino oscillation [23, 24, 25] as a unitary transformation that relates the eigenbasis of the flavour and the mass eigenbasis

$$\nu_i = U_i^a\nu_a,$$

where ν_i are neutrinos with definite mass m_i, ν_a are neutrinos with definite flavour $(\nu_e, \nu_\mu, \nu_\tau)$, and U_{ai} is the Pontecorvo–Maki–Nakagawa–Sakata matrix. The neutrino oscillation is the outcome of gauge theory with massive neutrinos and indeed this oscillation was measured [26, 27, 28, 29, 30].

Majorana neutrinos could solve this dispute. However, the Majorana neutrino mass term also brings about a violation of lepton-number conservation. This violation would make processes such as neutrinoless double-β decay would be possible. Despite all efforts, this neutrinoless double-β decay was not yet observed.

Neutrinos interact only through weak interaction. This makes any interaction with matter very complicated, and they can easily pass through the planet without any interaction very easily. The amount of neutrino flux from the Sun at Earth is around $\Phi = 7\cdot10^{10}$ cm^{-2}s^{-1} [31] and they are hardly detectable.

To complete the set of six leptons, there are three charged lepton flavours named electron e^-, muon μ^-, and tauon τ^-. Charged leptons (antileptons) carry a negative (positive) value of the elementary charge $|e|$ that can be expressed in SI units as $|e| = 1.602177\cdot10^{-19}$ Q [32]. Their charge causes a much stronger interaction with matter than in the case of neutrinos. Electron e^- was the very first particle of the Standard Model discovered in 1897 by J. J. Thomson [33] due to its intense interaction with matter on large length scales.

Positron, an antiparticle of an electron, was predicted in 1928 by Paul Dirac [34] in his famous paper where he also introduced the Dirac equation, which will be discussed here later in Section

2.2. The positron was discovered by Carl David Anderson in 1932 [35]. Its observable properties are the same as those for the electron, but the charge of the positron is opposite.

Muon μ^- was discovered in 1937 by Carl D. Anderson and Seth Neddermeyer [36]. The muon is heavier flavour of the electron. The heaviest lepton observed is tauon τ^-. This particle was discovered by Martin Lewis Perl, Yung-su Tsai, and his colleagues [20] at the Stanford Linear Accelerator Center (SLAC) and Lawrence Berkeley National Laboratory (LBL). The increase in mass is related to the decrease in the mean lifetime. Both the mass and the mean lifetime for all the tree electron flavours are shown in Table 2.1.

Table 2.1: Masses and mean lifetimes for charged leptons. All values were retrieved from the Review of Particle Physics 2020 [32]

Flavour	Mass m [MeV]	Mean lifetime τ [s]
e	0.510	$> 6.6 \times 10^{35}$
μ	105.658	2.197×10^{-6}
τ	1776.86 ± 0.12	$(290.3 \pm 0.5) \times 10^{-15}$

Leptons do not interact with a strong interaction. This could make them appear to be not that important in the case of studying energy loss in the medium. However, the fact that leptons are essentially connected to electroweak gauge bosons means that we can reconstruct those bosons with charged leptons. Furthermore, if one were to find an appropriate hadronic jet on the "other side" of the same event, one would obtain an energy of the electroweak probe that corresponds to an energy of the hadronic jet not modified by the medium. Comparing this to the actual measurement of modified energy of the hadronic jet, one can directly observe the energy loss inside the strongly interacting medium.

In the case of heavy-ion colliders, neutrinos are the so-called missing energy. This means that we cannot detect them well in those experiments because of their weak interaction with matter. Therefore, we cannot use them much for the study of jet energy loss in relativistic heavy-ion collisions. However, they can still remind us that there is something beyond the standard model.

Quarks and hadrons

Quarks as fundamental particles are confined inside the particles called hadrons. Throughout the last 105 years, numerous hadrons have been discovered that slowly solved the puzzle of more fundamental physics. The proton was discovered in 1886 because it corresponds to the hydrogen ion H^+. However, from a particle physics point of view, it was identified as a particle as we now know it from 1917 by no other than Ernest Rutherford [37]. 15 years after Rutherford's experimental observations on the atomic nucleus, James Chadwick discovered the neutron in 1932 [38] as the second component of the nucleus. Later, in 1947 two hadrons were discovered. The kaon K, the first strange particle was discovered by George Dixon Rochester and Clifford Charles Butler [39], and the pion π was discovered by Cecil Powell, César Lattes, and Giuseppe Occhialini [40].

This pattern of continuous discoveries made Enrico Fermi and Chen-Ning Yang propose the Fermi-Yang model based on the idea that mesons like pions are bound states of nucleon-antinucleon pair. Their 1949 paper [41] clearly states the motivation:

In recent years several new particles have been discovered which are currently assumed to be "elementary", that is, essentially, structureless. The probability that all such particles should really be elementary becomes less and less as their number increases.

This would be in conflict with the Yukawa theory of strong interactions [42], where pion is exchanged between nucleons as a force carrier.

This idea was further extended by Shoichi Sakata when Λ and $\overline{\Lambda}$ hyperons were discovered. Sakata model was introduced in 1956 [43] and effectively added Λ and $\overline{\Lambda}$ for the Fermi-Yang model. Although these models did not describe reality, they proposed a correct idea of the inner structure of some hadrons.

This idea of a hadronic inner structure was further explored by numerous physicists like Yval Ne'eman or Murray Gell-Mann. Their goal was to build a theory of strong interactions upon some symmetry and assign multiplets to mesons and baryons. Ne'eman [44] and Gell-Mann [45] independently described the strong interaction with non-Abelian gauge invariance according to the Yang-Mills prescription [10] with the underlying symmetry group SU(3) in 1961 [44]. The model assumed the existence of vector mesons, which have not yet been discovered, and their role was to be force carriers. Furthermore, vector mesons should have self-coupling interaction and should also carry a charge connected to this theory. Pseudoscalar mesons were connected to the octet, and in this model π^0 and η mesons were predicted. Later that year, Gell-Mann revisited his ideas and his eightfold way model began to focus more on categorisation of hadrons into multiplets as SU(3) representations [46].

With continuous experimental progress, many new resonances such as K^*, Σ^*, ρ, Δ, η, ϕ, Ξ^* were discovered. Both Gell-Mann and Ne'eman were able to fit those observations to their models, and both predicted the existence of a Ω baryon with mass around 1670 MeV. Later, it was discovered [47] and the actual mass of the Ω baryon is 1672.45 ± 0.29 MeV [32].

In 1964, Murray Gell-Mann [48] and George Zweig [49] independently introduced the additive quark model. Zweig called quarks aces. They should be isospin doublet and singlet, all of those three should carry baryon number $\frac{1}{3}$, and $SU(3)_f$ should be adopted as a higher symmetry for strong interactions. It is important to note that the Ne'eman [44] and Gell-Mann [45] work could very well resemble modern colour symmetry $SU(3)_c$. However, $SU(3)_f$ symmetry is flavour symmetry connected to aces (quarks). This symmetry was assumed to be universally broken because of the mass difference among the aces (quarks). Gell-Mann were more detached to making strong statements and wanted to leave the work to experimenters.

Zweig's aces did not remain in the particle physics nomenclature. This could also be due to the fact that George Zweig was a fresh postdoctoral researcher and Murray Gell-Mann was respected and established theoretical physicist. He named quarks after the word in the book Finnegans Wake by James Joyce. In the novel, the protagonist sees seagulls that fly behind the boat in a dream, and they say:

Three quarks for Muster Mark!
Sure he hasn't got much of a bark
And sure any he has it's all beside the mark.

The number three in the original text fits the nature of quarks in well-known baryons. The word itself in the book is taken from a German word of Slavic origin, which represents a dairy product.

The flavour $SU(3)_f$ model was powerful in predicting hadrons. This was due to its multiplet representation. Both baryons and mesons had multiplets. There was baryon octet and decuplet with $J^P = \frac{1}{2}^+$ and $J^P = \frac{3}{2}^+$, respectively. The mesons were represented as an octet of pseudoscalar mesons with $J^{PC} = 0^{-+}$ and an octet of vector mesons with $J^{PC} = 1^{--}$. See Figure 2.1.

The mesons are represented as the direct product of the triplet [3] and antitriplet $\overline{[3]}$ which are fundamental representations. These two fundamental representations correspond to three quarks (u, d, s) and three antiquarks $(\overline{u}, \overline{d}, \overline{s})$ of flavour symmetry $SU(3)_f$. The Kronecker product can be decomposed into the direct sum of multiplets

$$[3] \otimes \overline{[3]} = [8] \oplus [1].$$

This applies to both pseudoscalar and vector mesons. The two octets can be seen with their respective singlets in the middle in the bottom row of Figure 2.1. The singlets are η' for the pseudoscalar mesons and ϕ' for the vector mesons.

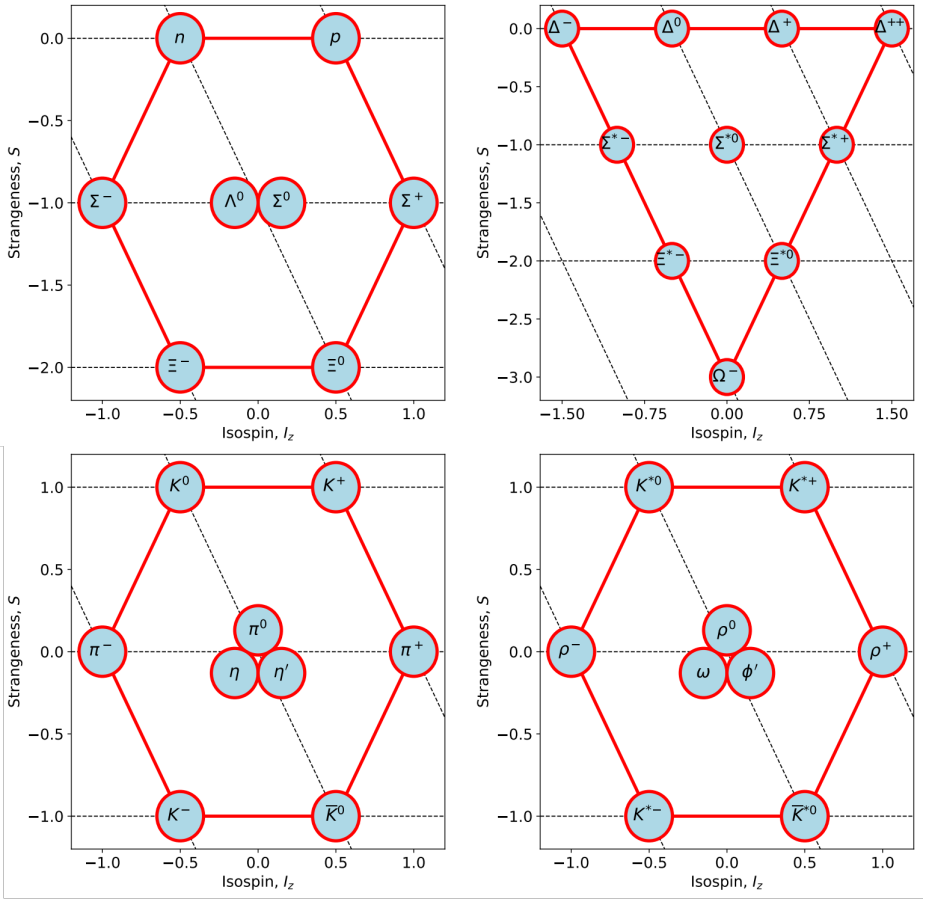

Figure 2.1: Baryon octet (*top left*), baryon decuplet (*top right*), pseudoscalar meson octet and singlet (*bottom left*), and vector meson octet and singlet (*bottom right*). [50]

Baryons (antibaryons) are made up of three quarks (antiquarks). That is why its representation is composed from direct product of three fundamental representations [3] ($\overline{[3]}$) and is decom-

posed into direct sum

$$[3] \otimes [3] \otimes [3] = [10]_S \oplus [8]_M \oplus [8]_M \oplus [1]_A,$$

where two octets with mixed symmetry in flavour are connected by unitary transformation and thus describe same physical states. Furthermore, a flavour singlet baryon that is antisymmetric in flavour cannot exist in the graund state. This leaves the mentioned octet $[8]_M$ and symmetric decuplet $[10]_S$. Both can be seen in the top row of Figure 2.1.

The strong interaction based on the flavour symmetry $SU(3)_f$ assumed the existence of three quarks ($\overline{u}$, $\overline{d}$, $\overline{s}$). However, physicists like James Bjorken and Sheldon Glashow theoretically proposed the fourth quark c in 1964 [51]. This would fix the suppression of flavour-changing neutral current processes and axial anomalies in electroweak interaction. Indeed, it was discovered in the charmonium meson composed of quark c and antiquark $\overline{c}$ in 1974 [52, 53]. This meson was discovered by two independent groups. BNL group led by Samuel Ting gave this new particle the name J [52]. SLAC research group led by Burton Richter called this particle ψ [53]. This resulted in the combined name J/ψ.

This obviously introduced a new underlying symmetry for strong interaction models at that time. A new $SU(4)_f$ symmetry would have fundamental representations of the quartet [4] and the antiquartet $\overline{[4]}$ and three generators of mutual commuting. This would introduce two baryon 20-plets

$$[4] \otimes [4] \otimes [4] = [20]_S \oplus [20]_M \oplus [20]_M \oplus [4]_A,$$

and a 15-plet with a singlet for both pseudoscalar and vector mesons as

$$[4] \otimes \overline{[4]} = [15] \oplus [1].$$

Since there are three commuting generators, multiplets can be displayed on a 3D grid, as can be seen in Figure 2.2.

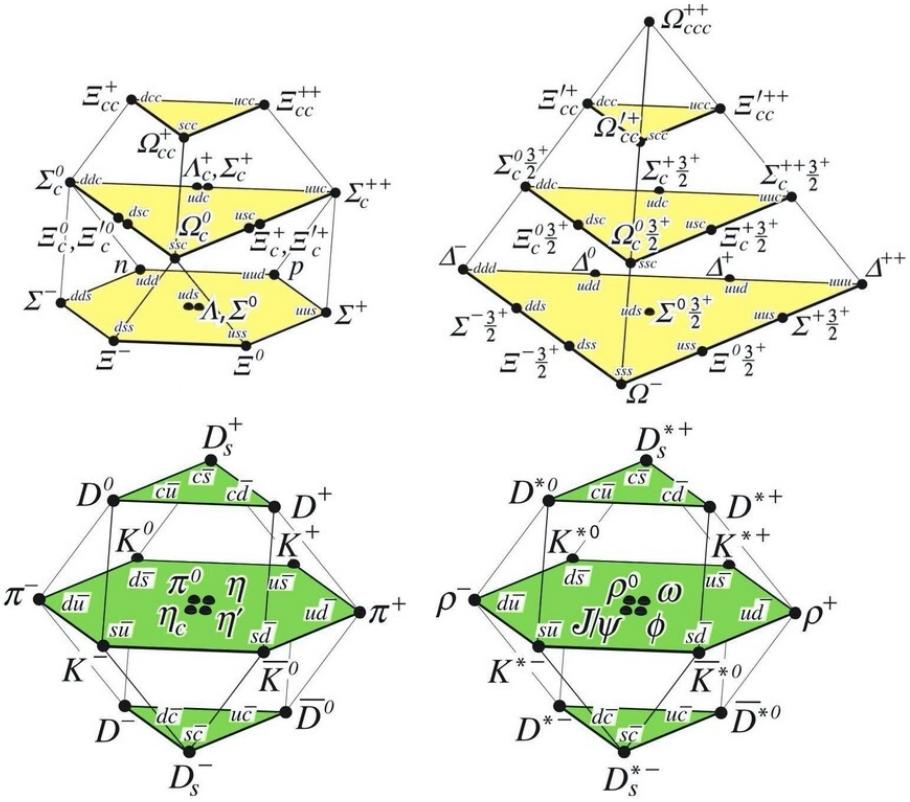

Figure 2.2: Baryon 20-plets (*top row*), pseudoscalar meson 15-plet and singlet (*bottom left*), and vector meson 15-plet and singlet (*bottom right*). [32]

Apart from including a new quark, there were attempts to use flavour-spin underlying symmetry. In the case of $SU(3)_f$, this would mean that the symmetry would be extended to the flavour-spin symmetry $SU(3)_f \times SU(2)_s = SU(6)_{fs}$. Therefore, baryons would be assigned to a fully symmetric 56-plet, despite fermions having fully antisymmetric wave function.

The model also does not explain why free quarks or other exotic bound states, such as diquarks, are not observed. Oscar Greenberg introduced the theoretical concept that quarks are parafermions of rank three in 1964 [54]. This idea could be connected to the later development of QCD and colour SU(3) symmetry. In 1966, Yoichiro Nambu constructed a simple colour confinment model in non-relativistic quantum mechanics [55, 56]. Quarks in this model are infinitely heavy, mesons and baryons have finite mass because of the attractive super-strong force mediated by eight gluons, and other bound states are infinitely heavy too because of the repulsive force. Infinitely heavy states are impossible to observe. More information about this colour confinement is given in Section 2.3 which is dedicated to QCD.

This was the foundation for the quarks with a colour charge. Another lead was also the existence of Δ^{++} baryon with spin $\frac{3}{2}$ that was composed of three u quarks. The fact that quarks are fermions and thus follow the fermi exclusion principle. They should have the same spin orientation, which indicates that there is some other quantum number with three levels or more. This turned out to be exactly three colours due to the measurement of the numerical factor $N_c = 3$ in the production ratio of hdrons to the muonic pair $\mu^-\mu^+$ in the anihilation of the electron e^- and the positron e^+ (see Section 4.3 for more information).

As the colour of the four quarks was established, a new quark was discovered. Similarly to J/ψ, SLAC announced the discovery of the Upsilon meson Υ in 1976-1977 [57, 58]. This quarkonium was composed of a new quark b and an antiquark $\overline{b}$. The last quark t was discovered in 1994 in multijet events [59, 60]. The bound state of the t quark has not yet been discovered.

Quarks experience colour confinement, and thus their bound states have to be colour singlet. The colourless state can be easily reached by combining all three colours, or all three anticolours, or combining the colour and the counterpart anticolour. This cobination represents baryons (three quarks qqq), antibaryons (three antiquraks $\overline{qqq}$), and mesons (quark-antiquark pair $q\overline{q}$).

Table 2.2: Masses and charges of the quarks. All values were retrieved from the Review of Particle Physics 2020 [32].

Flavour	Mass m	Charge Q
u	$2.16^{+0.49}_{-0.26}$ MeV	$\frac{2}{3}e$
d	$4.67^{+0.48}_{-0.17}$ MeV	$-\frac{1}{3}e$
s	93^{-11}_{+5} MeV	$-\frac{1}{3}e$
c	$1.27^{+0.02}_{-0.02}$ GeV	$\frac{2}{3}e$
b	$4.18^{+0.03}_{-0.02}$ GeV	$-\frac{1}{3}e$
t	$172.76^{+0.30}_{-0.30}$ GeV	$\frac{2}{3}e$

There are other ways to construct a colour singlet hadron. For example, tetraquarks that are two quarks and two antiquark states $qq\overline{qq}$, figuratively speaking, two mesons in one state. Another possible way is the pentaquark with a combination $qqqq\overline{q}$ or $q\overline{qqqq}$. Again, figuratively speaking, this combination would be a meson-baryon or a meson-antibaryon combination. Both tetraquarks [61, 62, 63, 64, 65, 66] and pentaquarks [67] were discovered.

The six quarks carry the full name **up** (u), **down** (d), **strange** (s), **charm** (c), **bottom** (b), **top** (t). Their masses and charges can be seen in Table 2.2. All have a colour charge either red r, green g, blue b and their antiparticle counterparts can have colour charges antired $\overline{r}$, antigreen $\overline{g}$, antiblue $\overline{b}$. Because of their charge, they interact strongly via eight gluons.

2.1.3 Force carriers and Higgs boson

The internal symmetry that essentially defines the Standard Model is the local gauge symmetry $\mathrm{SU}(3)_c \times \mathrm{SU}(2)_L \times \mathrm{U}(1)_Y$. SU(3), SU(2), and U(1) are compact reductive Lie groups. SU(3) and SU(2) are non-Abelian Lie groups and U(1) is the belian Lie group.

Intermediate particles arise from the theory when one assumes local gauge symmetry. Their kinetic term along with the interaction term is added to the Lagrangian density to fulfil the stationary action principle, thus making the Lagrangian density invariant.

For each generator of the Lie group, one gauge field has to be added. In total, there are 12

generators of $SU(3)_c \times SU(2)_L \times U(1)_Y$ local gauge symmetry. This means that there are 12 gauge vector fields and thus 12 particles of interaction with spin 1. One generator corresponds to $U(1)_Y$, then there are three generators of $SU(2)_L$, and finally eight generators of $SU(3)_c$ (more about this in Appendix A.4). Let us unravel $SU(2)_L \times U(1)_Y$ and $SU(3)_c$ apart, since the first one corresponds to the EWT and the second symmetry describes the QCD.

Electroweak bosons

Each gauge field is introduced to preserve electroweak symmetry $SU(2)_L \times U(1)_Y$. There are the same number of fields as there are generators of the Lie group. There are three weak isospin generators T^i and one weak hypercharge generator Y. The four Yang-Mills fields that arise directly from electroweak local symmetry, interestingly, do not correspond to physical electroweak bosons W^+, W^-, Z, γ. There are three gauge fields of $SU(2)_L$ symmetry that are called weak isospin bosons W^i and one field connected to $U(1)_Y$ called a weak hypercharge boson B. Gauge fields are massless vector fields. The mass term in Lagrangian density would violate the local gauge invariance.

The eigenvalues of the third component of the weak isospin generator T^3 and the weak hypercharge generator Y_W are connected to the charge of the particle as

$$Q = \left(T_3 + \frac{1}{2}Y\right).$$

Eigenvalues of the weak isospin projection and the weak hypercharge of the fermions can be seen in Table 2.3. They are divided into right-handed and left-handed components due to the different treatment of those cpmponents in EWT. The weak isospin field W^i couples only to left-handed particles. This is why interaction via $W^\pm$ shows a maximum parity, and thus the V-A theory works as a low-energy approximation violation. Furthermore, the interaction of the Z boson with fermions partially violates parity.

Table 2.3: Eigenvalues of the third component of the weak isospin generator T^3 and the weak hypercharge generator Y_W of quarks and leptons.

Left-handed			Right-handed		
fermion	T_3	Y_W	fermion	T_3	Y_W
u_L, c_L, t_L	$+\frac{1}{2}$	$+\frac{1}{3}$	u_R, c_R, t_R	0	$+\frac{4}{3}$
d_L, s_L, b_L	$-\frac{1}{2}$	$+\frac{1}{3}$	d_R, s_R, b_R	0	$-\frac{2}{3}$
e_L^-, μ_L^-, τ_L^-	$-\frac{1}{2}$	-1	e_R^-, μ_R^-, τ_R^-	0	-2
ν_L	$+\frac{1}{2}$	-1			

When gauge field is introduced into the Lagrangian density, there is a coupling constant in the covariant derivative that dictates the strength of the given interaction mediated by this gauge field. There are two couplings in electroweak theory that can be used to determine the coupling of electromagnetism e as

$$e = \frac{g g'}{\sqrt{g^2 + g'^2}}.$$

First, the weak isospin coupling g dictates the interaction strength of the weak isospin field W^i. Since Fermi theory was the precursor to EWT, the weak isospin coupling g is interlinked with the Fermi constant G_F as

$$\frac{G_\mathrm{F}}{\sqrt{2}} = \frac{g^2}{8m_W^2} \quad \Longrightarrow \quad g^2 = \frac{8G_\mathrm{F}m_W^2}{\sqrt{2}},$$

where $m_W = 80.4335 \pm 0.0094$ GeV [68] is the mass of the $W^\pm$ bosons. The weak hypercharge coupling g' represents the strength of the weak hypercharge field B.

Physical fields W^+, W^-, Z, γ emerge as a linear combination of the original Yang-Mills fields B, W_1, W_2, W_3. Neutral electroweak intermediate particles γ and Z are combination of the weak hypercharge boson B and the third component of the weak isospin triplet W^3 by means of the Weinberg angle θ_W rotation as

$$\begin{pmatrix} \gamma \\ Z \end{pmatrix} = \begin{pmatrix} \cos\theta_W & \sin\theta_W \\ -\sin\theta_W & \cos\theta_W \end{pmatrix} \begin{pmatrix} B \\ W_3 \end{pmatrix}.$$

$W^\pm$ are simply combined from the first and second components of the weak isospin bosons triplet

$$W^\pm = \frac{1}{\sqrt{2}}(W_1 \mp iW_2),$$

so they are Hermitian adjoint fields to each other $W^\pm = \left(W^\mp\right)^\dagger$. Weak bosons $W^\pm$ are the only gauge bosons that carry charge $Q = \pm e$ and have a non-zero third component of the weak isospin $T_3 = \pm 1$. All gauge bosons have zero weak hypercharge.

The photon γ has been established as a particle since Isac Newton. The observation of $W^\pm$ and Z had to wait a few centuries. The weak bosons were observed by the UA1 collaboration led by Carlo Rubbia [69, 70] and UA2 collaboration led by Pierre Darriulat [71, 72] at the Super Proton Synchrotron (SPS) in 1983.

The weinberg angle θ_W is related to electroweak coupling constants

$$\sin\theta_\mathrm{W} = \frac{e}{g}, \qquad \cos\theta_\mathrm{W} = \frac{g}{\sqrt{g^2 + g'^2}}, \qquad \sin\theta_\mathrm{W} = \frac{g'}{\sqrt{g^2 + g'^2}},$$

or to weak boson masses

$$\cos\theta_\mathrm{W} = \frac{m_W}{m_Z}.$$

It important to say once again that masses of weak bosons $m_W = 80.4335 \pm 0.0094$ GeV [68] and $m_Z = 91.1876 \pm 0.0021$ GeV [32] do not arise from gauge theory itself. This is also true for fermions. The reason, as already mentioned, is Lagrangian density invariance. The Standard Model includes ingenious solution to this issue in the form of spontaneous symmetry breaking.

Higgs field, Goldtone bosons, and spontaneous symmetry breaking

Higgs mechanism, also known as Anderson-Brout-Englert-Guralnik-Hagen-Higgs-Kibble-'t Hooft (ABEGHHK'tH) mechanism [73, 74, 75, 76, 77], along with the scalar field are necessary ingredients to achieve tree-level unitarity and mass terms for fermions and weak bosons without

violating Lagrangian density invariance.

The Higgs field, or alternatively the Higgs-Goldstone field, is a doublet of the complex scalar field in the Standard Model. This means that the Higgs-Goldstone field Φ has four independent real components

$$\Phi = \begin{pmatrix} \phi^+ \\ \phi^0 \end{pmatrix} = \begin{pmatrix} \phi_1 + i\phi_2 \\ \phi_3 + i\phi_4 \end{pmatrix}.$$

This scalar field is introduced to the Standard Model Lagrangian density with the usual kinetic term with covariant derivative, with the so-called potential $V(\Phi)$, and Higgs-fermion Yukawa interaction terms.

The Higgs potential reads as

$$V(\Phi) = -\mu^2 \Phi^\dagger \Phi + \lambda \left(\Phi^\dagger \Phi\right)^2.$$

It has a negative mass term with mass μ and a quadratic self-coupling term with the coupling constant λ. The doublet nature of the Higgs-Goldstone field implies $\Phi^\dagger\Phi = \phi_1^2 + \phi_2^2 + \phi_3^2 + \phi_4^2$ and thus the $O(4)$ symmetry of the Higgs potential $V(\Phi)$ in this parameterisation.

Higgs potential shifts the minimum energy density state of the Higgs-Goldstone field so that it does not lie at zero. The ground state of the Higgs-Goldstone field is described by a non-zero constant field that is also infinitely degenerate. This minimisation of energy happens for a field configuration

$$\Phi_0^\dagger \Phi_0 = \frac{v^2}{2}, \quad \text{where} \quad v = \frac{\mu}{\sqrt{\lambda}}.$$

The position of the ground state can be determined by one radial component and three angular components, since the potential possesses O(4) symmetry. The Higgs-Goldstone field can be effectively rewritten to those components with one massive Higgs field H and three Goldstone massless fields π^i as

$$\Phi = \exp\left(\frac{i}{v}\pi^i \sigma_i\right) \begin{pmatrix} 0 \\ \frac{1}{\sqrt{2}}(v + H) \end{pmatrix},$$

where the mass of the Higgs field is $m_H = \sqrt{2\lambda}v = \sqrt{2}\mu = 125.25 \pm 0.17$ GeV and σ_i are Pauli matrices (see Appendix A.4 for more details on Pauli matrices). The Lagrangian density is invariant with respect to the symmetry $\mathrm{SU}(2)_L$, but the ground state is not. This is called spontaneous symmetry braking. There are three unphysical, massless fields that are associated with the potential. Now, it is possible to employ the SU(2) gauge fixing transformation, that is called a U-gauge. With this choice, we require $\pi^i = 0$. This will remove unphysical Goldstone bosons from the Higgs-Goldstone field

$$\Phi_U = \begin{pmatrix} 0 \\ \frac{1}{\sqrt{2}}(v + H) \end{pmatrix}.$$

As a convenient byproduct, spontaneous symmetry braking will bring the mass terms to electroweak bosons via covariant derivative interaction and constant shift in the Higgs field with the U-gauge. Bosons B, W_1, W_2, W_3 will then decouple into W^+, W^-, Z, γ and the result is three

massive bosons $W^{\pm}, Z$ with masses

$$m_W = \frac{g}{2}v = \left(\frac{\pi\alpha}{\sqrt{2}G_{\mathrm{F}}}\right)\frac{1}{\sin\theta_{\mathrm{W}}},$$
$$m_Z = \frac{\sqrt{g^2+g'^2}}{2}v = \left(\frac{\pi\alpha}{\sqrt{2}G_{\mathrm{F}}}\right)\frac{1}{\sin\theta_{\mathrm{W}}\cos\theta_{\mathrm{W}}},$$

and one massless photon γ. It can also be understood that the massless Goldstone bosons transformed into the longitudinal polarisations of weak vector bosons and thus obtained mass. Since the photon γ does not have mass, it also lacks longitudinal polarisation in its non-virtual state.

The Higgs mechanism is the spontaneous braking of the symmetry $\mathrm{SU}(2)_L \times \mathrm{U}(1)_Y$ to the symmetry $\mathrm{U}(1)_{\mathrm{EM}}$. Lie group $\mathrm{U}(1)_{\mathrm{EM}}$ is the local underlying symmetry of QED. From the four-component Higgs-Goldstone field, only one physical field remains. It is commonly called the Higgs field carrying electric charge $Q = 0$, mass $m_H = 125.10 \pm 0.17$ GeV [32], weak isospin is $T_3 = \frac{1}{2}$, and weak hypercharge $Y_W = 1$.

It was experimentally confirmed by A Toroidal LHC ApparatuS (ATLAS) experiment [78] and the Compact Muon Solenoid (CMS) experiment [79] at LHC.

An additional important note is that recent results of $m_W = 80.4335 \pm 0.0094$ GeV from the Collider Detector at Fermilab II (CDF II) [68] show a discrepancy between experimental measurement and the Standard Model prediction. This could be an indication of BSM physics.

Gluons

The underlying symmetry of a strong interaction is $\mathrm{SU}(3)_c$ with a triplet of colours and an antitriplet of anticolours as a representation. Lie group SU(3) has eight generators $\lambda_{\text{д}}$, where д and other Cyrillic indices run from 1 to 8. Generators $\lambda_{\text{д}}$ are linearly independent 3×3 traceless Hermitian matrices. One possible representation is with Gell-Mann matrices, and in this thesis $\lambda_{\text{д}}$ will be assumed to represent eight Gell-Mann matrices (see Appendix A.4).

Eight gauge vector fields are introduced to preserve Lagrangian density invariance under $\mathrm{SU}(3)_c$. The colour representation of the gluons is according to $\mathrm{SU}(3)_c$. Gluons carry colour and anticolour, and therefore $\mathrm{SU}(3)_c$ adjoint multiplet of gluons can be described as

$$[3] \otimes \overline{[3]} = [8] \oplus [1].$$

Here we can see the colour octet [8] that can be expressed in the Gell-Mann matrix representation

$$\begin{aligned}
&(r\overline{b} + b\overline{r})/\sqrt{2}, && -i(r\overline{b} - b\overline{r})/\sqrt{2},\\
&(r\overline{g} + g\overline{r})/\sqrt{2}, && -i(r\overline{g} - g\overline{r})/\sqrt{2},\\
&(b\overline{g} + g\overline{b})/\sqrt{2}, && -i(b\overline{g} - g\overline{b})/\sqrt{2},\\
&(r\overline{r} - b\overline{b})/\sqrt{2}, && (r\overline{r} + b\overline{b} - 2g\overline{g})/\sqrt{6},
\end{aligned}$$

and colour singlet [1] that can be described as a normalised 3×3 unity matrix

$$\frac{1}{\sqrt{3}}(r\overline{r} + g\overline{g} + b\overline{b}).$$

Colour singlet gluon would not feel colour confinement (see Section 2.3.3). The reason is that the singlet gluon would be colour neutral. The white gluon would behave more like a photon, and it would imply an infinite range of the strong interaction. This behaviour was not experimentally observed in QCD. The exclusion of the colour neutral gluon reflects that the underlying symmetry of QCD is $SU(3)_c$ rather than $U(3)_c$ symmetry.

Unbroken gauge invariance requires that massless gauge bosons. This is also true for $W^{\pm}$ and Z. The mass terms with m_W and m_Z are obtained from the Higgs mechanism explained above. Only three Goldstone bosons are absorbed in the gauge and three mass terms are generated. The photon γ and eight gluons remain massless according to the Standard Model.

Ne'eman [44] and Gell-Mann [45] predicted the self-coupling interaction for vector mesons in their SU(3) strong interaction model. This was a decent prediction for QCD. Eight vector mesons are replaced by eight gluons, and they can interact with each other because of their colour charge. This self-interaction effectively limits the range of the stong interaction to ~ 1 fm. This still makes possible strong interaction between hadrons on short length scales. For example, nucleons can be bounded inside the atomic nucleus, but the nuleon density inside the nucleus shows saturation because of the limited reach of this interaction.

The gluon was experimentally measured by the experiments PLUTO, TASSO, MARK-J and JADE in anihilation of the electron e^- and the positron e^+[80, 81, 82, 83, 84, 85] between 1978-1980. Bottomonium Υ decays into three gluons ($e^-e^+ \to \Upsilon \to ggg$) approximately in 97% cases. Another measured process, dominant at that time, is $e^-e^+ \to q\overline{q}g$. After the anihilation, the photon splits into a quark-antiquark pair $q\overline{q}$, and one of the quarks radiates the gluon. In this process, three jets of hadrons are measured, where two of them are narrow and correspond to the quark and the antiquark. The last jet is wider and corresponds to gluon.

Gluon radiation is one of the primary sources of energy loss within the medium. When a electrically charged lepton goes through the electromagnetic medium (i.e. atmosphere), it radiates photons. Similarly to QED, when quarks or gluons, collectively called partons, go through the medium, they can radiate gluons. At the detector level, it is possible that the energy of this gluon falls outside the reconstructed jet cone. Energy loss of a composite object like a jet does not make sense at the parton level since energy is always conserved. However, we measure this phenomenon at the detector level as out-of-the-cone energy loss.

2.1.4 Summary of particles of the Standard Model

There are three generations of leptons and quarks. Regarding leptons, there are three charged leptons (e^-, μ^-, τ^-) and three neutrinos ($\nu_e^-, \nu_\mu^-, \nu_\tau^-$). Six quarks ($u, d, c, s, t, b$) have electric and colour charges. On top of that, there are another 12 antiparticles as a counterpart to each particle of matter. Antiparticles carry opposite electric and colour charges and, in the case of neutrinos , they exist with the opposite chirality.

The 24 particles of matter ($e^-, \mu^-, \tau^-, \nu_e^-, \nu_\mu^-, \nu_\tau^-, u, d, c, s, t, b$ + antiparticles) can interact through three weak bosons $W^{\pm}, Z$. Weak bosons can interact with each other as well. Only electrically charged particles can interact with the photon γ. This essentially excludes neutrinos ($\nu_e^-, \nu_\mu^-, \nu_\tau^-$), the Higgs boson H, gluons g, and γ itself. Higgs cannot interact with the photon γ and the gluons g. Since there is no experimentally established right-handed neutrino, the Standard Model

does not recognise the mass of the neutrino, and thus neutrinos do not interact with the Higgs boson. Finally, the gluons mediate a strong force between themselves and the quarks.

All the mentioned particles (apart from the antiparticles of matter) are visualised in Figure 2.3.

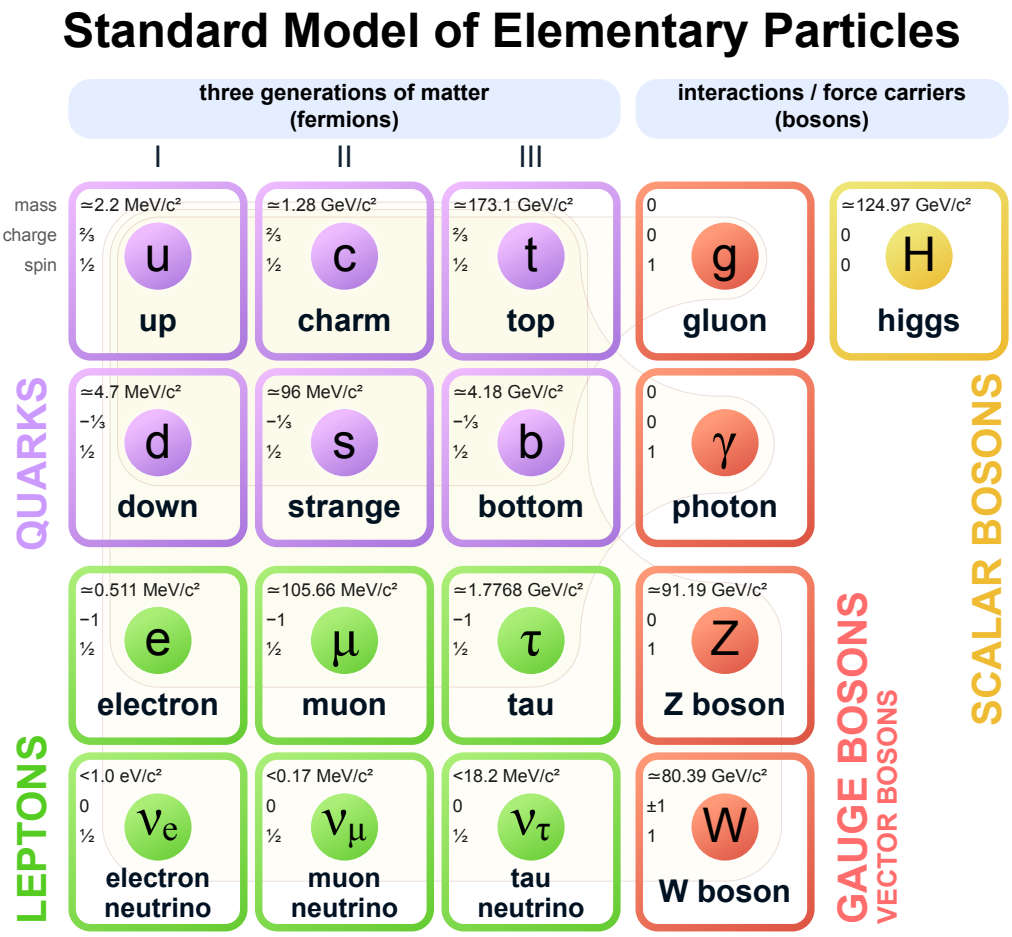

Figure 2.3: Particles of the Standard Model. [86]

2.2 Quantum Field Theory

2.2.1 Relativistic quantum mechanics introduction

Quantum mechanics had great success from the beginning and was essential in the foundation of modern particle physics. Max Planck, Albert Einstein, Niels Bohr, Erwin Schrödinger, Paul Dirac, Max Born, Louis de Broglie, Werner Heisenberg, Wolfgang Pauli, and many others introduced a way of treating the subatomic world between 1900 and 1930.

With the special theory of relativity, Oskar Klein [87] and Walter Gordon [88] introduced their

equation for a spinless particle in 1926

$$(\Box + m^2)\phi = 0,$$

where $\Box$ is the d'Alambert operator (see Appendix A.2). The wave function ϕ represents the solution of this Klein-Gordon equation for the scalar boson. Shortly after, in 1928, Paul Dirac introduced [34] his equation for particles with spin $\frac{1}{2}$

$$(i\not{\partial} - m)\psi = 0,$$

where $\not{\partial} = \gamma^\mu \partial_\mu$ is the 4×4 differential operator (see Appendix A.3 for more information on gamma matrices γ^μ, Clifford algebra $\mathrm{Cl}_{1,3}(\mathbb{R})$, or Feynman's slash notation). This makes m a diagonal 4×4 matrix with the mass of the Dirac particle on the diagonal. Finally, ψ is a reducible four-dimensional representation of $\left(\frac{1}{2}, 0\right) \oplus \left(0, \frac{1}{2}\right)$. Both $\left(\frac{1}{2}, 0\right)$ and $\left(0, \frac{1}{2}\right)$ are representations of the Lorentz group $\mathrm{SO}(3,1)$. It is also useful to define the Dirac adjoint $\psi^\dagger(x)\gamma^0 = \overline{\psi}(x)$ of the spinor field ψ for later use.

According to Richard Feynman, when he met Paul Dirac for the first time, after a long silence, Dirac said [89]:

I have an equation; do you have one too?

The last particle spices that occur in the Standard Model are vector gauge bosons with spin 1. Alexandru Proca introduced the equation [90] for this particle with mass m as

$$\partial_\mu F^{\mu\nu} + mA^\nu = 0,$$

where $F^{\mu\nu}$ is an electromagnetic tensor defined by the exterior derivative of a differential 1-form expressed as

$$F \equiv \mathrm{d}A,$$

where A^μ is a complex 4-potential of the vector boson (see Appendix A.2). Consequently, one can rewrite this in covariant form as

$$F_{\mu\nu} = \partial_\mu A_\nu - \partial_\nu A_\mu.$$

Relativistic quantum mechanics is lacking for our purposes. There is no simple and elegant way to include multiparticle interaction, and even the two-body problem is rather complicated. This kind of description is not utilisable for unstable particles or for higher energies, where pairs of particles can be created. Even energy fluctuations are enough to create and annihilate particles. There are also some problems with probabilistic interpretations of the Klein-Gordon equation. This thesis is focused on the evolution of a multiparticle object that interacts with the medium, where splittings and scatterings of its components often occur. This is why QFT has to be introduced.

2.2.2 Classical field theory

QFT is built on the classical field theory of Lagrangian and Hamiltonian mechanics. There are several options to express QFT. Richard Feynman even described it on QED as [89]:

Quantum electrodynamics is made to appear more difficult than it actually is by the very many equivalent methods by which it may be formulated.

The two complementary methods are Canonical quantisation and Functional integral approach. Both formulations start with the classical Lagrangian density $\mathscr{L}$ and evolve into the quantum field perturbation theory

Lagrangian density $\mathscr{L}$ is connected to action $\mathcal{S}$ as

$$\mathcal{S} = \int \mathrm{d}x^4 \mathscr{L}(\phi_i, \partial_\mu \phi_i),$$

where ϕ_i are fields included in classical field theory. It is possible to use variational derivative calculus to calculate the variation of an action

$$\delta\mathcal{S} = \int \mathrm{d}x^4 \left[\frac{\partial \mathscr{L}}{\partial \phi_i} \delta\phi_i + \frac{\partial \mathscr{L}}{\partial(\partial_\mu \phi_i)} \delta(\partial_\mu \phi_i) \right] = \int \mathrm{d}x^4 \left[\frac{\partial \mathscr{L}}{\partial \phi_i} \delta\phi_i - \partial_\mu \left(\frac{\partial \mathscr{L}}{\partial(\partial_\mu \phi_i)} \right) \delta\phi_i \right].$$

Action $\mathcal{S}$ is significant, since the equations of motion of the system can be derived from the stationary action principle

$$\delta\mathcal{S} = 0.$$

This principle leads to a powerful Euler-Lagrange equation

$$\partial_\mu \left(\frac{\partial \mathscr{L}}{\partial(\partial_\mu \phi_i)} \right) - \frac{\partial \mathscr{L}}{\partial \phi_i} = 0. \tag{2.2}$$

That is the key equation how to derive equations of motion in classical field theory. It is possible to employ it on the classical Lagrangian densities

$$\mathscr{L}_{\text{scalar}} = \frac{1}{2} \partial^\mu \phi \partial_\mu \phi - \frac{1}{2} m^2 \phi^2, \tag{2.3}$$

$$\mathscr{L}_{\text{Dirac}} = \overline{\psi}(i\not{\partial} - m)\psi, \tag{2.4}$$

$$\mathscr{L}_{\text{gauge}} = -\frac{1}{4} F^{\mu\nu} F_{\mu\nu} - \frac{1}{2} m^2 A_\mu A^\mu. \tag{2.5}$$

That leads to the Klein-Gordon, Dirac, and Proca equations. In field theory, the interaction arises with additional terms in the Lagrangian density. The interaction mediated by vector bosons A^μ is added via the covariant derivative

$$\partial^\mu \to D^\mu = \partial_\mu + ieA^\mu.$$

This ensures interaction with scalar fields, Dirac fields, and other vector fields. The interaction between the scalar field and the Dirac fields is carried out through the Yukawa interaction

$$\mathscr{L}_{\text{Yukawa}} = g_{\text{Y}} \overline{\psi} \phi \psi,$$

where g_{Y} is a coupling of the Yukawa interaction. [42] Scalar interaction is just simply

$$\mathscr{L}_{\text{int}} = -\frac{\lambda_3}{3!}\phi^3 - \frac{\lambda_4}{4!}\phi^4,$$

where first term denotes a three-point interaction and the second term stands for a four-point interaction. Other interaction terms like Fermi four-point-fermion interaction do not appear in the Standard Model.

Another classical formulation of classical field theory is made in terms of Hamiltonian density $\mathscr{H}$. The relationship between Lagrangian density $\mathscr{L}$ and Hamiltonian density $\mathscr{H}$ states

$$\mathscr{H} = \pi\dot{\phi} - \mathscr{L},$$

where π is conjugate momentum to field ϕ is defined as

$$\pi = \frac{\partial \mathscr{L}}{\partial \dot{\phi}} = \frac{\delta S[\phi]}{\delta \dot{\phi}}.$$

Now the transition from classical filet theory to quantum field theory can be made.

2.2.3 Canonical quantization

First, commutator of two operators is identified as the Poisson bracket

$$-\frac{i}{\hbar}\left[\hat{B},\hat{A}\right] = \{A(\pi,\phi), B(\pi,\phi)\}_{\mathrm{PB}},$$

where the Poisson bracket for the continuous degrees of freedom is defined as

$$\{A(\pi,\phi), B(\pi,\phi)\}_{\mathrm{PB}} = \sum_a \int \mathrm{d}^3x \left[\frac{\delta A}{\delta\phi_a(x)}\frac{\delta B}{\delta\pi_a(x)} - \frac{\delta A}{\delta\pi_a(x)}\frac{\delta B}{\delta\phi_a(x)}\right].$$

In the Shrödinger picture the canonical commutation relation for scalar are

$$[\pi(\vec{x},t),\phi(\vec{x}',t)] = -i\delta^{(3)}(\vec{x}-\vec{x}'), \quad \text{and} \quad [\phi(\vec{x},t),\phi(\vec{x}',t)] = [\pi(\vec{x},t),\pi(\vec{x}',t)] = 0.$$

Here, both the fields ϕ and π are promoted to operators. When the Klein-Gordon equation is solved and expressed in Fourier expansion

$$\phi(x) = \sum_p \left[a(p)e^{-ipx} + a^\dagger(p)e^{ipx}\right].$$

This promotion also includes the creation operator $a(p)$ and the annihilation operator $a^\dagger(p)$. The Lorentz invariant momentum measure in the expansion is defined as

$$\sum_p \equiv \int \frac{\mathrm{d}^3p}{\sqrt{(2\pi)^3 2\omega_p}},$$

where $\omega_p \equiv \sqrt{p^2+m^2}$. The commutation relations between the creation and annihilation operators are

$$\left[a(p), a^\dagger(p')\right] = \delta^{(3)}(\vec{p}-\vec{p}').$$

The Dirac equation can be solved and expanded into a Fourier expansion as

$$\psi(x) = \sum_p \sum_\lambda \left(a(p,\lambda)u(p,\lambda)e^{-ipx} + b^\dagger(p,\lambda)v(p,\lambda)e^{ipx}\right), \tag{2.6}$$

$$\psi^\dagger(x)\gamma^0 = \overline{\psi}(x) = \sum_p \sum_\lambda \left(b(p,\lambda)\overline{v}(p,\lambda)e^{-ipx} + a^\dagger(p,\lambda)\overline{u}(p,\lambda)e^{ipx}\right), \tag{2.7}$$

where λ denotes helicity

$$\lambda = \frac{1}{2}\vec{\sigma}\cdot\frac{\vec{p}}{|\vec{p}|}.$$

Then fields $\psi(x)$ and $\overline{\psi}(x)$, creation operators $a(p,\lambda)$, $b(p,\lambda)$ and annihilation operators $a^\dagger(p,\lambda)$, $b^\dagger(p,\lambda)$ are promoted to operators. Positive and negative energy plane wave solutions are represented by $u(p,\lambda)\mathrm{e}^{-ipx}$ and $v(p,\lambda)\mathrm{e}^{ipx}$ respectively.

In contrast to bosons, atomic spectroscopy showed that the wave function of two electrons is antisymmetric. This was already mentioned in Section 2.1.1 and this is true for all fermions. For this reason, the creation and annihilation operators must satisfy anticommutation relations rather than commutation.

The anticommutation relations of the field ψ and its conjugate momentum $\pi = i\psi^\dagger$ are

$$\left\{\psi\left(\vec{x},t\right),\pi\left(\vec{x}',t\right)\right\} = i\left\{\psi\left(\vec{x},t\right),\psi^\dagger\left(\vec{x}',t\right)\right\} = i\delta^{(3)}\left(\vec{x}-\vec{x}'\right),$$

$$\left\{\psi\left(\vec{x},t\right),\overline{\psi}\left(\vec{x}',t\right)\right\} = \gamma_0\delta^{(3)}\left(\vec{x}-\vec{x}'\right).$$

From anticommutation relations and the solutions in equations (2.6) and (2.7) it is easy to derive anticommutation relations of the creation and anihilation operators

$$\left\{a\left(p,\lambda\right),a^\dagger\left(p',\lambda'\right)\right\} = \left\{b\left(p,\lambda\right),b^\dagger\left(p',\lambda'\right)\right\} = \delta^{(3)}\left(\vec{p}-\vec{p}'\right)\delta_{\lambda\lambda'}.$$

Other anticommutation relations between ψ, $\overline{\psi}$, a, $a^\dagger$, b, $b^\dagger$ are equal to zero. In other words, they are anticommutative.

The similar procedure is applied for vector bosons. The solution of the Proca equation is

$$A_\mu(x) = \sum_p \sum_\alpha \varepsilon_\mu(p,\alpha)\left[a(p,\alpha)e^{-ip\cdot x} + a^\dagger(p,\alpha)e^{ip\cdot x}\right],$$

where $\varepsilon_\mu(p,\alpha)$ are polarisation unit vectors of polarisation α. There are two polarisations of α for the massless particle and three polarisations for the massive particle. Next, a and $a^\dagger$ are Heisenberg annihilation and creation operators. Since vector particles are bosons, they fulfil exactly the same commutation relations as scalars.

The goal of this theory is to reach perturbation theory. That stats with the normalised generating functional, also called partition function

$$\tilde{Z}\left[\eta,\overline{\eta},J,j^\mu\right] = \frac{Z\left[\eta,\overline{\eta},J,j^\mu\right]}{Z\left[0,0,0,0\right]},$$

where η and $\overline{\eta}$ are Grassmann sources, J is an external source of scalar bosons and j^μ is an external source of vector bosons. The generating functional is an analogue to the moment-generating function in mathematical statistics.

The generating functional is given by the Gell-Mann-Low formula [91] as

$$\tilde{Z}\left[\eta,\overline{\eta},J,j^\mu\right] = \frac{\left\langle 0\left|\hat{T}\left[\mathrm{e}^{i\int \mathrm{d}^4x\left(\mathscr{L}_{\mathrm{int}}+\overline{\psi}\eta+\overline{\eta}\psi+\phi J+j^\mu A_\mu\right)}\right]\right|0\right\rangle}{\left\langle 0\left|\hat{T}\left[\mathrm{e}^{i\int \mathrm{d}^4x\mathscr{L}_{\mathrm{int}}}\right]\right|0\right\rangle},$$

where $|0\rangle$ is the true ground state and $\hat{T}[\cdot]$ is time-ordered product. This can be formally rewritten as

$$\tilde{Z}[\eta,\overline{\eta},J,j^{\mu}] = \\ = \frac{\exp\left(i\int \mathrm{d}^4x \mathscr{L}_{\mathrm{int}}\left[-i\frac{\delta}{\delta\overline{\eta}(x)}, i\frac{\delta}{\delta\eta(x)}, -i\frac{\delta}{\delta J(x)}, -i\frac{\delta}{\delta j^{\mu}(x)}\right]\right)\left\langle 0\left|\hat{T}\left[\mathrm{e}^{i\int \mathrm{d}^4x[\overline{\psi}\eta+\overline{\eta}\psi+\phi J+j^{\mu}A_{\mu}]}\right]\right|0\right\rangle}{\exp\left(i\int \mathrm{d}^4x \mathscr{L}_{\mathrm{int}}\left[-i\frac{\delta}{\delta\overline{\eta}(x)}, i\frac{\delta}{\delta\eta(x)}, -i\frac{\delta}{\delta J(x)}, -i\frac{\delta}{\delta j^{\mu}(x)}\right]\right)\left\langle 0\left|\hat{T}\left[\mathrm{e}^{i\int \mathrm{d}^4x[\overline{\psi}\eta+\overline{\eta}\psi+\phi J+j^{\mu}A_{\mu}]}\right]\right|0\right\rangle\Big|_{\eta,\overline{\eta},J,j^{\mu}=0}},$$

where $\frac{\delta}{\delta\overline{\eta}(x)}$, $\frac{\delta}{\delta\eta(x)}$, $\frac{\delta}{\delta J(x)}$, and $\frac{\delta}{\delta j^{\mu}(x)}$ denote functional derivatives, also called variational derivatives. One can use Wick's theorem to rewrite the time-ordered product with the product of Feynman propagators.

$$\begin{aligned} i\Delta_F(x,y) &= \langle 0|\hat{T}\left[\phi(x)\phi(y)\right]|0\rangle, \\ iS_F(x,y) &= \langle 0|\hat{T}\left[\psi(x)\overline{\psi}(y)\right]|0\rangle, \\ iV_F^{\mu\nu}(x,y) &= \langle 0|\hat{T}\left[A^{\mu}(x)A^{\nu}(y)\right]|0\rangle, \end{aligned}$$

for the scalar field, the Dirac field, and the vector field. The expression for the nonnormalized generating functional $Z[\eta,\overline{\eta},J,j^{\mu}]$ according to Wick's theorem [92] will be

$$Z[\eta,\overline{\eta},J,j^{\mu}] = \exp\left(i\int \mathrm{d}^4x \mathscr{L}_{\mathrm{int}}\left[-i\frac{\delta}{\delta\overline{\eta}(x)}, i\frac{\delta}{\delta\eta(x)}, -i\frac{\delta}{\delta J(x)}, -i\frac{\delta}{\delta j^{\mu}(x)}\right]\right)\times \\ \times\exp\left[i\int \mathrm{d}^4x\mathrm{d}^4y\left(\overline{\eta}(x)S_F(x,y)\eta(y) - \frac{1}{2}J(x)\Delta_F(x,y)J(y) + \frac{1}{2}j_{\mu}(x)V_F^{\mu\nu}(x,y)j_{\nu}(y)\right)\right]. \tag{2.8}$$

This form of generating functional is used to calculate Green functions in QFT. However, it is not possible to express $\exp\left(i\int \mathrm{d}^4x \mathscr{L}_{\mathrm{int}}\left[-i\frac{\delta}{\delta\overline{\eta}(x)}, i\frac{\delta}{\delta\eta(x)}, -i\frac{\delta}{\delta J(x)}, -i\frac{\delta}{\delta j^{\mu}(x)}\right]\right)$ directly and it is necessary to use the Taylor expansion. The order of the Taylor expansion is the order of the perturbative calculation. After calculating $\tilde{Z}$ with this perturbative approach, one can use the functional derivative with respect to the source functions and calculate the $(2m+n+k)-$point Green function

$$\langle x_1...x_m y_1...y_m z_1...z_n w_1...w_k\rangle = \\ = \prod_{l=1}^{m}\left(-i\frac{\delta}{\delta\bar{\eta}(y_l)}\right)\prod_{j=1}^{m}\left(i\frac{\delta}{\delta\eta(z_j)}\right)\prod_{i=1}^{n}\left(-i\frac{\delta}{\delta J(x_i)}\right)\prod_{i=1}^{k}\left(-i\frac{\delta}{\delta j^{\mu}(x_i)}\right)\tilde{Z}[\eta,\overline{\eta},J,j^{\mu}]\Big|_{\eta,\bar{\eta},J,j^{\mu}=0}.$$

2.2.4 Functional integral

The functional integral formulation starts with the gauge-invariant functional integral measure composed of measures of the Grassman fields ψ and $\overline{\psi}$ and of the c-number fields ϕ and A^{μ} that are proportional to

$$\begin{aligned} \mathscr{D}\psi &\sim \lim_{N\to+\infty}\prod_{i=1}^{N}\mathrm{d}\psi(x_i), \quad \mathscr{D}\overline{\psi} \sim \lim_{N\to+\infty}\prod_{i=1}^{N}\mathrm{d}\overline{\psi}(x_i), \\ \mathscr{D}\phi &\sim \lim_{N\to+\infty}\prod_{i=1}^{N}\mathrm{d}\phi(x_i), \quad \mathscr{D}A \sim \lim_{N\to+\infty}\prod_{i=1}^{N}\prod_{\mu=0}^{4}\mathrm{d}A^{\mu}(x_i). \end{aligned}$$

The proportionality constant is not in the scope of interest, as it is cancelled out by normalisation of the partition function $\tilde{Z}[\eta,\overline{\eta},J,j^\mu]$. The generating function $\tilde{Z}[\eta,\overline{\eta},J,j^\mu]$ in the integral functional representation is expressed as

$$\tilde{Z}[\eta,\overline{\eta},J,j^\mu] = \frac{\int \mathscr{D}\psi\mathscr{D}\overline{\psi}\mathscr{D}\phi\mathscr{D}A\exp\left(i\mathcal{S}[\psi,\overline{\psi},\phi,A^\mu]+i\int \mathrm{d}^4x[\overline{\psi}\eta+\overline{\eta}\psi+\phi J+j^\mu A_\mu]\right)}{\int \mathscr{D}\psi\mathscr{D}\overline{\psi}\mathscr{D}\phi\mathscr{D}A\exp\left(i\mathcal{S}[\psi,\overline{\psi},\phi,A^\mu]\right)}, \quad (2.9)$$

where

$$\mathcal{S}[\psi,\overline{\psi},\phi,A^\mu] = \int \mathrm{d}^4x\left[\mathscr{L}_{\text{scalar}}+\mathscr{L}_{\text{Dirac}}+\mathscr{L}_{\text{gauge}}+\mathscr{L}_{\text{int}}(\psi,\overline{\psi},\phi,A^\mu)\right] =$$
$$= \int \mathrm{d}^4x\left[\frac{1}{2}\partial^\mu\phi\partial_\mu\phi-\frac{1}{2}m^2\phi^2+\overline{\psi}(i\not{\partial}-m)\psi-\frac{1}{4}F^{\mu\nu}F_{\mu\nu}-\frac{1}{2}m^2A_\mu A^\mu+\mathscr{L}_{\text{int}}(\psi,\overline{\psi},\phi,A^\mu)\right].$$

$\mathcal{S}[\psi,\overline{\psi},\phi,A^\mu]$ is the action of interacting scalar, Dirac, and vector fields. If vector field A^μ is a gauge field, then both action and integral measure are gauge invariant. This means that this naive approach would integrate over an infinite number of redundant degrees of freedom. This is solved by introducing the Faddeev-Popov ghost [93]. Introducing the Faddeev–Popov $\Delta[A]$ determinant in the partition function with the functional integral identity

$$1 = \Delta[A]\int \mathscr{D}U\delta[\mathscr{F}(A[U])],$$

where the Haar measure $\mathscr{D}U$ is on the infinite dimensional Lie group of gauge transformations U and $\mathscr{F}(A[U])$ as a gauge fixing condition. The partition function for the free gauge filed will look like this

$$Z[j^\mu] = \int \mathscr{D}U\int \mathscr{D}A\left(\Delta[A]\delta[\mathscr{F}(A)]e^{-S[A]}\right).$$

When the gauge is fixed, there are no longer redundant degrees of freedom, the partition function is well behaved, and ghost c and antighost $\overline{c}$ Grassman fields are introduced in the Lagrangian density. [94] Gauge-fixed Lagrangian density is no longer gauge invariant but is invariant under the Becchi-Rouet-Stora-Tyutin transformation. [94] In the functional derivative approach, the $(2m+n+k)$-point Green function can be calculated directly as

$$\langle x_1...x_m y_1...y_m z_1...z_n w_1...w_k\rangle =$$
$$= \frac{\int \mathscr{D}\psi\mathscr{D}\overline{\psi}\mathscr{D}\phi\mathscr{D}A\left[\psi(x_1)...\psi(x_m)\overline{\psi}(y_1)...\overline{\psi}(y_n)\phi(z_1)...\phi(z_n)A(w_1)...A(w_k)\exp\left(i\mathcal{S}[\psi,\overline{\psi},\phi,A^\mu]\right)\right]}{\int \mathscr{D}\psi\mathscr{D}\overline{\psi}\mathscr{D}\phi\exp\left(i\mathcal{S}[\psi,\overline{\psi},\phi,A^\mu]\right)}.$$

Alternatively, it is possible to obtain $(2m+n+k)$-point Green function from the partition function in equation (2.9) in the same manner as in the canonical quantisation formalism shown in equation (2.8).

The Green function generated from the generating functional $\tilde{Z}$ includes connected and disconnected diagrams. The disconnected diagram means that the full Green function is made up of two or more subdiagrams that are not connected via a propagator. To generate only connected diagrams of non-vacuum type, one can use the generating functional $W[\eta,\overline{\eta},J,j^\mu]$ that is connected with the original generating functional $\tilde{Z}[\eta,\overline{\eta},J,j^\mu]$ as

$$\tilde{Z}[\eta,\overline{\eta},J,j^\mu] = \exp(iW[\eta,\overline{\eta},J,j^\mu]) \quad \Leftrightarrow \quad W[\eta,\overline{\eta},J,j^\mu] = -i\ln Z[\eta,\overline{\eta},J,j^\mu].$$

After obtaining the Green functions in the position space, it is more convenient to transfer them to the momentum space. Working in a momentum space is often more simple and convenient to describe given processes. Furthermore, it is a great way to connect the Green function and scattering amplitudes. The Green function in a momentum space is defined as the Fourier transform of the Green function in a position space. The Green function in momentum space then reads as

$$\tilde{\tau}\left(p_1,...,p_n,-q_1,...,-q_m\right)=\left(\prod_{i=1}^{n}\int\ d^4x_i e^{-ip_ix_i}\right)\left(\prod_{j=1}^{m}\int\ d^4y_j e^{+iq_jy_j}\right)\langle x_1...x_n y_1...y_m\rangle,$$

where $p_1,\dots,p_n$ are the momenta of the incoming particles and $q_1,\dots,q_m$ are the momenta of the outgoing particles. This essentially denotes the $n\to m$ process.

2.2.5 S-matrix, cross-section, and decay width

We can finally define the scattering amplitudes that are also called $S-$matrix

$$S_{fi}={}_{out}\langle f|i\rangle_{in}={}_{in}\langle f|\hat{S}|i\rangle_{in},$$

that describes the transition from the incoming set of particles i to the final set of particles f. The connection between the $S-$matrix and the Green function in momentum space is provided by the Lehmann-Symanzik-Zimmerman (LSZ) formalism [95]. The LSZ reduction formula states that the $S-$matrix elements are proportional to the residue of the multipole structure of the full Green function and the proportionality factor is given by the renormalisation factor of the wave function Z_ϕ. The LSZ formula in the momentum space reads as

$$S_{fi}=\lim_{p^2,q^2\to m_p^2}\left(\prod_{i=1}^{n}\frac{-i(p_i^2-m_p^2)}{\sqrt{Z_\phi}}\right)\left(\prod_{j=1}^{m}\frac{-i(q_i^2-m_p^2)}{\sqrt{Z_\phi}}\right)\tilde{\tau}\left(p_1,...,p_n,-q_1,...,-q_m\right)+\mathscr{D}.\mathscr{T}.,$$

where m_p is a physical mass of the external propagator that is in the LSZ formula amputated from the full Green function in momentum space $\tilde{\tau}$. This is also called the amputated Green function. The "$\mathscr{D}.\mathscr{T}.$" represents the disconnected terms.

If only the interaction is within the scope of the study, it is possible to divide the operator $\hat{S}$ into two parts

$$\hat{S}=1+i\hat{T},$$

where $\hat{T}$ is called the $T-$matrix. This is equivalent to

$$S_{fi}={}_{in}\langle f|\hat{S}|i\rangle_{in}=\delta_{fi}+i{}_{in}\langle f|\hat{T}|i\rangle_{in},$$

where δ_{fi} represents instances where particles did not interact. The term $\langle f|T|i\rangle$ can be expressed using the LSZ formalism as

$$\langle f|T|i\rangle\equiv(2\pi)^4\delta^4(p_i-q_f)T_{fi},$$

where T_{fi} is the transition matrix. Furthermore, p_i is the total momentum of the incoming particles and q_f is the total momentum of the outgoing particles. The delta function $\delta^4(p_i-q_f)$ ensures the conservation of energy and momentum.

If the conservation of the momentum is implicitly understood and omitted and the external legs of the Green function are called amputated, we obtain the scattering amplitude $\mathscr{M}$. The square of the spin-averaged scattering amplitude $\overline{|\mathscr{M}|^2}$ can ultimately be connected to the differential cross-section. The most studied is the $m_1 + m_2 \to m_3 + m_4$ process and the differential cross-section is

$$\frac{\mathrm{d}^2\sigma}{\mathrm{d}^2\Omega_{\text{c.m.}}} = \frac{1}{64\pi^2 s}\frac{\left|\vec{p}'_{\text{c.m.}}\right|}{\left|\vec{p}_{\text{c.m.}}\right|}\overline{|\mathscr{M}|^2},$$

where

$$\left|\vec{p}_{\text{c.m.}}\right| = \sqrt{\frac{\lambda\left(s, m_1^2, m_2^2\right)}{4s}}, \qquad \left|\vec{p}'_{\text{c.m.}}\right| = \sqrt{\frac{\lambda\left(s, m_3^2, m_4^2\right)}{4s}},$$

$$\lambda(x, y, z) = x^2 + y^2 + z^2 - 2xy - 2xz - 2yz.$$

Alternatively $\overline{|\mathscr{M}|^2}$ can be used to determine the decay width Γ. Specifically for the $M \to m_1 + m_2$ process as

$$\Gamma = \frac{1}{2M}\overline{|\mathscr{M}|^2}\,\text{LIPS}_2,$$

where

$$\text{LIPS}_2 = \frac{|\vec{p}|}{4\pi M}, \quad \text{where} \quad |\vec{p}| = \frac{1}{2M}\left[\lambda\left(M^2, m_1^2, m_2^2\right)\right]^{1/2}.$$

Since scattering properties and decay rates are essential in particle physics, especially in the experimental sector, it is not surprising that they are extensively examined. The cross-section from the theory is directly measurable; it is a great comparison between theory and data.

All this is a rather complicated process. For this purpose, the scattering amplitudes $\mathscr{M}$ are usually not calculated from the Green functions using the LSZ formalism, which are obtained from functional derivatives of the generating functional. There is a shortcut with the established set of rules, called Feynman rules. These can immediately give the scattering amplitude $\mathscr{M}$ or the Green function $\tilde{\tau}(...)$. On top of that, there are Feynman diagrams that make Feynman rules much easier to apply.

2.2.6 Regularisation and renormalisation

Processes in QFT have to be treated perturbatively. Interaction is considered as a perturbation of free theory and is expanded into series. The interaction coupling g is the expansion constant that must fulfil $g \ll 1$ so that the series converges. Adding the order of perturbation means adding another vertex. Virtual particles can be emitted and reabsorbed. This is called a loop, and it has to be integrated over all possible momenta of the virtual particle. Loop essential add $\mathrm{d}^4 p$ to some integral. Even one-loop diagrams in many QFT interactions end up being divergent integrals. Since this divergence is connected to large momenta it is called ultraviolet divergence. This divergence is fixed by regularisation and renormalisation.

A very popular regularisation in particle physics is dimensional regularisation [96, 97]. The key to dimensional regularisation is integration in the number of dimensions d rather than 4. The number of dimensions d can be any real number. This procedure then continues with a rotation of the integral into Euclidean space. This is called a Wick rotation. After that, integrals

are usually solvable by established transformations and formulas. Then analytic continuation is applied and the dimension is said to be approaching 4 as $d = 4 - \varepsilon$. This will give the result

$$\mathcal{O}\left(\frac{1}{\varepsilon}\right) + \mathcal{O}(\gamma) + \mathcal{O}(\varepsilon) + ...,$$

where γ is the Euler-Mascheroni constant that usually appears in the finite term due to the presence of the gamma function $\Gamma(x)$ or the beta function $\mathrm{B}(x, y)$. The first term corresponds to an infiniteness that is undesirable in physical result.

The infinity of ultraviolet divergence can be absorbed by the bare parameters of Lagrangian density, such as coupling g_{B}, mass m_{B}, and external fields. These quantities can also depend on the cut-off point Λ and the scale μ. The cutoff Λ defines the applicability of the theory. This dependence should also be absorbed, and the physical quantity, such as the cross section σ should not depend on the scale Λ. The energy scale μ is then taken as some renormalisation point energy. The renormalisation group [98] is a very popular approach and represents one of the most conceptual advances in QFT. The renormalisation group is built on the flow equation

$$\mu \frac{\mathrm{d}g}{\mathrm{d}\mu} = \beta(g),$$

function $\beta(g)$ is also called the velocity.

There are also two types of so-called mass divergences. This occurs on the other side of the phase space than the ultraviolet divergences. The massless gauge boson can cause the so-called infrared singularity. This can be fixed by introducing the mass of the gauge boson. Another type of mass divergences are parallel singularities, when two out of three particles become parallel to each other. This is also caused by massless particles and can be solved in a same manner as infrared divergence.

Higher orders of QFT must be regularised and renormalised. This leads to improved results, which are necessary to confirm our theories. In fact, QFT is the most successful and accurate theory that has ever been developed, and perturbation calculations had a great impact on the development of particle physics. In high-energy physics specifically, it is of great interest to observe particle collisions at high energies. It is important to support the experimental measurements of those collisions with a theory that describes the interaction between multiple particles and can produce quantitative results.

Strong force is dominant for ion-ion collisions. QCD is essential since this work is focused on the description of the interaction of a quark-gluon plasma with hard partons in heavy-ion collisions. The QCD particles (quarks, gluons, and hadrons) have already been introduced. Now, let us proceed to the following section, where QCD is mathematically formulated in terms of QFT.

2.3 Quantum Chromodynamics

Quantum chromodynamics (QCD) is a key interaction in HIC. It describes the interaction between quarks and gluons that are components of QGP. QGP could be found in the early stages of the universe ($10^{-10} - 10^{-6}$ s), it is suspected to be present in the centre of compact stars, but the

only way to recreate the conditions that were at the beginning of the universe here on Earth are high-energetic collisions. We can then study it and compare our experimental measurements with the theoretical simulations.

QCD is built on the underlying symmetry $\mathrm{SU}(3)_c$. This symmetry represents the symmetry between colours (r, g, b). The field of the quark q is a triplet Dirac field

$$q \equiv \begin{pmatrix} q_r \\ q_g \\ q_b \end{pmatrix} = \begin{pmatrix} q_1 \\ q_2 \\ q_3 \end{pmatrix} = \begin{pmatrix} \psi_{q,1} \\ \psi_{q,2} \\ \psi_{q,3} \end{pmatrix},$$

where each component corresponds to colour r, g, or b. The field of gluons is described by an octet of gauge fields

$$G_\mu^{\text{д}},$$

where Cyrillic indices $(\text{д}, \text{ш}, \text{щ}, \text{з})$ run from 1 to 8. Gluons are an octet field due to the Kronecker product of colour multiplets $[3] \otimes \overline{[3]} = [8] \oplus [1]$, where the singlet is a non-existing white gluon.

The classical QCD Lagrangian density reads as

$$\mathscr{L}_{\text{QCD}}^{(\text{cl})} = \sum_q \overline{q}_i (i\not{\partial}_{ij} - m_q \delta_{ij}) q_j - \frac{1}{4} G_{\mu\nu}^{\text{д}} G_{\text{д}}^{\mu\nu}, \tag{2.10}$$

where $G_{\mu\nu}^{\text{д}}$ the gluon field strength tensor

$$G_{\mu\nu}^{\text{д}} = \partial_\mu G_\nu^{\text{д}} - \partial_\nu G_\mu^{\text{д}} + g_s f^{\text{дщз}} G_\mu^{\text{щ}} G_\nu^{\text{з}},$$

where $f^{\text{дщз}}$ is a structure constant and g_s is a dimensionless coupling constant. Furthermore, the covariant derivative is the matrix 3×3 given as

$$(D_\mu)_{ij} = \delta_{ij}\partial_\mu + i g_s \left(G_\mu^{\text{д}} \frac{\lambda_{\text{д}}}{2} \right)_{ij},$$

where $\lambda_{\text{д}}$ are eight Gell-Mann 3×3 matrices as a representation of SU(3) group. More relations between Gell-Mann matrices $\lambda_{\text{д}}$ and structure constants $f^{\text{дщз}}$ with their explicit forms are shown in the Appendix A.4.

With the notation

$$G_\mu \equiv G_\mu^{\text{д}} \frac{\lambda_{\text{д}}}{2}, \qquad G_{\mu\nu} \equiv G_{\mu\nu}^{\text{д}} \frac{\lambda_{\text{д}}}{2},$$

it is possible to show the relation between the gluon field strength tensor $G_{\mu\nu}$ and the covariant derivative D_μ as

$$F_{\mu\nu} = -\frac{i}{g}[D_\mu, D_\nu].$$

The equations of motion from the Euler-Lagrange equation (see Equation 2.2) are

$$(i\not{\partial} - m_i) q_i = 0, \qquad [D_\mu, G^{\mu\nu}] = \frac{g_s}{4} \lambda^{\text{д}} \overline{q} \gamma^\mu \lambda_{\text{д}} q = \frac{g_s}{2} \lambda^{\text{д}} j_{\text{д}}^\mu = g_s j^\mu,$$

where the first equation is for the quark fields and the second one is equivalent to Maxwell equations for gluon field.

The equations of motion are limited and the perturbation theory reached via generating functional

$$\tilde{Z}[\eta_q,\overline{\eta}_q,A^{\text{д}}_\mu] = \frac{\int \prod_q \left(\mathscr{D}q\mathscr{D}\overline{q}\right)\mathscr{D}A\exp\left\{i\mathcal{S}\left[q,\overline{q},A^{\text{д}}_\mu\right]+i\int \mathrm{d}^4x\left[\sum_q\left(\overline{q}\eta_q+\overline{\eta}_q q\right)+j^\mu_{\text{д}}A^{\text{д}}_\mu\right]\right\}}{\int \prod_q \left(\mathscr{D}q\mathscr{D}\overline{q}\right)\mathscr{D}A\exp\left(i\mathcal{S}\left[q,\overline{q},A^{\text{д}}_\mu\right]\right)},$$

where action is

$$\mathcal{S}\left[q,\overline{q},A^{\text{д}}_\mu\right] = \int \mathrm{d}^4x\,\mathscr{L}^{(\text{cl})}_{\text{QCD}} = \int \mathrm{d}^4x\left(\sum_q \overline{q}_i(i\not{\partial}_{ij}-m_q\delta_{ij})q_j-\frac{1}{4}G^{\text{д}}_{\mu\nu}G^{\mu\nu}_{\text{д}}\right).$$

However, as mentioned in Section 2.2, this naive approach would integrate over infinite redundant degrees of freedom. To avoid this, it is possible to use the Faddeev-Popov approach [93] that was also mentioned in Section 2.2. In this procedure, one can choose a gauge fix. One possible option is covariant gauge fixing

$$\mathscr{F}(A) = \partial_\mu A^\mu - f(x),$$

where $f(x)$ is some arbitrary function of space-time. This leads to partition function

$$\tilde{Z}[\eta_q,\overline{\eta}_q,A^{\text{д}}_\mu] = \frac{\int \prod_q \left(\mathscr{D}q\mathscr{D}\overline{q}\right)\mathscr{D}A\mathscr{D}c\mathscr{D}\overline{c}\exp\left\{i\int \mathrm{d}^4x\left[\mathscr{L}^{(\text{cg})}_{\text{QCD}}+\sum_q\left(\overline{q}\eta_q+\overline{\eta}_q q\right)+j^\mu_{\text{д}}A^{\text{д}}_\mu\right]\right\}}{\int \prod_q \left(\mathscr{D}q\mathscr{D}\overline{q}\right)\mathscr{D}A\mathscr{D}c\mathscr{D}\overline{c}\exp\left(i\int \mathrm{d}^4x\,\mathscr{L}^{(\text{cg})}_{\text{QCD}}\right)},$$

where $\mathscr{L}^{(\text{cg})}_{\text{QCD}}$ is covariant gauge fixed Lagrangian density [94] according to Faddeev-Popov [93]

$$\mathscr{L}^{(\text{cg})}_{\text{QCD}} = \sum_q \overline{q}_i(i\not{\partial}_{ij}-m_q\delta_{ij})q_j-\frac{1}{4}G^{\text{д}}_{\mu\nu}G^{\mu\nu}_{\text{д}}-\overline{c}_{\text{д}}\partial^\mu\mathscr{D}^{\text{дщ}}_\mu c_{\text{щ}}-\frac{1}{2\xi}\partial^\mu A^{\text{д}}_\mu\partial_\nu A^\mu_{\text{д}},$$

where $\mathscr{D}^{\text{дщ}}_\mu$ is octet covariant derivative

$$\mathscr{D}_\mu = \partial_\mu + ig_s T_{\text{д}}A^{\text{д}}_\mu,$$

where $(T_{\text{д}})_{\text{шз}} = -if_{\text{дшз}}$ is SU(3) adjoint representation of 3×3 matrices. Finally, ξ is a gauge parameter. Since the gauge is a free choice, it can depend on some real parameter ξ.

Since QCD is built on a non-Abelian group SU(3), it causes the appearance of the $g_s f^{\text{дщз}}G^{\text{щ}}_\mu G^{\text{з}}_\nu$ term in gluon field strength tensor $G^{\text{д}}_{\mu\nu}$. This is essentially the reason why gluons can have three- and four-point interactions with each other. This self-interaction has some intensely interesting physical implications.

2.3.1 The lattice QCD

The primary idea behind the lattice QCD is the discretization of Euclidean space-time, (x_1,x_2,x_3,x_4), with metric diag(1,1,1,1), into lattice $x_\mu = a n_\mu$, where a is called a lattice constant. Quark field $q(n)$ is placed on the lattice site and the gluon field occurs on the lattice links.

In the lattice QCD, the gluon field is defined as

$$U_\mu = \exp\left(iagG_\mu\right).$$

Here the a is also a ultraviolet cutoff that is required to have the gauge-invariant model. The operator $U_\mu(n)$ connects the sites n and $n+\mu$. Since this operator is unitary, the link with an opposite direction can be written as $U_\mu^\dagger(n)$. With the smallest possible loop [94]

$$U_{\mu\nu}(n) = U_\nu^\dagger(n) U_\mu^\dagger(n+\nu) U_\nu(n+\mu) U_\mu(n),$$

called Wilson loop. Wilson loop for continuous limit approaches

$$\lim_{a\to 0} U_{\mu\nu} = i a^2 g G_{\mu\nu}(n)$$

one can construct Wilson gauge-invariant action [99]

$$\mathcal{S}_g = \frac{3}{q^2} \sum_n \sum_{1\le\mu\neq\nu\le 4} \left(1 - \frac{1}{3}\Re\mathrm{e}\left[\mathrm{tr} U_{\mu\nu}\right]\right),$$

where $\Re\mathrm{e}[\cdot]$ denotes real part.

Fermions discretization of gauge-covariant derivative D_μ can be done as simple symmetric difference

$$D_\mu q(x) \longrightarrow \frac{1}{2a}\left[U_\mu(x) q(x+a\hat{\mu}) - U_\mu^\dagger(x-a\hat{\mu}) q(x-a\hat{\mu})\right].$$

However, this leads to a naive fermion action that carries the fermion doubling problem with it. To solve this issue, one has to introduce a more complex Wilson's Dirac operator

$$D_W = -\frac{1}{2a} \sum_{1\le|\mu|\le 4} \left[\delta^m_{n+\mu}(r - i\gamma_E^\mu) U_\mu(n) - r\delta^m_n\right],$$

where γ_E^μ are gamma matrices in Euclidean space.

The final partition function then takes the form of

$$Z = \int \mathscr{D}U \prod_q \mathscr{D}q \mathscr{D}\overline{q}\, e^{-S_g[U] - \Sigma_q \overline{q}\left(D_W[U] + m_q\right) q}$$

Integrating over quark and antiquark fields leads to form that is suitable for simulations

$$Z = \int \mathscr{D}U\, e^{-S_g[U]} \prod_q \overline{q}\left(D[U] + m_q\right) q.$$

Since the computational power increases exponentially since 1970 (Moore's law), it is not a surprise that the lattice QCD became the most powerful tool for QCD calculations from the first principle. However, even the most powerful non-perturbative tool for QCD has its limitations.

2.3.2 Coupling constant and asymptotic freedom

Since gluons can interact with each other, higher orders of perturbation theory can greatly affect the force mediated by gluons. Higher orders must be renormalised. This was introduced in the previous Section 2.2. The regularisation and renormalisation procedures are not unique and there are many possibilities to choose from. Probably the most popular choices are the dimensional regularisation and the renormalisation group. The strong coupling constant g_s satisfies the flow equation

$$\mu \frac{\mathrm{d}g_s}{\mathrm{d}\mu} = \beta(g).$$

In modified minimal subtraction scheme $\overline{\text{MS}}$ [100], velocity $\beta(g)$ takes a nice form of an expansion

$$\beta(g) = -\beta_0 g^3 - \beta_1 g^5 + ..., \quad \text{where}$$
$$\beta_0 = \frac{1}{(4\pi)^2}\left(11 - \frac{2}{3}N_f\right), \quad \beta_1 = \frac{1}{(4\pi)^4}\left(102 - \frac{38}{3}N_f\right).$$

Since both β_0 and β_1 are positive for the number of quark flavours $N_f \leq 6$, velocity β is negative. This means that the coupling constant g_s decreases as the energy scale increases. This behaviour for large energy scales is called an asymptotic freedom [101, 102, 103].

It is possible to express the QCD equivalent of the fine structure constant α. This is also called the strong coupling constant $\alpha_s(\mu)$. The same as $g(\mu)$, $\alpha_s(\mu)$ decreases with increasing energy scale μ. This asymptotic freedom behaviour can be seen in Figure 2.4.

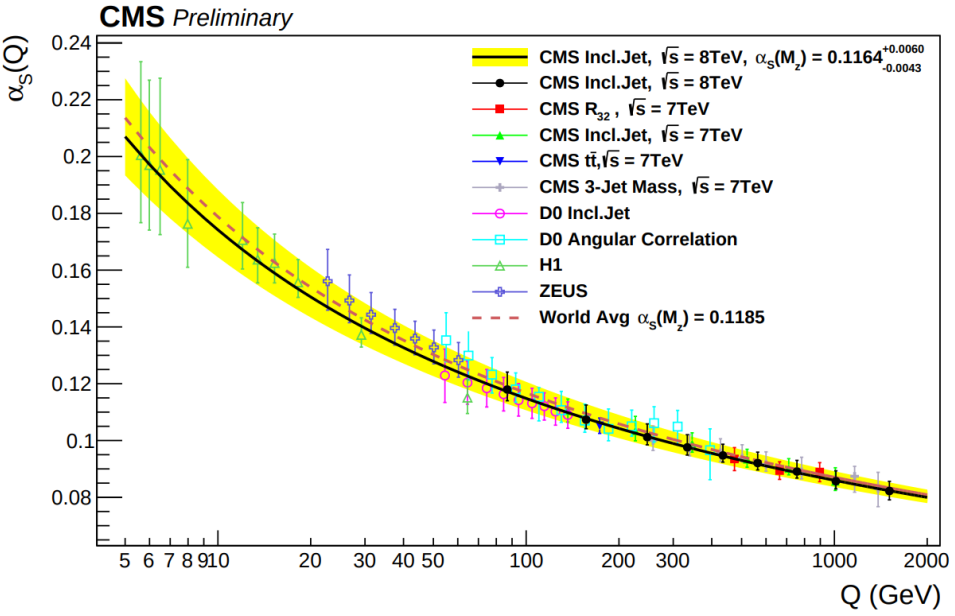

Figure 2.4: The strong coupling constant α_s is plotted as a function of the energy scale $Q = \mu$. [104]

Higher orders are much more important in the case of a strong coupling constant α_s than for the fine structure constant α. In a first order of $\overline{\text{MS}}$ calculation, $\alpha_s(\mu)$ takes a form as

$$\alpha_s(\mu) = \frac{1}{4\pi\beta_0 \ln\left(\frac{\mu^2}{\Lambda^2_{\text{QCD}}}\right)}\left[1 - \frac{\beta_1}{\beta_0^2}\frac{\ln\left(\ln\left(\frac{\mu^2}{\Lambda^2_{\text{QCD}}}\right)\right)}{\ln\left(\frac{\mu^2}{\Lambda^2_{\text{QCD}}}\right)}\right],$$

where Λ_{QCD} is integration constant that has to be determined by experiment. It is also important to take into account the number of quark flavours N_f. The increasing number of flavours N_f decreases Λ_{QCD}. QCD scale parameter for three quark flavours $\Lambda_{\text{QCD}}^{(N_f=3)} = 332 \pm 17$ MeV [105] is larger than that for five quark flavours $\Lambda_{\text{QCD}}^{(N_f=5)} = 210 \pm 14$ MeV [32]. All values are with respect to the modified minimal subtraction scheme $\overline{\text{MS}}$.

The fact that $\alpha_s(\mu)$ is small for large μ implies that the perturbation series behaves well for large energy scales μ. On the other hand, this is not the case for small energy scales μ. We say that perturbative QCD is not reliable approximately for energy scales $\mu \lesssim 5$ GeV. This divided QCD into perturbative calculations from the first principle (pQCD) and non-perturbative model calculations (nQCD).

2.3.3 Colour confinement and quark-gluon plasma

Running coupling constant $\alpha_s(\mu)$ exhibits very different values on the opposite side of the energy scale μ spectrum. Figure 2.4 shows how the running coupling constant $\alpha_s(\mu)$ increases rapidly for smaller μ. This trend continues for small μ until pQCD is no longer applicable.

This can be understood as an anti-screening of the colour charge in vacuum as one approaches closer to the charge. The effective colour charge decreases with decreasing distance. Anti-screening $\left(\varepsilon_0^{\mathrm{QCD}} < 1\right)$ corresponds to paramagnetism $\left(\mu_0^{\mathrm{QCD}} < 1\right)$ of QCD. [94] This is opposite behaviour to what we see in QED.

High values of $\alpha_s(\mu)$ for small μ essentially introduce the concept of colour confinement. If the interaction increases with distance, quarks and gluons will be bound inside hadrons. This is why physicists like Gell-Mann, Bjorken, or Gottfried did not believe that the quark model actually describes physical particles. It should be just a mathematical representation. Quarks and gluons, indeed, cannot exist separately and are confined inside colour singlet hadrons.

Introducing an extremely hot and/or dense medium for QCD greatly affects the behaviour of the colour charge. There is no anti-screening and paramagnetism. Colour charges become quasi-free, and they can travel inside the medium. This happens when hadronic matter converts into quark-gluon plasma (QGP). This occurs at high temperatures or densities. The temperature at which hadronic matter cannot exist is called the Hagedorn temperature $T_c \approx 160$ MeV. Rolf Hagedorn extrapolated the density of hadron resonances and calculated this limiting temperature for hadronic matter [106]. It was belied that it is the maximal temperature since the QGP was not known by then.

The density in which hadronic matter transits to QGP is just a few times higher than ordinary nuclear matter. It is discussed if larger neutron stars would be able to decouple nuclear matter inside their centres. There is extensive research [107] and this question will be decided by experiments. One possible way to experimentally resolve this question is to measure the tail of the gravitational wave signal of a neutron star merger event.

This extreme state of matter happens to be in the nQCD part of the energy scale μ spectrum. This means that its evolution cannot be calculated from the first principles, and it is necessary to use models.

Chapter 3

Modelling of Quark-Gluon Plasma

In an ideal case, we would like to describe the soft processes in a heavy-ion collision (HIC) from the first principles. This means using Standard Model as a framework. However, QFT has its limitations. When the HIC is reduced to only a strong interaction, therefore, within the QCD framework, there is a condition that the running coupling constant α_s must be sufficiently small, so the perturbative approach is applicable. This is fulfilled in the case of hard probes like heavy-flavour hadrons or jets. There is a wide range of applications of pQCD for hard processes, and they will be described in Chapter 4. For a small transfer of four-momentum q, the coupling constant is significantly larger and pQCD cannot be used. This applies to soft radiation and interactions within the medium.

It is a common agreement in the research field that in the early stages of a heavy-ion collision a medium is formed. With a sufficient number of particles and a short mean free path compared to the size of the system (Knudsen number), we can assume that the medium will behave as a fluid, and we can describe it with hydrodynamic approach. Since the collective flow of the fluid is comparable to the speed of light, we have to take into account the relativistic effects. Therefore, the framework for simulations of the medium is relativistic hydrodynamics.

Relativistic hydrodynamics is a powerful tool for describing HIC and results in a good agreement with the measured data [108, 109, 110, 111, 112, 113]. This mainly applies to the hadron p_{T} spectra and Fourier coefficients of harmonics of the azimuthal momentum distribution.

HIC experiments are located at the Relativistic Heavy Ion Collider (RHIC) at the Brookhaven National Laboratory (BNL) and the Large Hadron Collider (LHC) located at the European Organization for Nuclear Research (CERN) laboratory. It was experimentally confirmed that in such collisions, small volumes of matter are formed that consist of quasi-free quarks and gluons [114, 115, 116, 117, 118]. This matter is called quark-gluon plasma (QGP), and its properties allow us to describe its evolution with the second-order viscous relativistic hydrodynamics.

This chapter is dedicated to the different stages of the modelling of relativistic heavy-ion reactions that is tided with the QGP. The simulation starts with the initial state. The product of the initial state is usually an energy density profile ε or an entropy density profile s in mid-rapidity at the proper time τ_0. The initial state can be non-dynamical one; however, it is also possible to include preequilibrimu dynamics. This corresponds to a transition process between a non-dynamic initial state (before τ_s) and relativistic hydrodynamics (at τ_s). The next step is the

fluid stage itself. State-of-the-art is second-order hydrodynamics with temperature-dependent shear viscosity over the entropy density $\frac{\eta}{s}(T)$ and $\frac{\zeta}{s}(T)$ and a modern equation of state (EoS) of nuclear matter. With the hydrodynamic evolution, we obtain, besides other things, the temperature evolution of the medium. This determines the freeze-out hypersurface at critical temperature T_c. At this isotherm, the transition from fluid to hadronic degrees of freedom occurs. After that, hadrons collide with each other and unstable resonances decay. This must also be taken into account. In this thesis, `JETSCAPE` framework [9] is used to simulate all stages of heavy-ion collision.

3.1 The Initial State of Hydrodynamics

The first two segments of the simulation chain correspond to the initial state of the fluid. The first stage is a non-dynamical model that crates entropy density profile at mid-rapidity region. There are many models with very different approaches. TRENTo model [1] is a state-of-the-art non-dynamical model based on a reduced thickness function, where the inputs are physical parameters such as the impact parameter b and the nucleon-nucleon inelastic cross section $\sigma_{\mathrm{NN}}^{\mathrm{inel}}$. There are also model parameters that will be introduced later along with the model itself.

The second stage is called preequilibrium. This corresponds to a short period, where matter still experiences evolution, but the QGP is not yet formed. The initial profile obtained from TRENTo evolves for some time according to the collisionless Boltzmann equation. The code used in this work is called `freestream-milne` [2].

Regrettably, the initial state of HIC cannot be directly assessed with hadronic observables. This leaves us with the fact that this part of the HIC simulation contributes the most to the uncertainty of the final results [119, 120]. It is possible to employ Bayesian analysis to constrain the model parameters. However, it is still very difficult to test the physical assumptions behind the model itself. To show that the TRENTo model [1] is more realistic than the Monte Carlo Glauber model [121], for example, it is necessary to compare them in very specific ultracentral U+U collisions.

3.1.1 Physics input for non-dynamical initial state models

To produce an initial state of heavy-ion collision, it is necessary to provide some input to the model. There are physical parameters that are given to the non-dynamical initial state model, and there are model parameters that arise in the given framework. This section is devoted to the physical parameters. Namely, impact parameter b, inelastic nucleon-nucleon cross section $\sigma_{\mathrm{NN}}^{\mathrm{inel}}$, and nuclear density $\rho_A(\vec{x})$.

Impact parameter

The impact parameter b is defined as the perpendicular distance between the projectile trajectories and the target. In the case of classical physics, it is connected with particle scattering on the spherically symmetric potential $U(\vec{r})$. In ion-ion collisions, it is the distance between centre-of-mass of the nuclei in the direction perpendicular to the beam axis.

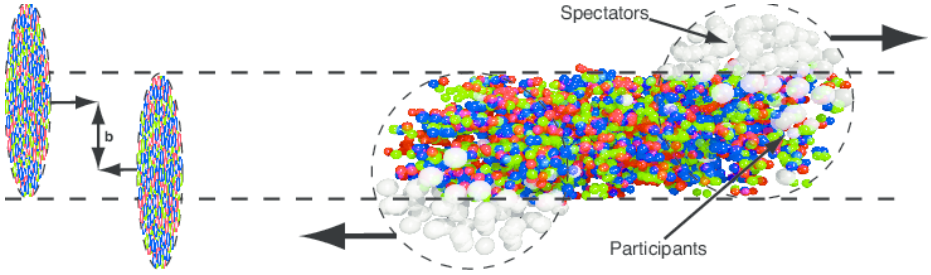

Figure 3.1: Impact parameter during heavy-ion collision. [122]

Left-hand side of the Figure 3.1 shows two nuclei flying towards each other. Those nuclei are contracted into very thin slabs. This is due to the Lorentz contraction caused by the ultrarelativistic velocity. The longitudinal size of the lead ion is approximately 10000 smaller at LHC energies. The arrow between the centres of the nuclei is the impact parameter b.

The right-hand side of Figure 3.1 shows how the nuclei collided. Nucleons that remained intact and did not interact are called spectators, and those that did interact are called participants. The number of participants N_{part} is one of the important variables in the initial state simulations. If we collide two nuclei with atomic mass numbers A_1 and A_2, it is clear that there is a relationship between the number of participants N_{part} and the number of spectators

$$N_{\text{spec}} = A_1 + A_2 - N_{\text{part}}.$$

The impact parameter b can be related to the centrality c. It is very difficult to measure the size of the medium by femtoscopy, and it would be even more challenging to determine the impact parameter directly from the observables, since it is $\lesssim 20$ fm in size and the measurement would have to be very accurate. Centrality c can be relatively easily estimated using observables, and this is why the results of the experimental measurements are expressed in terms of centrality c.

Centrality is defined as a cumulative probability distribution of the impact parameter b [123]

$$c(b) \equiv \frac{\int_0^b \frac{\mathrm{d}\sigma}{\mathrm{d}b'}\mathrm{d}b'}{\int_0^\infty \frac{\mathrm{d}\sigma}{\mathrm{d}b'}\mathrm{d}b'} = \frac{1}{\sigma^{\text{inel}}}\int_0^b P_{\text{inel}}(b')2\pi b'\mathrm{d}b',$$

where σ^{inel} is the inelastic nucleus-nucleus cross section. $P_{\text{inel}}(b')$ is the probability function of an inelastic collision at a given impact parameter b'. Centrality $c(b)$ is called b-centrality because it depends on the impact parameter b.

The centrality estimation based on the experimental measurement of the observable n is defined [123] as the cumulative distribution of observable n

$$c \equiv \int_n^\infty P(n')\mathrm{d}n'.$$

The observable n must be proportional to the number of participants N_{part}. Fortunately, there are many observables that meet this condition. An example of this measurement is shown in Figure 3.2, since the measurement of the distribution of energy deposited in calorimeters ΣE_T is proportional to the number of participants N_{part}.

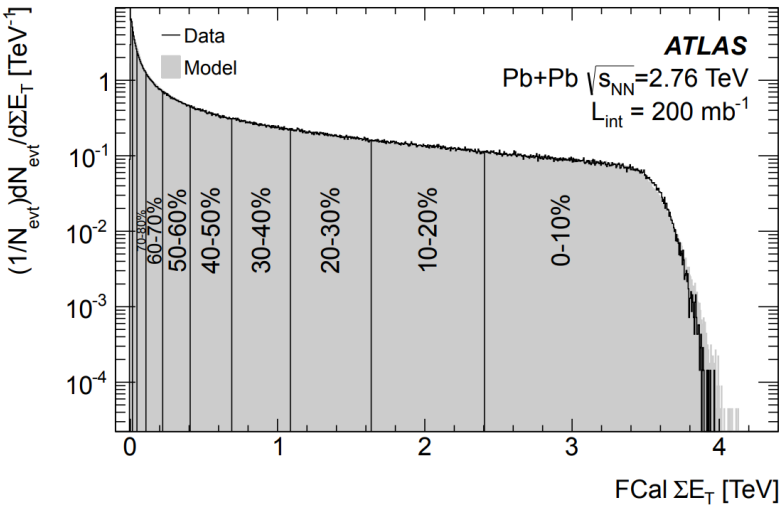

Figure 3.2: ATLAS collaboration measurement of FCal ΣE_T distribution for Pb+Pb at $\sqrt{s_{\mathrm{NN}}}$ = 2.76 TeV divided into 10% centrality bins. [124]

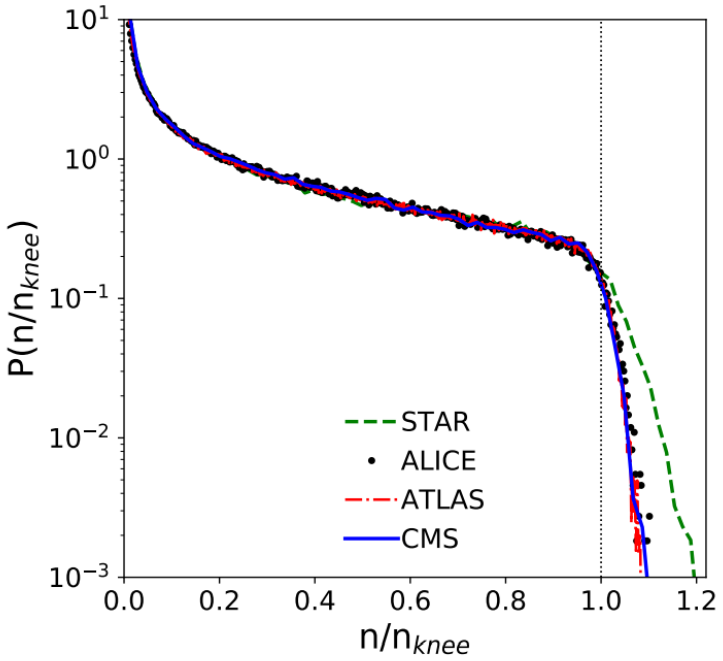

Figure 3.3: Histograms of probability P of observable n in STAR [125] (dashed line), ALICE [126] (dots), ATLAS [124] (dash-dotted line), and CMS [127] (solid line). Au+Au collisions at $\sqrt{s_{\mathrm{NN}}}$ = 140 GeV in case of STAR and Pb+Pb at $\sqrt{s_{\mathrm{NN}}}$ = 2.76 TeV in case of ALICE, ATLAS, and CMS. Figure was taken from [123].

The observable n differs from experiment to experiment. [123] The STAR collaboration uses the number of charged particles N_{ch} detected in the mid-pseudorapidity region $|\eta| < 0.5$. [128, 125] CMS experiment uses the value of the energy deposited in two forward calorimeters with two symmetric acceptance pseudorapidity windows $3.0 < |\eta| < 5.2$. [127] The ATLAS collaboration

uses the same method as CMS with different symmetric pseudorapidity windows $4.9 < |\eta| < 3.2$. [124] Finally, the ALICE experiment uses two scintillators with asymmetric pseudorapidity ranges $-3.7 < \eta < -1.7$ and $2.8 < \eta < 5.1$. [126]

Experimental centrality c is an estimate of b-centrality $c(b)$. In reality, there are fluctuations in the initial state for the given impact parameter b, and therefore the number of participants N_{part} fluctuates. This means that the observable n that is proportional to this quantity also fluctuates. The distribution $P(n)$ of the observable n is made up of overlapping Gaussian peaks. This is shown in Figure 3.4, where Monte Carlo Glauber [121] was employed. The Monte Carlo Glauber model introduces the mentioned fluctuations compared to the optical Glauber model [129].

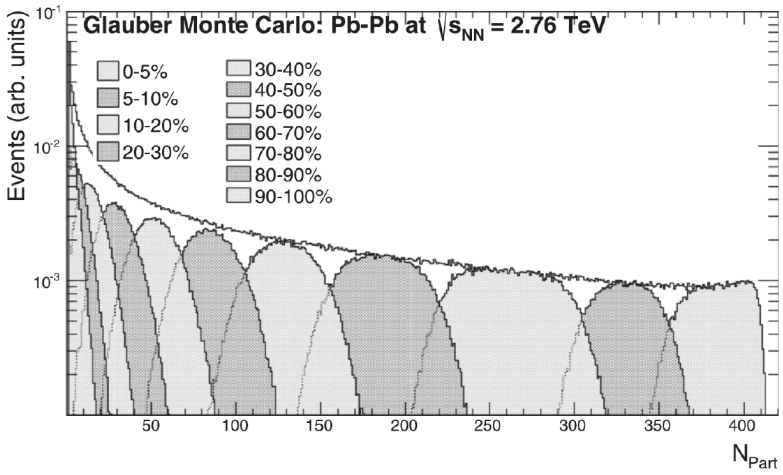

Figure 3.4: Number of participants N_{part} obtained from Monte Carlo Glauber model calculation divided into centrality $c(b)$ bins. [126]

Table 3.1: Relation between the centrality class c and the impact parameter b for PbPb collisions. [130]

(a) $\sqrt{s_{\text{NN}}} = 2.76$ TeV

c	b_{min} [fm]	b_{max} [fm]
0 – 5%	0.00	3.47
5 – 10%	3.47	4.91
10 – 20%	4.91	6.94
20 – 30%	6.94	8.50
30 – 40%	8.50	9.81
40 – 50%	9.81	11.00
50 – 60%	11.00	12.00

(b) $\sqrt{s_{\text{NN}}} = 5.02$ TeV

c	b_{min} [fm]	b_{max} [fm]
0 – 5%	0.00	3.49
5 – 10%	3.49	4.93
10 – 20%	4.93	6.98
20 – 30%	6.98	8.55
30 – 40%	8.55	9.87
40 – 50%	9.87	11.00
50 – 60%	11.00	12.10

Since initial state models take the impact parameter b as input and the experimental results are formulated in terms of centrality c, it is necessary to randomly generate events in the impact parameter range that correspond to a given centrality bin that is determined as a cumulative distribution of the number of participants N_{part}.

Tables 3.1a and 3.1a relate the centrality classes c to the ranges of the impact parameters b.

Inelastic nucleon-nucleon cross section $\sigma_{\mathrm{NN}}^{\mathrm{inel}}$

Nucleon-nucleon cross section $\sigma_{\mathrm{NN}}^{\mathrm{tot}}$ is a fundamental input for non-dynamical initial state models. Specifically, its inelastic component

$$\sigma_{\mathrm{NN}}^{\mathrm{inel}} = \sigma_{\mathrm{NN}}^{\mathrm{tot}} - \sigma_{\mathrm{NN}}^{\mathrm{el}},$$

where $\sigma_{\mathrm{NN}}^{\mathrm{el}}$ is the elastic nucleon-nucleon cross section. However, this quantity is not calculable within perturbative QCD calculations. The reason for this is that the nucleon-nucleon cross section σ_{NN} includes both hard processes ($p_{\mathrm{T}} \gtrsim 2$ GeV) and diffractive soft processes ($p_{\mathrm{T}} \sim \Lambda_{\mathrm{QCD}}^{(N_f)} \approx 250$ MeV). Processes that have a scale close to the QCD infrared cut-off parameter $\Lambda_{\mathrm{QCD}}^{(N_f)}$ are not possible to calculate within pQCD. In the future, it might be possible to compute it with an nQCD approach. For example, it might be possible with a more sophisticated lattice QCD that is capable of working outside the pQCD scale. For now, this quantity has to be taken exclusively from experimental measurements.

At larger center-of mass energy $\sqrt{s} \gtrsim 100$ GeV of two colliding nucleons, there is negligible dependence on nucleon species. In other words, proton p, antiproton $\overline{p}$, neutron n, and antineutron $\overline{n}$ are treated the same due to the strong relevance of sea quarks (see Section 4.2.1 for more details).

The first approach to measuring the inelastic nucleon-nucleon cross section $\sigma_{\mathrm{NN}}^{\mathrm{inel}}$ is to measure the total nucleon-nucleon cross section $\sigma_{\mathrm{NN}}^{\mathrm{tot}}$ with the optical theorem

$$\sigma_{\mathrm{NN}}^{\mathrm{tot}} \propto \mathrm{Im}\left[f_{\mathrm{el}}(t \to 0)\right],$$

where where f_{el} is the elastic scattering amplitude and t is the Mandelstam variable (see Appendix A.5). Then measure the elastic cross section $\sigma_{\mathrm{NN}}^{\mathrm{el}}$ in the Roman pot forward detectors and then subtract it. This approach is used by the TOTEM collaboration [131, 132, 133], the ATLAS collaboration with the ALFA detector [134, 135, 136], and the STAR collaboration [137].

The second approach is the measurement of minimum bias inelastic particle production [138, 139, 140, 141, 142, 143, 144, 145, 146, 147, 148]. This includes the use of central detectors for proton-proton and proton-antiproton collisions. However, this has generally higher uncertainties because the forward region of the phase space is not covered by detectors. This is solved by an extrapolation dominated by diffractive contributions.

In addition to proton-proton and proton-antiproton collisions in the collider, proton-air collisions from cosmic radiation can also be used [148]. For this purpose, the Pierre Auger Observatory [148] and Telescope Array Black Rock Mesa with Long Ridge fluorescence detectors [149] measure the distribution of the depth of the shower maximum X_{max}. The tail of this distribution is sensitive to the proton-air cross section $\sigma_{\mathrm{N-air}}$. The data for reconstruction of the geometry of the collision can be obtained from fluorescence telescopes and a surface detector array. With the Monte Carlo Glauber model [121], one can also deduce the inelastic nucleon-nucleon cross section $\sigma_{\mathrm{NN}}^{\mathrm{inel}}$. However, the combination of systematic uncertainties and uncertainty from the Monte Carlo Glauber model makes this measurement the least accurate. The

main benefit of measuring proton-air collisions is the possibility of a very large centre-of-mass energy per nucleon-nucleon pair $\sqrt{s_{\mathrm{NN}}}$ that can reach values such as $\sqrt{s_{\mathrm{NN}}} = 57$ TeV [148] or $\sqrt{s_{\mathrm{NN}}} = 73$ TeV [149]. At this time, it is not possible to reach those values of the centre-of-mass energy per nucleon-nucleon pair $\sqrt{s_{\mathrm{NN}}}$ at colliders.

Figure 3.5 shows the dependence of the inelastic nucleon-nucleon cross section σ_{NN} on the centre-of-mass nucleon-nucleon energy $\sqrt{s}$. It shows the results of $p\overline{p}$ collisions from UA5 [138] measured at $\sqrt{s} = 200$ GeV and $\sqrt{s} = 900$ GeV, Fermilab experiments E710 [139, 140] and CDF [141, 142] at $\sqrt{s} = 1.8$ TeV. Furthermore, the figure shows pp measurements from ATLAS [134, 135, 136, 144], TOTEM [131, 132, 133], ALICE [143], CMS [145, 146], and LHCb [147], all at the LHC energies $\sqrt{s} = 7$ TeV, $\sqrt{s} = 8$ TeV, and $\sqrt{s} = 13$ TeV. In addition to $p\overline{p}$ and pp collisions, proton-air collisions from the Pierre Auger Observatory [148] at $\sqrt{s_{\mathrm{NN}}} = 57$ TeV are also included.

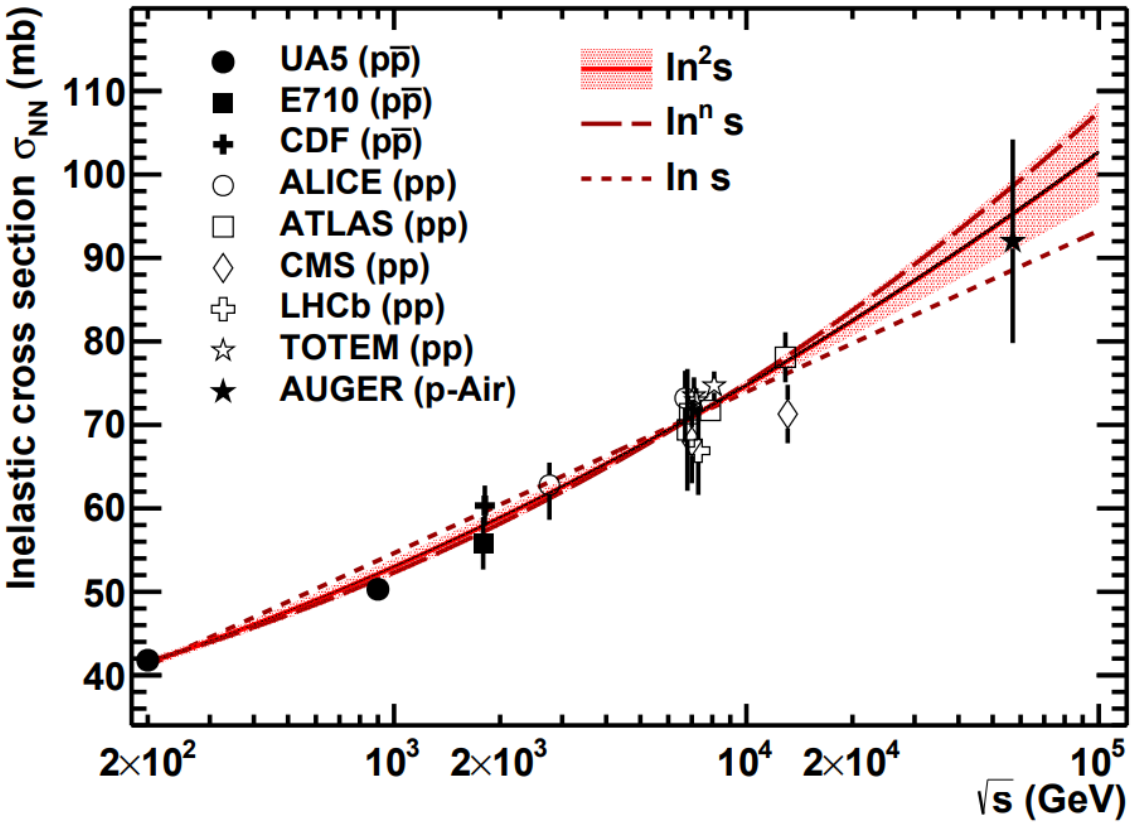

Figure 3.5: Inelastic nucleon-nucleon cross section $\sigma_{\mathrm{NN}}^{\mathrm{inel}}$ as a function of center-of-mass nucleon-nucleon energy $\sqrt{s}$. Experimental data are from UA5 [138], E710 [139, 140], CDF [141, 142], ALICE [143], ATLAS [134, 135, 136, 144], CMS [145, 146], LHCb [147], TOTEM [131, 132, 133], and Pierre Auger Observatory [148]. Retrieved from [150].

The values of $\sigma_{\mathrm{NN}}^{\mathrm{inel}}$ obtained from the fit $\ln^2(s)$ of all experiments are shown in table 3.2. The uncertainties were obtained from the difference between the fits $\ln(s)$ and $\ln^{2.43}(s)$. The reason for using fm^2 units instead of barns is because the input $\sigma_{\mathrm{NN}}^{\mathrm{inel}}$ for TRENTo must be expressed in fm^2.

Increasing the value of the inelastic nucleon-nucleon cross section $\sigma_{\mathrm{NN}}^{\mathrm{inel}}$ as a function of the nucleon-nucleon centre-of-mass energy $\sqrt{s_{\mathrm{NN}}}$ also causes a slightly increased value of the impact parameter b for the same centrality class c at different energies in Tables 3.1a and 3.1b.

Table 3.2: Inelastic nucleon-nucleon cross section $\sigma_{\mathrm{NN}}^{\mathrm{inel}}$ and full inelastic cross section of various collision systems relevant for RHIC, LHC, and FCC. The values of the inelastic nucleon-nucleon cross section $\sigma_{\mathrm{NN}}^{\mathrm{inel}}$ are obtained from the fit $\ln^2(s)$ with uncertainties as a difference between the fits $\ln(s)$ and $\ln^{2.43}(s)$ for multiple experiments (see Figure 3.5). [150]

$\sqrt{s_{\mathrm{NN}}}$ [TeV]	System	$\sigma_{\mathrm{NN}}^{\mathrm{inel}}$ [fm^2]	σ^{inel} [$10^3\times$fm^2=b]
0.027	AuAu	3.15 ± 0.07	–
0.0624	AuAu	3.52 ± 0.05	–
0.20	AuAu	4.16 ± 0.06	6.80 ± 0.03
0.20	CuCu	4.16 ± 0.06	3.43 ± 0.03
2.76	PbPb	6.18 ± 0.09	7.57 ± 0.03
5.02	PbPb	6.76 ± 0.06	7.66 ± 0.03
5.44	XeXe	6.84 ± 0.05	5.67 ± 0.02
5.50	PbPb	6.85 ± 0.05	7.67 ± 0.03
10.60	PbPb	7.53 ± 0.07	7.77 ± 0.03
39.00	PbPb	9.05 ± 0.33	7.90 ± 0.03
5.02	pPb	6.76 ± 0.06	2.08 ± 0.01
8.16	pPb	7.25 ± 0.05	2.12 ± 0.01
8.80	pPb	7.33 ± 0.06	2.13 ± 0.01
17.00	pPb	8.06 ± 0.15	2.18 ± 0.01
63.00	pPb	9.65 ± 0.46	2.28 ± 0.01

Nuclear density ρ_A

Electric charge density inside nucleus can be obtained experimentally via electron-nucleus elastic scattering. [151, 152] To probe the nucleus with diameter $\sim$ 10 fm and overcome the diffraction effects, it is necessary to use electrons with the De Broglie wavelength $\lambda \leq 10$ fm. This corresponds to the momentum of the electrons $p \geq 100$ MeV.

In Figure 3.6 one can see the nuclear charge distribution of ^{4}He, ^{12}C, ^{16}O, ^{40}Ca, ^{48}Ca, ^{90}Zr and ^{227}Pb measured by elastic electron scattering compared to mean field calculation. [153]

Several types of experiments can be performed to determine the distribution of nuclear charge or just parameters such as radius R. Such as optical isotope shift, X-ray isotope shift, μ X-rays or mirror nuclei energy difference. It is also possible to perform experiments where the output is a distribution of nuclear matter. This includes both protons and neutrons. Experiments such as quantum tunnelling through a potential barrier during α decay, Rutherford scattering, and π X-rays can interact with the nucleus through strong interaction. [154]

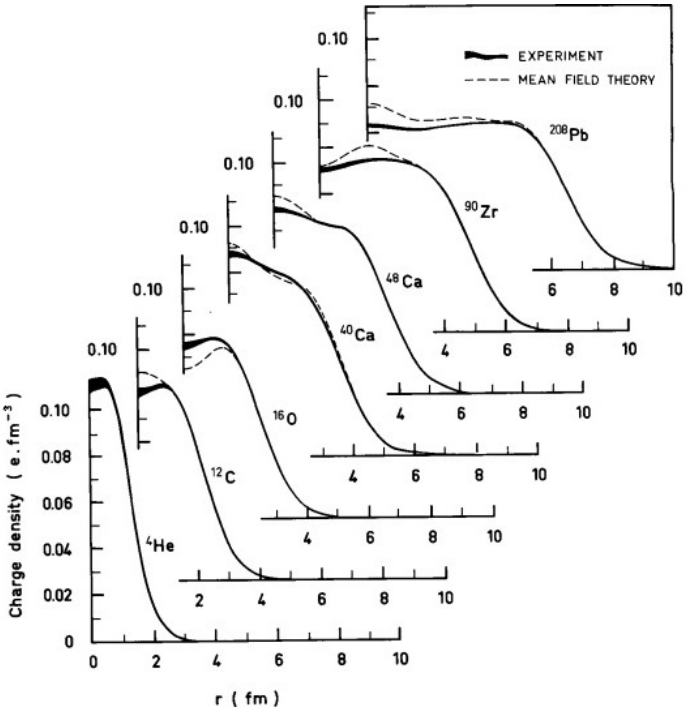

Figure 3.6: Measurements of nuclear charge density by elastic electron scattering on ^{4}He, ^{12}C, ^{16}O, ^{40}Ca, ^{48}Ca, ^{90}Zr and ^{227}Pb (solid line) compared to a mean field calculation by Dechargé and Gogny (dashed line). [153]

Furthermore, one can also measure the neutron density distribution from coherent pion photoproduction [155] or from antiprotonic atoms [156]. This actually results in a density profile that is different from that of the protons. Using different density profiles for protons and neutrons is a more realistic approach and also reduces the uncertainties [150], for example, in the Monte Carlo Glauber model [157].

These experiments agree on several observations. First of all, the nuclear radius scales as

$$R = r_0 A^{\frac{1}{3}}, \tag{3.1}$$

where A is a mass number and $r_0 \approx 1.2$ fm is the proportionality constant. [154] Furthermore, the experiments also agree on the shape of the nuclear matter/charge distribution. It has a constant plateau due to the saturation properties of the strong nuclear force that has a finite reach (~ 2 fm). Then it goes smoothly and relatively quickly to zero, as can be seen in Figure 3.6.

These properties are incorporated by the Woods-Saxon nucleon potential [158]

$$\rho(r) = \rho_0 \frac{1 + w\left(\frac{r}{R}\right)^2}{1 + \exp\left(\frac{r-R}{a}\right)},$$

where ρ_0 corresponds to the measured nucleon density in the centre of the nucleus, a is a skin depth, also called diffusivity parameter. The parameter R is the half-density nuclear radius that can be simply obtained from the empirical formula (3.1). Finally, a central depression parameter w is connected to central density depression or elevation. In this form, the parameterisation

is called a 3-parameter Fermi (3pF) distribution. For undepressed nuclear densities (i.e. $w \approx 0$) this parameterisation is called a 2-parameter Fermi (2pF) distribution and it is a good approximation for the distribution of nuclear matter of nuclei like ^{63}Cu, ^{63}Xe, ^{197}Au, ^{208}Pb. Even when the results from 2pF are acceptable, the 3pF distribution captures the nuclear density of heavy nuclei a lot better, since their ground state has a depression in the central density.

Not all nuclei are spherically symmetric or cannot be approximated by a spherically symmetric nucleon density (so-called near-spherical nuclei) that can be parametrised by 2pF or 3pF. For fairly deformed nuclei such as ^{238}U or ^{27}Al, the following nucleon density parameterisation is used [159]

$$\rho(\vec{r}) = \rho_0 \frac{1}{1 + \exp\left(\frac{r - R(1 + \beta_2 Y_{20} + \beta_4 Y_{40})}{a}\right)},$$

where β_2 and β_4 are parameters of spherical harmonics

$$Y_{20} = \sqrt{\frac{5}{16\pi}}(3\cos^2(\vartheta) - 1), \qquad Y_{40}\frac{3}{16\sqrt{\pi}}(35\cos^4(\vartheta) - 30\cos^2(\vartheta) + 3).$$

There are still some exceptions, such as ^{32}S and deuteron ^{2}d. In the case of ^{32}S the Gaussian form [159] is used to describe its nuclear density distribution

$$\rho(r) = \rho_0 \frac{1 + w\left(\frac{r}{R}\right)^2}{1 + \exp\left(\frac{r^2 - R^2}{a^2}\right)}.$$

Deuteron nuclear density can be described by Hulthén's form [160, 159, 161, 162] of the potential

$$\rho(r) = \rho_0 \left(\frac{\mathrm{e}^{-ar} - \mathrm{e}^{-br}}{r}\right)^2.$$

3.1.2 TRENTo

TRENTo model was introduced in 2014 in [1]. This model is based on the deposition of entropy via a reduced thickness function. It is a non-dynamical model that can be used for proton-proton, proton-nucleus, and nucleus-nucleus collisions.

The benefit of TRENTo model lies in its simplicity. The initial entropy is generated and assumed to correspond to the initial state of a thermalised fluid at a given starting time τ_0. Furthermore, its agreement with ultracentral U+U collisions is quite unique among binary-collision-based models.

The participant thickness function $T_A(x, y)$ of the nucleus A is defined as

$$T_A(x, y) \equiv \int \rho_A^{\mathrm{part}}(x, y, z)\mathrm{d}z,$$

where $\rho_A^{\mathrm{part}}(x, y, z)$ is the nuclear density function of the matter that participates in the collision. With this thickness function, the TRENTo model postulates two things.

- "The eikonal approximation is valid: entropy is produced if T_A and T_B eikonally overlap" [1].
- "There exists a scalar field $f(T_A, T_B)$ that converts projectile thicknesses into entropy deposition" [1].

The scalar field f mentioned in the second postulate is proportional to the entropy density in the mid-rapidity region

$$f \propto \frac{\mathrm{d}s}{\mathrm{d}y}\Big|_{\substack{\tau=\tau_0 \\ y=0}},$$

where τ_0 denotes the proper time for hydrodynamic thermalisation.

The most simple prescription for the scalar field f would be the sum of the thickness functions

$$f \sim T_A + T_B.$$

This actually corresponds to the wounded nucleon model, since participant thickness functions that include only participating nuclear matter are used. In the case of the Glauber model [121, 129], probably the most used initial state model in the heavy-ion field, the function f is

$$f \sim T_A + T_B + \alpha T_A T_B,$$

where a term $\alpha T_A T_B$ represents the addition of multiple inelastic binary collisions. However, as was mentioned at the beginning of this section, the results from ultracentral U+U collisions at the STAR experiment [163, 164] do not agree with this type of scaling.

As the dynamics of the ideal fluid conserves the total entropy of the fireball, the total initial entropy is equal to the total final entropy. The ratio of entropy S to the number of particles N is only slightly dependent on the temperature T and it is possible to say that these two variables are proportional to each other

$$\mathrm{d}S \propto \mathrm{d}N.$$

In other words, the average number of charged particles in the mid-rapidity region is proportional to

$$\langle N_{\mathrm{ch}} \rangle \propto \int f \mathrm{d}x\mathrm{d}y.$$

The particle production from ultracentral U+U collisions shows that f does not scale with the number of binary collisions. This conclusion excludes the Glauber model. [165]

The function f should be scale invariant

$$f\left(aT_A, aT_B\right) = af\left(T_A, T_B\right),$$

as it is expected that there will be the same entropy deposition a times nucleon-nucleon collisions as two thickness functions with $N_{\mathrm{part}} = a$. This property is violated by the term $\alpha T_A T_B$ in the Glauber model. Then TRENTo model proposes f to be the reduced thickness function defined as

$$f = T_R\left(p; T_A, T_B\right) \equiv \left(\frac{T_A^p + T_B^p}{2}\right)^{1/p},$$

where p is a dimensionless parameter of the TRENTo model. This prescription is known as the generalised mean, also known as the power mean or Hölder mean. This generalised mean

interpolates between $\max(T_A, T_B)$ and $\min(T_A, T_B)$ depending on the value of the parameter p. For some values of p this is known as quadratic, arithmetic, geometric, or harmonic mean:

$$T_R = \begin{cases} \max(T_A, T_B) & p \to +\infty, \\ \sqrt{T_A^2 + T_B^2}/\sqrt{2} & p = +2, \quad \text{(quadratic)} \\ (T_A + T_B)/2 & p = +1, \quad \text{(arithmetic)} \\ \sqrt{T_A T_B} & p = 0, \quad \text{(geometric)} \\ 2T_A T_B/(T_A + T_B) & p = -1, \quad \text{(harmonic)} \\ \min(T_A, T_B) & p \to -\infty. \end{cases}$$

However, those are just specific values and p can be any real number.

From the perspective of entropy deposition, as mentioned, $p = +1$ corresponds to the wounded nucleon model. The picture 3.7 shows a collision of two nucleons with a nonzero impact parameter. As one can see, for $p = 1$, the deposited entropy originating from nucleon-nucleon collision is wide across both nucleons. For $p = 0$, the deposited entropy corresponds to a narrower profile placed at the midpoint of the collision. The harmonic prescription, $p = -1$, suppresses the entropy deposition along the impact parameter even more.

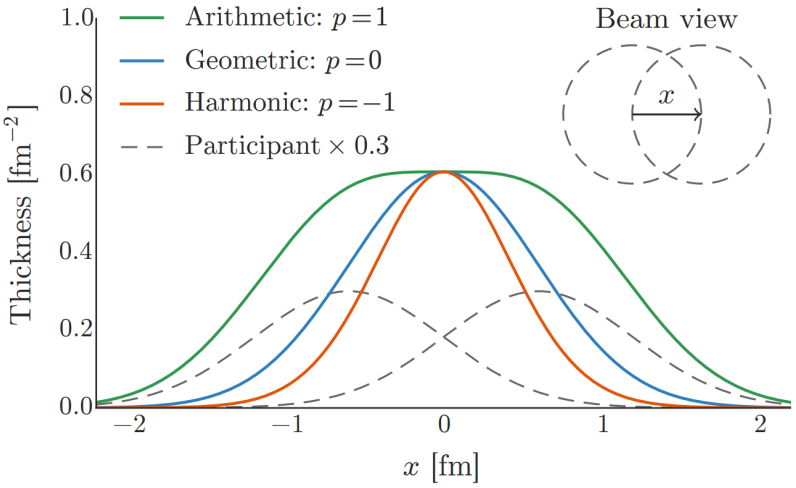

Figure 3.7: Reduced thickness T_R that corresponds to entropy deposition at mid-rapidity at equilibrium time for nucleon-nucleon inelastic collision with nonzero impact parameter. The green line denotes arithmetic prescription $p = +1$, the blue line corresponds to geometric prescription $p = 0$, and orange line is harmonic prescription $p = -1$. The gray dashed lines denote cross section of nucleons. Retrieved from [1].

When one considers the collision of two protons, their probability of collision at a fixed impact parameter will be [166]

$$P_{\text{coll}} = 1 - \exp\left[-\sigma_{gg}^{\text{inel}} \int dx\,dy\,T_p^- T_p^+\right], \tag{3.2}$$

where $T_p^{\pm}$ denotes the thickness functions of the protons that are shifted by half of the impact parameter b. Furthermore, $\sigma_{gg}^{\text{inel}}$ denotes an effective inelastic parton-parton cross section.

The inelastic parton-parton cross section $\sigma_{gg}^{\text{inel}}$ is taken so that the total inelastic proton-proton cross section is equal to the measured inelastic nucleon-nucleon cross section $\sigma_{\text{NN}}^{\text{inel}}$.

The probability in equation (3.2) determines whether the protons collide. If they do, they both receive the fluctuating thickness

$$T_p(x,y) = w_p \int \rho_p(x,y,z)\mathrm{d}z,$$

where w_p is an independently generated factor obtained from the gamma distribution with unit mean

$$P_k(w) = \frac{k^k}{\Gamma(k)} w^{k-1} e^{-kw}, \tag{3.3}$$

where k is another parameter of the TRENTo model. This provides the multiplicity fluctuation that is observed in the experimental data from proton-proton collisions. The small parameter k corresponds to a high value of multiplicity fluctuations, and $k \gg 1$ suppresses the multiplicity fluctuations.

In proton-nucleus and nucleus-nucleus reactions, each nucleon-nucleon collision is assumed to be independent. The nucleons in the nucleus are sampled according to the Woods-Saxon distribution or with a more realistic configuration if possible [167].

The fluctuating participant thickness function of nucleus A is

$$T_A = \sum_{i=1}^{N_{\text{part}}} w_i \int \rho_p^{\text{part}}(x-x_i, y-y_i, z-z_i)\mathrm{d}z,$$

where N_{part} is calculated during the collision, where nucleons that interacted at least once participants are labeled and are included in the number of participants N_{part}. Furthermore, (x_i, y_i, z_i) are coordinates of the i^{th} nucleon. Finally, w_i are the weights sampled from the gamma distribution defined in equation 3.3.

The average multiplicity of charged particles is proportional to the integrated reduced thickness function

$$\langle N_{\text{ch}} \rangle \propto \int T_R \mathrm{d}x\mathrm{y}.$$

The number of charged particles N_{ch} follows the Poisson distribution

$$P(N_{\text{ch}} = k) = \frac{\langle N_{\text{ch}} \rangle^k \exp\left(\langle N_{\text{ch}} \rangle\right)}{k!}.$$

This is how the multiplicity in a given event was calculated in Figure 3.8 for $p = +1, 0 - 1$. The left plot shows the proton-proton collision at $\sqrt{s} = 2.36$ TeV, the middle plot shows the proton-lead collision at $\sqrt{s_{\text{NN}}} = 5.02$ TeV, and finally, the right plot represents the lead-lead collision at $\sqrt{s_{\text{NN}}} = 2.76$ TeV. All plots are compared with data from ALICE [168, 169] measured in the $|\eta| < 1$ pseudorapidity range.

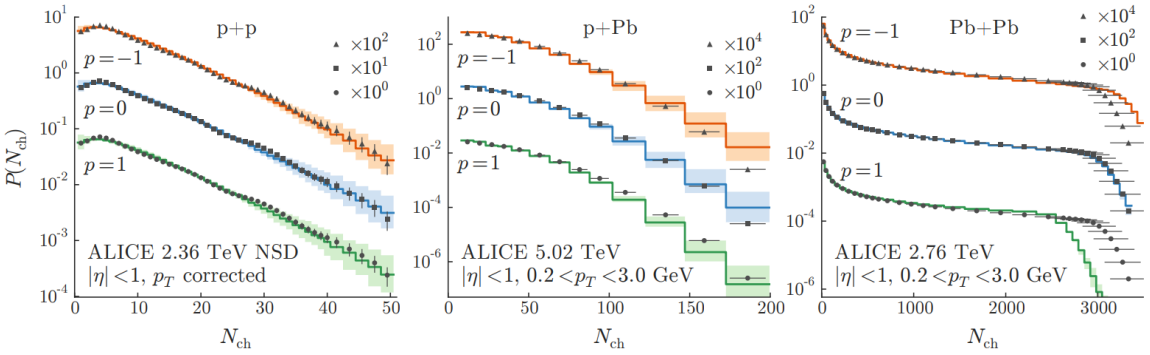

Figure 3.8: N_{ch} distributions for arithmetic prescription $p = +1$ (green line), geometric prescription $p = 0$ (blue line), and harmonic prescription $p = -1$ (orange line) computed from TRENTo for proton-proton at $\sqrt{s} = 2.36$ TeV (left), proton-lead at $\sqrt{s_{\mathrm{NN}}} = 5.02$ TeV (middle), and lead-lead at $\sqrt{s_{\mathrm{NN}}} = 2.76$ TeV (right) compared to data from ALICE [168, 169] measured in $|\eta| < 1$ pseudorapidity range. Retrieved from [1].

From Figure 3.8, it is clear that the prescription $p = 0$ favours lead-lead collisions. This is also why this value is used in this thesis.

Eccentricity harmonics are great tools for testing the initial state model. Especially ellipticity ε_2 and triangularity ε_3 as a function of centrality. In the case of TRENTo model, they are calculated as

$$\varepsilon_n e^{in\phi} = -\frac{\int r^n e^{in\phi} T_R \mathrm{d}x\mathrm{d}y}{\int r^n T_R \mathrm{d}x\mathrm{d}y}.$$

In Figure 3.9, one can see the ellipticity ε_2 on the left plot and the triangularity ε_3 on the middle plot. The graph on the right of Figure 3.9 shows the ratio of rms eccentricities

$$\frac{\sqrt{\langle \varepsilon_2^2 \rangle}}{\sqrt{\langle \varepsilon_3^2 \rangle}^{\kappa}},$$

where $\kappa = 0.6$ for LHC collisions.

In case of ellipticity ε_2 it is clear that it increases with decreasing parameter p. This is caused by the profile of the deposited entropy during the nucleon-nucleon collision (see Figure 3.7). With decreasing p, the deposited entropy is narrower. This causes sharper edges of the asymmetric regions that are responsible for the elliptical shape and thus higher ellipticity ε_2.

The parameter p has almost no influence on triangularity ε_3 up to semiperipheral collisions and little impact on peripheral collisions. This means that the ratio follows the same order as the ellipticity ε_2.

Figure 3.9 shows the ratio of the rms of eccentricities $\sqrt{\langle \varepsilon_2^2 \rangle} / \sqrt{\langle \varepsilon_3^2 \rangle}^{0.6}$ on the right-hand side. Among all initial condition models, only IP-Glasma was consistently in agreement with the experimental measurements. The IP-Glasma results are represented by empty circles, and the experimental results correspond to the grey area [170]. One can see that the TRENTo model with prescription $p = 0$ agrees with the dynamical model IP-Glasma and the experimental data.

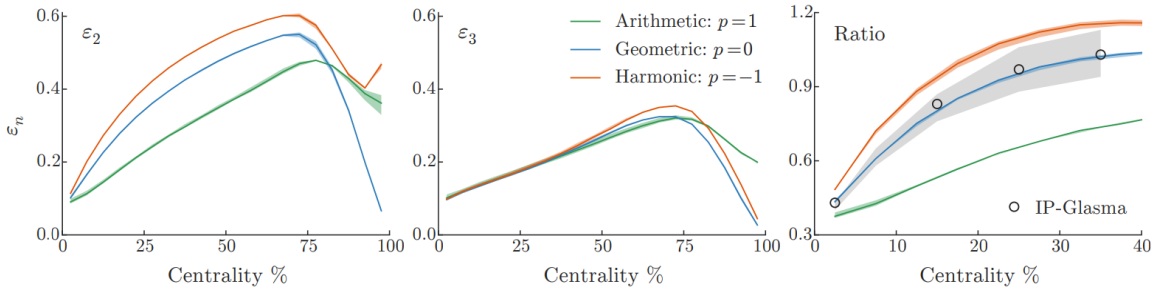

Figure 3.9: Ellipticity ε_2 (left), triangularity ε_3 (middle), and the ratio of the rms eccentricities $\sqrt{\langle\varepsilon_2^2\rangle}/\sqrt{\langle\varepsilon_3^2\rangle}^{0.6}$ for arithmetic prescription $p = +1$ (green line), geometric prescription $p = 0$ (blue line), and harmonic prescription $p = -1$ (orange line). Grey band represents allowed band by [170]. Empty circles represent IP-Glasma results for the ratio of the rms eccentricities. Retrieved from [1].

In the case of ultracentral uranium-uranium collisions, we assume only collisions with fewer than < 1% spectators. The uranium nucleus is greatly deformed. There are two possible ways in which they can collide with a small number of spectators. The first orientation is the tip-tip orientation, where the long axes of both spheroids are aligned with the beam axis. The second orientation occurs when the long axes of both spheroids are aligned with each other in the transverse plane. The second orientation has an elliptical profile in the transverse plane, and thus a larger ellipticity ε_2.

Glauber model predicts that the tip-tip orientation produces more binary nucleon-nucleon collisions than the side-side orientation. The tip-tip orientation has a smaller ellipticity ε_2 compared to the side-side orientation. Furthermore, the Glauber model predicts that there should be a decreasing trend in ellipticity ε_2 as a function of the charged multiplicity N_{ch} [171] that should be proportional to the number of binary collisions N_{coll}. In Figure 3.10, the Glauber model prediction is shown by a grey line.

However, there is no evidence of this decreasing behaviour in the data [163, 164]. The ellipticity ε_2 remains flat as for the Au+Au collision. There was a suspicion that fluctuations in the Monte Carlo Glauber model could correct its prediction [172], but it was unsuccessful.

The TRENTo model predicts roughly the same number of charged particles in the tip-tip and side-side orientation. There is no decrease in ellipticity ε_2 as a function of charged multiplicity, and the model agrees with the measured data from the STAR experiment [163, 164]. The blue dots with error bars represent the calculations produced by TRENTo. The blue lines are linear fits to TRENTo results.

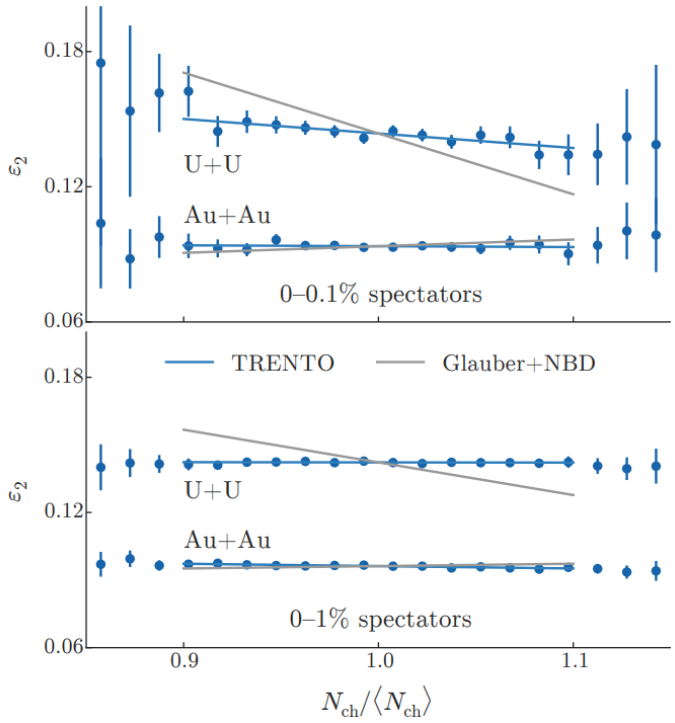

Figure 3.10: Ultra-central U+U and Au+Au collision with 0−0.1% spectators (upper panel) and 0 − 1% spectators (lower panel). Blue dots with blue error bars represent TRENTo calculations with blue lines as a linear fits to those results. Grey lines represent Glauber+NBD model predictions [163]. Retrieved from [1].

Bayesian analysis of TRENTo parameters

Since it is challenging to constrain the parameters of the initial state, it is necessary to use Bayesian parameter estimation and advanced statistical analysis techniques to effectively study the parameter space. [173, 174]

The first step is to define the prior $P(\mathbf{x})$ (i.e. uniform distribution) and randomly generate parameters with the Latin hypercube algorithm [175, 176]. Then the principal component analysis [177] is performed. This essentially takes the observables $\left(\frac{\mathrm{d}N_{\mathrm{ch}}}{\mathrm{d}\eta}, \langle p_{\mathrm{T}}\rangle, v_2\{2\}, v_3\{2\}, v_4\{2\}\right)$ and linearly transforms them into a new set of linearly uncorrelated variables. This reduces the number of variables that must be evaluated. The emulator is finished with a Gaussian process [178] that estimates the principal components without running the model. Finally, the Bayes theorem

$$P(\mathbf{x} \mid \mathbf{y}) \propto P(\mathbf{y} \mid \mathbf{x}) P(\mathbf{x})$$

is sampled by Markov chain Monte Carlo importance sampling with the Metropolis-Hastings algorithm [179, 180]. $P(\mathbf{y} \mid \mathbf{x})$ is called likelihood and is evaluated by emulator. $P(\mathbf{x} \mid \mathbf{y})$ is called posterior.

Optimal parameters of the TRENTo initial state were extracted from a model-to-data comparison using Bayesian analysis in [174]. The model comprised the TRENToinitial state, followed by

a 3+1 dimensional viscous hydrodynamics, followed by a particlisation and a hadronic cascade. The hadronic observables were compared with the Pb+Pb data measured by the ALICE collaboration [181, 182, 183, 184, 185, 186, 187]. Parameters obtained from this process are shown in Table 3.3. These specific parameters are used for the medium simulation in Chapter 5.

Table 3.3: Value of normalisation factors $N_{2.76}$ and $N_{5.02}$ for two LHC energies, reduced thickness parameter p, fluctuation k, nucleon width w, and minimum nucleon-nucleon distance d. The values of the TRENTo parameters were obtained from Bayesian analysis [173, 174].

Parameter	Value
$N_{2.76}$	13.94
$N_{5.02}$	18.50
p	0.0
k	1.044
w	0.956 fm
d	1.27 fm

3.1.3 Preequilibrium dynamics

Preequilibrium dynamics describe the stage of the collision before the QGP is formed. This can be done via kinetic theory. The evolution of the out-of-equilibrium system is described by the Boltzmann equation.

$$p^\mu \partial_\mu f(x;p) = C[f], \tag{3.4}$$

where f is the one-particle distribution function, p is the on-shell four-momentum, x are space-time coordinates and $C[f]$ is the collision kernel. For collisionless evolution, the collision kernel is zero $C[f] = 0$. This thesis uses free-streaming preequilibrium dynamics that corresponds to collisionless evolution.

The Boltzmann equation is formulated in Milne coordinates

$$\tau = \sqrt{t^2 - z^2}, \qquad x, \qquad y, \qquad \eta_s = \frac{1}{2}\ln\left(\frac{t+z}{t-z}\right);$$

$$E, \qquad p_x, \qquad p_y, \qquad y = \frac{1}{2}\ln\left(\frac{E+p_z}{E-p_z}\right).$$

Solving the Boltzmann equation (3.4) either analytically or numerically leads to the evolution of the distribution function in the phase space. If we use the initial state distribution from the TRENTo model as input at the proper time τ_0, we can obtain the distribution function at the proper time τ_s. From this free-streaming evolution, we can obtain the full energy-momentum tensor

$$T^{\mu\nu}(x_\mathrm{T}, \eta_s, \tau_s) = \frac{g}{(2\pi)^3}\int \frac{d^3p}{E} p^\mu p^\nu f(x_\mathrm{T}, \eta_s, \tau_s; p_\mathrm{T}, y),$$

where g is a degeneracy factor. The energy-momentum tensor $T^{\mu\nu}$ can be decomposed into hydrodynamic variables, such as the energy density ε, the (hydrostatic + bulk) pressure $\tilde{P}$, and the shear stress tensor $\pi^{\mu\nu}$. This will be shown in Section 3.2.2.

As a last step, the Landau matching condition is utilised

$$T^{\nu}_{\mu} u_{\nu} = \varepsilon u_{\mu}.$$

Landau matching condition defines the fluid rest frame velocity u_{μ} as the time-like eigenvector of the energy-momentum tensor $T^{\mu\nu}$. This condition produces a unique u_{μ} since the energy-momentum tensor has only one time-like eigenvector.

All these variables are then inserted into the hydrodynamic code as initial conditions. Free-streaming code `freestream-milne` [2] was used to produce observables in Chapter 5.

3.2 Relativistic Hydrodynamics

From the existing observations, we can tell that QGP behaves like an almost perfect fluid. The energy-momentum tensor of the perfect fluid in a rest frame is only characterised by the energy density $\varepsilon = \rho$ and the isotropic pressure P. In a perfect fluid, there would be no shear viscosity, bulk viscosity, or heat conductivity. Even when the ideal hydrodynamics of the perfect fluid could make some predictions such as mass ordering of second harmonics v_2 [108], it is still a simplification. To obtain a more accurate description of the QGP, we have to consider viscous corrections. This includes shear and bulk viscosity-to-entropy density ratios as dimensionless quantities and their temperature dependence.

Although the viscosity of QGP is not significantly large, it plays an important role in HIC simulations. Later, in this section, we will mention how shear and bulk viscosity appear in the hydrodynamic equations. Unsurprisingly, this implies that viscosity plays a key role in hydrodynamic evolution, such as temperature and size, which are very important for the simulation of jets inside the medium. Viscosity also affects the distribution of the outgoing particles and, therefore, low transverse momentum hadronic observables [188].

3.2.1 Ideal hydrodynamics

To obtain the ideal hydrodynamic equations, we have to start with the law of energy and momentum conservation and the k number of conserved charge currents

$$\partial_{\mu} T^{\mu\nu} = 0, \tag{3.5}$$

$$\partial_{\mu} N^{\mu}_{i} = 0, \qquad i = 1, ..., k. \tag{3.6}$$

Those $4 + k$ equations with $10 + 4k$ variables arise from Noether's theorem. The energy–momentum tensor $T^{\mu\nu}$ and all charge currents N^{μ}_{i} are Noether currents.

Since ideal and viscous fluids have different energy-momentum tensors and charge currents, there will be a subscript 'zero' that will denote the ideal case. This ideal case will also be part of the viscous quantities. The ideal energy-momentum tensor has form

$$T^{\mu\nu}_{0} = \varepsilon u^{\mu} u^{\nu} - P \Delta^{\mu\nu},$$

where ε is the energy density, P is the equilibrium pressure, $u^{\mu} = \gamma(1, \mathbf{v})$ denotes the four-velocity of flow and $\Delta^{\mu\nu} = \eta^{\mu\nu} - u^{\mu} u^{\nu}$ is the projection tensor operator. Next, the ideal current is the conserved charge density multiplied by four-velocity

$$N^{\mu}_{0,i} = n_i u^{\mu}.$$

There can be multiple conserved charges. That is why there is an index i as a subscript of the conserved charge densities n_i.

By construction, $\Delta^{\mu\nu}$ and u^μ are orthogonal to each other

$$u^\mu \Delta_{\mu\nu} = u^\mu(\eta_{\mu\nu} - u_\mu u_\nu) = u_\nu - u^\mu u_\mu u_\nu = u_\nu - u_\nu = 0.$$

The equations of motion

With the orthogonal projection of the energy-momentum conservation equation

$$u_\mu \partial_\nu T_0^{\mu\nu} = 0, \qquad \Delta^\alpha_\mu \partial_\nu T_0^{\mu\nu} = 0$$

one can obtain the relativistic continuity equation

$$\begin{aligned} u_\mu \partial_\nu T_0^{\mu\nu} &= u_\mu \partial_\nu (\varepsilon u^\mu u^\nu - P\Delta^{\mu\nu}) = u_\mu u^\mu u^\nu \partial_\nu \varepsilon + \varepsilon u_\mu u^\mu \partial_\nu u^\nu + \varepsilon u_\mu u^\nu \partial_\nu u^\mu - u_\mu \partial_\nu (P\Delta^{\mu\nu}) \overset{u_\mu u^\mu = 1}{=} \\ &= u^\nu \partial_\nu \varepsilon + \varepsilon \partial_\nu u^\nu + \varepsilon u_\mu u^\nu \partial_\nu u^\mu - u_\mu \Delta^{\mu\nu} \partial_\nu P - u_\mu P \partial_\nu \Delta^{\mu\nu} \overset{u_\mu \Delta^{\mu\nu} = 0}{=} \\ &= u^\nu \partial_\nu \varepsilon + \varepsilon \partial_\nu u^\nu + \varepsilon u_\mu u^\nu \partial_\nu u^\mu - u_\mu P \partial_\nu (g^{\mu\nu} - u^\mu u^\nu) = \\ &= u^\nu \partial_\nu \varepsilon + \varepsilon \partial_\nu u^\nu + \varepsilon u_\mu u^\nu \partial_\nu u^\mu + u_\mu u^\mu P \partial_\nu u^\nu + P u_\mu u^\nu \partial_\nu u^\mu = \\ &= u^\nu \partial_\nu \varepsilon + (\varepsilon + P) \partial_\nu u^\nu + (\varepsilon + P) u_\mu u^\nu \partial_\nu u^\mu \end{aligned}$$

$$u_\mu u^\nu \partial_\nu u^\mu = \frac{1}{2}(u_\mu u^\nu \partial_\nu u^\mu + u_\mu u^\nu \partial_\nu u^\mu) = \frac{1}{2}(u^\mu u^\nu \partial_\nu u_\mu + u_\mu u^\nu \partial_\nu u^\mu) = \frac{1}{2} u^\nu \partial_\nu (u_\mu u^\mu) = 0$$

$$u^\nu \partial_\nu \varepsilon + (\varepsilon + P) \partial_\nu u^\nu = 0 \tag{3.7}$$

and the relativistic Euler equation

$$\begin{aligned} \Delta^\alpha_\mu \partial_\nu T_0^{\mu\nu} =& \Delta^\alpha_\mu \partial_\nu (\varepsilon u^\mu u^\nu - P\Delta^{\mu\nu}) = \Delta^\alpha_\mu \varepsilon u^\nu \partial_\nu u^\mu + \Delta^\alpha_\mu u^\mu \partial_\nu (\varepsilon u^\nu) - \Delta^\alpha_\mu P \partial_\nu \Delta^{\mu\nu} - \Delta^\alpha_\mu \Delta^{\mu\nu} \partial_\nu P = \\ =& (\delta^\alpha_\mu - u^\alpha u_\mu) \varepsilon u^\nu \partial_\nu u^\mu + \Delta^\alpha_\mu u^\mu P \partial_\nu u^\nu + (\delta^\alpha_\mu - u^\alpha u_\mu) P u^\nu \partial_\nu u^\mu - \delta^\alpha_\mu (\eta^{\mu\nu} + u^\mu u^\nu) \partial_\nu P - \\ & - u^\alpha u_\mu \Delta^{\mu\nu} \partial_\nu P = \\ =& \delta^\alpha_\mu \varepsilon u^\nu \partial_\nu u^\mu + \delta^\alpha_\mu P u^\nu \partial_\nu u^\mu - (\eta^{\alpha\nu} + u^\alpha u^\nu) \partial_\nu P = (\varepsilon + P) u^\nu \partial_\nu u^\alpha - \Delta^{\alpha\nu} \partial_\nu P \end{aligned}$$

$$(\varepsilon + P) u^\nu \partial_\nu u^\alpha - \Delta^{\alpha\nu} \partial_\nu P = 0. \tag{3.8}$$

Entropy conservation

The first law of thermodynamics states

$$E = TS - PV + \sum_i \mu_i N_i.$$

This can be rewritten in terms of variables per unit volume

$$\varepsilon + P = Ts + \sum_i \mu_i n_i. \tag{3.9}$$

Combining this with the second law of thermodynamics leads to the differential form of this equation

$$\mathrm{d}\varepsilon = T\mathrm{d}s + \sum_i \mu_i \mathrm{d}n_i. \tag{3.10}$$

When we use equation equation (3.9) and equation (3.10) as a prescription for energy density derivatives and put them in the continuity equation (3.7) we obtain the following

$$u^\nu \partial_\nu \varepsilon + (\varepsilon + P)\partial_\nu u^\nu = u^\nu \left(T\partial_\nu s + \sum_i \mu_i \partial_\nu n_i \right) + \left(Ts + \sum_i \mu_i n_i \right) \partial_\nu u^\nu =$$
$$= T(u^\nu \partial_\nu s + s\partial_\nu u^\nu) + \sum_i \mu_i (u^\nu \partial_\nu n_i + n_i \partial_\nu u^\nu) = T\partial_\nu (s u^\nu) + \sum_i \mu_i \partial_\nu (n_i u^\nu),$$

where $n_i u^\nu$ is the conserved current N_i^ν and it is possible to use conservation laws (3.6) and the sum vanishes. Furthermore, we can define the entropy four-current as

$$S^\nu \equiv s u^\nu.$$

With continuity equation (3.7) being equal to zero we obtain

$$T\partial_\nu S^\nu = 0.$$

Since we have finite temperature T, it is possible to divide the whole expression by T and finally obtain the entropy conservation equation

$$\partial_\mu S^\mu = 0. \tag{3.11}$$

3.2.2 Viscous hydrodynamics

When assuming viscous effects, one can inspect the microscopic phase-space distribution and add a small correction to the equilibrium function

$$f(\vec{x}, \vec{p}) = f_0(\vec{x}, \vec{p}) + \delta f(\vec{x}, \vec{p}).$$

Then energy-momentum tensor and charge currents are connected with the kinetic theory as

$$T^{\mu\nu} = \sum_i \int \frac{\mathrm{d}^3 \vec{p}}{E} p^\mu p^\nu f_i(\vec{x}, \vec{p}),$$
$$N_i^\mu = n_i \int \frac{\mathrm{d}^3 \vec{p}}{E} p^\mu f_i(\vec{x}, \vec{p}).$$

After adding the corrections to the phase-space distribution function, it can be found that the energy-momentum tensor has an ideal part $T_0^{\mu\nu}$ plus a non-equilibrium contribution from δf

$$T^{\mu\nu} = T_0^{\mu\nu} + \delta T^{\mu\nu}.$$

Furthermore, the conserved currents with their ideal parts $N_{0,i}^\mu$ also obtain respective disipative flows

$$N_i^\mu = N_{0,i}^\mu + \delta N_i.$$

There are a few possible correction terms that can be found in the energy-momentum tensor with respect to covariance conditions. The decomposed energy-momentum tensor with those correction terms takes form as

$$T^{\mu\nu} = \varepsilon u^\mu u^\nu - P\Delta^{\mu\nu} + W^\mu u^\nu + W^\nu u^\mu + \Pi^{\mu\nu}. \tag{3.12}$$

Conserved charge currents with its correction term are

$$N_i^\mu = n_i u^\mu + V_i^\mu.$$

Energy-momentum tensor and conserved currents in this form are considered to be Noether currents. They hold the conservation equations (3.5) and (3.6). $T^{\mu\nu}$ and N_i^μ are frame-independent quantities. However, a choice of flow velocity u^μ is not unique. There are at least two known definitions of u^μ, called Eckart and Landau frames. There can be found two possible definitions of flow within two frames, Eckart frame and Landau frame.

Eckart frame (charge flow):

$$u_E^\mu = \frac{N^\mu}{\sqrt{N_\nu N^\nu}}.$$

In the Eckart frame [189], the collective flow is defined as the flow of conserved charge. Since flow is represented as the movement of particle density, the main benefit is that charge diffusion is zero

$$V_E^\mu = 0.$$

It is called that the total conserved charge flux is diffusionless. In the Eckart frame, the first-order theory is unstable due to the limit of relaxation time $\tau_W \to 0$. However, second-order theory can be stable because of the nonzero value of τ_W. [190]

Landau frame (energy flow):

$$u_L^\mu = \frac{T^{\mu\nu}u_\nu}{\sqrt{u_\rho T^{\rho\sigma}T_{\sigma\kappa}u^\kappa}}.$$

This form of flow represents the movement of the energy and momentum densities. For this reason, the dissipation of energy is equal to zero

$$W_L^\mu = 0.$$

Landau frame is used in most HIC numerical simulations.

The difference between those two definitions is

$$u_L^\mu - u_E^\mu = \frac{W_E^\mu}{\varepsilon_E + P_E} + \mathcal{O}(\delta^2) = -\frac{V_L^\mu}{n_L} + \mathcal{O}(\delta^2),$$

where $\mathcal{O}(\delta^2)$ denotes more than the first-order correction in terms of dissipative quantities. Since there are different definitions of flow, there are also differences in thermodynamic variables such as energy density ε and particle density n since they are directly related to the definitions of flow. Their second-order corrections are

$$\varepsilon_L - \varepsilon_E = \frac{W_E^\mu W_\mu^E}{\varepsilon_E + P_E} + \mathcal{O}(\delta^3) \tag{3.13}$$

$$n_L - n_E = -\frac{1}{2}\frac{V_L^\mu V_\mu^L}{n_L} + \mathcal{O}(\delta^3) \tag{3.14}$$

Equations (3.13) and (3.14) imply that corrections to the other thermodynamic variables (P, s, T, μ) are also of second order. [190]

For both Eckart and Landau frames, we can split the tensor $\Pi^{\mu\nu}$ into traceless part and non-traceless part

$$\Pi^{\mu\nu} = \pi^{\mu\nu} - \Delta^{\mu\nu}\Pi,$$

where the shear stress tensor $\pi^{\mu\nu}$ is a traceless part

$$\pi^{\mu}_{\mu} = 0,$$

and $\Delta^{\mu\nu}$ multiplied by thy bulk pressure Π is the non-traceless part

$$\Delta^{\mu}_{\mu}\Pi = (\delta^{\mu}_{\mu} - u^{\mu}u_{\mu})\Pi = 2\Pi.$$

Then, in Landau frame, we can rearrange the energy-momentum tensor (3.12) as

$$T^{\mu\nu}_{L} = \varepsilon u^{\mu}u^{\nu} - (P + \Pi)\Delta^{\mu\nu} + \pi^{\mu\nu},$$

where equilibrium pressure P plus bulk pressure Π can be labelled as total pressure $\tilde{P} = P + \Pi$. Since HIC simulations mainly use the Landau frame, there will be no subscript L if it is not explicitly needed.

Notation of relativistic viscous hydrodynamics

The projection tensor operator $\Delta^{\mu\nu}$ has already been defined as

$$\Delta^{\mu\nu} \equiv \eta^{\mu\nu} - u^{\mu}u^{\nu}$$

in contrast to the projection vector operator u^{μ}. The projection tensor operator $\Delta^{\mu\nu}$ projects in a direction perpendicular to u^{μ}, while u^{μ} projects in a direction parallel to itself.

It is convenient to denote the symmetric and traceless tensor $A^{\langle\mu\nu\rangle}$ constructed from an arbitrary tensor $A^{\mu\nu}$ that is also perpendicular to u^{μ} and u^{ν}

$$u_{\mu}A^{\langle\mu\nu\rangle} = u_{\nu}A^{\langle\mu\nu\rangle} = 0.$$

From now on the brackets like that will stand for

$$A^{\langle\mu\nu\rangle} \equiv \left[\frac{1}{2}(\Delta^{\mu}_{\alpha}\Delta^{\nu}_{\beta} + \Delta^{\mu}_{\beta}\Delta^{\nu}_{\alpha}) - \frac{1}{3}\Delta^{\mu\nu}\Delta_{\alpha\beta}\right]A^{\alpha\beta}.$$

Tensor constructed like that is indeed traceless

$$\begin{aligned} A^{<\mu}{}_{\mu>} &= \left[\frac{1}{2}(\Delta^{\alpha\mu}\Delta^{\beta}_{\mu} + \Delta^{\beta\mu}\Delta^{\alpha}_{\mu}) - \frac{1}{3}\Delta^{\mu}_{\mu}\Delta^{\alpha\beta}\right]A_{\alpha\beta} \\ &= \left[\frac{1}{2}(\Delta^{\alpha\beta} + \Delta^{\alpha\beta}) - \frac{1}{3}3\Delta^{\alpha\beta}\right]A_{\alpha\beta} \\ &= \left[\Delta^{\alpha\beta} - \Delta^{\alpha\beta}\right]A_{\alpha\beta} = 0. \end{aligned}$$

Identities $\Delta^{\mu\rho}\Delta^{\nu}_{\rho} = \Delta^{\mu\nu}$ and $\Delta^{\mu}_{\mu} = 3$ were used in last derivation.

Next, the divergence of the flow is denoted as

$$\theta \equiv \partial_{\mu}u^{\mu}.$$

This quantity is also called the expansion scalar.

Since the projection vector and the tensor operators in the local rest frame (LRF) are of the form

$$u^{\mu}_{\mathrm{LRF}} = (1,0,0,0),$$
$$\Delta^{\mu\nu}_{\mathrm{LRF}} = (0,-1,-1,-1),$$

the projections of the gradient operator are denoted as

$$D \equiv u_{\mu}\partial^{\mu},$$
$$\nabla^{\mu} \equiv \Delta^{\mu\nu}\partial_{\nu}.$$

D and ∇^{μ} are called substantial time and space derivatives, respectively. It is not hard to see that in the LRF those operators are indeed

$$D_{\mathrm{LRF}} = \partial_t$$
$$\nabla^{\mathrm{LRF}}_{\mu} = (0,\vec{\nabla}).$$

Decomposition of $T^{\mu\nu}$ and N^{μ}

Decomposition of the energy-momentum tensor with the projection operators u^{μ} and $\Delta^{\mu\nu}$. The quantities obtained from the decomposition of the energy-momentum tensor $T^{\mu\nu}$ are as follows:

$$\varepsilon = u_{\mu}T^{\mu\nu}u_{\nu},$$
$$\tilde{P} = P + \Pi = -\frac{1}{3}\Delta_{\mu\nu}T^{\mu\nu},$$
$$W^{\mu} = \Delta^{\mu}_{\alpha}T^{\alpha\beta}u_{\beta},$$
$$\pi^{\mu\nu} = T^{\langle\mu\nu\rangle}.$$

From the first two equations, it can be seen that the energy density ε is obtained from the time-like components of the energy-momentum tensor $T^{\mu\nu}$ and the total pressure $\tilde{P} = P + \Pi$ is obtained from the space-like components. The last equation is not a big revelation since we want $\pi^{\mu\nu}$ to be a traceless part of $T^{\mu\nu}$. This is ensured by the angular bracket operation on the indices.

The decomposition of N^{μ} is more straightforward. It is possible to obtain the charge density n_i and the dissipative charge current V_i^{μ} as follows:

$$n_i = u_{\mu}N_i^{\mu},$$
$$V_i^{\mu} = \Delta^{\mu}_{\nu}N_i^{\nu}.$$

Entropy production

When the theory of viscous hydrodynamics is constructed, the main assumption is that the entropy current has dissipative terms in addition to the equilibrium term. The dissipative terms would be constructed from V^{μ}, W^{μ}, $\pi^{\mu\nu}$, and Π. Within the Landau frame, the first-order correction reads as

$$S^{\mu} = su^{\mu} + \alpha V^{\mu},$$

Because $W_L^\mu = 0$. Furthermore, it is not possible to construct a Lorentz vector from $\pi^{\mu\nu}$, and a term with Π would violate the second law of thermodynamics. Therefore, a dissipative correction to the entropy current, which would be first-order in dissipative quantities, is not possible. [108]

For the ideal case, the proven equation (3.11) represents the conservation of entropy. However, in higher-order hydrodynamics, dissipative corrections are causing entropy production. The energy-momentum conservation law

$$\partial_\mu T^{\mu\nu} = 0$$

still holds for the viscous case. The projection of the energy-momentum conservation law in the direction of flow velocity is

$$u_\nu \partial_\mu T^{\mu\nu} = u_\nu \partial_\mu T_0^{\mu\nu} + u_\nu \partial_\mu \delta T^{\mu\nu} = 0,$$

where $u_\nu \partial_\mu T_0^{\mu\nu}$ can be recognized as $T\partial_\mu S^\mu$, since it was already proven. This leads to

$$\begin{aligned} T\partial_\mu S^\mu &= -u_\nu \partial_\mu \delta T^{\mu\nu} = -u_\nu \partial_\mu (\pi^{\mu\nu} - \Delta^{\mu\nu}\Pi) = \ldots = \\ &= \pi_{\mu\nu}\left[\frac{1}{2}(\Delta^\mu_{\ \alpha}\Delta^\nu_{\ \beta} + \Delta^\mu_{\ \beta}\Delta^\nu_{\ \alpha}) - \frac{1}{3}\Delta^{\mu\nu}\Delta_{\alpha\beta}\right]\Delta^{\alpha\gamma}\partial_\gamma u^\beta - \Pi\partial_\mu u^\mu. \end{aligned}$$

The divergence of entropy current reads as

$$\partial_\mu S^\mu = \frac{1}{T}(\pi_{\mu\nu}\nabla^\mu u^\nu - \Pi\theta). \tag{3.15}$$

Due to the non-vanishing dissipative part of the energy-momentum tensor $\delta T^{\mu\nu}$ there is a difference between the divergence of the entropy current in the ideal case in equation (3.11) and the first-order theory in equation (3.15). This result indicates the entropy production in absence of perfect equlibrium.

When considering second-order corrections, we can investigate the divergence of the entropy current within different frames. The second law of thermodynamics declares that entropy production can be expressed in a quadratic form. [190] Then the divergence of the entropy current in the Landau frame can be written as

$$\partial_\mu S_L^\mu = -\frac{V_\mu^L V_L^\mu}{\kappa_V},$$

and in the Eckart frame as

$$\partial_\mu S_E^\mu = -\frac{W_\mu^E W_E^\mu}{\kappa_W},$$

where κ_V is the baryon conductivity, and κ_W is the energy conductivity. Both κ_V and κ_W are positive

$$\kappa_V \geq 0,$$
$$\kappa_W \geq 0.$$

Due to entropy production (3.15), κ_V and κ_W are related as

$$\kappa_V = \kappa_W \left(\frac{n}{\varepsilon + P}\right)^2.$$

Divergence of entropy in both frames follows

$$\partial_\mu S^\mu \geq 0. \tag{3.16}$$

This result shows how a local second law of thermodynamics is postulated in the context of relativistic fluid dynamics. The difficulty here is that the entropy current S^μ is difficult to define outside the global thermal equilibrium, and the UV divergence is present in the case of working with the entanglement entropy.

The equations of motion

Derivation of the equations of motion in a viscous case follows the same direction as the derivation of the equation of motion in an ideal case. This means that the derivation starts with energy-momentum conservation

$$\partial_\mu T^{\mu\nu} = 0$$

and follows using projection operators u^μ and $\Delta^{\mu\nu}$.

One can start with the flow projection as

$$u_\nu \partial_\mu T^{\mu\nu} = 0$$

and obtain first equation of motion

$$u^\mu \partial_\mu \varepsilon + (\varepsilon + P + \Pi)\partial_\mu u^\mu - \pi_{\mu\nu}\left[\frac{1}{2}(\Delta^\mu{}_\alpha \Delta^\nu{}_\beta + \Delta^\mu{}_\beta \Delta^\nu{}_\alpha) - \frac{1}{3}\Delta^{\mu\nu}\Delta_{\alpha\beta}\right]\Delta^{\alpha\gamma}\partial_\gamma u^\beta = 0,$$

where using the previously defined notation will simplify it to

$$D\varepsilon = -(\varepsilon + P + \Pi)\theta + \pi_{\mu\nu}\nabla^{\langle\mu} u^{\nu\rangle}. \tag{3.17}$$

The second equation is obtained by means of an orthogonal projection $\Delta^{\mu\nu}$ of the energy-momentum conservation

$$\Delta_{\mu\alpha}\partial_\beta T^{\alpha\beta} = 0.$$

Then one can obtain the second equation of motion

$$(\varepsilon + P + \Pi)u^\nu \partial_\nu u^\mu - \Delta^{\mu\nu}\partial_\nu (P + \Pi) + \Delta^{\mu\alpha}\Delta^{\beta\nu}\partial_\nu \pi_{\alpha\beta} - \pi^{\mu\nu}u^\alpha \partial_\alpha u_\nu = 0,$$

where once again, the same notation can be used to simplify the equation

$$(\varepsilon + P + \Pi)Du^\mu = \nabla^\mu (P + \Pi) - \Delta^{\mu\alpha}\nabla^\beta \pi_{\alpha\beta} + \pi^{\mu\nu}Du_\nu. \tag{3.18}$$

Equations (3.17) and (3.18) lead to relativistic versions of the non-relativistic Navier-Stokes equations.

Navier-Stokes formalism

Navier-Stokes formalism arises from the relativistic generalisation of the non-relativistic Navier-Stokes equations

$$(\partial_t + \vec{v}\cdot\vec{\nabla})\vec{v} = -\frac{1}{\rho}\vec{\nabla}P + \frac{\eta}{\rho}\Delta\vec{v},$$

$$\partial_t \rho + \vec{\nabla} \cdot (\rho \vec{v}) = 0.$$

The main idea of this formalism is the linear relationship between dissipative flows and the corresponding thermodynamic forces. [108, 189, 191, 192]

Linear relationship in Navier-Stokes formalism is provided by the transport coefficients. There is a bulk viscosity ζ that is related to the scalar force. Then there is a shear viscosity η that is connected to the traceless tensor force.

The current that corresponds to the bulk viscosity ζ is the bulk pressure Π and the corresponding force is a negative expansion scalar $-\theta = -\partial_\mu u^\mu$. This leads to the equation for the bulk pressure Π within the Navier-Stokes formalism

$$\Pi = -\zeta\theta \tag{3.19}$$

Shear viscosity η can be associated with shear stress tensor $\pi^{\mu\nu}$. Shear viscosity ensures linearity between the shear stress tensor $\pi^{\mu\nu}$ and the corresponding thermodynamic tensor force $\nabla^{\langle\mu} u^{\nu\rangle}$. This leads to the equation for the shear stress tensor $\pi^{\mu\nu}$ within the Navier-Stokes formalism

$$\pi^{\mu\nu} = 2\eta\nabla^{\langle\mu} u^{\nu\rangle}. \tag{3.20}$$

Equations (3.19) and (3.20) are called constitutive equations and are phenomenological definitions.

Using constitutive equations from Navier-Stokes formalism, one can revisit the entropy production equation (3.15)and rewrite it as

$$T\partial_\mu S^\mu = \frac{\pi^{\mu\nu}\pi_{\mu\nu}}{2\eta} + \frac{\Pi^2}{\zeta}. \tag{3.21}$$

Since the shear viscosity η and bulk viscosity ζ are positive, this ensures the second law of thermodynamics (3.16).

One can also revisit the first equation of motion 3.17 and rewrite it as

$$D\varepsilon = -\varepsilon\theta - P\theta + \frac{\Pi^2}{\zeta} + \frac{\pi_{\mu\nu}\pi^{\mu\nu}}{2\eta}.$$

This equation describes the evolution of the energy density ε. The first term on the RHS describes the dilution/compression of energy density through the expansion scalar. The second term describes the work done by pressure. Finally, the third and fourth terms represent the production of entropy that heats up the system. [108]

The main problem with the Navier-Stokes approach is that the Navier-Stokes equations violate causality. [192, 193, 194, 195] This means that it is not ensured that the information speed does not exceed the speed of light. Not only this is not ensured, the short-wavelength modes can propagate with arbitrarily large velocity. However, macroscopic effects in the fluid that are caused by microscopic scatterings should be delayed by a relaxation time that is comparable to the scattering time. From this causality violation arise the numerical instabilities [192, 193, 194, 195], which makes the Navier-Stokes approach futile for numerical simulations [192]. Causality violation and thus also numerical instabilities from acausality are solved in the following Israel-Stewart formalism.

3.2.3 Israel-Stewart formalism

Entropy production equations

It can be derived [196] that the equilibrium entropy current from equation (3.10) takes form as

$$S_0^\mu = P(\alpha,\beta)\beta^\mu - \alpha N_0^\mu + \beta_\nu T_0^{\mu\nu},$$

where the thermal potential α and inverse temperature β are defined by temperature T, and the chemical potential μ as

$$\alpha \equiv \frac{\mu}{T}, \qquad \beta \equiv \frac{1}{T}, \qquad \beta^\mu \equiv \frac{u^\mu}{T}.$$

Furthermore, one can also derive [197] off-equilibrium entropy current as

$$S^\mu = P(\alpha,\beta)\beta^\mu - \alpha N^\mu + \beta_\nu T^{\mu\nu} + Q^\mu(\delta N^\mu, \delta T^{\mu\nu}),$$

where $N^\mu = N_0^\mu + \delta N^\mu$ and $T^{\mu\nu} = T_0^{\mu\nu} + \delta T^{\mu\nu}$ contains first order corrections and Q^μ as a function of deviations δN^μ and $\delta T^{\mu\nu}$ contains second and higher order corrections. Taking into account only first-order corrections from N^μ and $T^{\mu\nu}$ (i.e., $Q^\mu = 0$), one would obtain the entropy production mentioned in equation (3.21).

The Israel-Stewart formulation is the second-order theory of hydrodynamics. That is why Q^μ keeps all second-order terms as follows [192, 196, 197, 198]

$$Q^\mu = -\frac{u^\mu}{2T}(\beta_0\Pi^2 + \beta_2\pi_{\mu\nu}\pi^{\mu\nu}), \tag{3.22}$$

where β_0 and β_2 are phenomenological expansion coefficients. It is good to mention that these coefficients have nothing to do with the inverse temperature β^μ. There is a connection between the expansion coefficients and relaxation times

$$\beta_0 \equiv \frac{\tau_\Pi}{\zeta}, \qquad \beta_2 \equiv \frac{\tau_\pi}{2\eta}. \tag{3.23}$$

Since this thesis does not take into account the thermodynamic force caused by the heat conductivity λ, the rest of the expansion coefficients are equal to zero $\beta_1 = \alpha_0 = \alpha_1 = 0$ and their terms are not included in equation (3.22). This would lead us to second-order entropy production [196]

$$\begin{aligned}\partial_\mu S^\mu = &-\frac{1}{T}\left[\Pi\theta + \beta_0\Pi D\Pi + \frac{1}{2}T\Pi^2\partial_\mu\left(\frac{\beta_0}{T}u^\mu\right)\right] \\ &+\frac{1}{T}\left[\pi^{\mu\nu}\sigma_{\mu\nu} - \beta_2\pi^{\mu\nu}D\pi_{\mu\nu} + \frac{1}{2}T\pi^{\mu\nu}\pi_{\mu\nu}\partial_\rho\left(\frac{\beta_2}{T}u^\rho\right)\right],\end{aligned}$$

where the velocity stress tensor $\sigma_{\mu\nu}$ is defined as

$$\sigma_{\mu\nu} \equiv \nabla_{\langle\mu}u_{\nu\rangle}.$$

To ensure the second law of thermodynamics in the same form as equation 3.21, there are constraints for transport coefficients

$$D\Pi = -\frac{1}{\tau_\Pi}\left[\Pi + \zeta\theta + \Pi\zeta T\partial_\mu\left(\frac{\tau_\Pi u^\mu}{2\zeta T}\right)\right], \tag{3.24}$$

$$\Delta^{\mu\alpha}\Delta^{\nu\beta}D\pi_{\alpha\beta} = -\frac{1}{\tau_\pi}\left[\pi^{\mu\nu} - 2\eta\sigma^{\mu\nu} + \pi^{\mu\nu}\eta T\partial_\alpha\left(\frac{\tau_\pi u^\alpha}{2\eta T}\right)\right]. \tag{3.25}$$

Equations (3.24) and (3.25) are second-order hydrodynamic equations and are used in simulations for this work.

Kinetic theory equations

The kinetic approach for the Israel-Stewart equations arises from microscopic kinetic theory and consequently from corrections to the equilibrium distribution function

$$f(x,p) = f_0(x,p)[1 + (1 \pm f_0(x,p))\delta f(x,p)].$$

Then the Taylor expansion of the correction momentum is performed as

$$\delta f(x,p) = \epsilon(x) + \epsilon_\mu(x)p^\mu + \epsilon_{\mu\nu}(x)p^\mu p^\nu + \mathcal{O}(p^3),$$

where coefficients $\epsilon, \epsilon_\mu, \epsilon_{\mu\nu}$ can be related to dissipative flows. Since ϵ_μ is connected to the heat flow q_μ it will not be considered. Furthermore, the coefficient ϵ is related to the bulk pressure Π and the coefficient tensor $\epsilon_{\mu\nu}$ is related to the shear stress tensor $\pi_{\mu\nu}$. Those quantities are calculated using the kinetic prescription for the energy-momentum tensor

$$T^{\mu\nu} = \int \frac{\mathrm{d}^3\vec{p}}{E} p^\mu p^\nu f(\vec{x},\vec{p}).$$

The conservation laws and the second-order Israel-Steward equations are obtained by using the Boltzmann equation

$$p^\mu \partial_\mu f(x,p) = C[f],$$

and applying integration with measure

$$\frac{\mathrm{d}^3 p}{(2\pi)^3 p_0}$$

and weight p^μ in some form.

With this approach, it is possible to obtain conservation laws and Israel-Steward equations [199] for the bulk pressure Π and the shear stress tensor $\pi^{\mu\nu}$ that are obtained with Grad's 14-momentum approximation

$$D\Pi = \frac{-\zeta\theta - \Pi}{\tau_\Pi} - \frac{\delta_{\Pi\Pi}}{\tau_\Pi}\Pi\theta + \frac{\lambda_{\Pi\pi}}{\tau_\Pi}\pi^{\mu\nu}\sigma_{\mu\nu}, \tag{3.26}$$

$$D\pi^{\langle\mu\nu\rangle} = \frac{2\eta\sigma^{\mu\nu} - \pi^{\mu\nu}}{\tau_\pi} - \frac{\delta_{\pi\pi}}{\tau_\pi}\pi^{\mu\nu}\theta + \frac{\phi_7}{\tau_\pi}\pi_\alpha^{\langle\mu}\pi^{\nu\rangle\alpha} - \frac{\tau_{\pi\pi}}{\tau_\pi}\pi_\alpha^{\langle\mu}\sigma^{\nu\rangle\alpha} + \frac{\lambda_{\pi\Pi}}{\tau_\pi}\Pi\sigma^{\mu\nu}. \tag{3.27}$$

Equations (3.26) and (3.27) are second-order hydrodynamic equations.

3.2.4 Summary of relativistic hydrodynamics

There are several numerical implementations of hydrodynamic equations in simulation codes. First, both the Landau and Eckart frames can be used for the definition of the flow. Furthermore, in addition to the ideal and Navier-Stokes formalism, the Israel-Stewart formalism can be introduced in simplified forms [192]. Also, another second-order theory is the Öttinger-Grmela formalism, which can equivalently explain the evolution of a relativistic fluid. However, this work uses the second-order Israel-Stewart formalism implemented in `MUSIC` [3, 200]. Hydrodynamic equations are numerically solved with the Kurganov-Tadmor scheme [201, 202]

together with the Heun method to solve the resulting ordinary differential equations.

The equations derived from relativistic hydrodynamics are not a complete set of equations that the fluid evolves according to. To complete this set of equations, one has to introduce the equation of state that connects thermodynamic quantities such as energy density ε, pressure P, and baryon chemical potential μ_B. Furthermore, transport coefficients are dependent on temperature and should also be considered as a parameterisation that corresponds to overall evolution.

3.3 Equation of State

To complete the set of hydrodynamic equations, it is necessary to introduce the equation of state (EoS). This thermodynamic equation relates the state variables such as pressure P, temperature T, energy density ε, chemical potential μ, etc. The first expression of an EoS is from 1662 called Boyle's law

$$PV = \text{constant}.$$

More than a hundred years later, in 1789, Jacques Charles introduced his volume and temperature relation

$$\frac{V_1}{T_1} = \frac{V_2}{T_2}$$

In 1834, Émile Clapeyron combined Boyle's and Charles's laws and stated the EoS of an ideal non-relativistic gas for the first time as

$$PV = nRT,$$

where n is the amount of substance in moles and R is the universal gas constant.

Since then, many equations of state have been introduced for various systems. The important systems for this work are those at the QCD energy scale to describe the hot QGP and the hadronic resonance gas that are created in the HIC. At the beginning of relativistic hydrodynamics in 1965 introduced by Landau [203], the only option was the EoS derived in the following Section 3.3.1.

When QGP was discovered [114, 115, 116, 117, 118], attempts to reproduce the measurements started to appear and the first-order phase transition EoS was used. However, the QCD lattice calculations showed that at small baryon chemical potential $\mu_B \sim 0$ the transition to the deconfined phase is the crossover [204]. Today, it is common to use EoS with a crossover phase transition at high RHIC or LHC energies.

3.3.1 Massless ultrarelativistic gas

The ideal EoS describes non-interacting matter composed of massless particles ($m = 0$) or equivalently particles with ultrarelativistic speed $E = \sqrt{\vec{p}^2 + m^2} \approx ||\vec{p}|| \equiv p$. The ideal QGP EoS would include quarks with chemical potential $+\mu_q$, antiquarks with chemical potential $-\mu_q$, and gluons with chemical potential $\mu = 0$ because there is no limit on the boson number.

The quarks and antiquarks are fermions, so they follow Fermi-Dirac statistics (see Section 2.1.1)

$$f_{\text{FD}}(x,p) = \frac{g_q}{(2\pi)^3} \frac{1}{\exp\left(\frac{E-\mu}{T}\right)+1},$$

where the degeneracy factor of quarks is

$$g_q = (\text{colour}) \times (\text{spin}) \times (\text{flavour}) = 3 \times 2 \times N_f.$$

Furthermore, gluons are bosons that follow Bose-Einstein statistics (see Section 2.1.1)

$$f_{\text{BE}}(x,p) = \frac{g_g}{(2\pi)^3} \frac{1}{\exp\left(\frac{E-\mu}{T}\right) - 1},$$

where the degeneracy factor of gluons is

$$g_g = (\text{colour}) \times (\text{spin}) = 8 \times 2.$$

Even though the gluon has spin 1, its spin degeneracy is 2 because massless gauge bosons have only two polarisation states without longitudinal orientation with respect to the direction in which the gluon travels. This is because they are massless particles.

The distribution function $f(x,p)$ is connected in kinetic theory with particle density

$$n = \iiint_{\mathbb{R}^3} f(x,p) \mathrm{d}^3 p,$$

energy density

$$\varepsilon = \iiint_{\mathbb{R}^3} E f(x,p) \mathrm{d}^3 p$$

and pressure

$$P = \iiint_{\mathbb{R}^3} \frac{p^z p^z}{E} f(x,p) \mathrm{d}^3 p,$$

where instead of the square of the third component of momentum, there can be the square of any of the three components. However, the third component has a convenient form in the conventional spherical coordinates.

Starting with massless quarks and antiquarks, the energy density reads as

$$\begin{aligned}
\varepsilon_{q\overline{q}} &= \varepsilon_q + \varepsilon_{\overline{q}} = \iiint_{\mathbb{R}^3} E[f_q(x,p) + f_{\overline{q}}(x,p)] \mathrm{d}^3 p = \\
&= \frac{g_q}{(2\pi)^3} \iiint_{\mathbb{R}^3} E \left[\frac{1}{\exp\left(\frac{E-\mu_q}{T}\right) + 1} + \frac{1}{\exp\left(\frac{E+\mu_q}{T}\right) + 1} \right] \mathrm{d}^3 p \overset{m=0}{=} \\
&\overset{m=0}{=} \frac{g_q}{(2\pi)^3} \iiint_{\mathbb{R}^3} ||\vec{p}|| \left[\frac{1}{\exp\left(\frac{||\vec{p}||-\mu_q}{T}\right) + 1} + \frac{1}{\exp\left(\frac{||\vec{p}||+\mu_q}{T}\right) + 1} \right] \mathrm{d}^3 p = \\
&= \frac{g_q}{2\pi^2} \int_0^{+\infty} p^3 \left[\frac{1}{\exp\left(\frac{p-\mu_q}{T}\right) + 1} + \frac{1}{\exp\left(\frac{p+\mu_q}{T}\right) + 1} \right] \mathrm{d}p = g_q \left(\frac{7\pi^2}{360} T^4 + \frac{1}{12} T^2 \mu_q^2 + \frac{1}{24\pi^2} \mu_q^4 \right)
\end{aligned}$$

and pressure

$$\begin{aligned}
P_{q\bar{q}} &= P_q + P_{\bar{q}} = \iiint_{\mathbb{R}^3} \frac{p^z p^z}{E}[f_q(x,p) + f_{\bar{q}}(x,p)]\mathrm{d}^3p = \\
&= \frac{g_q}{(2\pi)^3}\iiint_{\mathbb{R}^3} \frac{p^2\cos^2\vartheta}{E}\left[\frac{1}{\exp\left(\frac{E-\mu_q}{T}\right)+1} + \frac{1}{\exp\left(\frac{E+\mu_q}{T}\right)+1}\right]\mathrm{d}^3p \overset{m=0}{=} \\
&\overset{m=0}{=} \frac{g_q}{(2\pi)^3}\iiint_{\mathbb{R}^3} ||\vec{p}||\cos^2\vartheta\left[\frac{1}{\exp\left(\frac{||\vec{p}||-\mu_q}{T}\right)+1} + \frac{1}{\exp\left(\frac{||\vec{p}||+\mu_q}{T}\right)+1}\right]\mathrm{d}^3p = \\
&= \frac{g_q}{(2\pi)^3}\int_0^{+\infty}\int_0^{\pi}\int_0^{2\pi} p^3\cos^2\vartheta\sin\vartheta\left[\frac{1}{\exp\left(\frac{p-\mu_q}{T}\right)+1} + \frac{1}{\exp\left(\frac{p+\mu_q}{T}\right)+1}\right]\mathrm{d}\varphi\mathrm{d}\vartheta\mathrm{d}p = \\
&= \frac{2}{3}\frac{g_q}{(2\pi)^2}\int_0^{+\infty} p^3\left[\frac{1}{\exp\left(\frac{p-\mu_q}{T}\right)+1} + \frac{1}{\exp\left(\frac{p+\mu_q}{T}\right)+1}\right]\mathrm{d}p = \frac{g_q}{3}\left(\frac{7\pi^2}{360}T^4 + \frac{1}{12}T^2\mu_q^2 + \frac{1}{24\pi^2}\mu_q^4\right).
\end{aligned}$$

Similarly, for gluons, the energy density reads as

$$\varepsilon_g = \iiint_{\mathbb{R}^3} Ef_g(x,p)\mathrm{d}^3p = \frac{g_g}{(2\pi)^3}\iiint_{\mathbb{R}^3} ||\vec{p}||\frac{1}{\exp\left(\frac{||\vec{p}||}{T}\right)-1}\mathrm{d}^3p = g_g\frac{\pi^2}{90}T^4$$

and the pressure

$$P_g = \iiint_{\mathbb{R}^3} \frac{p^z p^z}{E}f_g(x,p)\mathrm{d}^3p = g_g\iiint_{\mathbb{R}^3} ||\vec{p}||\cos^2\vartheta\frac{1}{\exp\left(\frac{||\vec{p}||}{T}\right)-1}\mathrm{d}^3p = g_g\frac{\pi^2}{270}T^4.$$

For both cases there are clear relations between energy density and pressure

$$P_{q\bar{q}} = \frac{1}{3}\varepsilon_{q\bar{q}}, \quad \text{and} \quad P_g = \frac{1}{3}\varepsilon_g.$$

A gas composed of massless quarks, antiquarks, and gluons has energy density $\varepsilon = \varepsilon_{q\bar{q}} + \varepsilon_g$ and isotropic pressure $P = P_{q\bar{q}} + P_g$.

We can finally introduce the EoS of a gas composed of massless quarks, antiquarks, and gluons

$$P = \frac{1}{3}\varepsilon.$$

This is generally true for any massless gas or if one takes the ultrarelativistic limit ($E \approx p$). This EoS is also compatible with black-body radiation. This result also makes the energy–momentum tensor $T^{\mu\nu_0}$ of the perfect fluid in thermodynamic equilibrium traceless

$$T^\mu_\mu = (\varepsilon + P)u^\mu u_\mu + Pg^\mu_\mu = 3P - \varepsilon = 0.$$

3.3.2 Hadron resonance gas and lattice equations of state

Hadron resonance gas prescription for EoS turned out to be very useful for reproducing particle abundances produced in heavy-ion collisions. Hadron gas at very low temperature ($T < 150$ MeV) and zero baryon density can be described by interacting pions, since they dominate matter.

However, the chiral three-loop perturbation calculation produced results similar to those of the ideal gas of pions [205]. Particle densities are suppressed by their mass m_i as

$$n_i \sim \exp\left(-\frac{m_i}{T}\right).$$

Heavier hadrons are less suppressed at higher temperatures, but their interaction is still very suppressed. The interaction between hadron i and hadron j is proportional to

$$n_i n_j \sim \exp\left(-\frac{m_i + m_j}{T}\right).$$

The interaction can then be estimated with virial expansion leading to chiral perturbation theory [205, 206]. Experiments showed [207] that rupulsion and attraction are characterised by negative and positive phase shifts, respectively.

This discovery showed that the interacting hadron gas can be well approximated by including free resonances instead. Partition functions Z_{m_i} for mesons and baryons with conserved charges Q^A (electric charge Q, baryon number B, strangness S, etc.) can be expressed as

$$\ln Z^{\mathrm{M}}_{m_i} = -g_i \frac{V}{2\pi^2} \int_0^\infty dk\, k^2 \ln\left[1 - \exp\left(\frac{\sum_A Q^A_i \mu_A}{T}\right) \exp\left(-\frac{\varepsilon_i}{T}\right)\right],$$
$$\ln Z^{\mathrm{B}}_{m_i} = +g_i \frac{V}{2\pi^2} \int_0^\infty dk\, k^2 \ln\left[1 + \exp\left(\frac{\sum_A Q^A_i \mu_A}{T}\right) \exp\left(-\frac{\varepsilon_i}{T}\right)\right],$$

where g_i is the degeneracy factor and μ_A are chemical potentials connected to conserved charges Q^A. Then it is possible to obtain the pressure of hadron resonance gas

$$\frac{P^{\mathrm{HRG}}}{T^4} = \frac{1}{VT^3} \sum_{i\in\{\mathrm{M}\}} \ln Z^{\mathrm{M}}_{m_i}(T, V, \mu_A) + \frac{1}{VT^3} \sum_{j\in\{\mathrm{B}\}} \ln Z^{\mathrm{B}}_{m_j}(T, V, \mu_A),$$

where {M} and {B} are mesons and baryons included in the calculation of EoS.

Lattice QCD can estimate EoS for higher temperatures, but its sensitivity to high-momentum modes causes problematic effects of finite lattice spacing for higher temperatures [208]. This was improved by the introduction of staggered fermions with higher-order discretisation of the lattice operators [209, 210]. This improves the situation for higher temperatures, but also violates the flavour symmetry of continuum QCD. This distorts the hadronic spectrum and introduces unwanted low-temperature effects.

When lattice calculations are performed with a fixed temporal extent N_τ (that is, $N_\tau = 4, 6, 8, \ldots$), the temperature changes by varying the lattice spacing a as

$$T = \frac{1}{N_\tau a}.$$

The decreasing temperature T increases the lattice spacing a and thus introduces greater cutoff effects $(\mathcal{O}(\alpha_s a^2))$ at low temperatures. This causes a distorted hadronic spectra that began to correspond to experimental measurement after proper continuum extrapolation. On the other hand, EoS can be calculated very accurately at high temperatures T.

The flavours of the quarks are not degenerate with finite lattice spacing $a > 0$. This implies a violation of the flavour symmetry $\mathrm{SU}_f(N_f)$ and there are flavour-changing effects $(\mathcal{O}(\alpha_s a^2))$. This causes unequal masses for the mesons and baryons.

For example, for four flavours $N_f = 4$, there are eight multiplets of pseudoscalar mesons characterised by different masses m_{ps}^i, where $i = 0, 1, ..., 7$. Furthermore, if the quark masses are zero $m_q \to 0$, only the multiplet 0 becomes massless because it is a Goldstone pseudoscalar meson. The pressure is then calculated as

$$\frac{P^{\pi,\mathrm{K}}}{T^4} = \frac{1}{16}\frac{1}{VT^3}\sum_{i=0}^{7} g_{\mathrm{ps}}^i \ln Z^{\mathrm{M}}\left(m_{\mathrm{ps}}^i\right),$$

where g_{ps}^i is the degeneracy of multiplet i and $g_{\mathrm{ps}}^0 = 1$. The mass m_{ps}^i of the multiplet $i \geq 1$ is given as

$$\left(m_{\mathrm{ps}}^i\right)^2 = \left(m_{\mathrm{ps}}^0\right)^2 + \left(\delta m_{\mathrm{ps}}^i\right)^2,$$

where m_{ps}^0 is proportional to the mass of quarks and quadratic splittings $\left(\delta m_{\mathrm{ps}}^i\right)^2$ are proportional to $\alpha_s a^2$ and are calculated via the asqtad action [208, 211, 212]. A similar calculation is performed for the vector mesons and baryons.

When P/T^4 is obtained, it is a straightforward path to obtain EoS. First, trace anomaly $\Theta(T) = \varepsilon(T) - 3P(T)$ can be connected to pressure difference

$$\frac{P(T)}{T^4} - \frac{P(T_{\mathrm{low}})}{T_{\mathrm{low}}^4} = \int_{T_{\mathrm{low}}}^{T} \frac{\mathrm{d}T'}{T'^5}\Theta(T'),$$

where $P(T_{\mathrm{low}})$ contribution can be neglected for sufficiently small T_{low}. Then the energy density ε and the entropy density s are obtained as

$$\varepsilon(T) = \Theta(T) + 3P(T), \qquad s(T) = \frac{\varepsilon(T) + P(T)}{T}.$$

Thermodynamic quantities calculated from lattice QCD are affected by low temperature T errors due to finite discretisation. Meanwhile, hadron resonance gas is the low-temperature model. It is possible to use lattice results for $T > 250$ MeV and hadron resonance gas results for $T <$ 180 MeV. Since the intermediate temperature region 180 MeV$< T <$ 250 MeV is affected by discretisation errors for the lattice QCD and the unreliability for the hadron resonance gas it is inadequate to use either.

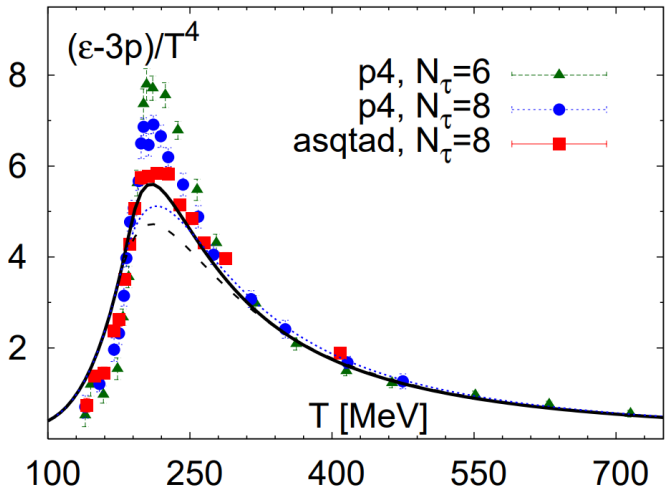

Figure 3.11: The trace anomaly $\Theta = \varepsilon - 3P$ to T^4 ratio for lattice QCD calculated via p4 and asqtad actions (symbols), $s95p$-v1 parametrisation (solid line). [208]

The parameterisation of the trace anomaly is fixed by lattice QCD for high temperature and hadron resonance gas for low temperature. Furthermore, the entropy density in the high temperature region $(4T_c)$ is fixed by perturbative pure gauge theory [213, 214, 215, 216] and QCD [217] to be ~ 5% less than the ideal gas limit. The intermediate temperature region is then interpolated.

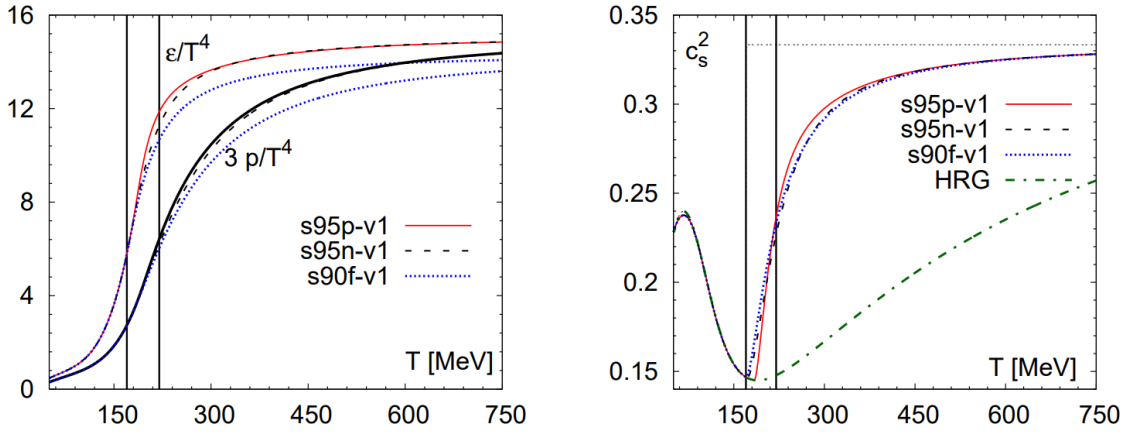

Figure 3.12: The pressure, energy density (left panel) and speed of sound (right panel) for various EoS parametrisations. Solid curve represents $s95p$-v1 .The vertical lines indicate the intermediate temperature region.

The equation of state that was introduced above is called $s95p$-v1 [208], where $s95$ represents 95% of the entropy density at high temperature compared to the ideal gas and p represents the treatment of interpolation. This equation of state is implemented in `MUSIC` [3, 200].

3.4 Transport coefficients

To consistently describe the various experimentally measured hadronic observables (transverse momentum spectra, elliptic and triangular flow coefficients, etc.) using a phenomenological approach via relativistic hydrodynamics, one needs to introduce viscosity. There are two first-order transport coefficients, shear viscosity η and the bulk viscosity ζ. For how they act in hydrodynamic equations, see Section 3.2.2. They are both important and both of them affect hadronic observables. That is why both viscosities must be thoroughly investigated.

3.4.1 Shear viscosity

Shear viscosity to the entropy density $\frac{\eta}{s}$ is a temperature-dependent quantity. Its temperature dependence cannot be calculated for a realistic medium from first-principle physics. However, the combination of conformal field theory and M-theory can put a physical limit on the shear viscosity to the entropy density ratio $\frac{\eta}{s}$. It is important to note that string theory does not have any experimental evidence that it is a true description of the underlying physics. However, its thorough development made it a decent model that can describe some phenomena. The anti-de Sitter/conformal field theory (AdS/CFT) limit

$$\frac{\eta}{s} \geq \frac{1}{4\pi}$$

is the only theoretical limit obtained at the QCD temperature. The actual value of $\frac{\eta}{s}$ of QGP is also expected to be very close to the AdS/CFT limit [188]. This assumption is based on hydrodynamic, lattice, and kinetic simulations. In contrast to the bulk viscosity, the shear viscosity to the entropy density $\frac{\eta}{s}$ can be taken as a constant function of temperature. Usually AdS/CFT limit $\frac{\eta}{s} \approx 0.08$ is multiplied by some numerical factor $c_\eta = 1, 1.5, 2$, etc.

The effects of constant shear viscosity on hadronic observables have been explored for many years. The most reliable observables sensitive to viscosity turned out to be the transverse momentum spectra

$$\frac{1}{2\pi p_\mathrm{T}} \frac{\mathrm{d}^3 N}{\mathrm{d}y \mathrm{d}p_\mathrm{T}},$$

and the harmonic coefficients v_n obtained from the Fourier expansion of the azimuthal distribution of hadrons

$$\frac{\mathrm{d}N}{\mathrm{d}\phi} = \frac{N}{2\pi}\left[1 + 2v_1 \cos(\phi) + 2v_2 \cos(2\phi) + \dots\right].$$

Those are then compared with the experimental measurements.

In the upper left panel of Figure 3.13, one can see the transverse momentum spectra of pions and protons at $\sqrt{s_\mathrm{NN}} = 200$ GeV for Au+Au collisions at $0-5\%$ centrality, measured by PHENIX [218] and `VISH2+1` simulations for several values of shear viscosity [219]. Furthermore, the spectra simulated by `VISH2+1` are shown with and without viscous correction for the distribution function δf to see how the constant shear viscosity affects only the hydrodynamic simulation (without δf) and the full hadronic spectra (with δf).

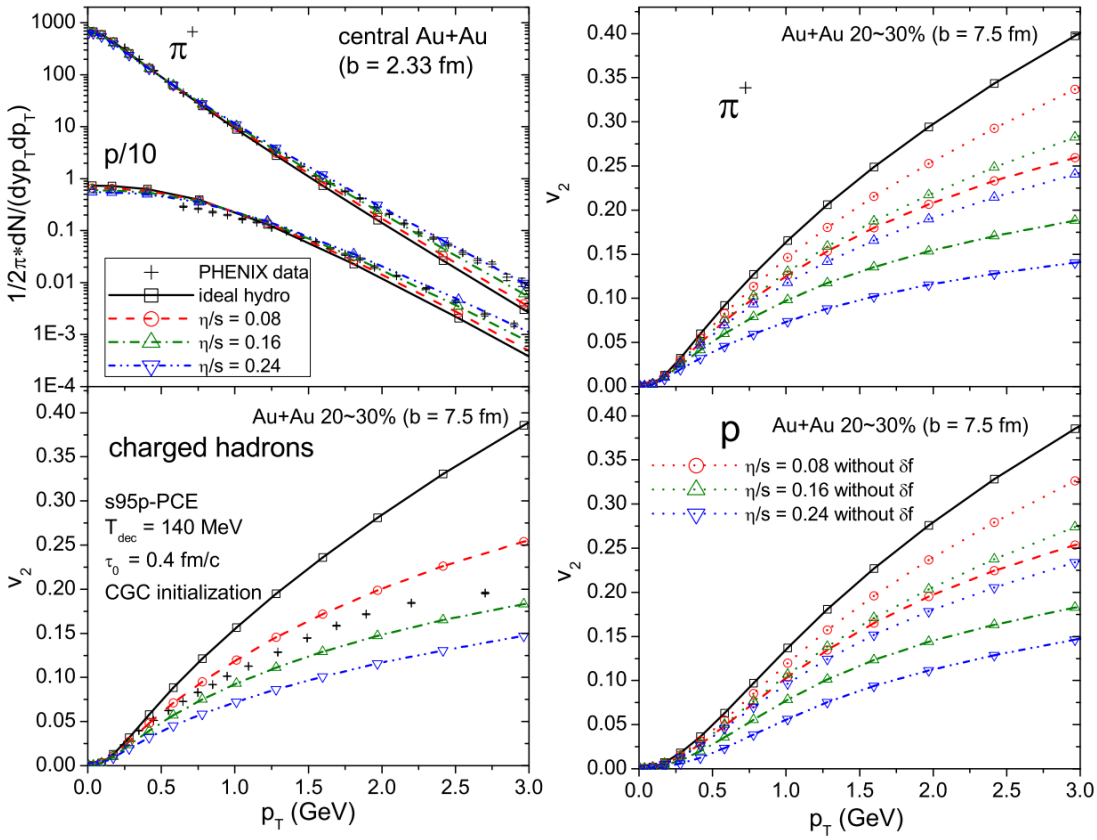

Figure 3.13: Proton and pion spectra for Au+Au collision at $\sqrt{s_{\mathrm{NN}}}$ = 200 GeV at $0-5\%$ centrality (top left panel). Differential elliptic flow v_2 of charged hadrons (bottom left panel), pions (top right panel), and protons (bottom right panel) for Au+Au collision at $\sqrt{s_{\mathrm{NN}}}$ = 200 GeV at $20-30\%$ centrality. Results from `VISH2+1` with equilibrium proper time $\tau_0 = 0.4$ fm/c, initial CGC energy density profile, decomposition temperature $T_{\mathrm{dec}} = 140$ MeV and $s95p$-PCE EoS are represented by lines [219]. The multiplication factor c_η is taken to be either 0, 1, 2 or 3. Furthermore, results are displayed with and without viscous distribution function correction δf. This is compared to PHENIX data [218] represented by crosses. Retrieved from [219].

One can see that the higher values of $\frac{\eta}{s}$ result in flatter spectra. This effect is particularly strong for protons at low p_{T}. This is caused by the positive contribution of $\pi^{\mu\nu}$ to transverse flow and effective transverse pressure gradients [219]. Other simulations [220, 221] showed that the sign of δf is fragile and sensitive to EoS, initial state model, and $\frac{\eta}{s}$ value. The results for near-central collisions $b \approx 0$ show the highest positive values δf at large p_{T}. This can even lead to a positive contribution to differential elliptic flow v_2. For a larger impact parameter b, the contributions of δf to differential elliptic flow v_2 remain negative. This can be seen on the right-hand side of Figure 3.13.

The constant $\frac{\eta}{s}$ could be a good approximation. However, it was already mentioned that the shear viscosity-entropy density ratio $\frac{\eta}{s}$ is temperature dependent [188, 222]. Furthermore, parameterisations incorporating the baryon chemical potential μ_B were introduced [223]. For

example, parameterisation

$$\frac{\eta T}{\varepsilon + P}(T) = \left(\frac{\eta T}{\varepsilon + P}\right)_{\min} + a(T_c - T)\theta(T_c - T) + b(T - T_c)\theta(T - T_c), \tag{3.28}$$

where $\theta(x)$ is the Heaviside step function. The quantity on the left-hand side is equal to $\frac{\eta}{s}(T)$ for $\mu_B = 0$. Some favourable parameterisations at $\mu_B = 0$ can be seen in Figure 3.14.

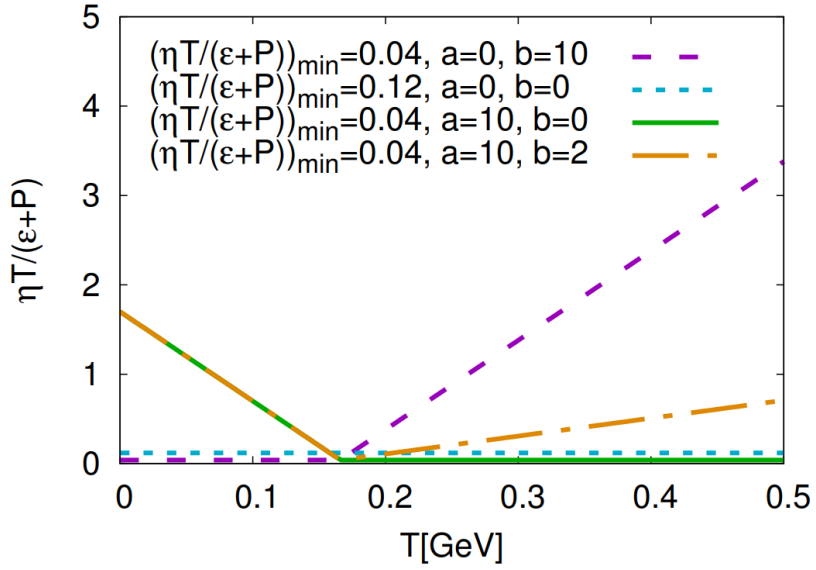

Figure 3.14: The four examples of temperature-dependent $\frac{\eta T}{\varepsilon + P}$ at $\mu_B = 0$. Retrieved from [223].

In case of LHC energies simulated in this work, the dependence on baryon chemical potential is not important since the baryon chemical potential is practically zero $\mu_B = 0$. An extensive Bayesian analysis of a parameterisation at $\mu_B = 0$ was provided [224]. Temperature dependent parameterisation reads as

$$\frac{\eta}{s}(T) = \left(\frac{\eta}{s}\right)_{\min} + S_{\mathrm{HG}}(T_{\mathrm{H}} - T)\theta(T_{\mathrm{H}} - T) + S_{\mathrm{QGP}}(T - T_{\mathrm{Q}})\theta(T - T_{\mathrm{Q}}).$$

Compared to the parameterisation of equation (3.28), this parameterisation has a plateau for $T_{\mathrm{H}} < T < T_{\mathrm{Q}}$ and is independent of μ_B. For the eight free parameters, the posterior probability distribution of the values of the best-fit parameters was introduced using the Bayes theorem. Four different parameterisations of the EoS ($s83s_{18}$, $s87h_{04}$, $s88h_{18}$, and $s95p$) were compared. This was fitted to five centrality classes of charged particle multiplicity in mid-rapidity and four-particle cumulant p_{T} averaged elliptic flow $v_2\{4\}$ of Au+Au collisions at $\sqrt{s_{\mathrm{NN}}} = 200$ GeV [225, 226], Pb+Pb collisions at $\sqrt{s_{\mathrm{NN}}} = 2.76$ TeV [227, 228] and $\sqrt{s_{\mathrm{NN}}} = 5.02$ TeV [228, 229], to five centrality classes of multiplicities in midrapidity, and the average transverse momentum spectra of pions, kaons, and protons in Au+Au collisions at RHIC [230] and Pb+Pb collisions at the lower LHC energy [231]. The estimated parameterizations for different EoS can be seen in Figure 3.15.

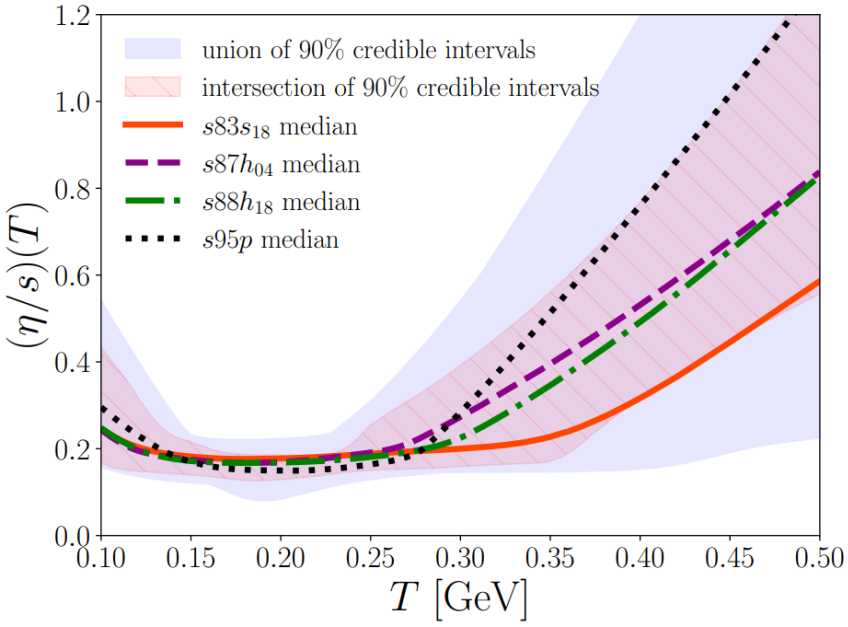

Figure 3.15: Temperature-dependent $\frac{\eta}{s}(T)$ for four different EoS parametrizations with the union and intersection of the 90% credible intervals of the distributions by using Bayesian statistical analysis. Retrieved from [224].

One can see that even though the width of the plateau is a free parameter, the statistical analysis showed that there is a plateau compared to a parameterisation in equation (3.28) and the plateau is in the temperature region most relevant for HIC simulations. This, to some extent, supports the constant parameterisation of $\frac{\eta}{s}$ which is still widely used. This work uses the temperature dependent parameterisation

$$\frac{\eta}{s}(T) = 0.21 + 0.38(T_k - T)\theta(T_k - T) + 0.38(T - T_k)\theta(T - T_k),$$

where $T_k = 110$ MeV.

3.4.2 Bulk viscosity

For the EoS of a massless ultrarelativistic gas (see Section 3.3.1) with weakly coupled QGP, the bulk viscosity to entropy density ratio $\frac{\zeta}{s}$ vanishes at the classical level due to conformal symmetry. However, the conformal symmetry is broken in QCD and this results in finite bulk viscosity. QGP becomes more conformal at very high temperature. This is shown by both perturbative and lattice QCD calculations of the trace anomaly [232]. This means that $\frac{\zeta}{s}$ goes to zero for high temperatures. For QCD with three massless quark flavours, it is possible to derive the relation between bulk and shear viscosity [192, 233, 234] as

$$\frac{\zeta}{s} \sim \frac{\eta}{s}\left(c_s^2 - \frac{1}{3}\right)^2. \tag{3.29}$$

However, this relation does not hold exactly [235]. This was a starting point for the early temperature-dependent $\frac{\zeta}{s}(T)$ parametrizations.

For low temperatures, deep in the hadronic phase ($T \ll 150$ MeV), it was shown that the bulk viscosity should be exponentially high

$$\zeta \sim \frac{f_\pi^8}{m_\pi^5} \mathrm{e}^{\frac{2m_\pi}{T}},$$

where m_π is the mass of the pion and f_π is a decay constant [236]. However, this was derived for the equilibrium system, where the bulk viscosity is dominated by the rate of number-changing processes. These processes are very slow, and the bulk viscosity depends on the time scale. In a HIC system that is slightly out-of-equilibrium, the timescale is much shorter, and the changing processes are not sufficiently fast to contribute to the bulk viscosity so much. This means that the low temperature $\frac{\zeta}{s}(T)$ is actually extremely small [237].

Recently, three parameterisations of the temperature-dependent bulk viscosity to entropy density ratio $\frac{\zeta}{s}(T)$ were introduced. The first parameterisation [238] reads as

$$\zeta/s = \begin{cases} c_1 + 0.08 \exp\left[\frac{T/T_p - 1}{0.0025}\right] + \\ \quad +0.22 \exp\left[\frac{T/T_p - 1}{0.022}\right] & T < T_p \\ c_2 + 27.55\left(T/T_p\right) - \\ \quad -13.77\left(T/T_p\right)^2 & T_p < T < T_P \\ c_3 + 0.9 \exp\left[\frac{-\left(T/T_p - 1\right)}{0.0025}\right] + \\ \quad +0.25 \exp\left[\frac{-\left(T/T_p - 1\right)}{0.13}\right] & T > T_P, \end{cases} \tag{3.30}$$

where $T_p = 180$ MeV, $T_P = 200$ MeV, $c_1 = 0.03$, $c_2 = -13.45$ and $c_3 = 0.001$. This parameterisation is actually more than 420 times higher at peak compared to the parameterisation in equation (3.29) in its explicit form with $\frac{\eta}{s} = 0.12$. The second parameterisation of the temperature-dependent bulk viscosity to entropy density ratio was introduced [239] as

$$\zeta/s = \begin{cases} B_{\mathrm{norm}} \exp\left[-\left(\frac{T - T_{\mathrm{peak}}}{T_{\mathrm{width}}}\right)^2\right] & T < T_{\mathrm{peak}} \\ B_{\mathrm{norm}} \frac{B_{\mathrm{width}}^2}{(T/T_{\mathrm{peak}} - 1)^2 + B_{\mathrm{width}}^2} & T > T_{\mathrm{peak}}, \end{cases} \tag{3.31}$$

where $T_{\mathrm{peak}} = 165$ MeV, $B_{\mathrm{norm}} = 0.24$ and $B_{\mathrm{width}} = 1.5$. The last parameterisation that was introduced most recently [240] takes the form of

$$\zeta/s = \begin{cases} B_n \exp\left[-\left(\frac{T - T_\mu}{B_1}\right)^2\right] & T < T_\mu \\ B_n \exp\left[-\left(\frac{T - T_\mu}{B_2}\right)^2\right] & T > T_\mu, \end{cases} \tag{3.32}$$

where $B_{\mathrm{peak}} = 0.13$, $B_1 = 10$ MeV, $B_2 = 120$ MeV and $T_\mu = 160$ MeV. The three mentioned parameterisations can be seen in Figure 3.16.

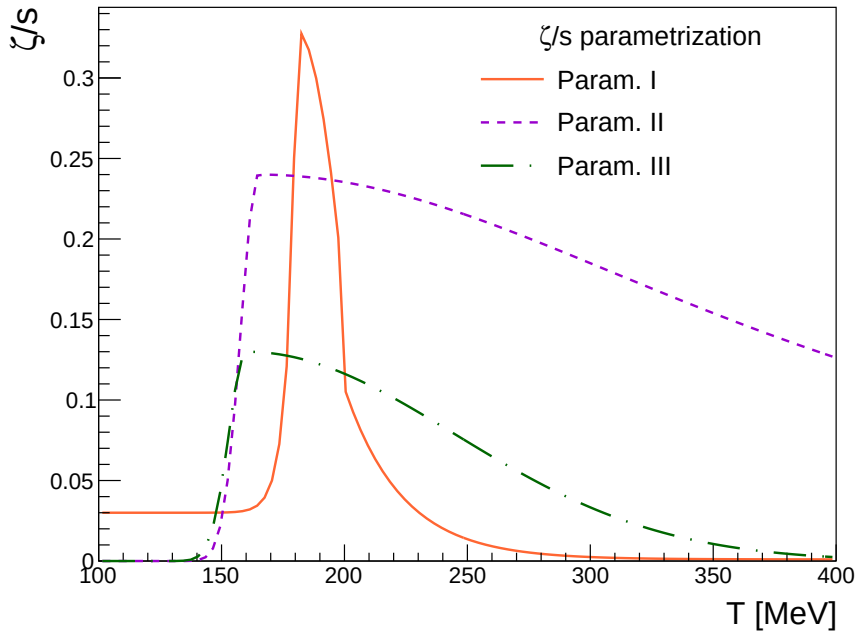

Figure 3.16: Temperature-dependent parametrizations of $\frac{\zeta}{s}(T)$. [238, 239, 240]

Large values of $\frac{\zeta}{s}$ cause a large negative bulk pressure Π. Since the bulk pressure Π is negative, the total pressure $\tilde{P} = P + \Pi$ decreases with larger bulk viscosity. Previously used parameterisations introduced small bulk viscous corrections that had a small if not negligible influence on the evolution of the dense QGP medium. Recent bulk viscosity parameterisations [238, 239, 240] create large bulk viscosity corrections in the form of negative bulk pressure. [241] This suppresses the transverse expansion and effectively decreases the average transverse momentum $\langle p_{\mathrm{T}} \rangle$. In addition, bulk viscosity is associated with greater entropy production and thus higher charged multiplicity N_{ch}. To support the impact of bulk viscosity, it was shown [242] that the average transverse momentum $\langle p_{\mathrm{T}} \rangle$ of the identified hadrons is too large with viscous hydrodynamics that includes only shear viscosity.

This led to recent improvements in relativistic hydrodynamic simulations and the inclusion of modern bulk viscosity parameterisations. The exploration of the temperature dependence of bulk viscosity is in active phase now. The bulk viscosity to the entropy density is also investigated with the use of Bayesian analysis.

This thesis uses default `JETSCAPE` parameterisation

$$\frac{\zeta}{s}(T) = \frac{\left(\frac{\zeta}{s}\right)_{\max} \Lambda^2}{\Lambda^2 + \left(T - T_{\zeta,c}\right)^2}, \quad \text{where} \quad \Lambda = w_\zeta \left[1 + \lambda \, \mathrm{sign}\left(T - T_{\zeta,c}\right)\right],$$

where maximum parameterisation $\left(\frac{\zeta}{s}\right)_{\max} = 0.1$, width of the peak $w_\zeta = 0.05$ GeV, temperature of the peak $T_{\zeta,c} = 0.18$ GeV, and skewness $\lambda = 0$. Those are the default parameter values of the `MUSIC` code.

3.4.3 Second-order transport coefficients

Equations (3.26) and (3.27) are frame-independent. In other words, Israel-Steward second-order equations in this form are the same in both Landau and Eckart frames. However, the coefficients are not only frame dependent, but they are also dependent on temperature T and baryon chemical potential μ_B. In the case of HIC at higher energies ($\sqrt{s_{\mathrm{NN}}} \gtrsim 100$ GeV), it is more significant to explore the temperature dependence of these coefficients than the dependence on the chemical potential, since the baryon chemical potential is small $\mu_B \sim 0$ for this type of collisions. The properties of the transport coefficients are extracted from microscopic theory. This means that one can obtain those coefficients from the relativistic Boltzmann equation, similarly to one can derive second-order Israel-Steward equations. The coefficients $\delta_{\pi\pi}$, $\tau_{\pi\pi}$, and ϕ_7 can be calculated from the massless limit [243, 244], since they do not vanish. In the massless limit, $\delta_{\pi\pi}$, $\tau_{\pi\pi}$, and ϕ_7 can be written in terms of the relaxation time of the shear viscosity τ_π and the equilibrium pressure P [245]

$$\delta_{\pi\pi} = \frac{4}{3}\tau_\pi, \qquad \tau_{\pi\pi} = \frac{10}{7}\tau_\pi, \qquad \phi_7 = \frac{9}{70P}.$$

Since other coefficients vanish in the massless limit, one has to investigate the limit for the small mass to temperature ratio $z \equiv \frac{m}{T}$. In this limit, it is possible to express the transport coefficients related to both the bulk pressure Π and the shear stress tensor $\pi^{\mu\nu}$. [245] The transport coefficients related to the bulk pressure Π are [245]

$$\begin{aligned}
\frac{\zeta}{\tau_\Pi} &= 14.55 \times \left(\frac{1}{3} - c_s^2\right)^2 (\varepsilon + P) + \mathcal{O}(z^5), \\
\frac{\delta_{\Pi\Pi}}{\tau_\Pi} &= \frac{2}{3} + \mathcal{O}(z^2 \ln z), \\
\frac{\lambda_{\Pi\pi}}{\tau_\Pi} &= \frac{8}{5}\left(\frac{1}{3} - c_s^2\right) + \mathcal{O}(z^4).
\end{aligned}$$

Then the transport coefficients related to the shear stress tensor $\pi^{\mu\nu}$ for the small mass to temperature ratio z are as follows [245]

$$\begin{aligned}
\frac{\eta}{\tau_\pi} &= \frac{\varepsilon + P}{5} + \mathcal{O}(z^2), \\
\frac{\delta_{\pi\pi}}{\tau_\pi} &= \frac{4}{3} + \mathcal{O}(z^2), \\
\frac{\tau_{\pi\pi}}{\tau_\pi} &= \frac{10}{7} + \mathcal{O}(z^2), \\
\frac{\lambda_{\pi\Pi}}{\tau_\pi} &= \frac{6}{5} + \mathcal{O}(z^2 \ln z).
\end{aligned}$$

To summarize it, the transport coefficients are

$$\frac{\delta_{\Pi\Pi}}{\tau_\Pi} = \frac{2}{3}, \quad \frac{\lambda_{\Pi\pi}}{\tau_\Pi} = \frac{8}{5}\left(\frac{1}{3} - c_s^2\right), \quad \frac{\delta_{\pi\pi}}{\tau_\pi} = \frac{4}{3}, \quad \phi_7 = \frac{9}{70P}, \quad \frac{\tau_{\pi\pi}}{\tau_\pi} = \frac{10}{7}, \quad \frac{\lambda_{\pi\Pi}}{\tau_\pi} = \frac{6}{5}$$

and the relaxation times are

$$\tau_\pi = \frac{5\eta}{sT}, \quad \tau_\Pi = \frac{\zeta}{15(\frac{1}{3} - c_s^2)^2 sT}.$$

3.5 Conversion to Particle Spectra

To obtain hadronic observables from relativistic hydrodynamics, each fluid cell must be converted into discrete particles. This process is known as particlisation. The combination of hydrodynamics and microscopic simulations is called a hybrid model. Both stages describe different stages of the collision and the outcome is a set of individual particles with four-momenta that can be analysed in a way similar to experimentally measured events.

3.5.1 Cooper-Frye formula

The key element of the particlisation procedure is the Cooper-Frye formula [246]

$$\frac{\mathrm{d}N^i}{p_\mathrm{T}\mathrm{d}y\mathrm{d}p_\mathrm{T}\mathrm{d}\phi_p} = \frac{g}{(2\pi)^3}\int_\Sigma \mathrm{d}^3\sigma_\mu p^\mu \left(f_0^i(x,p) + \delta f^i(x,p)\right), \tag{3.33}$$

where g is the spin degeneracy. This formula connects three key aspects. First, particle i momentum distribution on the left-hand side of the Cooper-Frye formula (3.33). The second is the isothermal freezout hypersurface Σ with the volume element

$$\mathrm{d}^3\sigma_\mu = \varepsilon_{\mu\nu\rho\sigma}\frac{\mathrm{d}\Sigma^\mu}{\mathrm{d}r_x}\frac{\mathrm{d}\Sigma^\rho}{\mathrm{d}r_y}\frac{\mathrm{d}\Sigma^\sigma}{\mathrm{d}\eta_s}\cdot \mathrm{d}r_x\mathrm{d}r_y\mathrm{d}\eta_s.$$

Finally, local thermal equilibrium distribution function $f_0^i(x,p)$ with out-of-equilibrium corrections $\delta f^i(x,p)$ [247, 248].

Kinetic theory can be connected with a four-current J^μ flowing through a hypersurface Σ as

$$J^\mu(x) = \int \frac{\mathrm{d}^3p}{E}p^\mu f(x,p).$$

Then multiplicity N is the integrated current J^μ over the hypersurface

$$N = \int_\Sigma \mathrm{d}^3\sigma_\mu J^\mu(x) = \int \frac{\mathrm{d}^3p}{E}\int_\Sigma \mathrm{d}^3\sigma_\mu p^\mu f(x,p).$$

This leads to the Cooper-Frye formula (3.33) since

$$E\frac{\mathrm{d}N}{\mathrm{d}^3p} = \frac{\mathrm{d}N}{p_\mathrm{T}\mathrm{d}y\mathrm{d}p_\mathrm{T}\mathrm{d}\phi_p}.$$

The last thing that needs clarification is the out-of-equilibrium distribution function f. It is possible to use the linear transformation matrix [249] for the four-momentum

$$p_i \to p_i' = p_i + \sum_j \lambda_{ij}p_j,$$

instead of linear corrections δf. Furthermore, the out-of-equilibrium corrections δf are not unequivocally defined. One of the possibilities to incorporate out-of-equilibrium corrections is to use the relaxation time approximation (RTA) [249, 250, 251]. Linear corrections with RTA are

$$\delta f = f_0 \left(1 \pm f_0\right) \frac{\tau}{ET} \left[\frac{1}{2\eta} p^i p^j \pi_{ij} + \frac{1}{\zeta} \left(\frac{p^2}{3} - c_s^2 E^2 \right) \Pi \right].$$

The explicit forms of the equilibrium distribution functions f_0 for both bosons and fermions were derived in Section 2.1.1.

A numerical implementation: iSS

Monte Carlo sampler `iSS` [4, 252] stands for "iSpectraSampler". `iSS` used to obtain particles on the isothermal freeze-out hypersurface Σ_μ using the calculated particle momentum distributions as the relative emission probability.

The first step is the average total number of particles of species i per unit of rapidity. This is obtained from equation (3.33). Equation (3.33) is integrated over all freeze-out cells, transverse momenta of the particles, and the azimuthal angle. An inverse cumulative distribution function is calculated and the random variables are divided into two sets $(\tau, \vec{x}_\mathrm{T}, \eta_s)$ and $\left(p_\mathrm{T}, \phi_p, y\right)$. Spatial information is first sampled with the inverse cumulative distribution function method, and then the distribution can be evaluated at any spatial point for the probability in momentum space of the particle species i. Then the direct probability distribution function method is used to sample in momentum space.

3.5.2 Hadronic afterburner

The hadronic afterburner is a microscopic treatment of particles obtained from particlisation. At this stage, hadrons are not in equilibrium and have a long mean free path. However, they still interact with each other. Furthermore, resonances can decay. This changes hadronic observables, and it must be included in the simulation. Relativistic hadronic transport `SMASH` was used in this thesis.

SMASH

Simulating Many Accelerated Strongly-interacting Hadrons (`SMASH`) [5, 253] is a relativistic hadronic transport model. `SMASH` includes all well-established hadrons up to a mass of ~ 2 GeV as degrees of freedom, and as all transport approaches it is based on the Boltzmann equation

$$\frac{\partial f}{\partial t} + \frac{\vec{p}}{m} \cdot \nabla_{\vec{x}} f + \vec{F} \cdot \frac{\partial f}{\partial \vec{p}} = \left(\frac{\partial f}{\partial t} \right)_{\mathrm{coll}}, \tag{3.34}$$

where $f_i(x,p)$ are the particle density distribution functions for each particle species i. f can be interpreted as the number of particles per phase space cell

$$\mathrm{d}N_i = f(x,p) \mathrm{d}^3\vec{x} \mathrm{d}^3\vec{p}.$$

The term $\frac{\vec{p}}{m} \cdot \nabla_{\vec{x}} f$ describes the free streaming, and $\vec{F} \cdot \frac{\partial f}{\partial \vec{p}}$ is the external force term. The free-streaming term is responsible for the free propagation of particles, where particles are propagated according to their momenta along straight lines. The treatment of potentials can be different across the models. `SMASH` is using the Boltzmann-Ühling-Uhlenbeck (BUU) approach,

where f is represented by test particles. This means increasing the number of particles by some factor $\mathscr{T}$ and further conserving the dynamics by decreasing the cross section by the same factor $\mathscr{T}$. Along with it there is the density-dependent mean field potential $U(\rho)$ that changes dynamics as

$$\frac{d\vec{p}}{dt} = -\nabla_{\vec{x}} U.$$

Finally, Boltzmann equations are solved at the limit of $\mathscr{T} \to +\infty$. Another (not used by SMASH) treatment of potentials in the system is the quantum molecular dynamics (QMD) approach, which is also widely used. This assumes that the particles are Gaussian wave packets and that the potentials are the sum of pairwise potentials. Then QMD solves the many-body Hamiltonian.

The right side of the Boltzmann equation (3.34) is the collision integral that is not trivial. It can be connected with a change in the number of particles in the phase-space cell.

$$\frac{\mathrm{d}}{\mathrm{d}t} N(\vec{x}, \vec{p}, t) = \mathrm{d}N_{\mathrm{coll}}\left(p', \cdots \to p, \ldots\right) - \mathrm{d}N_{\mathrm{coll}}\left(p, \cdots \to p', \ldots\right),$$

where the first term on the right-hand side is the gain of the particles and the second term on the right-hand side is the loss of the particles. With 2-to-2 scatterings, one gets the collision integral

$$\left(\frac{\partial f}{\partial t}\right)_{\mathrm{coll}} = \int \frac{\mathrm{d}^3\vec{p}_2}{(2\pi)^3}\left(f_1' f_2' - f_1 f_2\right) v_{rel} \int d\sigma.$$

The cross section at the end is obtained from QFT

$$\sigma_{12\to 1'2'} = \frac{1}{2E_1}\frac{1}{2E_2}\frac{1}{v_{rel}}\frac{1}{S_{1'2'}} \int \frac{\mathrm{d}^3\vec{p}_1'}{(2\pi)^3 2E_1'}\frac{\mathrm{d}^3\vec{p}_2'}{(2\pi)^3 2E_2'} \left|\mathscr{M}_{12\to 1'2'}\right|^2 (2\pi)^4 \delta^{(4)}\left(P_1 + P_2 - P_1' - P_2'\right),$$

where $\mathscr{M}_{12\to 1'2'}$ is the appropriate matrix element.

This approach is built on the assumption that the space and time span of the collisions are small compared to the mean free path. In contrast to hydrodynamics, the system does not have to be in local thermal equilibrium.

For the realistic system of ~ 100 different particle species, the relativistic hadronic transport approach results in a coupled system of ~ 100 integro-differential equations

$$\begin{aligned}
\frac{\mathrm{d}}{\mathrm{d}t} f_\pi &= I_{\mathrm{coll}}\left(f_\pi, f_N, f_\Delta, \ldots\right) \\
\frac{\mathrm{d}}{\mathrm{d}t} f_N &= I_{\mathrm{coll}}\left(f_\pi, f_N, f_\Delta, \ldots\right) \\
\frac{\mathrm{d}}{\mathrm{d}t} f_\Delta &= I_{\mathrm{coll}}\left(f_\pi, f_N, f_\Delta, \ldots\right) \\
&\ldots
\end{aligned} \tag{3.35}$$

This is impossible to solve analytically, and one needs to resort to the numerical Monte Carlo approach with an effective description of the different equation terms.

Collision of two particles occurs when the mentioned particles are close. The definition of

closeness is ambiguous in the relativistic case. This allows for a multiparticle reaction. Another approach is the geometric collision criterion. This is a commonly used approach in hadronic transport models, including SMASH. It is based on the particle distance criterion when collisions occur

$$d \leq \sqrt{\frac{\sigma}{\pi}}.$$

However, this introduces the time of the closest approach, and the time classification depends on the reference frame. This causes problems with Lorentz invariance. However, this can be improved by using the Kodama criterion. Alternatively, in a regime of high particle density, one can use a stochastic collision criterion. It is the Lorentz-invariant collision probability for particles in the same phase-space cell.

In addition to particle propagation and intraction with other particles, there is another important element of transport models, namely resonance decays. For all particles there is a relativistic Breit-Wigner spectral function

$$\mathcal{A}(E) = \frac{k}{\left(E^2 - M^2\right)^2 + M^2\Gamma^2},$$

where k is the proportionality constant. It is the probability of producing the resonance at a given energy E with resonance width Γ (inverse mean lifetime). Particles with a small resonance width ($\Gamma < 10$ keV) are considered stable.

To summarise all possible interactions, there are $2 \to 2$ ellastic and inellastic scatterings, $2 \to 1$ processes, and decays. Furthermore, for high centre-of-mass energy ($\sqrt{\hat{s}} \sim 3$ GeV) scatterings, Lund string fragmentation is used, which is implemented in Pythia [6, 254]. For more information on Lund string fragmentation, see Section 4.5.1.

SMASH can be used for lower-energy collision simulations, higher-energy hybrid simulations with relativistic hydrodynamics or for some infinite systems of hadrons. In this thesis it is used only to simulate rescatterings of hadrons and resonance decays that are obtained from iSS particlisation.

3.6 Summary of the medium modelling

Heavy-ion collisions at high collision energies are rapid explosive processes with changing physics regimes and degrees of freedom. Therefore, they are simulated with multistep approaches. For the initial state of HIC, the research community is currently using several models. There are also several numerical implementations of hydrodynamic equations in the form of simulation codes. It is possible to use Landau or Eckart frames for the flow velocity definition. Furthermore, there are Öttinger-Grmela formalism and the Israel-Stewart formalism as second-order hydrodynamics. Hydrodynamics includes parameterisations of the EoS and transport coefficients. Finally, there are multiple particlisation approaches.

Medium modelling may look like an equivocal field. However, different approaches do not usually contradict each other and are compared quantitatively. Particle spectra are more sensitive to some parts of the simulations than others. For example, the initial state is harder to access from the data. However, with the utilisation of Bayesian analysis and other statistical methods,

it is possible to constrain the parameter space. Bayesian analysis is also very valuable for the study of the temperature dependence of transport coefficients.

The simulation of the medium has to be very accurate to correctly describe the jet energy loss inside the medium. The omission of shear viscosity causes a different temperature profile. The exclusion of bulk viscosity causes different sizes of the medium. The preequilibrium evolution is connected with the evolution of the jet before the formation of the medium. These steps are important for simulation of jet evolution.

All simulations presented in Chapter 5 use TRENTo initial state, `freestream-milne` preequilibrium evolution, `MUSIC` Israel-Stewart hydrodynamics, `iSS` particlisation, and `SMASH` hadronic afterburner were used.

Chapter 4

Hard Probes in Heavy-Ion Collisions

At the beginning of the heavy-ion collision (HIC), quarks and gluons can collide with a high-momentum transfer q. These processes can be described by pQCD if they have a sufficiently large scale $Q^2 = -q^2 \gg \Lambda_{\mathrm{QCD}}$. Collectively, this part of the QCD is referred to as improved parton model, and it will be introduced in this chapter. Partons are elementary particles that carry a colour charge and thus interact via the strong interaction. This means that quarks and gluons are collectively referred to as partons.

The parton model was introduced by Richard Feynman in 1969 [255]. His motivation was to describe the inner structure of hadrons that are composed of partons. For example, the proton is known to be composed of three quarks u, u, d. We call them valence quarks or constituent quarks. They are responsible for the quantum numbers of the proton and are real particles. However, the tree-quark model is just an approximation. Because quarks are not free inside the proton, they emit and absorb gluons. At higher orders, gluons can create quark-antiquark $q\overline{q}$ pairs [256]. It is understood now that the particles are virtual, and their existence is limited by the Heisenberg uncertainty principle. We understand that the particles are excitations of quantum fields. However, in the case of virtual particles, they never reach asymptotic states and do not contribute to the S-matrix [257]. This is why we cannot detect them directly, but we can detect the interaction between real and virtual particles.

The great benefit of an improved parton model is that hard processes can be factorised. The factorisation theorem can be described as a hard cross section separation process into pQCD and nQCD processes. For example, the cross section of the production of hadron h can be factorised as

$$\frac{\mathrm{d}\sigma^{p+p\longrightarrow h+X}}{\mathrm{d}p_T\mathrm{d}\eta} = \sum_{abc} f_{a/p} \star f_{b/p} \star \hat{\sigma}_{a+b\longrightarrow c} \star D_c^h, \tag{4.1}$$

where $f_{a/p}$ and $f_{b/p}$ are proton distribution functions (PDFs), $\sigma_{a+b\longrightarrow c}$ is the parton-parton cross section, and D_c^h model dependent hadron fragmentation function. PDF $f_{a/p}(x)$ describes the probability of finding a parton a with a momentum fraction x within the proton p. The convolution $\star$ in equation (4.1) represents

$$f \star g = g \star f = \frac{\alpha_s(Q)}{2\pi} \int_x^1 \frac{f(y)}{y} g\left(\frac{x}{y}\right)\mathrm{d}y. \tag{4.2}$$

For small momentum transfer processes, it is possible to describe PDF $f_{a/p}$ with a three-quark model. For our purposes, where hard observables have high momentum transfer, it is necessary to include sea quarks $q_i^{(s)}$ from higher-order gluon interaction and gluons g themselves.

However, PDFs $f_{a/p}$ cannot be calculated from pQCD since they are determined by interactions of partons at large distances. It is possible to measure structure functions from deep inelastic scattering (DIS) and obtain PDFs $f_{a/p}$.

4.1 Deep inelastic scattering

Deep inelastic scattering (DIS) is the scattering of a lepton and a nucleon at high energies, where the nucleon as a target absorbs some kinetic energy. The basic kinematics of this process is as follows

$$W^2 = (p_N + q)^2 = p_N^2 + q^2 + 2p_N \cdot q,$$

where W is the four-momentum of the target after collision, p_N is the four-momentum of the nucleon before collision, and q is the four-momentum of the virtual weak boson that is transferred between lepton and target. Since $q^2 < 0$ since q is a space-like vector (see Appendix A.2), a positive square of the exchanged momentum is defined as

$$Q^2 \equiv -q^2$$

To differentiate deep inelastic scattering from elastic scattering, the Bjorken variable x_B is introduced as

$$x_B = \frac{Q^2}{2p_N q},$$

where $x_B = 1$ for elastic scattering, $x_B < 1$ for inelastic scattering and $x_B \ll 1$ for deep inelastic scattering. Finally, the fraction of energy lost by the incoming lepton y_L is defined as

$$y_L \equiv \frac{p_N q}{p_N k}.$$

This closes the set of variables (Q^2, x_B, y_L) that will be mentioned in this thesis. There is also the energy loss of the incoming lepton ν_L. However, y_L and ν_L have a trivial relationship and Q^2, x_B, and y_L are sufficient to describe DIS kinematics. It is also important to mention that Q^2, x_B, and y_L are Lorentz-invariant variables.

DIS cross section can be factorised into a leptonic $L^{\mu\nu}$ and a hadronic $W^{\mu\nu}$ tensors

$$\frac{\mathrm{d}\sigma}{\mathrm{d}x_B \mathrm{d}y_L} = x_B s \frac{\mathrm{d}\sigma}{\mathrm{d}x_B \mathrm{d}Q^2} = \frac{2\pi y \alpha}{Q^4} \sum_{ij} \eta_i \eta_j L_{ij}^{\mu\nu} W_{\mu\nu}^{ij}, \tag{4.3}$$

Since σ is proportional to the square of the amplitude, there are two factors η_i that arise from the weak vertex. The exact form for each vertex is

$$\begin{aligned}
\eta_\gamma(Q^2) &= 1, \\
\eta_Z(Q^2) &= \frac{g^2}{(2\cos\theta_w)^2 e^2} \frac{Q^2}{Q^2 + M_Z^2} = \frac{G_F}{\sqrt{2}} \frac{M_Z^2}{2\pi\alpha} \frac{Q^2}{Q^2 + M_Z^2}, \\
\eta_W(Q^2) &= \frac{g^2}{(2\sqrt{2})^2 e^2} \frac{Q^2}{Q^2 + M_W^2} = \frac{G_F}{\sqrt{2}} \frac{M_W^2}{4\pi\alpha} \frac{Q^2}{Q^2 + M_W^2}.
\end{aligned}$$

Hardonic tensor $W^{\mu\nu}$ cannot be calculated from pQCD and it has to be parametrised. Since it is a Lorentz tensor, there are six possible terms

$$W^{\mu\nu}(p,q) = -g^{\mu\nu} W_1 + \frac{p^\mu p^\nu}{M^2} W_2 - i\epsilon^{\mu\nu\rho\sigma} \frac{p_\rho q_\sigma}{M^2} W_3 + \frac{q^\mu q^\nu}{M^2} W_4 + \frac{p^\mu q^\nu + p^\nu q^\mu}{M^2} W_5 + \frac{p^\mu q^\nu - p^\nu q^\mu}{M^2} W_6.$$

Gauge invariance condition $q_\mu W^{\mu\nu} = 0$ impies

$$W_6 = 0, \qquad W_5 = -W_2 \frac{p_N q}{q^2 M_N^2}, \quad \text{and} \quad W_4 = W_1 \frac{1}{q^2} + W_2 \frac{(p_N q)^2}{q^4 M_N^2}.$$

Gauge invariance simplifies the hadronic tensor $W^{\mu\nu}$ and can be reformulated in terms of structure functions

$$F_1 = W_1, \qquad F_2 = W_1 \frac{Q^2}{2x_B M_N^2}, \quad \text{and} \quad F_3 = W_3 \frac{Q^2}{2x_B M_N^2}.$$

Final form of the hadronic tensor takes the form

$$W_{\mu\nu} = \left(-g_{\mu\nu} + \frac{q_\mu q_\nu}{q^2}\right) F_1\left(x_B, Q^2\right) + \frac{\hat{P}_\mu \hat{P}_\nu}{p \cdot q} F_2\left(x_B, Q^2\right) - i\varepsilon_{\mu\nu\alpha\beta} \frac{q^\alpha p^\beta}{2q \cdot p} F_3\left(x_B, Q^2\right). \tag{4.4}$$

The last term violates parity; this means that the term with structure function F_3 is zero for photon exchange.

Three structure functions can be measured in DIS experiments. Different species of leptons and nucleons can collide, and the inner structure of the proton can be untangled with arithmetic operations. For example, the second structure function F_2 can be expressed as

$$F_2\left(x_B, Q^2\right) = \sum_i e_i^2 x_B f_{i/p}\left(x_B, Q^2\right). \tag{4.5}$$

Bjorken variable x_b corresponds to the momentum fraction carried by the parton $x = \frac{p_a}{p_N}$.

4.2 Initial Conditions of Hard Partons

The initial conditions in terms of hard processes represent the four-momenta of specific partons created at the beginning of the collision with a sufficiently large momentum transfer q. This means transverse momentum p_{T}, spatial pseudorapidity η_s, azimuth angle ϕ, and species of the parton. This can be obtained from the convolution of nuclear parton distribution functions (nPDF) and the multiparton interaction (MPI) cross section.

4.2.1 Parton distribution function

It is possible to determine the parton distribution functions (PDF) using the results of the neutral current DIS cross section measured in H1 [258, 259, 260], ZEUS [261, 262], BCDMS [263], and NMC [264, 265], inclusive jet cross section measured in DØ [266, 267] and CDF [268], Drell-Yan deuteron-proton ratio measured in E866 [269] and E605 [270], F_2 and F_3 measured in CCFR [271, 272], and finally the W-lepton asymmetry measured by CDF collaboration [273].

Furthermore, the pQCD parameters must be introduced. That is, $\alpha_s(M_Z) = 0.118$ [32] and quark masses. Quarks u, d, and s can be taken as massless. PDF evolution kernels of the are mass independent in the $\overline{MS}$ scheme, so masses of heavy-flavour quarks should be taken as the scales at which they are turned on in evolution ($Q^2 \geq m_q^2$). The masses of heavy quarks are taken as $m_c = 1.3$ GeV and $m_b = 4.5$ GeV. [274]

PDFs can be parametrised and the parameters can be determined by fitting the data. One possible parameterisation is

$$x f_{i/p}^{\mathrm{CTEQ6.1M}}\left(x, Q^2\right) = A_0 x^{A_1} (1-x)^{A_2} e^{A_3 x} \left(1 + e^{A_4} x\right)^{A_5}.$$

This parameterisation is called Padé expansion. The singularity at $x = 0$ corresponds to the Regge behaviour at small x. Then the singularity at $x = 1$ is associated with the quark-counting rules at large x.

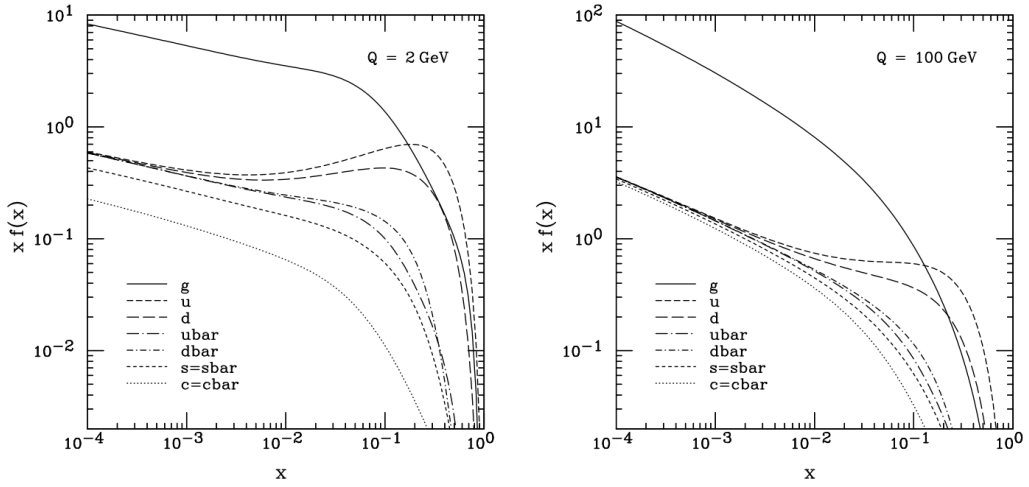

Figure 4.1: Overview of the CTEQ6M PDFs $f_{i/p}^{\mathrm{CTEQ6M}}$ at $Q = 2$ GeV and $Q = 100$ GeV. [274]

With the theoretical calculations and experimental measurements, PDFs can be derived. CTEQ6M PDFs [274, 275] at the scale $Q = 2$ GeV and $Q = 100$ GeV are shown in Figure 4.1. One can see that the sea quarks located at the small x are more prominent for larger values of Q. It can be interpreted that the interaction with a higher momentum transfer can probe smaller structures of the nucleon. This means more fermion loops that are associated with sea quarks.

The evolution of PDFs in Q can be calculated using the DGLAP equation (forsee equation (4.9)). DGLAP equation will be introduced in Section 4.3.1. The evolution of PDFs is obtained as a convolution of PDFs and splitting functions. The splitting function is a probability function that can be calculated within pQCD up to some order. This work considers the next-to-leading-order (NLO) PDFs derived in the $\overline{MS}$ scheme.

Nuclear parton distribution function

Even though the nucleus is made up of individual nucleons, partons are not distributed in the same manner as individual nucleons. This is why it is necessary to introduce nuclear parton distribution functions (nPDFs). The PDF of the nucleon incide nucleus A can be parameterised as

$$f_{i/A}\left(x, Q^2\right) \equiv R_i^A\left(x, Q^2\right) f_{i/p}^{\mathrm{CTEQ6.1M}}\left(x, Q^2\right),$$

where $R_i^A(x)$ is the nuclear modification of the PDF of free proton. Parameterisation of nuclear modification $R_i^A(x)$ can be expressed as

$$R_i^A(x) = \begin{cases} a_0 + (a_1 + a_2 x)\left[\exp(-x) - \exp(-x_a)\right] & x \le x_a \\ b_0 + b_1 x + b_2 x^2 + b_3 x^3 & x_a \le x \le x_e \\ c_0 + (c_1 - c_2 x)(1-x)^{-\beta} & x_e \le x \le 1 \end{cases}, \tag{4.6}$$

where 6 of the 13 parameters are eliminated by matching conditions at points x_a and x_e and one parameter is fixed as $c_0 = 2y_e$.

The outline of the parameterisation of nuclear modification $R_i^A(x)$ is shown in Figure 4.2. There are four characteristic regions called shadowing, antishadowing, EMC-effect, and Fermi motion. The depth of shadowing effect ($x \to 0$) is associated with the parameter y_0. Position of the antishadowing maximum x_a and $y_a \equiv R_i^A(x_a)$. The position of the minimum of the EMC-effect is associated with x_e and $y_e \equiv R_i^A(x_e)$. Finally, the parameter β is associated with the slope of the Fermi motion ($x \to 1$).

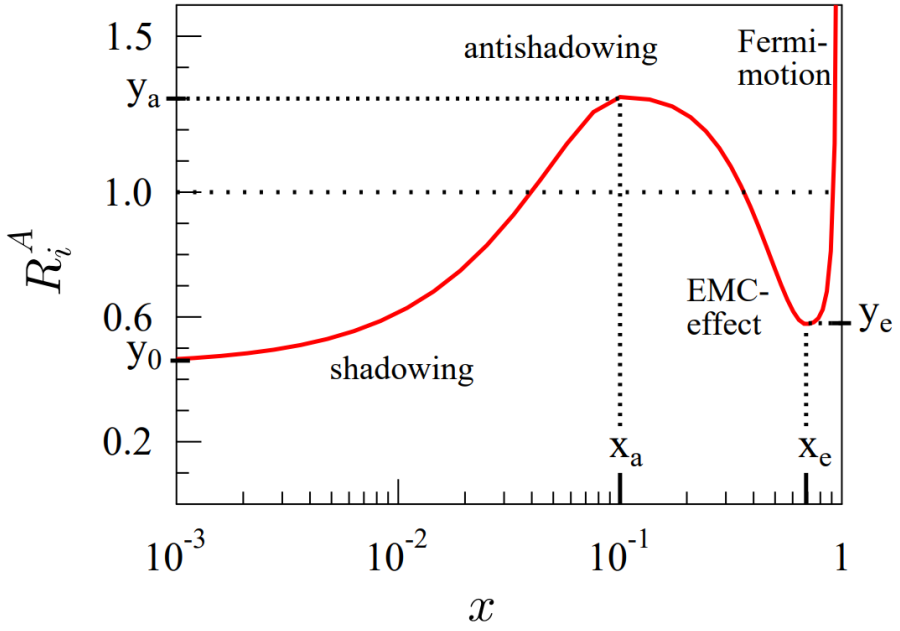

Figure 4.2: An illustration of the $R_i^A(x)$ with relevant parameters $(y_0, x_a, y_a, x_e, y_e, \beta)$. [276]

Six parameters $(y_0, x_a, y_a, x_e, y_e, \beta)$ of nuclear modification $R_i^A(x)$ depend on the number of nuclear masses A. This A-dependence is usually parameterised by the power law

$$d_i^{(A)} = d_i^{(12)} \left(\frac{A}{12}\right)^{p_{a_i}},$$

where $d_i^{(A)}$ are nuclear modification $R_i^A(x)$ $A-$dependent parameters $(y_0, x_a, y_a, x_e, y_e, \beta)$ and p_{d_i} are power parameters of the $A-$dependence. The reference mass number $A = 12$ corresponds to the carbon ^{12}C.

Parameter space can be eliminated with momentum and baryon number sum rules

$$\sum_{i=q,\bar{q},g} \int_0^1 \mathrm{d}x\, x f_{i/A}\left(x, Q_0^2\right) = 1, \quad \int_0^1 \mathrm{d}x \left[f_{u_V/A}\left(x, Q_0^2\right) + f_{d_V/A}\left(x, Q_0^2\right) \right] = 3.$$

Namely parameters y_0 and p_{y_0} for the valence quarks u_v and d_v and gluons g can be removed from the parameter space that has to be determined by experiments. This means that there are 32 free parameters.

The parameters of nPDF can be obtained with an analysis consisting of $\ell + A$ DIS experiments, Drell-Yan dilepton production measured in $p + A$ collisions. Finally, since nuclear modification of the deuteron can be estimated to be of the order 2% [277], neutral pion π^0 production measured in d+Au and p+p collisions. Observables of nuclear modification are formulated as

$$R^{\mathrm{A}}_{\mathrm{DIS}}\left(x_B, Q^2\right) \equiv \frac{\frac{1}{A}\frac{\mathrm{d}\sigma^{\ell\,\mathrm{A}}_{\mathrm{DIS}}}{\mathrm{d}Q^2\mathrm{d}x_B}}{\frac{1}{2}\frac{\mathrm{d}\sigma^{\ell\,\mathrm{d}}_{\mathrm{DIS}}}{\mathrm{d}Q^2\mathrm{d}x_B}},$$

$$R^{\mathrm{A}}_{F_2}\left(x_B, Q^2\right) \equiv \frac{F_2^A\left(x_B, Q^2\right)}{F_2^{\mathrm{d}}\left(x_B, Q^2\right)},$$

$$R^{\mathrm{A}}_{\mathrm{DY}}\left(x_B^{(1,2)}, M^2\right) \equiv \frac{\frac{1}{A}\frac{\mathrm{d}\sigma^{\mathrm{pA}}_{\mathrm{DY}}}{\mathrm{d}M^2\mathrm{d}x_B^{(1,2)}}}{\frac{1}{2}\frac{\mathrm{d}\sigma^{\mathrm{pd}}_{\mathrm{DY}}}{\mathrm{d}M^2\mathrm{d}x_B^{(1,2)}}},$$

$$R^{\pi}_{\mathrm{dAu}} \equiv \frac{1}{\langle N_{\mathrm{coll}}\rangle}\frac{\frac{\mathrm{d}^2N^{\mathrm{dAu}}_{\pi}}{\mathrm{d}p_T\mathrm{d}y}}{\frac{\mathrm{d}^2N^{\mathrm{pp}}_{\pi}}{\mathrm{d}p_T\mathrm{d}y}} \overset{\text{min.bias}}{=} \frac{\frac{1}{2A}\frac{\mathrm{d}^2\sigma^{\mathrm{dAu}}_{\pi}}{\mathrm{d}p_T\mathrm{d}y}}{\frac{\mathrm{d}^2\sigma^{\mathrm{pp}}_{\pi}}{\mathrm{d}p_T\mathrm{d}y}},$$

where M is the invariant mass of the lepton pair, then $x_{1,2} \equiv \sqrt{\frac{M^2}{s}}e^{\pm y}$ and $\langle N_{\mathrm{coll}}\rangle$ is the average number of binary collisions.

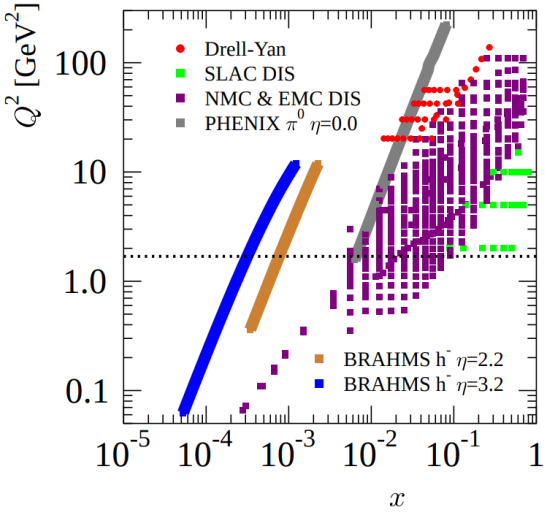

Figure 4.3: The kinematical reach of the DIS, Drell-Yan dilepton production, and an inclusive neutral pion π_0 production. [276]

All cross sections can be calculated with the collinear factorisation formalism

$$\sigma_{\mathrm{DIS}}^{\ell A\to\ell X} = \sum_{i=q,\bar{q},g} f_{i/A}\left(Q^2\right)\star\hat{\sigma}_{\mathrm{DIS}}^{\ell+i\to\ell+X}\left(Q^2\right),$$
$$\sigma_{\mathrm{DY}}^{pA\to l^+l^-X} = \sum_{i,j=q,\bar{q},g} f_{i/p}\left(Q^2\right)\star f_{j/A}\left(Q^2\right)\star\hat{\sigma}^{ij\to l^+l^-X}\left(Q^2\right),$$
$$\sigma^{AB\to\pi X} = \sum_{i,j,k=q,\bar{q},g} f_{i/A}\left(Q^2\right)\star f_{j/B}\left(Q^2\right)\star\hat{\sigma}^{ij\to k+X}\left(Q^2\right)\star D_{k\to\pi}\left(Q^2\right),$$

where $\hat{\sigma}$ are calculable quantities in pQCD and are calculated in NLO.

DIS put constraints on the power parameters for the valence and sea quarks in the range $0.01 \leq x \leq 1$. [276] Separation of valence and sea quarks is not possible around the antishadowing peak ($x \sim 0.1$). DIS is primarily sensitive for valence quarks at high x and for sea quarks at small x. The Drell-Yan dilepton production can distinguish between valence and sea quarks around the antishadowing peak ($x \sim 0.1$). [276] Currently, precision for larger x is not sufficient to constrain the parameters. Drell-Yan dilepton production for $M^2 \gg Q_0^2$ constrains gluons. Finally, the inclusive production of neutral pion π_0 has large uncertainties originating from the model-dependent number of binary collisions $\langle N_{\mathrm{coll}}\rangle$. However, important constraints on gluon parameters can be obtained from inclusive production of the neutral pion π_0. Namely, EMC-effect and shadowing. [276] The kinematical reach of the DIS, the Drell-Yan dilepton production, and the inclusive production of neutral pions π_0 are shown in Figure 4.3.

Parameters are obtained through the iteration of minimisation of a global χ^2-function. NLO nuclear modifications $R_i^A(x)$ for lead Pb can be seen in Figure 4.4. Nuclear PDFs obtained from this process are called EPS09NLO nPDFs [276] and are implemented in `Pythia` [6, 254].

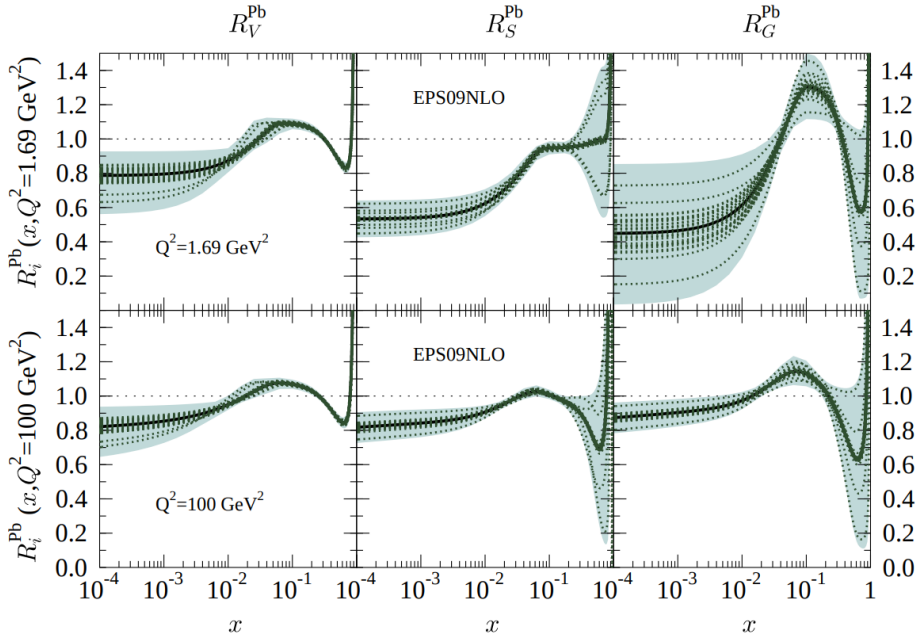

Figure 4.4: NLO nuclear modifications R_V, R_S, R_G for lead at $Q^2 = 1.69$ GeV^2 and $Q^2 = 100$ GeV^2. [276]

Pythia initial state

The initial state of partons (PID, p_T, y, ϕ) is obtained from `Pythia 8` [6] implemented in `Jetscape` [9] as PythiaGun. This initial-state generator is a p_T-ordered multiparton interaction (MPI) [278] Monte Carlo framework with initial-state radiation [279]. A much closer mathematical description of parton evolution will be given in the following Section 4.3.

Hard $2 \to 2$ processes can be obtained from the factorisation theorem

$$\sigma^{\text{hard}} = \sum_r \sum_{ijkl} f_{i/A}(Q^2) \star f_{j/B}(Q^2) \star \hat{\sigma}_r^{ij\to kl}(\hat{s}, \hat{t}, \hat{u}),$$

where r is the subprocess of some order of perturbative theory and $\hat{s}, \hat{t}, \hat{u}$ are mandelstam variables of quarks. This is accompanied by initial-state radiation, which makes it a $2 \to n$ process.

In `Pythia 8`, parton emissions are ordered in p_{T}^2 and evolved according to the Sudakov form factor [280] which will also be introduced in Section 4.3. This makes the transverse momentum squared p_{T}^2 an evolution variable. `Pythia` framework construct preliminary kinematics of the unevolved partons explicitly on the mass shell directly after each branching; then the partons acquire virtuality Q. The total transverse momentum and other kinematic variables are conserved with the recoil partner that can also undergo initial-state radiation.

4.3 Jet evolution in the vacuum

Jet is a collimated cone of hadrons. Jets originate from hard processes with quarks and/or gluons. This essentially means that when the interaction with the high-momentum transferred q produces partons, they evolve into a shower of hadrons. This is due to the colour confinement described in Section 2.3.3. Partons undergo the so-called hadronisation, where the transition from quarks and gluons to hadrons is made. Hadronisation itself is an nQCD process and has to be described with a model. This will be introduced in Section 4.5. Since the time scale of the hard process $\sim \frac{1}{\sqrt{s}}$ is much smaller than the time scale of hadronisation, hadronisation does not influence the hard vertex and cross sections can be factorised with the factorisation theorem.

To properly introduce the concept of a jet, consider two Feynman diagrams of electron-positron annihilation:

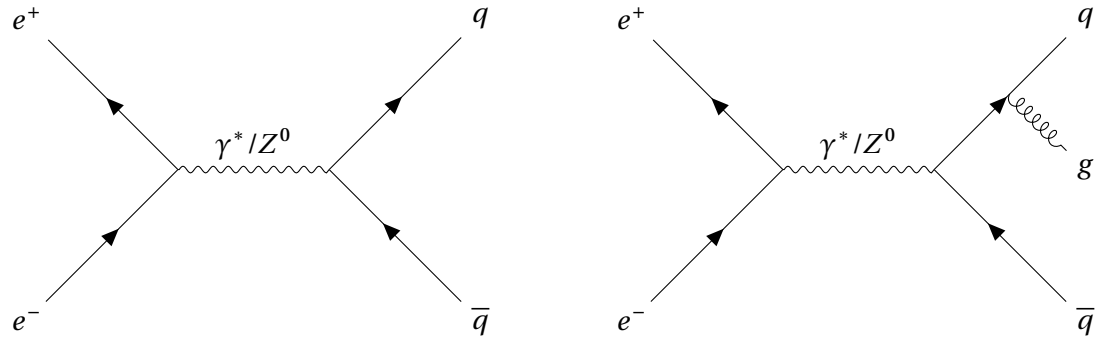

The first diagram represents the LO creation of the quark-antiquark pair $q\overline{q}$ from either of the chargeless electroweak bosons. The second diagram represents a similar process, but the quark

q radiates the gluon g. The diagram of the process, where the gluon g is radiated by the antiquark $\overline{q}$, results in the same cross section and they have to be added together.

When the quark and antiquark are created from a photon γ^* or zero Z^0 originating from annihilation, they create the so-called back-to-back jets. This event has two jets of hadrons that have the same absolute transverse momenta p_T with the opposite position at the azimuthal angle ϕ space. This originates from the conservation law of three components of the momenta. If the electron and the positron have the same momentum, the jets will have opposite rapidity y. However, it is important to note that this does not apply to nucleon-nucleon, nucleon-ion, or ion-ion collisions because partons inside nucleons can carry a different fraction x of the nucleon momentum.

The cross section for the first diagram can be calculated from QED as

$$\sigma_{\mathrm{LO}}\left(e^+e^- \to q\bar{q}\right) = N_{\mathrm{c}}\frac{4\pi\alpha^2}{3s}\sum_q e_q^2.$$

It is quite interesting to compare it to muon pair production $e^-e^+ \to \mu^-\mu^+$

$$R = \frac{\sigma_{\mathrm{LO}}\left(e^+e^- \to q\bar{q}\right)}{\sigma_{\mathrm{LO}}\left(e^+e^- \to \mu^+\mu^-\right)} = N_{\mathrm{c}}\sum_q e_q^2, \tag{4.7}$$

since one can obtain direct access to the number of colours N_c and compare it with the experiment. This simple comparison does not work for more accurate measurements. There is a discrepancy between the LO production ratio in equation (4.7). This originates from higher-order corrections. For example, the NLO cross section of the quark-antiquark pair $q\overline{q}$ production, also called vertex correction, is

$$\sigma_{\mathrm{NLO}} = N_c\frac{4\pi\alpha^2}{3s}\sum_q e_q^2\left(1+\frac{\alpha_{\mathrm{s}}}{\pi}\right),$$

where renormalisation removes ultraviolet (UV) divergencies.

The second diagram corresponding to the 3-jet event can be calculated from QCD as

$$\sigma_{\mathrm{LO}}^{q\bar{q}g} = N_c\frac{4\pi\alpha^2}{3s}\sum_q e_q^2\int \mathrm{d}x_1\,\mathrm{d}x_2\frac{4}{3}\frac{\alpha_{\mathrm{s}}}{2\pi}\frac{x_1^2+x_2^2}{(1-x_1)(1-x_2)}. \tag{4.8}$$

Here, x_1 and x_2 are fractions of energy carried by the quark and antiquark, respectively. The cross section has infrared (IR) singularities that appear for $E_g \to 0$. This can be fixed with the introduction of a gluon mass m_g. This might seem unphysical. However, the Kinoshita-Lee-Nauenberg theorem [281, 282] states that the Standard Model as a whole is infrared (IR) finite, and cross sections are independent of unphysical masses. For this 3-jet process, this means that if we sum all gluon radiations/absorbtions up to arbitrary order, the result is finite for $m_g \to 0$ and independent of the gluon mass m_g. Originally, the total 3-jet cross section was used in `Pythia` to generate initial-state partons. This was replaced with more sophisticated initial-state radiation [278]. 3-jet event at the detector level can be seen in Figure 4.5, where the jets pointing left and right are the quark and antiquark jets, and the jet with downward direction is the gluon jet. However, gluon jets have usually wider angular distribution and more particles with less momenta.

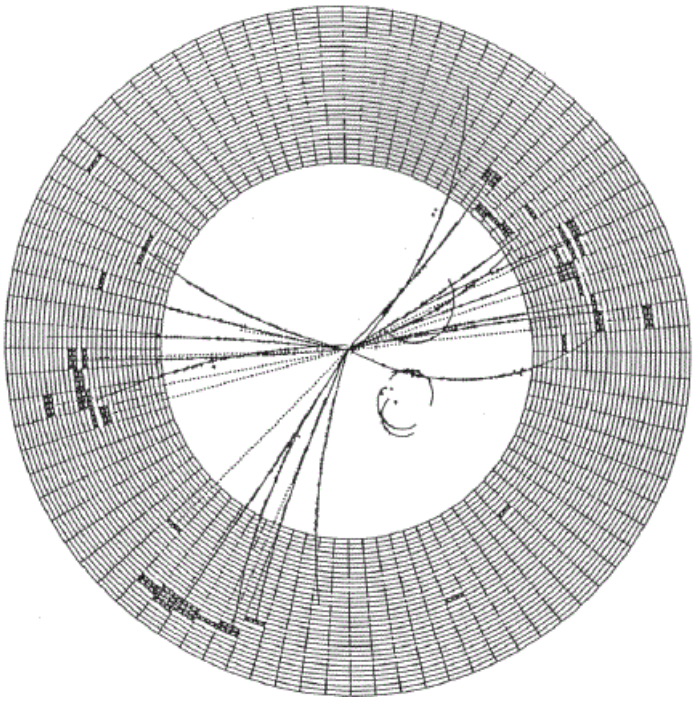

Figure 4.5: Three-jet event ($q\overline{q}g$) in the JADE detector at DESY from electron-positron annihilation.

In a sense, the 3-jet event can be understood as a radiation modification of the 2-jet event. Since partons can split and partonic shower can evolve before hadronisation even in vaccum. Those effects are much more significant for evolution inside the medium (see Section 4.4), but let us start with the investigation of the vacuum evolution first.

4.3.1 Splitting functions and the DGLAP equations

Dokshitzer-Gribov-Lipatov-Alterelli-Parisi (DGLAP) are evolution equations of partons. Guido Altarelli and Giorgio Parisi introduced them in 1977 [283] to western research community. In the same year, Yurii L. Dokshitzer published the same evolution equation [284] in the Soviet Union. However, later it was found that Vladimir Gribov and Lev Lipatov introduced an equivalent evolution equation 1972 [285] in the Soviet Union as well.

DGLAP equations are based on the assumption that partons can split and consequently the probability that parton splits into n number of partons is somehow related to the probability that parton splits into $n-1$ number of partons, where this relation is provided with the splitting kernel as a probability of parton split. For particle distribution functions, this essentially means that

$$f(x) \to f_0(x,t) = f(x) + \frac{\alpha_s(Q)}{2\pi}\int_x^1 \frac{f(y)}{y} P\left(\frac{x}{y}\right) \mathrm{d}y + \mathcal{O}\left(\alpha_s^2(t)\right),$$
$$\Delta f(x,t) = f_0 \star P,$$

where P is the splitting kernel and t is not time, but rather the evolution variable

$$t = \ln \frac{Q^2}{\Lambda^2_{\mathrm{QCD}}}.$$

This behaviour in LO describes the valence-quark model f_0. The distribution function f_0 is also called primordial or bare and depends only on x. However, there are higher-order processes that contribute to the particle distribution functions, and the number of particles is not conserved. This behaviour can be put into ordinary differential equation

$$\frac{\mathrm{d}f(x,t)}{\mathrm{d}t} = \frac{\alpha_s(t)}{2\pi}\int_x^1 \frac{f(y,t)}{y} P\left(\frac{x}{y}\right)\mathrm{d}y + \mathcal{O}\left(\alpha_s^2(t)\right) = f \star P + \mathcal{O}\left(\alpha_s^2(t)\right).$$

This incorporates this branching behaviour mentioned at the beginning of this section.

Now, in the case of QCD, there are four types of splitting functions.

$$\begin{aligned}
P_{qq} &= \frac{4}{3}\left[\left(\frac{1+z^2}{1-z}\right)_+ + \frac{3}{2}\delta(1-z)\right] + \mathcal{O}(\alpha_s),\\
P_{gq} &= \frac{4}{3}\frac{1+(1-z)^2}{z} + \mathcal{O}(\alpha_s),\\
P_{qg} &= \frac{1}{2}(z^2+(1-z)^2) + \mathcal{O}(\alpha_s),\\
P_{gg} &= 6\left[\left(\frac{z}{1-z}\right)_+ + \frac{1-z}{z} + z(1-z)\right] + \frac{33-2n_f}{6}\delta(1-z) + \mathcal{O}(\alpha_s),
\end{aligned}$$

where any of them can be calculated up to some order within pQCD and they are probabilities of parton splitting. Furthermore, the + subscript notation $g(x)_+$ represents

$$\int_0^1 g(x)_+ f(x)\mathrm{d}x = \int_0^1 (f(x)-f(1))g(x)\mathrm{d}x,$$

where f is from the test function space.

Finally, we can introduce the DGLAP evolution equations for QCD partons as

$$\begin{aligned}
\frac{\mathrm{d}f_a(x,t)}{\mathrm{d}t} &= \frac{\alpha_s(Q)}{2\pi}\sum_b \int_x^1 \frac{f_b(y,t)}{y} P_{ab}\left(\frac{x}{y}\right)\mathrm{d}y\\
&= \sum_b f_b \star P_{ab}.
\end{aligned} \tag{4.9}$$

4.3.2 Sudakov form factor

It is possible to describe the multi-gluon emission. First, radiated gluons have virtuality Q ordering. Taking into account the initial-state shower, the virtuality Q is the evolution parameter and increases toward the hard scattering. Now, for the final-state shower, the virtuality of the emissions decreases, and evolution moves further from the hard scattering. It is possible to construct the so-called ladder of n radiated gluons. The cross section of this is proportional to

$$\sigma^{ng} \sim \alpha_s^n \left[\underbrace{A_n \ln^n\left(\frac{Q^2}{n_g^2}\right)}_{\text{Leading logarithm}} + \underbrace{B_n \ln^{n-1}\left(\frac{Q^2}{n_g^2}\right)}_{\text{Next-to-leading logarithm}} + \ldots \right],$$

where the scale of α_s should be the highest virtuality Q_k of all partons interacting in that vertex. If we consider radiation of the i -th gluon, the scale of α_s should be the virtuality of the incoming quark that carries virtuality Q_{i-1} from the previous vertex. This makes $\alpha_s\left(Q_{i-1}^2\right)$ dependent on the vertex i.

Now, if we consider the correction of the first gluon emission as an emission and reabsorbtion of another gluon (loop), it will lead to logarithms $\ln\left(\frac{\mu}{Q_i}\right)$. Since the scale μ is chosen as Q_i, it will moderate potentially large logarithms. Then it is possible to sum σ^{ng} with the DGLAP equations.

The probability of gluon emission increases with n because there are more positive logarithms. The probability density of parton branching is

$$\sum_{bc} I_{a\to bc}(Q^2) = \sum_{bc} \int_{z^-}^{z^+} \mathrm{d}z \frac{\alpha_s}{2\pi} P_{a\to bc}(z),$$

where $I_{a\to bc}$ is a probability density of a specific event and (z^-, z^+) is allowed region of momentum fraction. Consequently, the probability of no splitting in the (Q_i^2, Q_f^2) interval is suppressed and takes the form

$$\mathscr{S}_{\mathrm{q}}\left(Q_i^2, Q_f^2\right) = \exp\left(-\int_{Q_f^2}^{Q_i^2} \frac{\mathrm{d}Q'^2}{Q'^2} \int \mathrm{d}z \frac{\alpha_{\mathrm{s}}}{2\pi} \hat{P}_{\mathrm{qq}}(z)\right)$$

$$\mathscr{S}_{\mathrm{g}}\left(Q_i^2, Q_f^2\right) = \exp\left(-\int_{Q_f^2}^{Q_i^2} \frac{\mathrm{d}Q'^2}{Q'^2} \int \mathrm{d}z \frac{\alpha_{\mathrm{s}}}{2\pi} \left[\hat{P}_{\mathrm{gg}}(z) + \hat{P}_{\mathrm{qg}}(z)\right]\right).$$

This equation is called the Sudakov form factor and is the foundation of many Monte Carlo simulators including Modular All Twist Transverse-scattering Elastic-drag and Radiation (`MATTER`) model [7, 286] which was used with `Pythia` [6, 254] initial state to generate $p+p$ collisions in this thesis. Both frameworks were used as a modules implemented in `Jetscape` [9].

Finally, the specific channel i in which parton j splits is determined by branching ratio

$$\mathrm{BR}_{ij}(Q^2) = \int_{Q_{\min}^2/Q^2}^{1-Q_{\min}^2/Q^2} \mathrm{d}y P_{ij}(y). \tag{4.10}$$

This process describes evolution in vacuum from a QCD point of view. Another layer of Monte Carlo simulation is kinematics. Momentum and energy must be conserved and distributed between the daugheter particles. If we assume that y and $(1-y)$ are fractions of momenta of daughter partons, respectively, their maximum possible virtualities are $Q_1^{\max} = y^2 Q_0$ and $Q_1^{\max} = (1-y^2)Q_0$. [287] Their transverse momentum with respect to the original parton k_{T} can be obtained as

$$k_{\mathrm{T}}^2 = y(1-y)Q_0 - (1-y)Q_1 - yQ_2.$$

This finalises the vacuum evolution. It is possible to introduce medium modifications to this process and use `MATTER` [7, 286] to simulate the evolution of high-virtuality ($Q_0 \geq 2$ GeV) partons inside the medium.

4.4 Jet evolution inside the medium

This work focusses on heavy-ion collisions, where a hot and dense medium is created. Partons that travel through this medium experience what is called quenching. This is associated with energy loss. It is important to note that energy is, in fact, not lost, but conserved. Since partons originating from the hard interaction vertex are not measured directly, it is unlikely that reconstructed jets (see Section 4.6 for details on reconstruction) composed of hadrons carry all the energy of the original parton. In other words, energy is not lost in a physical process but rather not fully recovered in the jet-reconstruction process. Nevertheless, hadronic jets are defined on the detector level and they still carry information about the medium. The reason is that their evolution is different compared to the $e^- + e^+$ and $p + p$ collisions. Even a simple comparison between $p + p$ and heavy-ion collision can be very valuable (see Chapter 5).

It is important to treat high-virtuality partons ($Q_0 \geq 2$ GeV) differently compared to low-virtuality partons ($Q_0 < 2$ GeV). The reason is included in the previous Section 4.3.2. The scale in which α_s is taken is the virtuality of the parton before it splits. This is done to avoid large logaithms. However, this also means that α_s can grow large for small-scale Q (see Section 2.3.2) and pQCD is not applicable. However, since virtuality is small due to previous splittings, it is possible to use an on-shell approach with evolution according to the linear Boltzmann equation.

4.4.1 Medium-modified vacuum evolution

When a jet parton travels through the medium, it experiences elastic or inelastic interactions with medium partons. For high-virtuality partons ($Q_0 \geq 2$ GeV), medium effects can be considered as a perturbation of their vacuum evolution [288, 289, 290]. As such, splitting function is modified as

$$P_i(y, \tilde{Q}^2) = P_i^{\text{vac}}(y) + P_i^{\text{med}}(y, \tilde{Q}^2),$$

where $P_i^{\text{med}}(y, \tilde{Q}^2)$ is medium modification of splitting function [291, 292, 293, 294] in a higher-twist formalism, takes the following form

$$P_i^{\text{med}}(y, \tilde{Q}^2) = \frac{P_i^{\text{vac}}(y)}{y(1-y)\tilde{Q}^2} \int_0^{\tau_f^+} d\zeta^+ \hat{q}(r+\zeta) \left[2 - 2\cos\left(\frac{\zeta^+}{\tau_f^+}\right) - 2\frac{\zeta^+}{\tau_f^+}\sin\left(\frac{\zeta^+}{\tau_f^+}\right) + 2\left(\frac{\zeta^+}{\tau_f^+}\right)^2 \cos\left(\frac{\zeta^+}{\tau_f^+}\right) \right],$$

where $\hat{q}$ is the gluon jet transport coefficient. This denotes its transverse momentum broadening squared per unit length due to elastic scatterings with medium partons. The transport coefficient $\hat{q}$ is evaluated at the location of the scattering $\zeta^+ = \vec{r} + \hat{n}\zeta$, where $\hat{n}$ denotes $\hat{n} = \vec{p}/|\vec{p}|$. The offset of the location of the splitting ζ^+ is obtained from the Gaussian distribution with the mean value as the formation time τ_f^+. This distribution then takes the form

$$\rho(\zeta^+) = \frac{2}{\tau_f^+ \pi} \exp\left[-\left(\frac{\zeta^+}{\tau_f^+ \sqrt{\pi}} \right)^2 \right].$$

Finally, the mean formation time τ_f^+ is defined as

$$\tau_f^+ = \frac{2p^+}{\tilde{Q}^2},$$

where $p^+ = \frac{1}{\sqrt{2}}(p^0 + \hat{n} \cdot \vec{p})$.

The splitting channel i of parton j is obtained by branching ratio

$$\mathrm{BR}_{ij}(Q^2) = \int_{Q^2_{\mathrm{min}}/Q^2}^{1-Q^2_{\mathrm{min}}/Q^2} \mathrm{d}y P_{ij}(y, Q^2).$$

This approach is again similar as for the vacuum case in equation 4.10, however, there are corrections $P_i^{\mathrm{med}}(y, \tilde{Q}^2)$.

The higher twist formalism can fairly well describe some jet modifications in relativistic nuclear collisions with high transverse momentum p_{T} at RHIC and LHC with the assumption that partons with low virtuality ($Q < 1$ GeV) are absorbed by the medium. However, this is not the case. A low-virtuality parton can carry high transverse momentum p_{T}. It is possible to use on-shell evolution within a linear Boltzmann transport model.

In the hydrodynamic simulation, the medium is continuous and is not composed of individual partons. However, this is just a viable approximation with sufficiently small Knudsen and Reynolds numbers. For practical calculations, one typically considers the medium as a set of scattering centres and samples elastic and inelastic interactions between the jet parton and medium partons on its way. It may happen that the medium parton acquires a significant kick and becomes more energetic than a typical medium parton. As such, the affected medium parton should be treated as a part of the jet rather than as a constituent of the medium, from the moment of interaction. For the purpose of overall energy conservation in the process, a hole is introduced in the place of the original medium parton, such that the energy of the incoming jet and medium parton equals to the sum of energies of the outgoing jet parton, medium parton, and the hole (which by construction possesses negative energy).

4.4.2 Linear Boltzmann transport model

Low-virtuality treatment can be described with the linearised Boltzmann transport (LBT) model [8, 295, 296, 297]. As the name indicates, this model is based on the Boltzmann equation (already introduced in Section 3.1 and Section 3.5) with the elastic and inelastic collision integrals

$$p^\mu \partial_\mu f(x;p) = E C_{\mathrm{el}}[f] + C_{\mathrm{inel}}[f].$$

Elastic integral can be expressed as

$$C_{\mathrm{el}}[f] \equiv \sum_{12\to 23} \int \mathrm{d}^3 k \left[\Gamma_{12\to 34}\left(\vec{p}+\vec{k}, \vec{k}\right) f\left(\vec{p}+\vec{k}\right) - \Gamma_{12\to 34}\left(\vec{p}, \vec{k}\right) f\left(\vec{p}\right) \right],$$

where $\Gamma_{12\to 34}$ describes the elastic $2 \to 2$ scattering as

$$\int \mathrm{d}^3 k \Gamma_{12\to 34}\left(\vec{p}, \vec{k}\right) = \frac{\gamma_2}{2E_1} \int \frac{\mathrm{d}^3 p_2}{(2\pi)^3 2E_2} \frac{\mathrm{d}^3 p_3}{(2\pi)^3 2E_3} \frac{\mathrm{d}^3 p_4}{(2\pi)^3 2E_4} f_2\left(\vec{p}_2\right) \left[1 \pm f_3\left(\vec{p}_3\right)\right] \left[1 \pm f_4\left(\vec{p}_4\right)\right] \times \\ \times S_2(s,t,u) (2\pi)^4 \delta^4\left(p + p_2 - p_3 - p_4\right) \left|\mathscr{M}_{12\to 34}\right|^2,$$

where the signs $\pm$ represent the Bose enhancement or Pauli blocking. Furthermore, $\mathscr{M}_{12\to 34}$ is the LO scattering amplitude obtained from QCD and factor $S_2(s,t,u)$ is introduced to avoid possible divergence of the amplitude for small angles as

$$S_2(s,t,u) = \theta\left(s \geq 2\mu_{\mathrm{D}}^2\right) \theta\left(-s + \mu_{\mathrm{D}}^2 \leq t \leq -\mu_{\mathrm{D}}^2\right).$$

Debye screening mass in QGP medium for massless partons takes form

$$\mu_{\mathrm{D}}^2 = \frac{g_s^2}{3} T^2 \left(N_c + \frac{N_f}{2} \right),$$

where $N_c = 3$ is the number of colours and N_f is the number of active quark flavours.

For the inelastic part, it is possible that the parton travelling through the medium radiates the medium-induced gluon. The average number of gluons radiated by parton which carries energy E can be obtained from higher-twist framework as

$$\left\langle N_g \right\rangle = \Delta t \int \mathrm{d}x \mathrm{d}k_{\mathrm{T}}^2 \frac{\mathrm{d}^3 N_g}{\mathrm{d}x \mathrm{d}k_{\mathrm{T}}^2 \mathrm{d}t},$$

where T is the temperature of the medium and Δt is a time step. The distribution of radiated gluons can be calculated [291, 292, 298] as

$$\frac{dN_g}{dx dk_{\mathrm{T}}^2 dt} = \frac{2\alpha_s C_A \hat{q} P(x) k_{\mathrm{T}}^4}{\pi \left(k_{\mathrm{T}}^2 + x^2 m^2 \right)^4} \sin\left(\frac{t - t_i}{2\tau_f} \right),$$

where τ_f is the formation time of the radiated gluon defined as

$$\tau_f = \frac{2Ex(1-x)}{k_{\mathrm{T}}^2 + x^2 M^2},$$

where M is the mass of the parent parton.

It is possible that there are multiple gluon radiations since $\left\langle N_g \right\rangle$ can be of order of one. This multigluon radiation is incorporated in the LBT with the Poisson distribution

$$\mathscr{P}(n) = \frac{\left\langle N_g \right\rangle^n}{n!} e^{-\left\langle N_g \right\rangle}.$$

Now, the probability of radiating at least one gluon is

$$P_{\mathrm{inel}} = \mathbf{1} - e^{-\left\langle N_g \right\rangle}. \tag{4.11}$$

This essentially states the probability of the inelastic scattering and is used in Monte Carlo simulation to determine if the gluon is radiated.

Since gluon radiation is medium-induced, before the parton undergoes inelastic scattering, it has to interact elastically with the medium. Then if the sampling of the probability P_{inel} in equation 4.11 is positive, then the Poisson distribution determines the number n of radiated gluons, and then this inelastic process is $2 \to 2 + n$.

Figure 4.6 shows a comparison of the elastic and inelastic energy loss of heavy quarks c and b. It shows that even though they are comparable at an early time, the inelastic scattering ($2 \to 2+n$) modify the energy of the original parton more than the elastic processes ($2 \to 2$). This is the expected result and shows the importance of inelastic processes. Also, a lighter quark c loses less energy than a heavier quark b. This is due to the mass effect, which is present in both processes.

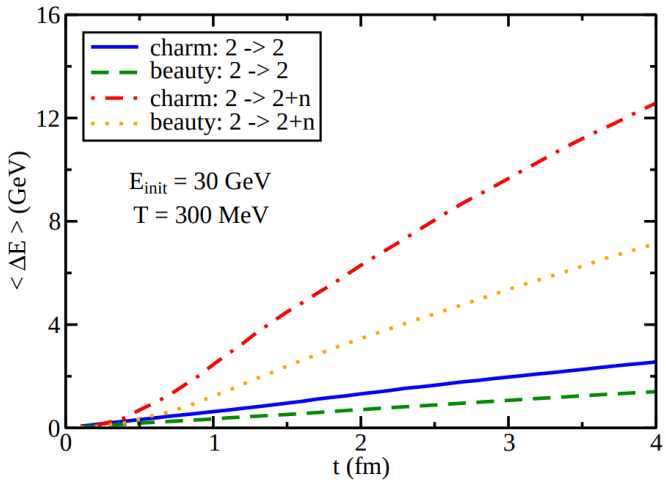

Figure 4.6: [299]

Medium partons that are called thermal partons can be ejected from the medium by jet partons, also called leading partons. When a thermal parton is scattered out of the medium, a hole is created. Leading and ejected partons are evolved according to the framework described above. Holes travels freely through the medium. Leading partons and ejected thermal partons are hadronised together and produce usual hadrons. Holes, however, are separated and in LBT they hadronise into hole hadrons. This represents energy that is missing from the medium. Treatment of those negative hadrons at the notional detector will be described in the Section 4.6.2. But there is one more step between jet evolution inside the medium and analysis of the observable hadrons and that is hadronisation.

4.5 Hadronisation

When final-state partons are collected from evolution frameworks, they have to be hadronised. This is the process in which the quarks are transformed into an observable hadronic shower. This is an nQCD process since the hadronisation energy scale is well below Λ_{QCD}. This is actually the least understood part of the hard process during the collision, and it has to be described by the models.

The first popular approach was the independent fragmentation model [300]. This model is based on independent fragmentations of the partons. The quark-antiquark pair is produced independently in vacuum, and one of the partons is paired with the original parton. This creates the so-called primary meson with the fraction of momentum x and the other parton carries the rest of the momenta (1-x). This is iterated until some cut-off point is reached.

Since the creation of the quark-antiquark pairs is independent, the probability that hadron h is created must be defined, This is incorporated in the fragmentation function $D_i^h(z)$ that appears in the factorised cross section of hadron h production

$$\frac{\mathrm{d}\sigma^{p+p\rightarrow h+X}}{\mathrm{d}p_T\mathrm{d}\eta} = \sum_{abc} f_{a/p} \star f_{b/p} \star \hat{\sigma}_{a+b\rightarrow c} \star D_c^h.$$

Fragmentation functions $D_i^h(z)$ are actually model dependent and also satisfy the DGLAP equations

$$Q\frac{\mathrm{d}D_c^h}{\mathrm{d}Q} = \sum_d P_{dc} \star D_d^h.$$

Independent fragmentation model was the starting point of the hadronisation description and it is no longer used.

One of the two most popular models nowadays is the cluster model [301]. It is based on the preconfinement flow of the colour charge. There are colour-neutral clusters that decay into known resonances and hadrons. This naturally brings up suppression of the heavier hadrons, baryons, and strangeness. This model is implemented in a well-known Monte Carlo generator `Herwig`. The illustration of the cluster model event can be seen in Figure 4.7.

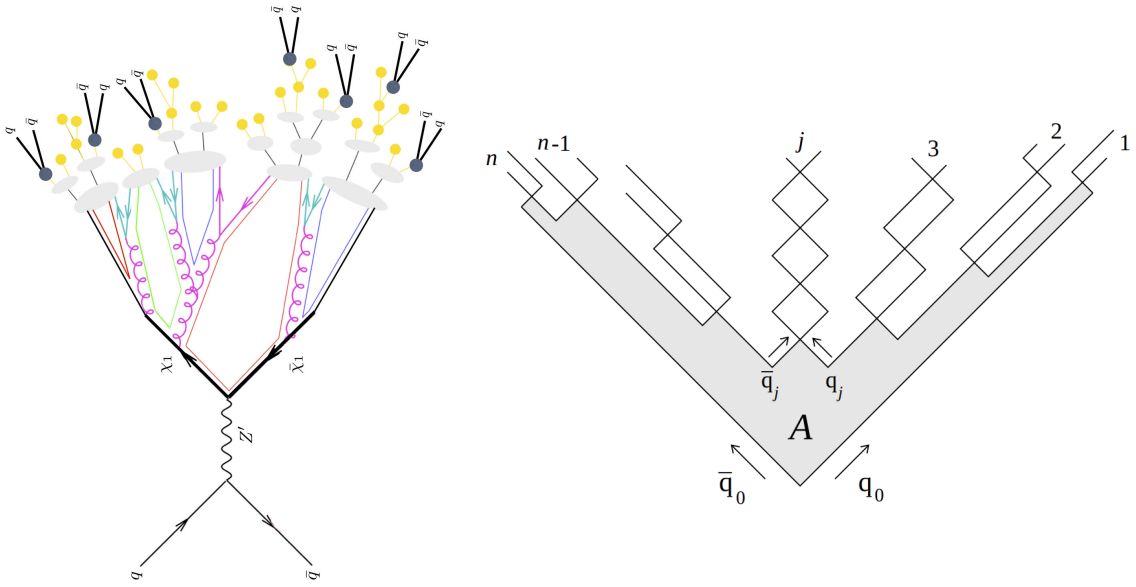

Figure 4.7: Illustration of cluster model (left) implemented in `Herwig` and Lund string model (right) implemented in `Pythia`. Left figure is from D. Zeppenfeld. Right figure retrieved from [302].

Another popular hadronisation model is the Lund string model [303] implemented in `Pythia` [6, 254]. It is based on the assumption of quark-antiquarks pairs $q\overline{q}$ being connected by a string, and when sufficient energy is exceeded, a quark-antiquark pair $q\overline{q}$ is created. `Pythia` and consequently the Lund string model is used in this thesis to hadronise hadrons. This is why it is described more closely later in this section. The illustration of the Lund string model event can be seen in the right panel of Figure 4.7.

In Table 4.1, there is a comparison between hadronisation models of `Pythia` and `Herwig`. You can see that the Lund string model is focused on a correct description of the energy-momentum picture with just a few parameters. However, it is not very predictive with regard to the flavour of the hadrons. The cluster model is much better for studying the flavour of the hadrons and jets. Both benefits for the respective models arise from their construction.

Table 4.1: Overview of strengths and weaknesses of the `Pythia` and `Herwig` Lund string and cluster hadronisation models, respectively.

Framework	`Pythia`	`Herwig`
Model	Lund string	Cluster
Energy-momentum picture	Predictive Powerful	Unpredictive Simple
Energy-momentum picture parameters	Few	Many
Flavour composition picture	Unpredictive Complicated	Adequate Simple
Flavour composition picture parameters	Many	Few

4.5.1 Lund string model hadronization

Lattice QCD calculations can fairly easily show colour confinement with the approximation as time-independent potential V of the quark-antiquark pair $q\overline{q}$, where the distance between quark q and antiquark $\overline{q}$ is R.

The Euclidian action $\mathcal{S}_E$ of the time-invariant potential reads

$$\mathcal{S}_E = \int \mathrm{d}t\, V(R) = T\, V(R).$$

Then the partition function is consequently

$$Z = \exp\left[-T\, V(R)\right].$$

External current of this static system can be described as $j_\mu(x)$, where $j_0(\vec{x}) = \delta(\vec{x} - \vec{R}) - \delta(\vec{x})$ and action that describes gluon interaction of static pair can be calculated as

$$\mathcal{S}_E = -ig \int \mathrm{d}^4 x j^\mu(x) A_\mu(x) = -ig \int dt \left[A_\tau(R) - A_\tau(0)\right]$$

Then with the assumption $T \gg R$, we can obtain the average value of the path-ordered links as

$$W(c) = \frac{\int \mathscr{D}U\, e^{-S_E[U]} \mathrm{Tr}\left[\prod_i U(c_i)\right]}{\int \mathscr{D}U\, e^{-S_E[U]}} = \exp\left(-\frac{RT}{a^2} \ln g_s^2\right),$$

and relate it to the original partition function

$$\exp\left[-T\, V(R)\right] = \exp\left[-\frac{RT}{a^2} \ln g_s^2\right],$$
$$V(R) = \frac{\ln g_s^2}{a^2} R = \kappa R,$$

where κ can be estimated [304] as $\kappa \approx (0.42\ \mathrm{GeV})^2 = 0 = 0.9\ \mathrm{GeVfm}^{-1}$

This result outlines two important observations. The first is the colour confinement for large distances. Since the potential increases with the distance, there is a point where the potential

energy will be greater than $2m_g$ and the quark-antiquark will be created. The second observation is that we can approximate the interaction between the quark q and the antiquark $\overline{q}$ on a large distance with a string potential $V(R) = \kappa r$.

The actual form of the nQCD potential was introduced by Yoichiro Nambu [56] as

$$V_{\mathrm{QCD}} = -\frac{4}{3}\frac{\alpha_s}{r} + \kappa r + ...,$$

where "..." are corrections like hyper-fine term, spin-orbit term, etc. Nambu actually proposed colour confinement [55] and this model could incorporate it. Furthermore, the Coulomb term (the first term on the right-hand side) is important for the inner structure of the hadrons. This potential was used to describe heavy non-relativistic quarkonia with the Schrödinger equation, and it had great success.

The QCD potential model is still widely used. Arguably, the most extensively used is to model hadronisation is the Lund string model [303]. If we consider only the lenear part of the nQCD potential model energy and momentum fulfils

$$\left|\frac{\mathrm{d}E}{\mathrm{d}z}\right| = \left|\frac{\mathrm{d}p_z}{\mathrm{d}z}\right| = \left|\frac{\mathrm{d}E}{\mathrm{d}t}\right| = \left|\frac{\mathrm{d}p_z}{\mathrm{d}t}\right| = \kappa.$$

This means that energy–momentum quantities can be read off from space–time.

String breaking mechanism should be responsible to reproduce the data as well as possible. This means common Gaussian p_{T} spectrum and suppression of heavy quarks

$$u\bar{u} : d\bar{d} : s\bar{s} : c\bar{c} \approx 1 : 1 : 0.3 : 10^{-11}.$$

This is fulfilled with the production probability using the WKB approximation

$$\frac{1}{\kappa}\frac{\mathrm{d}\mathscr{P}_q}{\mathrm{d}^2 p_\perp} \propto \exp\left(-\frac{\pi m_{\perp q}^2}{\kappa}\right) = \exp\left(-\frac{\pi p_\perp^2}{\kappa}\right)\exp\left(-\frac{\pi m_q^2}{\kappa}\right).$$

Baryons are produced as if diquarks would break break inside wrong-colour region. This gives a modified fragmentation function as

$$f(z) \propto \frac{1}{z} z^{a_\alpha}\left(\frac{1-z}{z}\right)^{a_\beta}\exp\left(-\frac{b m_\perp^2}{z}\right).$$

Finally, gluons are treated as a kink on the string. Model states the ratio of gluons to quarks and it is taken as 2 since

$$\frac{N_c}{C_F} = \frac{9}{4} \xrightarrow{N_c \to +\infty} 2.$$

This treatment reproduces the behaviour of gluon jets as they have more hadrons with a smaller momentum and wider angular distribution. There are no additional parameters for the gluon jets, but there are 10-20 parametes in this model. Lund string model has no predictive power regarding understanding the effects of hadron masses and, as was already mentioned, it does not describe the flavour of the hadrons well. However, those are no problems for the research of this thesis. Lund string model implemented in `Pythia` [6, 254] can hadronise partons obtained from `LBT` [8, 295, 296, 297] and `MATTER` [7, 286] and produce observable hadrons. Hadrons can be later analysed with sophisticated algorithms to produce jet observables.

4.6 Jet reconstruction

From the beginning of jet physics, it was necessary to analyse the data obtained from the detectors to obtain information about the original parton and essentially about the hard vertex for elementary collisions. Accessing a vertex like that would mean a direct connection between measurements and theory, but jets would have to be reconstructed as precisely as possible. This is essentially not possible even for the simplest collisions like $e^- e^+ \rightarrow q\overline{q}$. The reason is colour confinement and the fact that we do not observe individual partons but hadronic jets. Since one parton with a colour charge cannot produce a colour neutral hadronic jet, it is not possible to make this perfect connection between the detector level and the hard parton (see Figure 4.8). This makes jet reconstruction not universal procedure.

There are several algorithms that are used to reconstruct jets, subtract background, and inspect jet substructure. Most of them can be classified into two families: cone algorithms and sequential clustering algorithms. The jet algorithms have a parameter R that dictates the size of the shower in $(y-\phi)$ or alternatively $(\eta-\phi)$ space. This parameter is called the jet radius R. The name originates from earlier simple algorithms that considered a jet a cone with radius $R = \sqrt{\eta^2_{\text{jet}} + \phi^2_{\text{jet}}}$ that meets some criteria in the form of cuts. This was called a fixed cone approach.

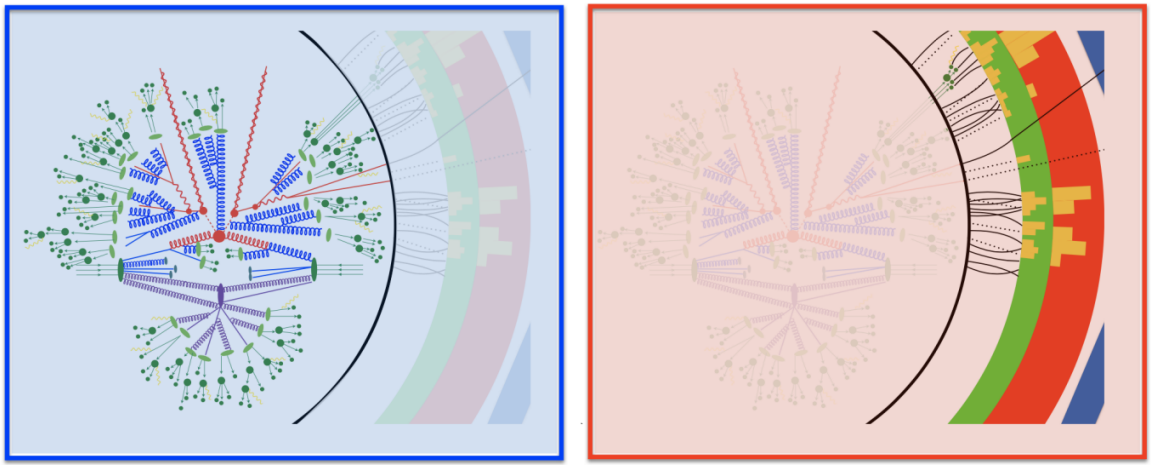

Figure 4.8: Illustration of the difference between parton level and detector level jet. Figure credit to Ben Nachman.

Those simple algorithms usually had a few issues. They were not infrared (IR) or collinear safe. Those two are very important properties. IR safety essentially means that the jet remains unchanged if soft radiation is added. Similarly, collinear safety stands for the insensitivity of reconstruction to collinear splitting when collinear splitting occurs. Collectively, those conditions are referred to as IRC safety.

IRC safety is very important. In Section 4.3 it was mentioned that collinear-gluon radiation causes divergency of the cross section in equation 4.8. This divergency is cancelled when the vertex correction loop is included in pQCD calculations. If collinar splitting would modify the jets, divergences would not cancel and it would lead to infinities in cross section obtained from pQCD. Both soft radiation and collinear splitting cause divergence and are present in the pQCD

and nQCD stages of jet evolution. Furthermore, the effects of soft radiation and collinear splitting are hard to predict [305, 306]. This is a good motivation to use the IRC safe algorithm for jet reconstruction.

Cone algorithms such as the progressive removal IC-PR [307] or the split-merge IC-SM [308] iterative cone algorithms were previously used to reconstruct jets. They were easy to implement, and they were preferred by experimentalists. However, IC-PR is collinear unsafe and IC-SM is not IR save. This issue was solved for cone algorithms using the seedless cone algorithm SISCone [309].

Cone algorithms had easier implementation and seemed to be faster than their counterpart group sequential clustering algorithms. However, this changed when they were properly implemented in `FastJet` [310] and rapidly became standard algorithms that are used for inclusive reconstruction, background subtraction, and jet substructure inspection. Sequential clustering algorithms are based on the assumption that particles in the jet will have a similar transverse momentum p_{T} and will be relatively close to each other in the $(y-\phi)$ plane. The framework is built upon $\frac{1}{2}(n+1)^2$ distance variables for the event with n hadrons. The first is the particle i-beam distance

$$d_{iB} = p_{\mathrm{T}i}^{a},$$

where a is free parameter and defines the specific algorithms that will be introduced below. The second distance variable is distance between two particles i-j

$$d_{ij} = \min(p_{\mathrm{T}i}^{a}, p_{\mathrm{T}j}^{a})\frac{R_{ij}^2}{R},$$

where $R_{ij} = \sqrt{(y_i - y_j)^2 + (\phi_i - \phi_j)^2}$. It is easy to see that the distance variables d_{iB} and d_{ij} do not denote the space-time distance but rather some sort of distance in the $(p_{\mathrm{T}}, y, \phi)$-space. That is exactly what we would expect since the assumption of the sequential clustering algorithms is the closeness of hadrons in this 3D space. The parameterisation of what is close provides parameters $a = 2, -2, 0, ...$ and $R = \sqrt{y_{\mathrm{jet}}^2 + \phi_{\mathrm{jet}}^2}$.

The algorithm iteratively calculates minima from the $\frac{1}{2}(n+1)^2$ set $\{d_{ij}, d_{iB}\}$. If d_{ij} is determined as the minimum, the four-momenta of particles i and j combine. Then there are $n-1$ particles and affected elements of the set $\{d_{ij}, d_{iB}\}$ are recalculated for a new "$i+j$" particle. If d_{iB} is the minimum, then the particle i is considered as a jet and removed from the set. The particle i can be composed of several physical hadrons from previous iterations. This process is repeated until there are no particles in the set.

Sequential clustering algorithms do not have to resemble the cone shape, and this applies to SISCone as well. This can be seen in Figure 4.9. However, for historical reasons, R is still referred to as cone radius.

All sequential clustering algorithms are IRC safe and have wide applications in jet physics. There are three choices of power parameter a that are preferred in the field. The best option for inclusive jet reconstruction is $a = -2$ and is called anti-k_{T} [311, 310].

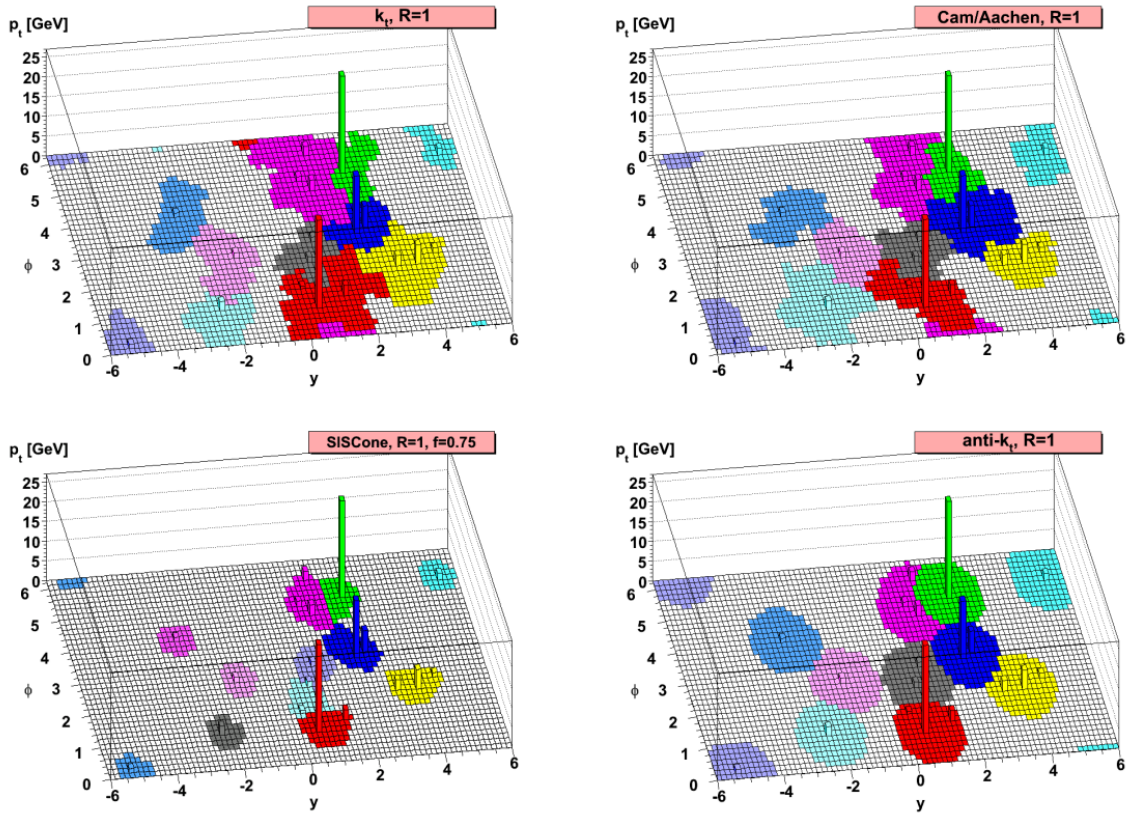

Figure 4.9: A sample parton-level event reconstructed by three sequential clustering algorithms (k_{T} [312], Cambridge-Aachen [313], anti-k_{T} [311]) and one cone algorithm (SISCone [309]). Retrieved from [311].

4.6.1 Anti-k_{T} algorithm

Sequential clustering algorithms with choice $a = -2$ particle distances take form as

$$d_{ij} = \min\left(\frac{1}{p_{\mathrm{T}i}^2}, \frac{1}{p_{\mathrm{T}j}^2}\right)\frac{R_{ij}^2}{R^2},$$

and

$$d_{iB} = \frac{1}{p_{\mathrm{T}i}^2}.$$

This algorithm is called anti-k_{T} [311, 310] and favours the clustering of hard particles first. This arises from the minimum function in d_{ij}. This means that jets grow from the hard centre outwards. This is very effective for inclusive jet reconstruction. This is a collinear safe growth as a consequence of the involvement of energy and angle in its distance.

The area of the jet A_{jet} fluctuates only slightly for anti-k_{T}. This is shown in figure 4.9, where event reconstructed with the anti-k_{T} has the most circular shape.

Reconstruction with anti-k_{T} is not sensitive to pile-ups or underlying events. This makes it well suited for inclusive jet reconstruction.

4.6.2 k_{T} background subtraction and hole treatment

In case of $e^- e^+ \to \text{jet} + X$ or $pp \to \text{jet} + X$, it is fairly straightforward to reconstruct jets. The jet reconstruction algorithm is used and cuts are applied, such as a minimum transverse momentum of the jet transverse momentum $p_{\mathrm{T}}^{\mathrm{jet}}$, a transverse momentum of the leading particle $p_{\mathrm{T}}^{\mathrm{lead}}$, or a rapidity cut $|y| < y_{\mathrm{range}} - R$. For heavy-ion collisions, the situation is much more complicated. The highly fluctuating background can be comparable to the signal. Figure 4.10 shows Au+Au event at $\sqrt{s_{\mathrm{NN}}} = 200$ GeV.

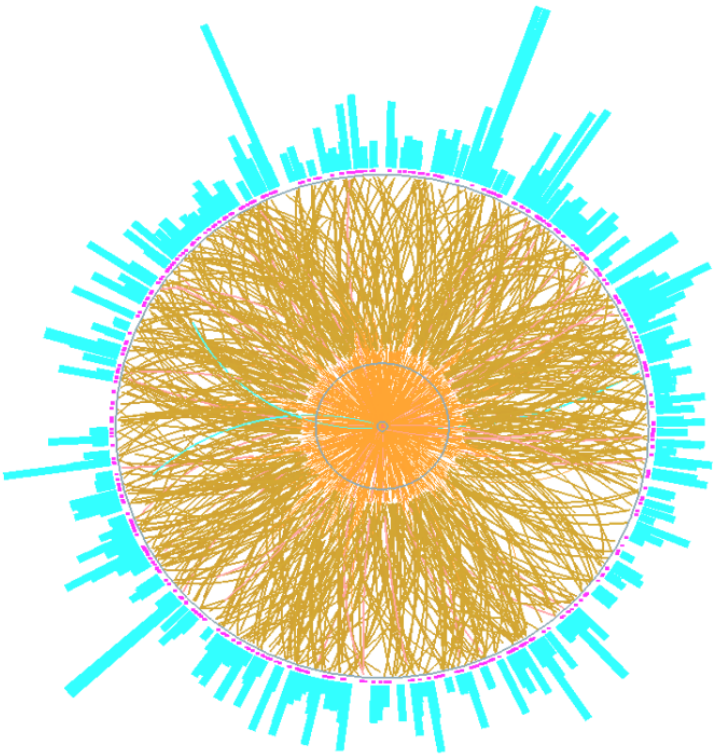

Figure 4.10: Jet event measured in experiment STAR. Tracks from time projection chamber are shown with light brown colour and calorimeter towers are represented by light blue rectangles. Figure credit to Alexander Schmah.

Looking at Figure 4.10 with the naked eye, there are some indications of jets. However, it is also visible that the background is a large portion of the data. We can use anti-k_{T} algorithm to reconstruct jets, but since it is only slightly susceptible to background, the signal will be polluted.

It is possible to use k_{T} algorithm [312, 310] to subtract unwanted background [314, 315, 316, 317]. k_{T} algorithm is the sequential clustering algorithms with $a = 2$. Particle distances take the form of

$$d_{ij} = \min\left(p_{\mathrm{T}i}^2, p_{\mathrm{T}j}^2\right) \frac{R_{ij}^2}{R^2},$$

and

$$d_{iB} = p_{\mathrm{T}i}^2.$$

Since there is a positive power in the minimum function, it is clear that the k_{T} algorithm clusters the soft particle first. This is actually a reverse direction, as is the evolution of the jet. This fact makes the k_{T} reconstruction compatible with the jet evolution, as particles should be clustered in opposite direction to the evolution.

First, the k_{T} algorithm [312, 310] is used to cluster particles in the event and find jets with uncorrected momentum $p_{T,\,\mathrm{jet}}^{\mathrm{raw},i}$. Furthermore, the ghost particle algorithm [310] will determine the area of the jet A. The event-by-event background density is then measured as the median of the jet momentum density

$$\rho = \mathrm{median}\left\{ \frac{p_{\mathrm{T,\,jet}}^{\mathrm{raw},j}}{A_{\mathrm{jet}}^{j}} \right\},$$

where 1-2 hardest jets are excluded from the median calculation. The number of excluded jets depends on the centrality class. Then, the particles are clustered by anti-k_{T} [311, 310] and the ghost particle algorithm [310] will determine the area of the jet A again, this time for anti-k_{T} jets. The background density is then subtracted as

$$p_{\mathrm{T,jet}} = p_{\mathrm{T,jet}}^{\mathrm{raw}} - \rho A.$$

This is a necessary procedure in the experiment. It is easier to measure very hard jets ($p_{\mathrm{T,jet}} \gtrsim 100$ GeV) in ATLAS or CMS than to measure softer jets in ALICE or even STAR. The reason is a large background-to-signal ratio with large event-to-event fluctuations. In simulations, we can almost omit background that originates mainly from the bulk medium. However, there are hole partons that hadronised into hole hadrons. They originate from a jet-medium interaction, where a thermal parton was knocked out of the medium. This means that there is less energy inside the medium. This would be visible in the absence of the energey in the background that would be subtracted. Hole hadrons with negative energy can substitute for this. The holes are subtracted from the final shower as

$$p_{\mathrm{jet}}^{\mu} = p_{\mathrm{shower}}^{\mu} - \sum_{\substack{i \in \mathrm{holes} \\ \Delta r_i < R}} p_i^{\mu},$$

where shower is composed of jet and thermal partons that hadronised into ordinary hadrons. In case of exclusive observables, where we consider the distribution of jet constituents, holes are taken with weight -1.

Chapter 5

Results of High Energy Collision Simulations

Multistage simulation of the heavy-ion collision was outlined in the two previous chapters. Chapter 3 introduced the concept of medium modelling by relativistic hydrodynamics. The first two stages simulated the initial profile that was plugged into the hydrodynamic code, where the evolution of the medium is obtained.

Chapter 4 described how jets can be simulated. Starting with the initial-state partons and evolving them according to three theoretical frameworks: vacuum, high-virtuality in-medium and low-virtuality in-medium evolution.

This procedure can produce many soft and hard hadronic observables. An example of representative observables could be a transverse momentum p_{T} distribution of identified hadrons for the soft sector ($p_{\mathrm{T}} < 5$ GeV) or jet nuclear modification factor $R_{\mathrm{AA}}^{\mathrm{jet}}\left(p_{\mathrm{T}}^{\mathrm{jet}}\right)$ in the hard sector $\left(p_{\mathrm{T}}^{\mathrm{jet}} > 60 \text{ GeV}\right)$.

Except for the general interest in soft observables, they provide control over accuracy medium simulations. Measurements of medium size (i.e., femtoscopy) or medium temperature (i.e., quarkonia) directly brings uncertainties that are too large to distinguish a few percent variations that are caused by bulk and shear viscosity, for example. If bulk and shear viscosity reproduce soft hadronic observables well enough, it is possible that the description of the medium is close to reality and we do not have to left with medium parameterisations.

Before hadronic observables are introduced in Section 5.2 (soft) and Section 5.3 (hard) , we will investigate the space-time evolution of the medium.

5.1 Medium simulation results

Medium evolution is simulated with three-stage chain. The first stage is the non-dynamical model TRENTothat produces an initial entropy profile at the proper time τ_0. The dynamic IP-Glasma model predicts a high initial transverse flow velocity profile [318, 319]. However, the validity of the assumptions made into the IP-Glasma model is not completely proven.

However, it was shown that the initial transverse flow velocity could increase the quality of the reproduced hadronic observables [320]. It is possible to employ a simple approach - free-streaming, where the initial state profile obtained from TRENTo is evolved according to the collision-free Boltzmann equations. The idea behind free-streaming is that before QGP is formed, the medium evolves with a much longer mean free path. This can also be handled with hydro ($\tau_\pi \to +\infty$) or RTA [321]. There is no wide consensus on how preequilibrium should be handled. Free-streaming is a good approximation but there is some space for improvement in future work.

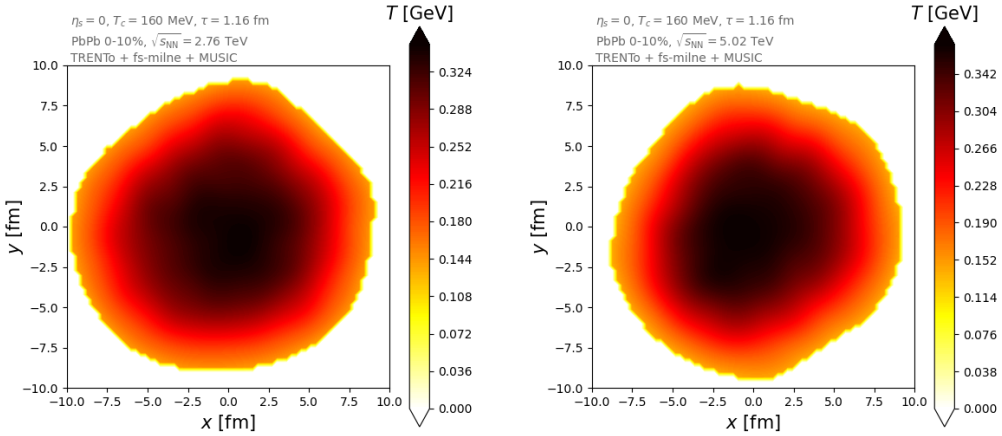

Figure 5.1: Initial temperature profile at switching proper time $\tau_s = 1.16$ for 0-10% PbPb collisions at $\sqrt{s_{\mathrm{NN}}} = 2.67$ TeV (left) and $\sqrt{s_{\mathrm{NN}}} = 5.02$ TeV (right) obtained from TRENTo [1] + `freestream-milne` [2] + `MUSIC` [3] implemented in `Jetscape` [9].

Preequilibrium is important for the medium simulation with respect to jet observables. It affects medium evolution, temperature, and frezze-out hypersurface. However, it can also delay medium formation (about $\tau_s \sim 1$ fm for LHC energies [173]). However, this is $5-10\%$ of the evolution time and if jet partons evolve freely too, their energy loss can be shifted.

Further investigation on this topic will be necessary. For now, we can assume that free-streaming indirectly affects simulated jet quenching.

Figure 5.1 shows the initial temperature profile in the transverse plane at $\tau = \tau_s$ that is obtained essentially from TRENTo and `freestream-milne` and is plugged into the $s95p$-v1 EoS [208] implemented in `MUSIC` [3, 200].

The left-hand side of Figure 5.1 shows the temperature profile for central PbPb $\sqrt{s_{\mathrm{NN}}} = 2.67$ TeV. The right-hand side of the Figure 5.1 represents same collision system at $\sqrt{s_{\mathrm{NN}}} = 2.67$ TeV.

You can see that the contour scales differently for the temperature profiles T in Figure 5.1. The highest value on the temperature T axis corresponds to the highest value in the temperature profile. You can see that even though the collision energy is ~ 1.8 times higher, there is only a few MeV difference in the highest initial temperature. This will also be visible in the average

temperature introduced later, and this fact will be also important for a later discussion.

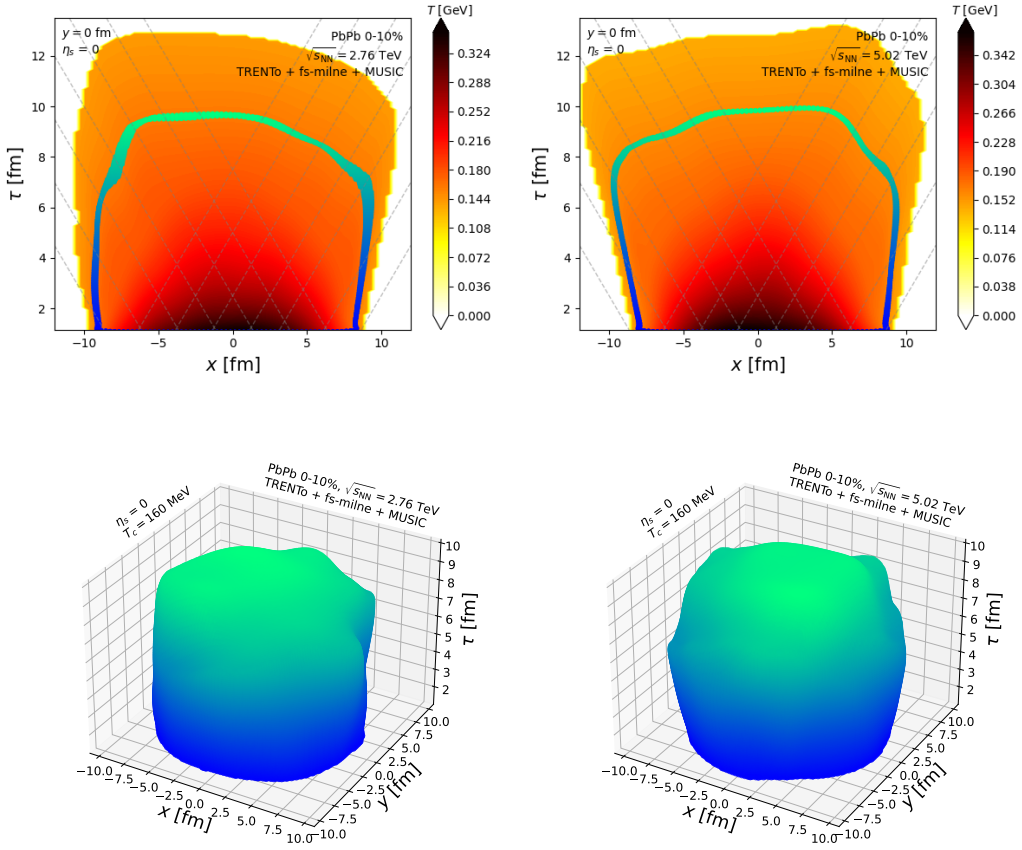

Figure 5.2: Temperature evolution (upper plots) and freeze-out hypersurface evolution (lower plots) for 0-10% PbPb collisions at $\sqrt{s_{\mathrm{NN}}} = 2.67$ TeV (left) and $\sqrt{s_{\mathrm{NN}}} = 5.02$ TeV (right) obtained from TRENTo [1] + `freestream-milne` [2] + `MUSIC` [3] implemented in `Jetscape` [9].

Next, we examine the evolution of the medium according to the Israel-Steward hydrodynamic equations and $s95p$-v1 EoS [208]. The evolution of temperature and freeze-out hyperfurface is shown in Figure 5.2. The medium created during the collision at $\sqrt{s_{\mathrm{NN}}} = 2.67$ TeV is slightly smaller in transverse size and has a very similar lifespan. Let us now proceed to the discussion of the medium evolution.

The choice of EoS is very important. Different EoS can easily produce a difference of ~ 1 fm in femtoscopy radii [322]. EoS used in this thesis, $s95p$-v1 is the default EoS in `MUSIC` [3]. Relatively recently, the authors of $s95p$-v1 EoS produced new EoS parameterisations $s83s_{18}$ and $s88h_{18}$ [224], where the peak of the trace anomaly of $s95p$ is approximately 1.5 and 1.3 times larger compared to $s83s_{18}$ and $s88h_{18}$, respectively.

Furthermore, sice EoS relates pressure P and energy density ϵ, it also has a great impact on the temperature of the medium. The indirect impact of EoS on hard observables was not investigated in depth in this thesis, and it is important to note that $s95p$ proved to be reliable EoS.

However, this part of the heavy-ion collision can be further investigated and improved in future work.

Next are the transport coefficients. Since second-order transport coefficients are not well constrained, they will not be part of this discussion. However, bulk and shear viscosity are highly investigated. Inclusion of both shear and bulk viscosity arguably improved hydrodynamic calculations from qualitative to quantitative in many aspects.

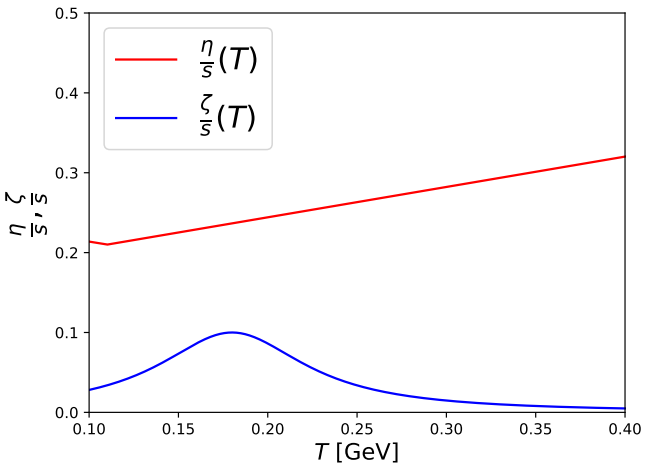

Figure 5.3: Temperature-dependent parameterisations of the bulk viscosity to entropy density rario $\frac{\zeta}{s}(T)$ (blue line) and the shear viscosity to entropy density rario $\frac{\eta}{s}(T)$ (red line) used in this thesis.

Bulk viscosity plays an important role in terms of the size and lafespan of the medium. Modern large bulk viscosity parameterisations [232, 236, 237] have been shown [241] to have a great impact on size at a later proper time. The medium without bulk viscosity can be up to 20% smaller at the time of the peak of the freeze-out hypersurface radius compared to the simulation with large bulk viscosity parameterisations [241]. In addition, the useful life of the medium can be shorter up to 10% [241]. This implies that partons can spend more time in the medium, and quenching of the jet could be larger. This aspect will also require further investigation. The bulk viscosity parameterisation used in this thesis is shown in Figure 5.3

The shear viscosity affects the average medium temperature up to ~ 5 MeV at intermediate times [192]. This may seem insignificant, but keep in mind that the difference of the higest temperature between $\sqrt{s_{\mathrm{NN}}} = 2.67$ TeV and $\sqrt{s_{\mathrm{NN}}} = 5.02$ TeV is only 18 MeV. However, later, it will be shown that those temperature corrections probably do not play a significant role.

Shear viscosity also affects the homogeneity and flow velocity of the medium. This might be insignificant for current `Jetscape` framework but very recent models showed jet-broadening effects from inhomogenity and flow velocity effects. Shear viscosity parameterisation used in this thesis is shown in Figure 5.3

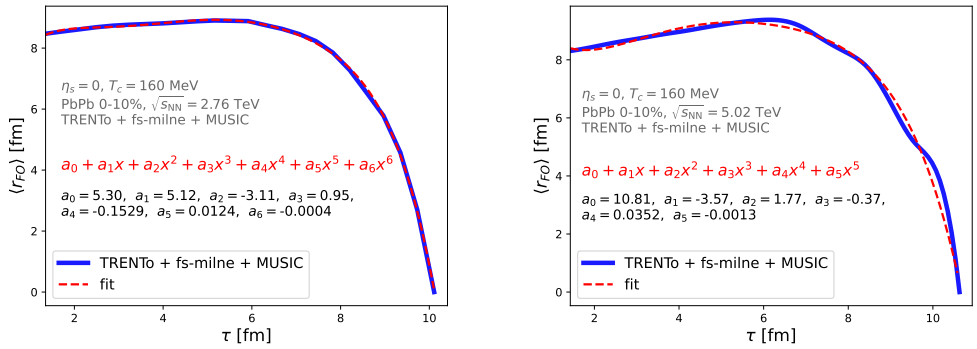

Figure 5.4: Average freeze-out hyperspace and its polynomial parametrisation for 0-10% PbPb collisions at $\sqrt{s_{\mathrm{NN}}} = 2.67$ TeV (left) and $\sqrt{s_{\mathrm{NN}}} = 5.02$ TeV (right) obtained from TRENTo [1] + `freestream-milne` [2] + `MUSIC` [3] implemented in `Jetscape` [9].

For later use, it is necessary to parameterise the average freeze-out hypersurface in Figure 5.4. Parameterisation is made with the sixth and fifth order of polynomial fit for $\sqrt{s_{\mathrm{NN}}} = 2.67$ TeV (left) and $\sqrt{s_{\mathrm{NN}}} = 5.02$ TeV respectively. More sophisticated functions were tried to properly fit the freeze-out hypersurface, but simple polynomial fit was much more reliable.

5.2 Simulated soft observables

It was already mentioned in the Introduction to this chapter that the soft observables can provide us with information that leads to constraints on models. In this section there are a few observables that show general agreement with the experimental data.

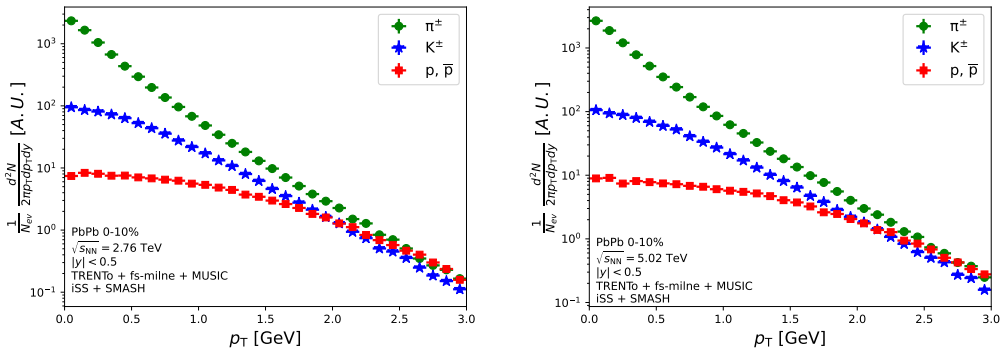

Figure 5.5: Transverse momentum p_{T} distribution of protons $p, \overline{p}$, kaons $K^{\pm}$, and pions $\pi^{\pm}$ for 0-10% PbPb collisions at $\sqrt{s_{\mathrm{NN}}} = 2.67$ TeV (left) and $\sqrt{s_{\mathrm{NN}}} = 5.02$ TeV (right) obtained from TRENTo [1] + `freestream-milne` [2] + `MUSIC` [3] implemented in `Jetscape` [9].

Hadronisation was obtained from `iSS` [4] and `SMASH` [5]. The reason for the two-stage conversion from fluid to obtain the final hadronic shower is that hadrons can evolve further after they are sampled into the Cooper-Frye formula in equation (3.33). Several thousand hadrons can

rescatter with each other, and resonances naturally decay. This is actually an important part of the simulation in order to obtain the correct final hadronic spectra.

The first observale is shown in Figure 5.5 and it is transverse momentum p_T distribution of $p, \overline{p}$, kaons $K^{\pm}$, and pions $\pi^{\pm}$, where the shape and overall order correspond to the experimental measurements [183, 323, 324].

The second observable is the mid-rapidity multiplicity of several identified hadrons shown in Figure 5.6. Here, we can also see a comparison with the experimental data [325] measured in the ALICE experiment. One can notice the inconsistency with the Λ and $\overline{\Lambda}$ baryons. This is probably due to contributions from Σ and Σ^*.

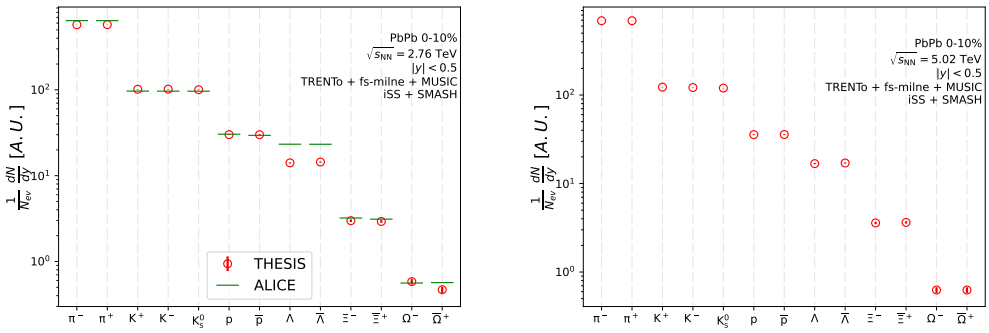

Figure 5.6: Mid rapidity multiplicity of several identified hadrons for 0-10% PbPb collisions at $\sqrt{s_{\mathrm{NN}}}$ = 2.67 TeV (left, red circles) and $\sqrt{s_{\mathrm{NN}}}$ = 5.02 TeV (right) obtained from TRENTo [1] + `freestream-milne` [2] + `MUSIC` [3] implemented in `Jetscape` [9]. ALICE measurements of mid rapidity multiplicity for 0-10% PbPb collisions at $\sqrt{s_{\mathrm{NN}}}$ = 2.67 TeV (left, green bars)

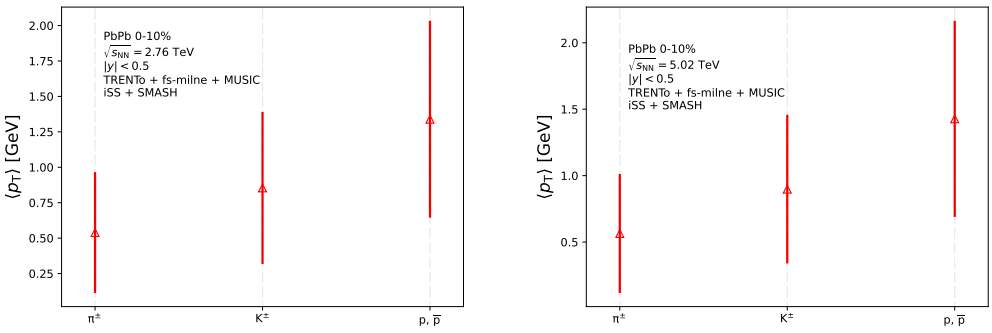

Figure 5.7: Average transverse momentum $\langle p_T \rangle$ of protons $p, \overline{p}$, kaons $K^{\pm}$, and pions $\pi^{\pm}$ for 0-10% PbPb collisions at $\sqrt{s_{\mathrm{NN}}}$ = 2.67 TeV (left) and $\sqrt{s_{\mathrm{NN}}}$ = 5.02 TeV (right) obtained from TRENTo [1] + `freestream-milne` [2] + `MUSIC` [3]implemented in `Jetscape` [9].

The last hadronic observable is the average transverse momentum $\langle p_T \rangle$ of protons $p, \overline{p}$, kaons

$K^{\pm}$, and pions $\pi^{\pm}$. This plot fairly well represents the magnitude of a large fluctuating soft background. It is important to study the background of hard observables so that proper medium subtraction can be performed.

5.3 Jet simulation results

Chapter 4 described how partons evolve into fully reconstructed jets at the detector level. This section presents the simulation results of reconstructed observables, such as the nuclear modification factor $R_{\mathrm{AA}}^{\mathrm{jet}}\left(p_{\mathrm{T}}^{\mathrm{jet}}\right)$.

The first step of the jet simulation is the initial state. There is a multi-parton interaction (MPI) at the beggining of the collision. The result is a several (≥ 2) initial-state parton. Parton-level jets are connected to hadron-level jets by using the reconstruction procedure on both. In other words, we can identify these multiple partons as unquenched jets based on their transverse momentum p_{T}, rapidity y, and azimuthal angle ϕ_p with the help of anti-k_{T} [311] implemented in `FastJet` [310].

It would not be wise to consider each parton as an individual jet since MPI can include soft-gluon emission, and all arise from a single interaction $2 \to n$. This is the benefit of initial simulation that we can have one hard vertex for a single event. However, we cannot treat them as back-to-back jets either, since it is possible that the event will be a three-jet event that was introduced in Section 4.3. Furthermore, the sum over their transverse momentum should be zero. The reasonable way to treat the initial state of the jets is through the mentioned reconstruction procedure.

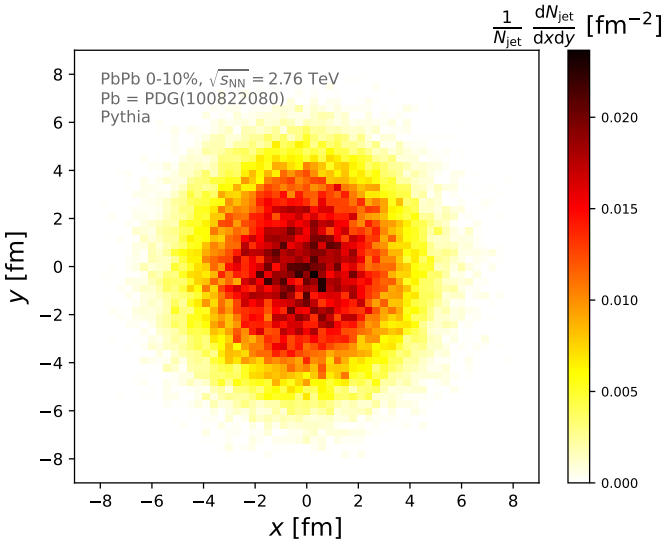

Figure 5.8: Initial position of jets in the transverse plane for 0-10% PbPb collisions at $\sqrt{s_{\mathrm{NN}}}$ = 2.67 TeV obtained from `Pythia` [6] implemented in `Jetscape` [9] and reconstructed wit anti-k_{T} algorithm [311] implemented in `FastJet` [310].

Figure 5.8 shows the spatial distribution of the jets in the transverse plane. It can be seen that it is well correlated with the temperature distribution in Figure 5.1. At first glance, it would seem

that all partons experience medium to at least some extent. However, in the case of LHC energies, the collision is almost instant compared to the time scale of the simulation. The reason is the Lorentz contraction of the nuclei.

Hard collisions occur at the beginning of the collision and start to evolve instantly. On the other hand, there is an equilibrium proper time that is connected with the formation of the medium. This means that some jets should be able to escape the medium before the formation of QGP.

Since we consider the free-streaming preequilibrium for the energy-momentum tensor medium $T^{\mu\nu}$, it is reasonable to assume that hard partons can also evolve freely. In case of partonic evolution, free means vacuum evolution.

If we go back to the medium simulation, we obtained a freeze-out hypersurface evolution in Figure 5.2. Later, we parameterised its average with a polynomial fit in Figure 5.4. We can simplify the jet as a single light-like object, and we can calculate the proper time τ_{med} distribution of how approximately long the jet evolved in the medium. The jet starts to evolve from the start of the collision, but experiences a medium from the switching proper time $\tau_s = 1.16$ fm. The τ_{med} distribution for the 0-10% PbPb collisions is shown in Figure 5.9.

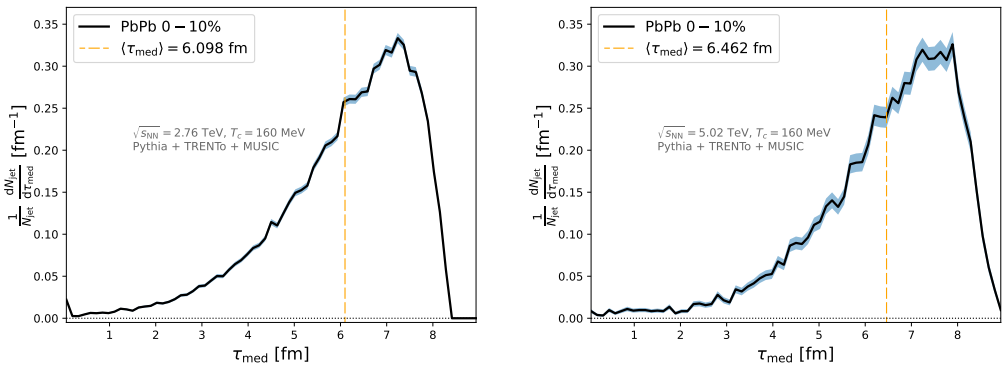

Figure 5.9: Initial position of jets in the transverse plane for 0-10% PbPb collisions at $\sqrt{s_{\text{NN}}} = 2.67$ TeV (left) and $\sqrt{s_{\text{NN}}} = 5.02$ TeV (right) obtained from TRENTo [1] + `freestream-milne` [2] + `MUSIC` [3] + `Pythia` [6] implemented in `Jetscape` [9]. Orange dashed line denotes the averege of the distribution.

The distribution of τ_{med} can show us the average time the jet travels through the medium. This can be used to simulate the so-called brick simulation, where the medium evolution is not considered.

5.3.1 Jet evolution inside the brick simulation

Brick medium is the medium with simplified evolution (i.e. Bjorken expansion) or with no evolution at all. We consider the medium to be constant in temperature and size. The size of the brick medium can be obtained from Figure 5.9 as $\langle\tau_{\text{med}}\rangle$ since it is reasonable to assume massless partons.

The temperature of the constant brick medium can be obtained from hydrodynamic simulation. The benefit of this is that the hydrodynamic simulation has to be performed only once.

The disadvantage of this is that it is a very strong approximation.

Figure 5.10 shows the average temperature of the medium in the transverse plane and the integrated average of this as

$$\langle T^{\mathrm{med}}_{\mathrm{ave}} \rangle(\tau) = \frac{\int_{\tau}^{\tau_0} T^{\mathrm{med}}_{\mathrm{ave}}(\tau')\mathrm{d}\tau'}{\tau}.$$

When we evaluate this average temperature at average medium time as $\langle T^{\mathrm{med}}_{\mathrm{ave}} \rangle \left(\langle \tau_{\mathrm{med}} \rangle \right)$, we obtain the brick temperature T_{brick}. We can see that the difference of T_{brick} between $\sqrt{s_{\mathrm{NN}}} = 2.67$ TeV and $\sqrt{s_{\mathrm{NN}}} = 5.02$ TeV is actually comparable to what shear viscosity introduces to the evolution of the medium. This means that we can also study these small temperatuche changes and how they affect the jet observables.

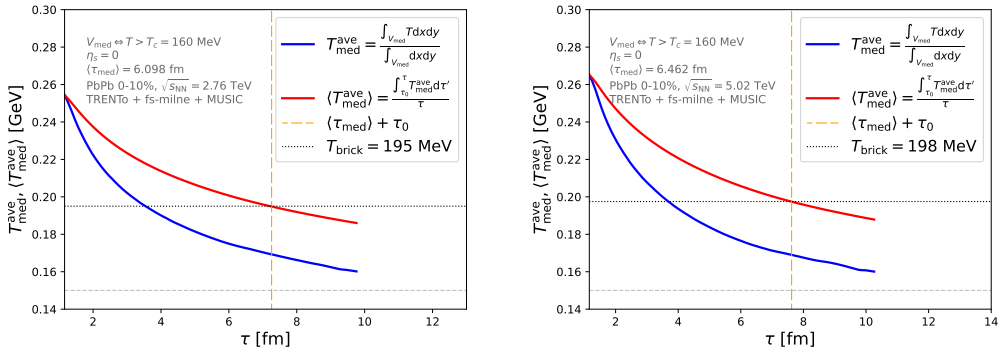

Figure 5.10: Temperature T averaged over transverse plane (blue line), T averaged over transverse plane and proper time (red line), and estimated brick medium temperature T_{brick} (black dotted line) for 0-10% PbPb collisions at $\sqrt{s_{\mathrm{NN}}} = 2.67$ TeV (left) and $\sqrt{s_{\mathrm{NN}}} = 5.02$ TeV (right) obtained from TRENTo [1] + `freestream-milne` [2] + `MUSIC` [3]implemented in `Jetscape` [9].

Finally, we can simulate the parton without hydrodynamics in homogeneous medium with constant temperature and size. We sample partons in the "centre" of this brick with pythia MPI initial state. This initial state is also obtained from the nPDFs [276], and we perform a full parton cascade evolution with `MATTER` [7] for high-virtuality ($Q \geq 2$ GeV) partons and `LBT` [8] for low-virtuality ($Q < 2$ GeV) partons.

After evolution reaches the time $\langle \tau_{\mathrm{med}} \rangle$, partons are considered on-shell and final. Then hadronisation is performed by `Pythia` [6]. The hadrons are reconstructed with anti-k_{T} algorithm [311, 310] with $R = 0.4$. Holes from the jet-medium scattering are treated as particles with negative energy.

This procedure simulates the detector-level jets. In the experiment, there is some rapidity reagion that is covered by the detector. It is also important to introduce some cuts for the simulation. First, it has to be compatible with the experimental data. Second, the applicability of hydrodynamics decreases with the increasing rapidity.

It is now possible to obtain jet observables. First of all, we can calculate transverse momen-

tum spectra

$$\frac{1}{N_{\text{ev}}} \frac{d^2 N_{\text{jet}}}{2\pi p_{\text{T}}^{\text{jet}} dp_{\text{T}}^{\text{jet}} dy}.$$

This is inclusive observable. This means that the jet is treated as a single object. We can compare this to the collisions of pp obtained from `Pythia` [6] + `MATTER` [7] and obtain the nuclear modification factor

$$R_{\text{AA}}^{\text{jet}} = \frac{\frac{\mathrm{d}^2 N_{\text{AA}}^{\text{jet}}}{\mathrm{d}y\ \mathrm{d}p_{\text{T}}^{\text{jet}}}}{\langle T_{\text{AA}} \rangle \frac{\mathrm{d}^2 \sigma_{\text{pp}}^{\text{INEL}}}{\mathrm{d}y\ \mathrm{d}p_{\text{T}}^{\text{jet}}}}$$

Figure 5.11 shows the jet nuclear modification factor $R_{\text{AA}}^{\text{jet}}$. Although this overestimates the value of $R_{\text{AA}}^{\text{jet}}$, it could be with an increase in the value of the free parameter α_s (see Appendix C). Furthermore, we can see that the slight temperature difference caused by different $\sqrt{s_{\text{NN}}}$ did not affect $R_{\text{AA}}^{\text{jet}}$ above the statistical uncertainty. This indicates that temperature corrections caused by shear viscosity would have a similar effect. However, jet-broadening effects from inhomogenity and flow velocity effects are still unkown.

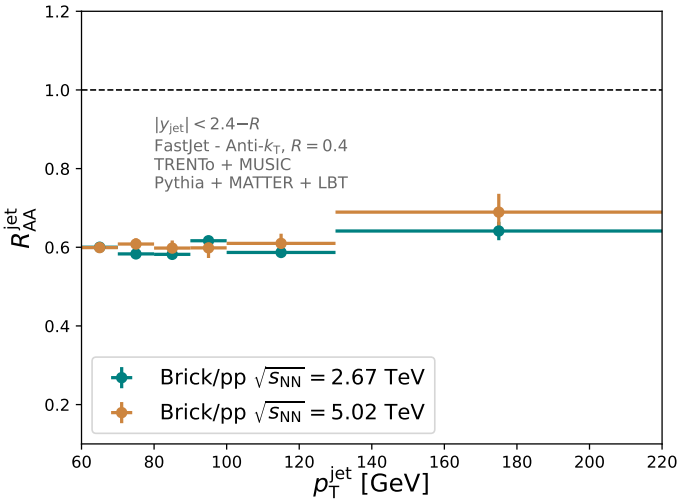

Figure 5.11: Jet nuclear modification factor $R_{\text{AA}}^{\text{jet}}$ for pp collisions (black squares), and 0-10% (purple squares), 10-20% (blue squares), 20-30% (green squares), 30-40% (orange squares), 40-50% (red squares) PbPb collisions at $\sqrt{s_{\text{NN}}} = 2.67$ TeV (left) and $\sqrt{s_{\text{NN}}} = 5.02$ TeV (right) obtained from TRENTo [1] + `freestream-milne` [2] + `MUSIC` [3] + `Pythia` [6] + `MATTER` [7] + `LBT` [8] implemented in `Jetscape` [9].

Another inclusive observable can be seen in the first row of Figure 5.12. It is the jet mass M^{jet} spectrum and its ratio to pp collisions. This reproduces experimental fairly well comparison between small and large systems measured by ALICE [326].

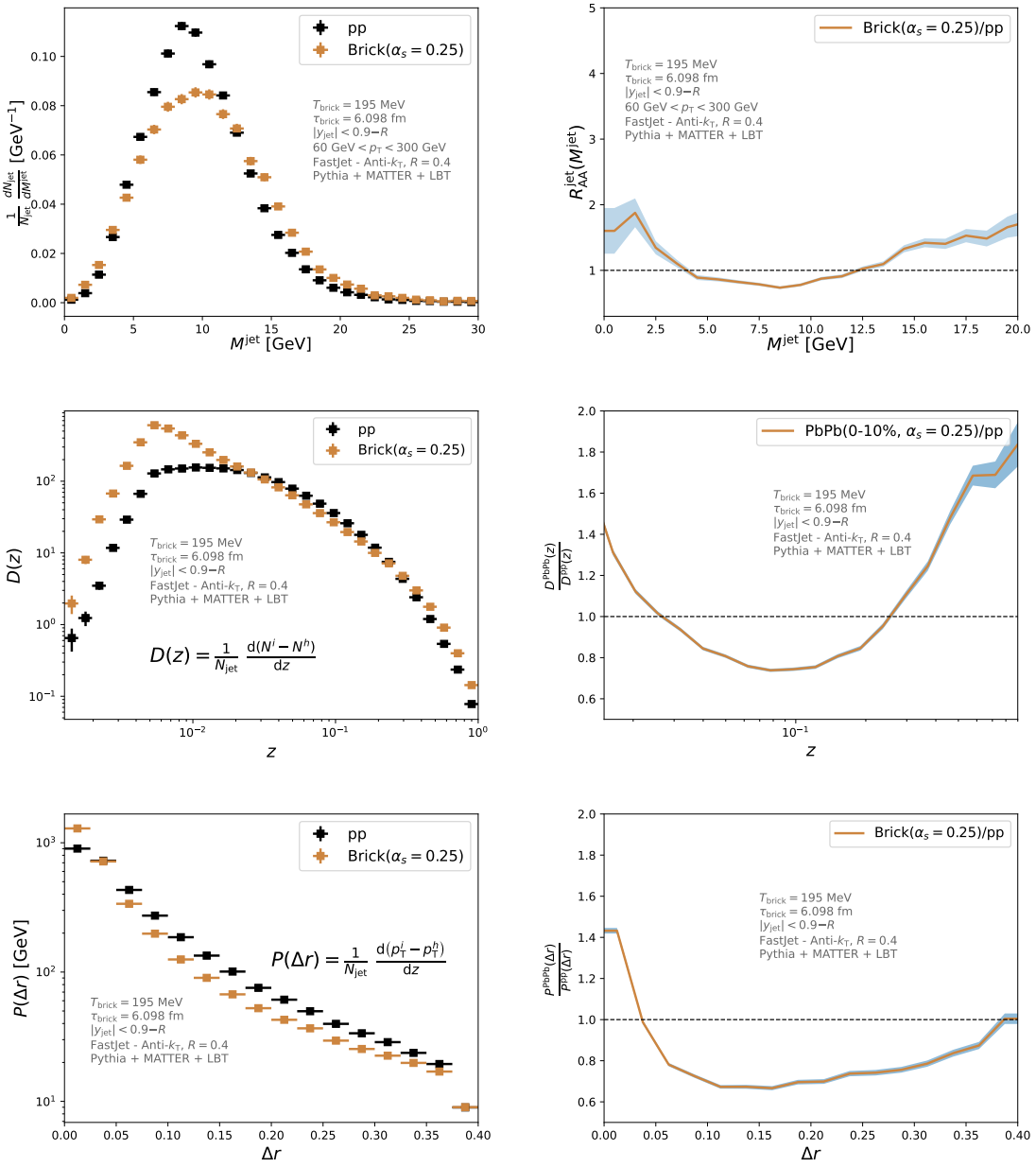

Figure 5.12: Jet mass M^{jet} spectra (top left), mass-dependent jet nuclear modification factor (top right), jet fragmentation function $D(z)$ (middle left) and ratio $D^{\text{PbPb}}(z)/D^{pp}(z)$ (middle right), Jet shape $P(\Delta r)$ (bottom left) and ratio $P^{\text{PbPb}}(\Delta r)/P^{pp}(\Delta r)$ (bottom right) for pp collisions (black squares), and static brick medium (brown squares) at $\sqrt{s_{\text{NN}}} = 2.67$ TeV obtained from `Pythia` [6] + `MATTER` [7] + `LBT` [8] implemented in `Jetscape` [9].

Then there are two exclusive observables in the middle and bottom of the Figure 5.12. The middle row represents the jet fragmentation function $D(z)$. Here we can see fairly well reproduced behaviour for such a simplified system in the middle region of z. The steep increase at the end magnitude but steep increase at the end does not corresponds to data [327]. There is a strong enhancement for small fraction of momenum z due to the larger presence of soft particles.

The last experimental result for the brick medium is the jet shape $P(\Delta r)$. The tail of this distribution is sensitive to recoil effects. There are recoil effects included in the brick simulation. This should cause the enhancment close to the $\Delta r \sim 4$. There is an increase at the end of the spectra and it is indeed associated with the recoil because it is not present for the simulation without recoil. However, ratio of the jet shape does not rise above one in this region.

5.3.2 Jet evolution with realistic medium

This section presents the results on observables obtained from the entire simulation chain. Compared to the brick medium, `MUSIC` [3] 2+1D second order hydrodynamic simulation was used to simulate the medium. The initial state was obtained from the TRENTo model [1] and `freestream-milne` [2] with parameters constrained by Bayesian analysis [173].

The medium-modified vacuum evolution `MATTER` [7] and the linear Boltzmann transport model `LBT` [8] were used to create a partonic cascade that hadronizes and is clustered with the anti-k_T algorithm with $R = 0.4$.

Five cetrality bins of PbPb collisions at $\sqrt{s_{\mathrm{NN}}} = 2.67$ TeV and $\sqrt{s_{\mathrm{NN}}} = 5.02$ TeV were simulated and reconstructed. Figure 5.13 shows jet transverse momentum spectra for the five centality bins and pp collisions simulated with the initial state of the initial state of the `Pythia` [6] MPI initial state and `MATTER` vacuum evolution.

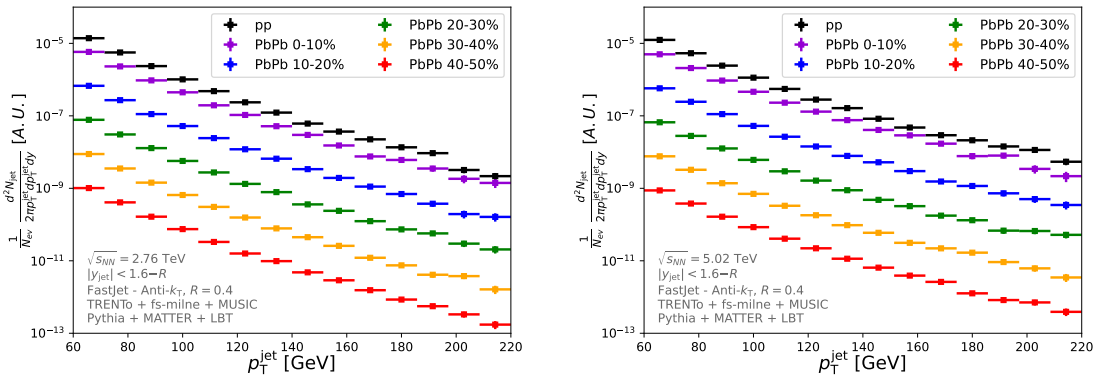

Figure 5.13: Transverse momentum $p_{\mathrm{T}}^{\mathrm{jet}}$ distribution of the jets for pp collisions (black squares), and 0-10% (magenta squares), 10-20% (blue squares; divided by 10^1), 20-30% (green squares; divided by 10^2), 30-40% (orange squares; divided by 10^3), 40-50% (red squares; divided by 10^4) PbPb collisions at $\sqrt{s_{\mathrm{NN}}} = 2.67$ TeV (left) and $\sqrt{s_{\mathrm{NN}}} = 5.02$ TeV (right) obtained from TRENTo [1] + `freestream-milne` [2] + `MUSIC` [3] + `Pythia` [6] + `MATTER` [7] + `LBT` [8] implemented in `Jetscape` [9].

Jet transverse momentum spectra in Figure 5.13 are multiplied by powers of ten to make them more visible. One can see that the jet momentum specra for the centrality bins at $\sqrt{s_{\mathrm{NN}}} =$ 5.02 TeV are more flat. The reason is, of course, the higher collisional energy.

In general, the jet transverse momentum spectra correspond to the experimental measurements in the LHC experiments. This can be seen in Figure 5.14 where the jet nuclear modifica-

tion factor $R_{\mathrm{AA}}^{\mathrm{jet}}$ is plotted for the five centality bins and the two centre-of-mass nucleon-nucleon energies $\sqrt{s_{\mathrm{NN}}}$ along with the experimental measurements from ATLAS [328, 329], CMS [330], and ALICE [331]. We can see that the simulated data correlate with the experimental measurements. At around $p_{\mathrm{T}}^{\mathrm{jet}} \sim 200$ GeV, simulations underestimate the data. This may be due to lower statistics and a wide bin between 130 and 220 GeV.

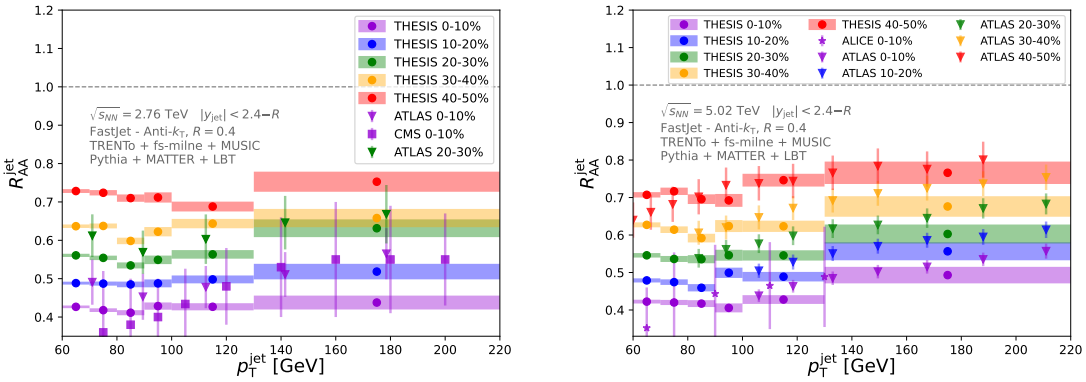

Figure 5.14: Jet nuclear modification factor $R_{\mathrm{AA}}^{\mathrm{jet}}$ 0-10% (magent squares), 10-20% (blue squares), 20-30% (green squares), 30-40% (orange squares), 40-50% (red squares) PbPb collisions at $\sqrt{s_{\mathrm{NN}}} = 2.67$ TeV (left) and $\sqrt{s_{\mathrm{NN}}} = 5.02$ TeV (right) obtained from TRENTo [1] + `freestream-milne` [2] + `MUSIC` [3] + `Pythia` [6] + `MATTER` [7] + `LBT` [8] implemented in `Jetscape` [9]. Experimental values of jet nuclear modification factor $R_{\mathrm{AA}}^{\mathrm{jet}}$ from ATLAS [328, 329] (triangles) ALICE [331] (stars) and CMS [330] (squares).

Similarly to the brick medium, we calculated the following jet observables. First, in the upper row of Figure 5.15 there are jet mass M^{jet} spectra and the mass-dependent jet nuclear modification factor $R_{\mathrm{AA}}^{\mathrm{jet}}\left(M^{\mathrm{jet}}\right)$ for a 30-40% PbPb collision at $\sqrt{s_{\mathrm{NN}}} = 2.67$ TeV (see Appendix B). Here, we can see a relatively steep increase of $R_{\mathrm{AA}}^{\mathrm{jet}}\left(M^{\mathrm{jet}}\right)$ after $M^{\mathrm{jet}} \sim 10$ GeV. This does not correspond to the experimental measurements [326]. The situation is even worse for the central collisions that are presented in [326].

It is a puzzling problem, since the brick simulation in Figure 5.12 does not rise like that. This can essentially exclude the possibility of some heavy hadron that does not decay in the simulation. This was the previous issue of the simulation that shifted the mass spectra to the right for about 15 GeV. However, both brick and realistic simulators have the same settings for hadronic decays.

Middle row of the Figure 5.15 represents jet fragmentation function $D(z)$ and the ratio of fragmentation functions $D^{\mathrm{PbPb}}(z)/D^{pp}(z)$. Here we can see sudden decrease compared to the brick medium. This result agrees with the data more that the brick medium for large fraction of momenta z. We can see same enhancement for the small z in case of PbPb collisions as for the brick medium. Dip of the $D^{\mathrm{PbPb}}(z)/D^{pp}(z)$ in the intermedieate z agrees with the experimental measuremets. It is still puzzeling that the tail of the $D^{\mathrm{PbPb}}(z)/D^{pp}(z)$ is so much different compared to the brick medium simulation.

Finally, we can see the presence of holes and jet-medium recoil effect on the bottom row of the

Figure 5.15. There is jet shape $P(\Delta r)$ (bottom left), and ratio $P^{\mathrm{PbPb}}(\Delta r)/P^{pp}(\Delta r)$. The enhancement of the tail of the ratio is sensitive to recoil effect. Again, there is a discrepancy between PbPb relaistic medium and the brick medium.

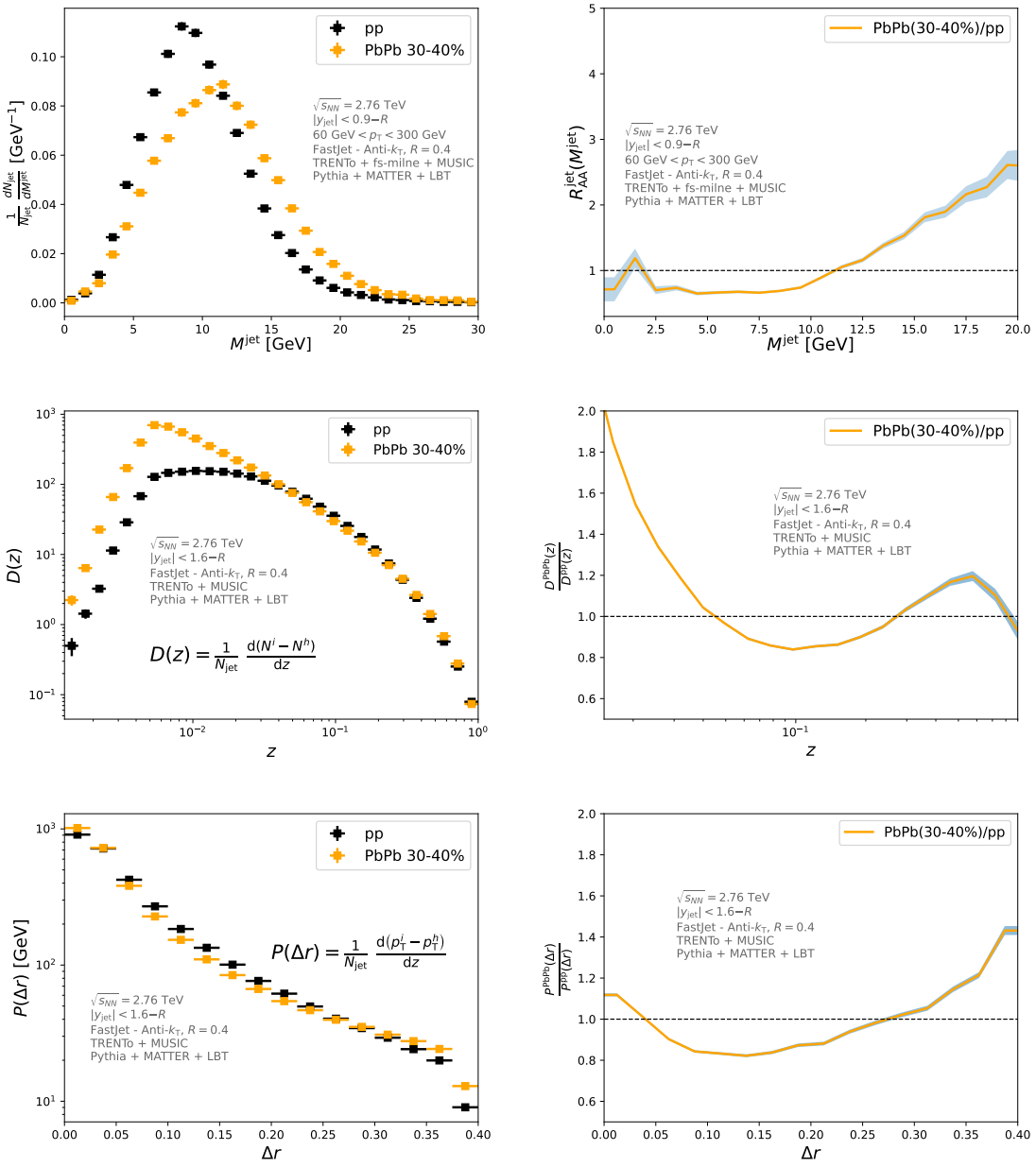

Figure 5.15: Jet mass M^{jet} spectra (top left), mass-dependent jet nuclear modification factor (top right), jet fragmentation function $D(z)$ (middle left), ratio $D^{\mathrm{PbPb}}(z)/D^{pp}(z)$ (middle right), Jet shape $P(\Delta r)$ (bottom left), and ratio $P^{\mathrm{PbPb}}(\Delta r)/P^{pp}(\Delta r)$ (bottom right) for pp collisions (black squares) and 30-40% PbPb (orange squares) at $\sqrt{s_{\mathrm{NN}}}$ = 2.67 TeV obtained from TRENTo [1] + `freestream-milne` [2] + `MUSIC` [3] + `Pythia` [6] + `MATTER` [7] + `LBT` [8] implemented in `Jetscape` [9].

At the end, Figure 5.16 there are jet scatter plots in the $(p_{\mathrm{T}}^{\mathrm{jet}}, E^{\mathrm{jet}})$ space for different rapidity intervals $|y_{\mathrm{jet}}| \leq 0.9 - R$, $|y_{\mathrm{jet}}| \leq 1.6 - R$, and $|y_{\mathrm{jet}}| \leq 2.4 - R$ from top to bottom. Those rapidity intervals were used to produce observables presented in this thesis. Cuts are clearly visible as the red area of the scatter plots are thin at the top. We can see that we do not lose many high $p_{\mathrm{T}}^{\mathrm{jet}}$ jets for more strict cuts.

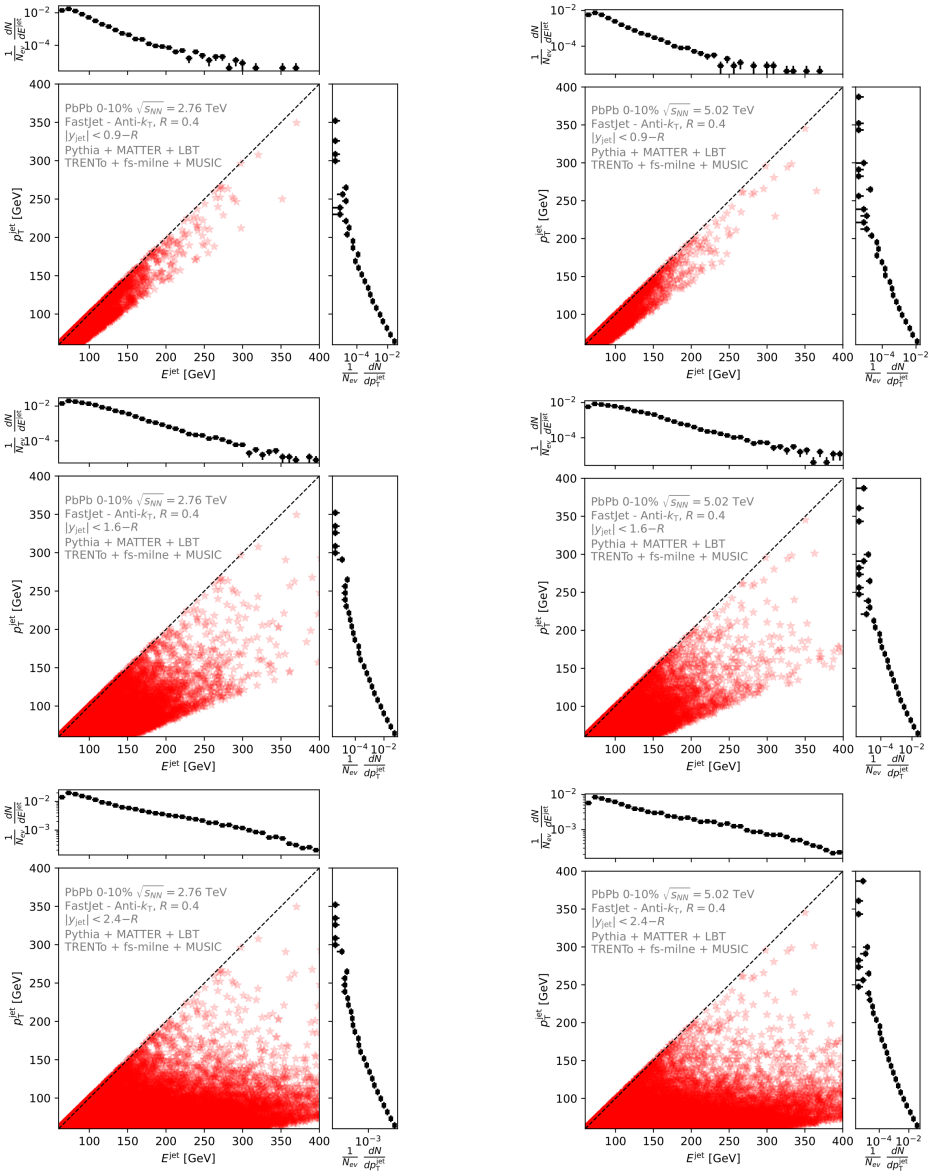

Figure 5.16: Jet scatter plots in the $(p_{\mathrm{T}}^{\mathrm{jet}}, E^{\mathrm{jet}})$ space for different rapidity intervals $|y_{\mathrm{jet}}| \leq 0.9 - R$ (upper row), $|y_{\mathrm{jet}}| \leq 1.6 - R$ (middle row), and $|y_{\mathrm{jet}}| \leq 2.4 - R$ (lower row) for 0-10% PbPb collisions at $\sqrt{s_{\mathrm{NN}}} = 2.67$ TeV (left column) and $\sqrt{s_{\mathrm{NN}}} = 5.02$ TeV (right column) obtained from TRENTo [1] + `freestream-milne` [2] + `MUSIC` [3] + `Pythia` [6] + `MATTER` [7] + `LBT` [8] implemented in `Jetscape` [9].

Chapter 6

Conclusion

This theses presented the estabilished jet and medium simulation framework `Jetscape` [9]. Jet observables such as jet transverse momentum spectra, jet nuclear modification factor $R_{\mathrm{AA}}^{\mathrm{jet}}\left(p_{\mathrm{T}}^{\mathrm{jet}}\right)$. and jet shape $P(\Delta r)$ were obtained from simulations composed of numerous stages.

First, the medium is simulated with second-order hydrodynamics within the `MUSIC` code [3]. The dynamical initial state was simulated by TRENTo model [1] and preequilibrium `freestream-milne` [2]. It is important to compare soft hadronic observables with experimental measurements to check the reliability of the framework and how well it describes reality. This brings about two additional simulation stages in the form of a `iSS` particle sampler and `SMASH` hadronic afterburner, the latter simulating interactions between hadrons in the posthydrodynamic stage.

Observables such as transverse momentum spectra and the average momentum of pions, kaons, and protons were obtained. Hadronic observables were compared with the experimental data, and there is general quantitative agreement. However, there are areas for improvement. For example, the preequilibrium stage or EoS could be upgraded.

Inputs to the medium simulation can affect medium size, lifespan, or temperature. It is important to match them with reality as best we can since jet quenching is driven by those medium properties.

For example, free-streaming preequilibrium takes up to 10% of the effective lifespan of the medium. Modern bulk viscosity parameterisations can reduce the length of the medium lifespan by 10% and also its size up to 20% at later time. The shear viscosity slightly alters the temperature of the medium. Although there are significant temperature effects, shear viscosity can affect the anisotropy of the medium, and the impact of the anisotropy on the medium-induced gluon spectra could be significant. Different EoS can cause a $\sim$ 1 fm difference in the femtoscopy radii. Furthermore, EoS defines the temperature of the system.

There are unanswered questions on how preequilibrim, bulk viscosity, shear viscosity, EoS, and other aspects of medium simulation affect the jet evolution.

The evolution of the jet starts at the hard vertex. This was simulated with `Pythia` [6] MPI. The partons obtained from MPI can be identified as jets using the anti-k_{T} algorithm implemented in `FastJet` [310]. After that, it is possible to calculate the average proper time that jets spend

inside the medium. This can be used to create a static medium with size equal to this average in-medium proper time and average temperature of the hydrodynamic simulation.

Partonic cascades inside the brick medium were simulated with `MATTER` [7] for high-virtuality ($Q \geq 2$ GeV) partons and `LBT` [8] for low-virtuality ($Q < 2$ GeV) partons. For the jet energy loss, two scenarios were used for background medium: brick medium and realistic medium.

This produced decent results in terms of transverse momentum spectra and consequently nuclear modification factor $R_{\mathrm{AA}}^{\mathrm{jet}}\left(p_{\mathrm{T}}^{\mathrm{jet}}\right)$. Similarly, the jet fragmentation function $D(z)$ had the enhancement for large fraction of momenta z compared to pp collisions. This is not observed in the experimental data. The ratio of jet shape $P^{\mathrm{PbPb}}(\Delta r)/P^{pp}(\Delta r)$ increased slightly for large Δr for evolution in the brick medium. However, the enhancement at large Δr was absent. This enhancement is connected to recoil scatterings between jet partons and thermal partons. Those interactions were present during the partonic evolution.

The realistic medium was simulated with the T$_{\mathrm{R}}$ENTo + `freestream-milne` initial state and `MUSIC` 2+1D second order hydrodynamics for five centrality bins of PbPb collisions at the centre-of-mass nucleon-nucleon energies $\sqrt{s_{\mathrm{NN}}} = 2.67$ TeV and $\sqrt{s_{\mathrm{NN}}} = 5.02$ TeV. Then the same parton evolution was used as for the brick medium, that is, `MATTER` and `LBT`.

Transverse momentum spectra and consequently nuclear modification factor $R_{\mathrm{AA}}^{\mathrm{jet}}\left(p_{\mathrm{T}}^{\mathrm{jet}}\right)$ were successfully reproduced and compared with the experimental data. They are compatible with each other within the uncertainty. The jet shape $P(\Delta r)$ was also successfully reproduced with the tail enhancement of the ratio. The jet fragmentation function for realistic medium simulation encapsulates the general behaviour. The puzzeling part was the jet mass spectra. Realistic medium simulation shows positive shifts of the mass spectra. However, this is not observed in the experiment. This fact makes the brick medium more predictive about the jet mass.

Future research on this topic will be carried out using the hydrodynamic simulation code `vHLLE` [332] as it is a more familiar software and thus more controllable. The goal will be to build a framework that can simulate jet energy loss with `vHLLE` as a hydrodynamic simulation code. It will be easier to implement and modify various details of medium, jet modelling and jet-medium interaction in such framework.

This work was presented at the 22nd Zimányi school winter workshop on heavy-ion physics in Budapest in the form of a poster.

Bibliography

[1] J. Scott Moreland, Jonah E. Bernhard, and Steffen A. Bass. "Alternative ansatz to wounded nucleon and binary collision scaling in high-energy nuclear collisions". In: (2014). DOI: 10.1103/PhysRevC.92.011901. eprint: arXiv:1412.4708.

[2] Derek Everett. *Derekeverett/Freestream-Milne*. URL: https://github.com/derekeverett/freestream-milne.

[3] Bjoern Schenke, Sangyong Jeon, and Charles Gale. "3+1D hydrodynamic simulation of relativistic heavy-ion collisions". In: (2010). DOI: 10.1103/PhysRevC.82.014903. eprint: arXiv:1004.1408.

[4] Chun Shen et al. "The iEBE-VISHNU code package for relativistic heavy-ion collisions". In: *Computer Physics Communications* 199 (2016), pp. 61–85.

[5] Janus Weil et al. "Particle production and equilibrium properties within a new hadron transport approach for heavy-ion collisions". In: *Physical Review C* 94.5 (2016), p. 054905.

[6] Torbjörn Sjöstrand, Stephen Mrenna, and Peter Skands. "A brief introduction to PYTHIA 8.1". In: *Computer Physics Communications* 178.11 (2008), pp. 852–867.

[7] Abhijit Majumder. "Incorporating Space-Time Within Medium-Modified Jet Event Generators". In: (2013). DOI: 10.1103/PhysRevC.88.014909. eprint: arXiv:1301.5323.

[8] Shanshan Cao et al. "Heavy and light flavor jet quenching at RHIC and LHC energies". In: (2017). DOI: 10.1016/j.physletb.2017.12.023. eprint: arXiv:1703.00822.

[9] J. H. Putschke et al. *The JETSCAPE framework*. 2019. eprint: arXiv:1903.07706.

[10] Chen-Ning Yang and Robert L Mills. "Conservation of isotopic spin and isotopic gauge invariance". In: *Physical review* 96.1 (1954), p. 191.

[11] Chien-Shiung Wu et al. "Experimental test of parity conservation in beta decay". In: *Physical review* 105.4 (1957), p. 1413.

[12] Enrico Fermi. "Sulla quantizzazione del gas perfetto monoatomico". In: *Rendiconti Lincei* (1926).

[13] Alberto Zannoni. *On the Quantization of the Monoatomic Ideal Gas*. 1999. eprint: arXiv:cond-mat/9912229.

[14] Paul Adrien Maurice Dirac. "On the theory of quantum mechanics". In: *Proceedings of the Royal Society of London. Series A, Containing Papers of a Mathematical and Physical Character* 112.762 (1926), pp. 661–677.

[15] Wolfgang Pauli. "Über den Zusammenhang des Abschlusses der Elektronengruppen im Atom mit der Komplexstruktur der Spektren". In: *Zeitschrift für Physik* 31.1 (1925), pp. 765–783.

[16] Satyendra Nath Bose. "Plancks gesetz und lichtquantenhypothese". In: *Zeitschrift für Physik* 26 (1924), pp. 178–181. DOI: 10.1007/BF01327326.

[17] Laurie M Brown. "The idea of the neutrino". In: *Physics today* 31.9 (1978), p. 23.

[18] Fred Reines and Clyde Cowan. "The Reines-Cowan experiments: detecting the poltergeist". In: *Los Alamos Science* 25 (1997), pp. 4–6.

[19] Gaillard Danby et al. "Observation of high-energy neutrino reactions and the existence of two kinds of neutrinos". In: *Physical Review Letters* 9.1 (1962), p. 36.

[20] Martin L Perl et al. "Evidence for anomalous lepton production in e+- e- annihilation". In: *Physical Review Letters* 35.22 (1975), p. 1489.

[21] K Kodama et al. "Observation of tau neutrino interactions". In: *Physics Letters B* 504.3 (2001), pp. 218–224.

[22] M Aker et al. "Direct neutrino-mass measurement with sub-electronvolt sensitivity". In: *Nature Physics* 18.2 (2022).

[23] Bruno Pontecorvo. "Mesonium and antimesonium". In: *Zhur. Eksptl'. i Teoret. Fiz.* 33 (1957).

[24] Ziro Maki, Masami Nakagawa, and Shoichi Sakata. "Remarks on the unified model of elementary particles". In: *Progress of Theoretical Physics* 28.5 (1962), pp. 870–880.

[25] Bruno Pontecorvo. "Neutrino experiments and the problem of conservation of leptonic charge". In: *Sov. Phys. JETP* 26.984-988 (1968), p. 165.

[26] Raymond Davis Jr, Don S Harmer, and Kenneth C Hoffman. "Search for neutrinos from the sun". In: *Physical Review Letters* 20.21 (1968), p. 1205.

[27] Q Retal Ahmad et al. "Measurement of the Rate of $\nu_e + d \rightarrow p + p + e^-$ Interactions Produced by B 8 Solar Neutrinos at the Sudbury Neutrino Observatory". In: *Physical review letters* 87.7 (2001), p. 071301.

[28] Yoshiyuki Fukuda et al. "Evidence for oscillation of atmospheric neutrinos". In: *Physical review letters* 81.8 (1998), p. 1562.

[29] FP An et al. "Observation of electron-antineutrino disappearance at Daya Bay". In: *Physical Review Letters* 108.17 (2012), p. 171803.

[30] N Agafonova et al. "Observation of a first $\nu\tau$ candidate event in the OPERA experiment in the CNGS beam". In: *Physics Letters B* 691.3 (2010), pp. 138–145.

[31] Claus Grupen et al. *Astroparticle physics*. Vol. 50. Springer, 2005.

[32] Particle Data Group et al. "Review of particle physics". In: *Progress of Theoretical and Experimental Physics* 2020.8 (2020), p. 083C01.

[33] Joseph John Thomson. "XL. Cathode rays". In: *The London, Edinburgh, and Dublin Philosophical Magazine and Journal of Science* 44.269 (1897), pp. 293–316.

[34] Paul Adrien Maurice Dirac. "The quantum theory of the electron". In: *Proceedings of the Royal Society of London. Series A, Containing Papers of a Mathematical and Physical Character* 117.778 (1928), pp. 610–624.

[35] Carl D Anderson. "The positive electron". In: *Physical Review* 43.6 (1933), p. 491.

[36] Seth H Neddermeyer and Carl D Anderson. "Note on the nature of cosmic-ray particles". In: *Physical Review* 51.10 (1937), p. 884.

[37] Ernest Rutherford. "LIV. Collision of α particles with light atoms. IV. An anomalous effect in nitrogen". In: *The London, Edinburgh, and Dublin Philosophical Magazine and Journal of Science* 37.222 (1919), pp. 581–587.

[38] James Chadwick. "The existence of a neutron". In: *Proceedings of the Royal Society of London. Series A, Containing Papers of a Mathematical and Physical Character* 136.830 (1932), pp. 692–708.

[39] George Dixon Rochester and Clifford Charles Butler. "Evidence for the existence of new unstable elementary particles". In: *Nature* 160.4077 (1947), pp. 855–857.

[40] Celso MG LATTES et al. "Processes involving charged mesons". In: *Nature* 159.4047 (1947), pp. 694–697.

[41] Enrico Fermi and Chen-Ning Yang. "Are mesons elementary particles?" In: *Physical Review* 76.12 (1949), p. 1739.

[42] Hideki Yukawa. "On the interaction of elementary particles. I". In: *Proceedings of the Physico-Mathematical Society of Japan. 3rd Series* 17 (1935), pp. 48–57.

[43] Shoichi Sakata et al. "On a composite model for the new particles". In: *Prog. Theor. Phys* 16.6 (1956), pp. 686–688.

[44] Yuval Ne'eman. "Derivation of strong interactions from a gauge invariance". In: *Nuclear physics* 26.2 (1961), pp. 222–229.

[45] M Gell-Mann. "The Eightfold Way: A Theory of Strong Interaction Symmetry, Report Number TID-12608". In: *Caltech Preprint CTSL-20* (1961).

[46] Murray Gell-Mann. "Symmetries of baryons and mesons". In: *The Eightfold Way*. CRC Press, 2018, pp. 216–233.

[47] VE Barnes et al. "Observation of a hyperon with strangeness minus three". In: *Physical Review Letters* 12.8 (1964), p. 204.

[48] Murray Gell-Mann. "A schematic model of baryons and mesons". In: *Phys. Letters* 8 (1964).

[49] George Zweig. *An SU _3 model for strong interaction symmetry and its breaking*. Tech. rep. CM-P00042884, 1964.

[50] Matthew Kenzie. *Warwick Week 2022*. Apr. 2022. URL: `https://indico.cern.ch/event/1130558/contributions/4746840/attachments/2424867/4151252/`.

[51] BJ Bjørken and Sheldon L Glashow. "Elementary particles and SU (4)". In: *Physics Letters* 11.3 (1964), pp. 255–257.

[52] Jean-Jacques Aubert et al. "Experimental observation of a heavy particle J". In: *Physical Review Letters* 33.23 (1974), p. 1404.

[53] J-E Augustin et al. "Discovery of a Narrow Resonance in e+ e- Annihilation". In: *Physical Review Letters* 33.23 (1974), p. 1406.

[54] Oscar W Greenberg. "Spin and unitary-spin independence in a paraquark model of baryons and mesons". In: *Physical Review Letters* 13.20 (1964), p. 598.

[55] Y Nambu. "Preludes in theoretical physics". In: *in honor of VF Weisskopf* (1966).

[56] Yoichiro Nambu. "The confinement of quarks". In: *Scientific American* 235.5 (1976), pp. 48–63.

[57] DC Hom et al. “Observation of high-mass dilepton pairs in hadron collisions at 400 GeV”. In: *Physical Review Letters* 36.21 (1976), p. 1236.

[58] SW Herb et al. “Observation of a dimuon resonance at 9.5 GeV in 400-GeV proton-nucleus collisions”. In: *Physical Review Letters* 39.5 (1977), p. 252.

[59] Fumio Abe et al. “Observation of top quark production in p p collisions with the Collider Detector at Fermilab”. In: *Physical review letters* 74.14 (1995), p. 2626.

[60] Shahriar Abachi et al. “Observation of the top quark”. In: *Physical review letters* 74.14 (1995), p. 2632.

[61] Eric Swanson. “New particle hints at four-quark matter”. In: *Physics* 6 (2013), p. 69.

[62] LHCb collaboration. “Observation of the resonant character of the $Z(4430)^-$ state”. In: (2014). DOI: 10.1103/PhysRevLett.112.222002. eprint: arXiv:1404.1903.

[63] LHCb collaboration. “Observation of $J/\psi\phi$ structures consistent with exotic states from amplitude analysis of $B^+ \to J/\psi\phi K^+$ decays”. In: (2016). DOI: 10.1103/PhysRevLett.118.022003. eprint: arXiv:1606.07895.

[64] LHCb collaboration. “Amplitude analysis of $B^+ \to J/\psi\phi K^+$ decays”. In: (2016). DOI: 10.1103/PhysRevD.95.012002. eprint: arXiv:1606.07898.

[65] LHCb collaboration. “Observation of structure in the J/ψ-pair mass spectrum”. In: (2020). DOI: 10.1016/j.scib.2020.08.032. eprint: arXiv:2006.16957.

[66] LHCb collaboration. *Observation of new resonances decaying to $J/\psi K^+$ and $J/\psi\phi$*. 2021. eprint: arXiv:2103.01803.

[67] LHCb collaboration. “Observation of $J/\psi p$ resonances consistent with pentaquark states in $\Lambda_b^0 \to J/\psi K^- p$ decays”. In: (2015). DOI: 10.1103/PhysRevLett.115.072001. eprint: arXiv:1507.03414.

[68] CDF Collaboration†‡ et al. “High-precision measurement of the W boson mass with the CDF II detector”. In: *Science* 376.6589 (2022), pp. 170–176.

[69] G Arnison et al. “Experimental observation of isolated large transverse energy electrons with associated missing energy at $\sqrt{s}$ = 540 GeV”. In: *Physics Letters B* 122.1 (1983), pp. 103–116.

[70] G Arnison et al. “Experimental observation of lepton pairs of invariant mass around 95 GeV/c^2 at the CERN SPS collider”. In: *Physics Letters B* 126.5 (1983), pp. 398–410.

[71] Marcel Banner et al. “Observation of single isolated electrons of high transverse momentum in events with missing transverse energy at the CERN pp collider”. In: *Physics Letters B* 122.5-6 (1983), pp. 476–485.

[72] Po Bagnaia et al. “Evidence for $Z^0 \to e^+e^-$ at the CERN pp Collider”. In: *Physics Letters B* 129.1-2 (1983), pp. 130–140.

[73] Peter W Higgs. “Broken symmetries and the masses of gauge bosons”. In: *Physical Review Letters* 13.16 (1964), p. 508.

[74] Philip W Anderson. “Plasmons, gauge invariance, and mass”. In: *Physical Review* 130.1 (1963), p. 439.

[75] François Englert and Robert Brout. “Broken symmetry and the mass of gauge vector mesons”. In: *Physical review letters* 13.9 (1964), p. 321.

[76] Gerald S Guralnik, Carl R Hagen, and Thomas WB Kibble. "Global conservation laws and massless particles". In: *Physical Review Letters* 13.20 (1964), p. 585.

[77] Martinus Veltman et al. "Regularization and renormalization of gauge fields". In: *Nuclear Physics B* 44.1 (1972), pp. 189–213.

[78] Georges Aad et al. "Observation of a new particle in the search for the Standard Model Higgs boson with the ATLAS detector at the LHC". In: *Physics Letters B* 716.1 (2012), pp. 1–29.

[79] Serguei Chatrchyan et al. "Observation of a new boson at a mass of 125 GeV with the CMS experiment at the LHC". In: *Physics Letters B* 716.1 (2012), pp. 30–61.

[80] R Brandelik et al. "Evidence for planar events in e^+e^- annihilation at high energies". In: *Physics Letters B* 86.2 (1979), pp. 243–249.

[81] R Brandelik et al. "Evidence for a spin-1 gluon in three-jet events". In: *Physics Letters B* 97.3-4 (1980), pp. 453–458.

[82] Coll PLUTO. "Evidence for Gluon Bremsstrahlung in e^+e^- Annihilations at High Energies". In: *Phys. Lett. B* 86 (1979), p. 418.

[83] Ch Berger et al. "A study of multi-jet events in e^+e^- annihilation". In: *Physics Letters B* 97.3-4 (1980), pp. 459–464.

[84] Wulfrin Bartel et al. "Observation of planar three-jet events in e+ e- annihilation and evidence for gluon bremsstrahlung". In: *Physics Letters B* 91.1 (1980), pp. 142–147.

[85] DP Barber et al. "Discovery of three-jet events and a test of quantum chromodynamics at PETRA". In: *Physical Review Letters* 43.12 (1979), p. 830.

[86] *The elegant universe*. URL: `https://www.pbs.org/wgbh/nova/series/the-elegant-universe/`.

[87] Oskar Klein. "Quantentheorie und fünfdimensionale Relativitätstheorie". In: *Zeitschrift für Physik* 37.12 (1926), pp. 895–906.

[88] Walter Gordon. "Der comptoneffekt nach der schrödingerschen theorie". In: *Zeitschrift für Physik* 40.1 (1926), pp. 117–133.

[89] Anthony Zee. *Quantum field theory in a nutshell*. Vol. 7. Princeton university press, 2010.

[90] AL Proca. "Sur la théorie ondulatoire des électrons positifs et négatifs". In: *Journal de Physique et le Radium* 7.8 (1936), pp. 347–353.

[91] Murray Gell-Mann and Francis Low. "Bound states in quantum field theory". In: *Physical Review* 84.2 (1951), p. 350.

[92] Gian-Carlo Wick. "The evaluation of the collision matrix". In: *Physical review* 80.2 (1950), p. 268.

[93] Ludvig D Faddeev and Victor N Popov. "Feynman diagrams for the Yang-Mills field". In: *Physics Letters B* 25.1 (1967), pp. 29–30.

[94] Kohsuke Yagi, Tetsuo Hatsuda, and Yasuo Miake. *Quark-gluon plasma: From big bang to little bang*. Vol. 23. Cambridge University Press, 2005.

[95] Harry Lehmann, Kurt Symanzik, and Wolfhart Zimmermann. "Zur formulierung quantisierter feldtheorien". In: *Il Nuovo Cimento (1955-1965)* 1.1 (1955), pp. 205–225.

[96] Martinus Veltman et al. "Regularization and renormalization of gauge fields". In: *Nuclear Physics B* 44.1 (1972), pp. 189–213.

[97] Gerard t Hooft and M Veltman. "Combinatorics of gauge fields". In: *Nuclear Physics B* 50.1 (1972), pp. 318–353.

[98] Ernst Carl Gerlach Stueckelberg von Breidenbach and André Petermann. "La normalisation des constantes dans la theorie des quanta". In: *Helvetica Physica Acta* 26.5 (1953), pp. 499–520.

[99] Kenneth G Wilson. "Confinement of quarks". In: *Physical review D* 10.8 (1974), p. 2445.

[100] Taizo Muta. *Foundations of quantum chromodynamics: an introduction to perturbative methods in gauge theories*. world scientific, 1998.

[101] David J Gross and Frank Wilczek. "Ultraviolet behavior of non-abelian gauge theories". In: *Physical Review Letters* 30.26 (1973), p. 1343.

[102] H David Politzer. "Reliable perturbative results for strong interactions?" In: *Physical Review Letters* 30.26 (1973), p. 1346.

[103] Gerard't Hooft. "The birth of asymptotic freedom". In: *Nuclear Physics, B* 254 (1985), pp. 11–18.

[104] CMS Collaboration. "Measurement and QCD analysis of double-differential inclusive jet cross-sections in pp collisions at sqrt(s) = 8 TeV and ratios to 2.76 and 7 TeV". In: (2016). DOI: 10.1007/JHEP03(2017)156. eprint: arXiv:1609.05331.

[105] Alexandre Deur, Stanley J Brodsky, and Guy F de Téramond. "The QCD running coupling". In: *Progress in Particle and Nuclear Physics* 90 (2016), pp. 1–74.

[106] Rolf Hagedorn. "Statistical thermodynamics of strong interactions at high energies". In: *Nuovo Cimento, Suppl.* 3.CERN-TH-520 (1965), pp. 147–186.

[107] G. F. Burgio et al. "Neutron Stars and the Nuclear Equation of State". In: (2021). DOI: 10.1016/j.ppnp.2021.103879. eprint: arXiv:2105.03747.

[108] Tetsufumi Hirano, Naomi van der Kolk, and Ante Bilandzic. "Hydrodynamics and Flow". In: (2008). DOI: 10.1007/978-3-642-02286-9_4. eprint: arXiv:0808.2684.

[109] Paul Romatschke and Ulrike Romatschke. *Relativistic Fluid Dynamics In and Out of Equilibrium – Ten Years of Progress in Theory and Numerical Simulations of Nuclear Collisions*. 2017. eprint: arXiv:1712.05815.

[110] Peter F Kolb et al. "Elliptic flow at SPS and RHIC: From kinetic transport to hydrodynamics". In: *Physics Letters B* 500.3-4 (2001), pp. 232–240.

[111] Paul Romatschke and Ulrike Romatschke. "Viscosity Information from Relativistic Nuclear Collisions: How Perfect is the Fluid Observed at RHIC?" In: (2007). DOI: 10.1103/PhysRevLett.99.172301. eprint: arXiv:0706.1522.

[112] Bjoern Schenke, Sangyong Jeon, and Charles Gale. "(3+ 1) D hydrodynamic simulation of relativistic heavy-ion collisions". In: *Physical Review C* 82.1 (2010), p. 014903.

[113] Charles Gale et al. "Event-by-event anisotropic flow in heavy-ion collisions from combined Yang-Mills and viscous fluid dynamics". In: (2012). DOI: 10.1103/PhysRevLett.110.012302. eprint: arXiv:1209.6330.

[114] Johann Rafelski. "Melting Hadrons, Boiling Quarks". In: (2015). DOI: 10.1140/epja/i2015-15114-0. eprint: arXiv:1508.03260.

[115] I Arsene et al. "Quark-gluon plasma and color glass condensate at RHIC? The perspective from the BRAHMS experiment". In: *Nuclear Physics A* 757.1-2 (2005), pp. 1–27.

[116] K Adcox et al. "Formation of dense partonic matter in relativistic nucleus-nucleus collisions at RHIC: experimental evaluation by the PHENIX collaboration". In: *Nuclear Physics A* 757.1-2 (2005), pp. 184–283.

[117] BB Back et al. "The PHOBOS perspective on discoveries at RHIC". In: *Nuclear Physics A* 757.1-2 (2005), pp. 28–101.

[118] John Adams et al. "Experimental and theoretical challenges in the search for the quark–gluon plasma: The STAR Collaboration's critical assessment of the evidence from RHIC collisions". In: *Nuclear Physics A* 757.1-2 (2005), pp. 102–183.

[119] Huichao Song et al. "200 A GeV Au+Au collisions serve a nearly perfect quark-gluon liquid". In: (2010). DOI: 10.1103/PhysRevLett.106.192301. eprint: arXiv:1011.2783.

[120] Ekaterina Retinskaya, Matthew Luzum, and Jean-Yves Ollitrault. "Constraining models of initial conditions with elliptic and triangular flow data". In: (2013). DOI: 10.1103/PhysRevC.89.014902. eprint: arXiv:1311.5339.

[121] B Alver et al. "Importance of correlations and fluctuations on the initial source eccentricity in high-energy nucleus-nucleus collisions". In: *Physical Review C* 77.1 (2008), p. 014906.

[122] Raimond Snellings. "Collective Expansion at the LHC: selected ALICE anisotropic flow measurements". In: *Journal of Physics G: Nuclear and Particle Physics* 41.12 (2014), p. 124007.

[123] Sruthy Jyothi Das et al. "Relating centrality to impact parameter in nucleus-nucleus collisions". In: (2017). DOI: 10.1103/PhysRevC.97.014905. eprint: arXiv:1708.00081.

[124] Lucian Ancu et al. "Measurement of the pseudorapidity and transverse momentum dependence of the elliptic flow of charged particles in lead–lead collisions at View the MathML source with the ATLAS detector". In: *Physics letters. B* 707.3-4 (2012), pp. 330–348.

[125] C. Adler et al. "Multiplicity Distribution and Spectra of Negatively Charged Hadrons in $Au+Au$ Collisions at $\sqrt{s_{\mathrm{NN}}} = 130$GeV". In: *Phys. Rev. Lett.* 87 (11 Aug. 2001), p. 112303. DOI: 10.1103/PhysRevLett.87.112303. URL: https://link.aps.org/doi/10.1103/PhysRevLett.87.112303.

[126] B. Abelev et al. "Centrality determination of Pb-Pb collisions at $\sqrt{s_{NN}} = 2.76$ TeV with ALICE". In: *Phys. Rev. C* 88 (4 Oct. 2013), p. 044909. DOI: 10.1103/PhysRevC.88.044909. URL: https://link.aps.org/doi/10.1103/PhysRevC.88.044909.

[127] CMS Collaboration. "Dependence on pseudorapidity and centrality of charged hadron production in PbPb collisions at a nucleon-nucleon centre-of-mass energy of 2.76 TeV". In: (2011). DOI: 10.1007/JHEP08(2011)141. eprint: arXiv:1107.4800.

[128] L. Adamczyk et al. "Azimuthal Anisotropy in U + U and Au + Au Collisions at RHIC". In: *Phys. Rev. Lett.* 115 (22 Nov. 2015), p. 222301. DOI: 10.1103/PhysRevLett.115.222301. URL: https://link.aps.org/doi/10.1103/PhysRevLett.115.222301.

[129] Tadeusz Wibig and Dorota Sobczynska. "Proton-nucleus cross section at high energies". In: *Journal of Physics G: Nuclear and Particle Physics* 24.11 (1998), p. 2037.

[130] ALICE Collaboration. "Centrality determination of Pb-Pb collisions at $\sqrt{s_{\mathrm{NN}}} = 2.76$ TeV with ALICE". In: (2013). DOI: 10.1103/PhysRevC.88.044909. eprint: arXiv:1301.4361.

[131] and G. Antchev et al. “First measurement of the total proton-proton cross-section at the LHC energy of \chem{\sqrt{s} = 7\,TeV}”. In: *EPL (Europhysics Letters)* 96.2 (Oct. 2011), p. 21002. DOI: 10.1209/0295-5075/96/21002. URL: https://doi.org/10.1209/0295-5075/96/21002.

[132] and G. Antchev et al. “Luminosity-independent measurements of total, elastic and inelastic cross-sections at \chem{\sqrt {s} = 7\,TeV}”. In: *EPL (Europhysics Letters)* 101.2 (Jan. 2013), p. 21004. DOI: 10.1209/0295-5075/101/21004. URL: https://doi.org/10.1209/0295-5075/101/21004.

[133] G. Antchev et al. “Luminosity-Independent Measurement of the Proton-Proton Total Cross Section at $\sqrt{s}$ = 8 TeV”. In: *Phys. Rev. Lett.* 111 (1 July 2013), p. 012001. DOI: 10.1103/PhysRevLett.111.012001. URL: https://link.aps.org/doi/10.1103/PhysRevLett.111.012001.

[134] Morad Aaboud et al. “Measurement of the Inelastic Proton-Proton Cross Section at $\sqrt{s}$ = 13 TeV with the ATLAS Detector at the LHC”. In: *Physical review letters* 117.18 (2016), p. 182002.

[135] Georges Aad et al. “Measurement of the total cross section from elastic scattering in pp collisions at $\sqrt{s}$ = 7 TeV with the ATLAS detector”. In: *Nuclear Physics B* 889 (2014), pp. 486–548.

[136] Morad Aaboud et al. “Measurement of the total cross section from elastic scattering in pp collisions at $\sqrt{s}$ = 8 TeV with the ATLAS detector”. In: *Physics Letters B* 761 (2016), pp. 158–178.

[137] J. Adam et al. “Results on total and elastic cross sections in proton–proton collisions at s=200 GeV”. In: *Physics Letters B* 808 (2020), p. 135663. ISSN: 0370-2693. DOI: https://doi.org/10.1016/j.physletb.2020.135663. URL: https://www.sciencedirect.com/science/article/pii/S0370269320304664.

[138] GJ Alner et al. “Antiproton-proton cross sections at 200 and 900 GeV cm energy”. In: *Zeitschrift für Physik C Particles and Fields* 32.2 (1986), pp. 153–161.

[139] Norman A Amos et al. “A luminosity-independent measurement of the pp total cross section at $\sqrt{s}$ = 1.8 TeV”. In: *Physics Letters B* 243.1-2 (1990), pp. 158–164.

[140] NA Amos et al. “Measurement of ρ, the ratio of the real to the imaginary part of the $\overline{p}p$ forward elastic-scattering amplitude, at $\sqrt{s}$ = 1.8 TeV”. In: *Physical review letters* 68.16 (1992), p. 2433.

[141] F. Abe et al. “Measurement of the antiproton-proton total cross section at $\sqrt{s}$ =546 and 1800 GeV”. In: *Phys. Rev. D* 50 (9 Nov. 1994), pp. 5550–5561. DOI: 10.1103/PhysRevD.50.5550. URL: https://link.aps.org/doi/10.1103/PhysRevD.50.5550.

[142] F. Abe et al. “Measurement of small angle antiproton-proton elastic scattering at $\sqrt{s}$ =546 and 1800 GeV”. In: *Phys. Rev. D* 50 (9 Nov. 1994), pp. 5518–5534. DOI: 10.1103/PhysRevD.50.5518. URL: https://link.aps.org/doi/10.1103/PhysRevD.50.5518.

[143] Betty Abelev et al. “Measurement of inelastic, single-and double-diffraction cross sections in proton–proton collisions at the LHC with ALICE”. In: *The European Physical Journal C* 73.6 (2013), pp. 1–20.

[144] Atlas Collaboration et al. “Measurement of the inelastic proton-proton cross-section at $\sqrt{s}$ = 7 TeV with the ATLAS detector”. In: *Nature communications* 2 (2011), p. 463.

[145] CMS collaboration et al. "Measurement of the inelastic proton-proton cross section at $\sqrt{s}$ = 7 TeV". In: *Physics Letters, Section B: Nuclear, Elementary Particle and High-Energy Physics* 722.1-3 (2013), pp. 5–27.

[146] CMS Collaboration and H. Van Haevermaet. *Measurement of the inelastic proton-proton cross section at $\sqrt{s}$ = 13 TeV*. 2016. eprint: arXiv:1607.02033.

[147] LHCb Collaboration et al. "Measurement of the inelastic pp cross-section at a centre-of-mass energy of $\sqrt{s}$ = 7 TeV". In: *Journal of High Energy Physics* 2015.2 (2015), pp. 1–16.

[148] Pedro Abreu et al. "Measurement of the proton-air cross section at $\sqrt{s}$ = 57 TeV with the pierre auger observatory". In: *Physical review letters* 109.6 (2012), p. 062002.

[149] RU Abbasi et al. "Measurement of the proton-air cross section with Telescope Array's Black Rock Mesa and Long Ridge fluorescence detectors, and surface array in hybrid mode". In: *Physical Review D* 102.6 (2020), p. 062004.

[150] Constantin Loizides, Jason Kamin, and David d'Enterria. "Improved Monte Carlo Glauber predictions at present and future nuclear colliders". In: (2017). DOI: 10.1103/PhysRevC.97.054910;10.1103/PhysRevC.99.019901. eprint: arXiv:1710.07098.

[151] H De Vries, CW De Jager, and C De Vries. "Nuclear charge-density-distribution parameters from elastic electron scattering". In: *Atomic data and nuclear data tables* 36.3 (1987), pp. 495–536.

[152] C.W. De Jager, H. De Vries, and C. De Vries. "Nuclear charge- and magnetization-density-distribution parameters from elastic electron scattering". In: *Atomic Data and Nuclear Data Tables* 14.5 (1974). Nuclear Charge and Moment Distributions, pp. 479–508. ISSN: 0092-640X. DOI: https://doi.org/10.1016/S0092-640X(74)80002-1. URL: https://www.sciencedirect.com/science/article/pii/S0092640X74800021.

[153] Bernard FROIS. "Nuclear charge and magnetization densities of single particle states". In: (1985). Ed. by Ricardo Boglia, Gudrun Hagemann, and Bent Hersind, pp. 25–43. DOI: https://doi.org/10.1016/B978-0-444-86979-1.50008-9. URL: https://www.sciencedirect.com/science/article/pii/B9780444869791500089.

[154] Kenneth S Krane, David Halliday, et al. *Introductory nuclear physics*. Vol. 465. Wiley New York, 1988.

[155] C. M. Tarbert et al. "Neutron Skin of ^{208}Pb from Coherent Pion Photoproduction". In: *Phys. Rev. Lett.* 112 (24 June 2014), p. 242502. DOI: 10.1103/PhysRevLett.112.242502. URL: https://link.aps.org/doi/10.1103/PhysRevLett.112.242502.

[156] B. Kłos et al. "Neutron density distributions from antiprotonic ^{208}Pb and ^{209}Bi atoms". In: *Phys. Rev. C* 76 (1 July 2007), p. 014311. DOI: 10.1103/PhysRevC.76.014311. URL: https://link.aps.org/doi/10.1103/PhysRevC.76.014311.

[157] Michael L. Miller et al. "Glauber Modeling in High Energy Nuclear Collisions". In: (2007). DOI: 10.1146/annurev.nucl.57.090506.123020. eprint: arXiv:nucl-ex/0701025.

[158] Roger D. Woods and David S. Saxon. "Diffuse Surface Optical Model for Nucleon-Nuclei Scattering". In: *Phys. Rev.* 95 (2 July 1954), pp. 577–578. DOI: 10.1103/PhysRev.95.577. URL: https://link.aps.org/doi/10.1103/PhysRev.95.577.

[159] C. Loizides, J. Nagle, and P. Steinberg. "Improved version of the PHOBOS Glauber Monte Carlo". In: *SoftwareX* 1-2 (2015), pp. 13–18. DOI: 10.1016/j.softx.2015.05.001. arXiv: 1408.2549 [nucl-ex].

[160] Lamek Hulthén et al. *Structure of Atomic Nuclei/Bau der Atomkerne*. Vol. 8. Springer, 1957.

[161] S. S. Adler et al. "Nuclear effects on hadron production in d+Au collisions at $\sqrt{s_{_{NN}}} = 200$ GeV revealed by comparison with $p+p$ data". In: *Phys. Rev. C* 74 (2 Aug. 2006), p. 024904. DOI: 10.1103/PhysRevC.74.024904. URL: https://link.aps.org/doi/10.1103/PhysRevC.74.024904.

[162] S. S. Adler et al. "Absence of Suppression in Particle Production at Large Transverse Momentum in $\sqrt{s_{NN}} = 200$ GeV $d+$Au Collisions". In: *Phys. Rev. Lett.* 91 (7 Aug. 2003), p. 072303. DOI: 10.1103/PhysRevLett.91.072303. URL: https://link.aps.org/doi/10.1103/PhysRevLett.91.072303.

[163] Yadav Pandit. "Azimuthal Anisotropy in U+U Collisions at $\sqrt{s_{NN}} = 193$ GeV with STAR Detector at RHIC". In: (2013). DOI: 10.1088/1742-6596/458/1/012003. eprint: arXiv:1305.0173.

[164] Hui Wang and Paul Sorensen. "Azimuthal anisotropy in U+U collisions at STAR". In: (2014). DOI: 10.1016/j.nuclphysa.2014.09.111. eprint: arXiv:1406.7522.

[165] Andy Goldschmidt et al. *Collision Geometry and Flow in Uranium+Uranium Collisions*. 2015. eprint: arXiv:1502.00603.

[166] D. d'Enterria et al. "Estimates of hadron azimuthal anisotropy from multiparton interactions in proton-proton collisions at sqrt(s) = 14 TeV". In: (2009). DOI: 10.1140/epjc/s10052-009-1232-7. eprint: arXiv:0910.3029.

[167] M. Alvioli, H. -J. Drescher, and M. Strikman. "A Monte Carlo generator of nucleon configurations in complex nuclei including Nucleon-Nucleon correlations". In: (2009). DOI: 10.1016/j.physletb.2009.08.067. eprint: arXiv:0905.2670.

[168] ALICE Collaboration. "Charged-particle multiplicity measurement in proton-proton collisions at $\sqrt{s} = 0.9$ and 2.36 TeV with ALICE at LHC". In: (2010). DOI: 10.1140/epjc/s10052-010-1339-x. eprint: arXiv:1004.3034.

[169] ALICE Collaboration. "Multi-particle azimuthal correlations in p-Pb and Pb-Pb collisions at the CERN Large Hadron Collider". In: (2014). DOI: 10.1103/PhysRevC.90.054901. eprint: arXiv:1406.2474.

[170] Ekaterina Retinskaya, Matthew Luzum, and Jean-Yves Ollitrault. "Constraining models of initial conditions with elliptic and triangular flow data". In: (2013). DOI: 10.1103/PhysRevC.89.014902. eprint: arXiv:1311.5339.

[171] Mikolaj Chojnacki et al. "THERMINATOR 2: THERMal heavy IoN generATOR 2". In: (2011). DOI: 10.1016/j.cpc.2011.11.018. eprint: arXiv:1102.0273.

[172] Maciej Rybczynski, Wojciech Broniowski, and Grzegorz Stefanek. "Influence of initial fluctuations on geometry measures in relativistic U-U and Cu-Au collisions". In: (2012). DOI: 10.1103/PhysRevC.87.044908. eprint: arXiv:1211.2537.

[173] Jonah E. Bernhard. *Bayesian parameter estimation for relativistic heavy-ion collisions*. 2018. eprint: arXiv:1804.06469.

[174] J. Scott Moreland, Jonah E. Bernhard, and Steffen A. Bass. "Estimating nucleon substructure properties in a unified model of p-Pb and Pb-Pb collisions". In: (2018). DOI: 10.1016/j.nuclphysa.2018.07.011. eprint: arXiv:1806.04802.

[175] Boxin Tang. "Orthogonal array-based Latin hypercubes". In: *Journal of the American statistical association* 88.424 (1993), pp. 1392–1397.

[176] Max D Morris and Toby J Mitchell. "Exploratory designs for computational experiments". In: *Journal of statistical planning and inference* 43.3 (1995), pp. 381–402.

[177] Michael E Tipping and Christopher M Bishop. "Mixtures of probabilistic principal component analyzers". In: *Neural computation* 11.2 (1999), pp. 443–482.

[178] Christopher KI Williams and Carl Edward Rasmussen. *Gaussian processes for machine learning*. Vol. 2. 3. MIT press Cambridge, MA, 2006.

[179] Nicholas Metropolis et al. "Equation of state calculations by fast computing machines". In: *The journal of chemical physics* 21.6 (1953), pp. 1087–1092.

[180] W Keith Hastings. "Monte Carlo sampling methods using Markov chains and their applications". In: (1970).

[181] ALICE Collaboration. "Centrality dependence of the charged-particle multiplicity density at mid-rapidity in Pb-Pb collisions at $\sqrt{s_{\mathrm{NN}}}$ = 2.76 TeV". In: (2010). DOI: 10.1103/PhysRevLett.106.032301. eprint: arXiv:1012.1657.

[182] ALICE Collaboration. "Higher harmonic anisotropic flow measurements of charged particles in Pb-Pb collisions at 2.76 TeV". In: (2011). DOI: 10.1103/PhysRevLett.107.032301. eprint: arXiv:1105.3865.

[183] ALICE Collaboration. "Centrality dependence of , K, p production in Pb-Pb collisions at $\sqrt{s_{\mathrm{NN}}}$ = 2.76 TeV". In: (2013). DOI: 10.1103/PhysRevC.88.044910. eprint: arXiv:1303.0737.

[184] ALICE Collaboration. "Event-by-event mean p_{T} fluctuations in pp and Pb-Pb collisions at the LHC". In: (2014). DOI: 10.1140/epjc/s10052-014-3077-y. eprint: arXiv:1407.5530.

[185] ALICE Collaboration. "Centrality dependence of the charged-particle multiplicity density at mid-rapidity in Pb-Pb collisions at $\sqrt{s_{\mathrm{NN}}}$ = 5.02 TeV". In: (2015). DOI: 10.1103/PhysRevLett.116.222302. eprint: arXiv:1512.06104.

[186] ALICE Collaboration. "Measurement of transverse energy at midrapidity in Pb-Pb collisions at $\sqrt{s_{\mathrm{NN}}}$ = 2.76 TeV". In: (2016). DOI: 10.1103/PhysRevC.94.034903. eprint: arXiv:1603.04775.

[187] ALICE Collaboration. "Anisotropic flow of charged particles in Pb-Pb collisions at $\sqrt{s_{\mathrm{NN}}}$ = 5.02 TeV". In: (2016). DOI: 10.1103/PhysRevLett.116.132302. eprint: arXiv:1602.01119.

[188] Charles Gale, Sangyong Jeon, and Bjoern Schenke. "Hydrodynamic Modeling of Heavy-Ion Collisions". In: (2013). DOI: 10.1142/S0217751X13400113. eprint: arXiv:1301.5893.

[189] Carl Eckart. "The thermodynamics of irreversible processes. III. Relativistic theory of the simple fluid". In: *Physical review* 58.10 (1940), p. 919.

[190] Akihiko Monnai. "Landau and Eckart frames for relativistic fluids in nuclear collisions". In: (2019). DOI: 10.1103/PhysRevC.100.014901. eprint: arXiv:1904.11940.

[191] L.D Landau and E.M Lifshitz. *Fluid mechanics*. Pergamon Press, 1963.

[192] Huichao Song. *Causal Viscous Hydrodynamics for Relativistic Heavy Ion Collisions*. 2009. eprint: arXiv:0908.3656.

[193] William A Hiscock and Lee Lindblom. "Stability and causality in dissipative relativistic fluids". In: *Annals of Physics* 151.2 (1983), pp. 466–496.

[194] William A Hiscock and Lee Lindblom. "Generic instabilities in first-order dissipative relativistic fluid theories". In: *Physical Review D* 31.4 (1985), p. 725.

[195] William A Hiscock and Lee Lindblom. "Linear plane waves in dissipative relativistic fluids". In: *Physical Review D* 35.12 (1987), p. 3723.

[196] Azwinndini Muronga. "Causal theories of dissipative relativistic fluid dynamics for nuclear collisions". In: *Phys. Rev. C* 69 (3 Mar. 2004), p. 034903. DOI: 10.1103/PhysRevC.69.034903. URL: https://link.aps.org/doi/10.1103/PhysRevC.69.034903.

[197] Werner Israel and John M Stewart. "Transient relativistic thermodynamics and kinetic theory". In: *Annals of Physics* 118.2 (1979), pp. 341–372.

[198] Werner Israel. "Nonstationary irreversible thermodynamics: a causal relativistic theory". In: *Annals of Physics* 100.1-2 (1976), pp. 310–331.

[199] B. Betz, D. Henkel, and D.H. Rischke. "From kinetic theory to dissipative fluid dynamics". In: *Progress in Particle and Nuclear Physics* 62.2 (2009). Heavy-Ion Collisions from the Coulomb Barrier to the Quark-Gluon Plasma, pp. 556–561. ISSN: 0146-6410. DOI: https://doi.org/10.1016/j.ppnp.2008.12.018. URL: https://www.sciencedirect.com/science/article/pii/S0146641008001361.

[200] Bjoern Schenke, Sangyong Jeon, and Charles Gale. "Higher flow harmonics from (3+1)D event-by-event viscous hydrodynamics". In: (2011). DOI: 10.1103/PhysRevC.85.024901. eprint: arXiv:1109.6289.

[201] Alexander Kurganov and Eitan Tadmor. "New high-resolution central schemes for nonlinear conservation laws and convection–diffusion equations". In: *Journal of computational physics* 160.1 (2000), pp. 241–282.

[202] R Naidoo and S Baboolal. "Application of the Kurganov–Levy semi-discrete numerical scheme to hyperbolic problems with nonlinear source terms". In: *Future Generation Computer Systems* 20.3 (2004), pp. 465–473.

[203] Lev Davidovich Landau. *Collected papers of LD Landau*. Pergamon, 1965.

[204] Yasumichi Aoki et al. "The order of the quantum chromodynamics transition predicted by the standard model of particle physics". In: *Nature* 443.7112 (2006), pp. 675–678.

[205] P Gerber and H Leutwyler. "Hadrons below the chiral phase transition". In: *Nuclear Physics B* 321.2 (1989), pp. 387–429.

[206] Pasi Huovinen and Péter Petreczky. "QCD equation of state and hadron resonance gas". In: *Nuclear Physics A* 837.1-2 (2010), pp. 26–53.

[207] Raju Venugopalan and Madappa Prakash. "Thermal properties of interacting hadrons". In: *Nuclear Physics A* 546.4 (1992), pp. 718–760.

[208] P. Huovinen and P. Petreczky. "QCD Equation of State and Hadron Resonance Gas". In: (2009). DOI: 10.1016/j.nuclphysa.2010.02.015. eprint: arXiv:0912.2541.

[209] C Bernard et al. "QCD equation of state with 2+ 1 flavors of improved staggered quarks". In: *Physical Review D* 75.9 (2007), p. 094505.

[210] M Cheng et al. "QCD equation of state with almost physical quark masses". In: *Physical Review D* 77.1 (2008), p. 014511.

[211] A. Bazavov et al. "Full nonperturbative QCD simulations with 2+1 flavors of improved staggered quarks". In: (2009). DOI: 10.1103/RevModPhys.82.1349. eprint: arXiv:0903.3598.

[212] C. Aubin et al. "Light hadrons with improved staggered quarks: approaching the continuum limit". In: (2004). DOI: 10.1103/PhysRevD.70.094505. eprint: arXiv:hep-lat/0402030.

[213] J. -P. Blaizot, E. Iancu, and A. Rebhan. "The entropy of the QCD plasma". In: (1999). DOI: 10.1103/PhysRevLett.83.2906. eprint: arXiv:hep-ph/9906340.

[214] J. -P. Blaizot, E. Iancu, and A. Rebhan. "Quark number susceptibilities from HTL-resummed thermodynamics". In: (2001). DOI: 10.1016/S0370-2693(01)01316-8. eprint: arXiv:hep-ph/0110369.

[215] Jens O. Andersen, Eric Braaten, and Michael Strickland. "Hard-thermal-loop Resummation of the Free Energy of a Hot Gluon Plasma". In: (1999). DOI: 10.1103/PhysRevLett.83.2139. eprint: arXiv:hep-ph/9902327.

[216] Jens O. Andersen, Michael Strickland, and Nan Su. "Gluon Thermodynamics at Intermediate Coupling". In: (2009). DOI: 10.1103/PhysRevLett.104.122003. eprint: arXiv:0911.0676.

[217] P. Petreczky. "Lattice QCD at finite temperature : present status". In: (2009). DOI: 10.1016/j.nuclphysa.2009.10.086. eprint: arXiv:0908.1917.

[218] Stephen Scott Adler et al. "Identified charged particle spectra and yields in Au+ Au collisions at s N N= 200 GeV". In: *Physical Review C* 69.3 (2004), p. 034909.

[219] Chun Shen et al. "Systematic parameter study of hadron spectra and elliptic flow from viscous hydrodynamic simulations of Au+Au collisions at $\sqrt{s_{NN}} = 200$ GeV". In: (2010). DOI: 10.1103/PhysRevC.82.054904. eprint: arXiv:1010.1856.

[220] Huichao Song and Ulrich Heinz. "Causal viscous hydrodynamics in 2+ 1 dimensions for relativistic heavy-ion collisions". In: *Physical Review C* 77.6 (2008), p. 064901.

[221] K. Dusling and D. Teaney. "Simulating elliptic flow with viscous hydrodynamics". In: *Phys. Rev. C* 77 (3 Apr. 2008), p. 034905. DOI: 10.1103/PhysRevC.77.034905. URL: https://link.aps.org/doi/10.1103/PhysRevC.77.034905.

[222] Laszlo P. Csernai, Joseph. I. Kapusta, and Larry D. McLerran. "On the Strongly-Interacting Low-Viscosity Matter Created in Relativistic Nuclear Collisions". In: (2006). DOI: 10.1103/PhysRevLett.97.152303. eprint: arXiv:nucl-th/0604032.

[223] Gabriel Denicol, Akihiko Monnai, and Bjoern Schenke. "Moving forward to constrain the shear viscosity of QCD matter". In: (2015). DOI: 10.1103/PhysRevLett.116.212301. eprint: arXiv:1512.01538.

[224] Jussi Auvinen et al. "Temperature dependence of η/s of strongly interacting matter: effects of the equation of state and the parametric form of $(\eta/s)(T)$". In: (2020). DOI: 10.1103/PhysRevC.102.044911. eprint: arXiv:2006.12499.

[225] PHENIX Collaboration and S. S. Adler. "Systematic Studies of the Centrality and $\sqrt{s_{NN}}$ Dependence of dE_T/δ and dN_{ch}/δ in Heavy Ion Collisions at Mid-rapidity". In: (2004). DOI: 10.1103/PhysRevC.71.03490810.1103/PhysRevC.71.049901. eprint: arXiv:nucl-ex/0409015.

[226] STAR Collaboration. "Azimuthal anisotropy in Au+Au collisions at $\sqrt{s_{NN}}$ = 200 GeV". In: (2004). DOI: 10.1103/PhysRevC.72.014904. eprint: arXiv:nucl-ex/0409033.

[227] ALICE Collaboration. "Centrality dependence of the charged-particle multiplicity density at mid-rapidity in Pb-Pb collisions at $\sqrt{s_{NN}}$ = 2.76 TeV". In: (2010). DOI: 10.1103/PhysRevLett.106.032301. eprint: arXiv:1012.1657.

[228] ALICE Collaboration. "Centrality dependence of the charged-particle multiplicity density at mid-rapidity in Pb-Pb collisions at $\sqrt{s_{NN}}$ = 5.02 TeV". In: (2015). DOI: 10.1103/PhysRevLett.116.222302. eprint: arXiv:1512.06104.

[229] ALICE Collaboration. "Anisotropic flow of charged particles in Pb-Pb collisions at $\sqrt{s_{NN}}$ = 5.02 TeV". In: (2016). DOI: 10.1103/PhysRevLett.116.132302. eprint: arXiv:1602.01119.

[230] PHENIX Collaboration and S. S. Adler. "Identified Charged Particle Spectra and Yields in Au+Au Collisions at $\sqrt{s_{NN}}$ = 200 GeV". In: (2003). DOI: 10.1103/PhysRevC.69.034909. eprint: arXiv:nucl-ex/0307022.

[231] ALICE Collaboration. "Centrality dependence of π, K, p production in Pb-Pb collisions at $\sqrt{s_{NN}}$ = 2.76 TeV". In: (2013). DOI: 10.1103/PhysRevC.88.044910. eprint: arXiv:1303.0737.

[232] M. Byres et al. "The Skinny on Bulk Viscosity and Cavitation in Heavy Ion Collisions". In: (2019). DOI: 10.1103/PhysRevC.101.044902. eprint: arXiv:1910.12930.

[233] Peter Arnold, Guy D. Moore, and Laurence G. Yaffe. "Transport coefficients in high temperature gauge theories: (I) Leading-log results". In: (2000). DOI: 10.1088/1126-6708/2000/11/001. eprint: arXiv:hep-ph/0010177.

[234] Peter Arnold, Guy D. Moore, and Laurence G. Yaffe. "Transport coefficients in high temperature gauge theories: (II) Beyond leading log". In: (2003). DOI: 10.1088/1126-6708/2003/05/051. eprint: arXiv:hep-ph/0302165.

[235] Peter Arnold, Caglar Dogan, and Guy D. Moore. "The Bulk Viscosity of High-Temperature QCD". In: (2006). DOI: 10.1103/PhysRevD.74.085021. eprint: arXiv:hep-ph/0608012.

[236] Egang Lu and Guy D. Moore. "The Bulk Viscosity of a Pion Gas". In: (2011). DOI: 10.1103/PhysRevC.83.044901. eprint: arXiv:1102.0017.

[237] Antonio Dobado, Felipe J. Llanes-Estrada, and Juan M. Torres-Rincon. "Bulk viscosity of low-temperature strongly interacting matter". In: *Physics Letters B* 702.1 (2011), pp. 43–48. ISSN: 0370-2693. DOI: 10.1016/j.physletb.2011.06.059. eprint: arXiv:1103.0735. URL: https://www.sciencedirect.com/science/article/pii/S0370269311007143.

[238] Sangwook Ryu et al. "Effects of bulk viscosity and hadronic rescattering in heavy ion collisions at energies available at the BNL Relativistic Heavy Ion Collider and at the CERN Large Hadron Collider". In: *Phys. Rev. C* 97.3 (2018), p. 034910. DOI: 10.1103/PhysRevC.97.034910. arXiv: 1704.04216 [nucl-th].

[239] Björn Schenke, Chun Shen, and Prithwish Tribedy. "Multi-particle and charge-dependent azimuthal correlations in heavy-ion collisions at the Relativistic Heavy-Ion Collider". In: *Phys. Rev. C* 99.4 (2019), p. 044908. DOI: 10.1103/PhysRevC.99.044908. arXiv: 1901.04378 [nucl-th].

[240] Bjoern Schenke, Chun Shen, and Prithwish Tribedy. "Running the gamut of high energy nuclear collisions". In: *Phys. Rev. C* 102.4 (2020), p. 044905. DOI: 10.1103/PhysRevC.102.044905. arXiv: 2005.14682 [nucl-th].

[241] Josef Bobek and Iurii Karpenko. *Bulk pressure in fluid-dynamical simulations of Pb-Pb and p-Pb collisions at the LHC energies*. 2022. eprint: arXiv:2205.05358.

[242] S. Ryu et al. "Importance of the Bulk Viscosity of QCD in Ultrarelativistic Heavy-Ion Collisions". In: *Phys. Rev. Lett.* 115.13 (2015), p. 132301. DOI: 10.1103/PhysRevLett.115.132301. arXiv: 1502.01675 [nucl-th].

[243] GS Denicol et al. "Derivation of transient relativistic fluid dynamics from the Boltzmann equation". In: *Physical Review D* 85.11 (2012), p. 114047.

[244] E Molnár et al. "Relative importance of second-order terms in relativistic dissipative fluid dynamics". In: *Physical Review D* 89.7 (2014), p. 074010.

[245] GS Denicol, S Jeon, and C Gale. "Transport coefficients of bulk viscous pressure in the 14-moment approximation". In: *Physical Review C* 90.2 (2014), p. 024912.

[246] Fred Cooper and Graham Frye. "Single-particle distribution in the hydrodynamic and statistical thermodynamic models of multiparticle production". In: *Physical Review D* 10.1 (1974), p. 186.

[247] James L Anderson and HR Witting. "A relativistic relaxation-time model for the Boltzmann equation". In: *Physica* 74.3 (1974), pp. 466–488.

[248] Amaresh Jaiswal, Radoslaw Ryblewski, and Michael Strickland. "Transport coefficients for bulk viscous evolution in the relaxation-time approximation". In: *Physical Review C* 90.4 (2014), p. 044908.

[249] Piotr Bożek. "Bulk and shear viscosities of matter created in relativistic heavy-ion collisions". In: *Physical Review C* 81.3 (2010), p. 034909.

[250] Kevin Dusling and Thomas Schäfer. "Bulk viscosity, particle spectra, and flow in heavy-ion collisions". In: *Physical Review C* 85.4 (2012), p. 044909.

[251] Derek Teaney. "Effect of shear viscosity on spectra, elliptic flow, and Hanbury Brown–Twiss radii". In: *Physical Review C* 68.3 (2003), p. 034913. DOI: 10.1103/PhysRevC.68.034913. eprint: arXiv:nucl-th/0301099.

[252] Shen Chun. *CHUNSHEN1987/ISS: Monte Carlo Sampler for particle distribution from Cooper-Frye Freeze-Out procedure*. URL: https://github.com/chunshen1987/iSS.

[253] Dmytro Oliinychenko et al. *smash-transport/smash: SMASH-2.2*. Version SMASH-2.2. May 2022. DOI: 10.5281/zenodo.6535237. URL: https://doi.org/10.5281/zenodo.6535237.

[254] Torbjörn Sjöstrand, Stephen Mrenna, and Peter Skands. "PYTHIA 6.4 physics and manual". In: *Journal of High Energy Physics* 2006.05 (2006), p. 026.

[255] Richard P Feynman. "The behavior of hadron collisions at extreme energies". In: *Special Relativity and Quantum Theory*. Springer, 1988, pp. 289–304.

[256] Henry W Kendall. "Deep Inelastic Scattering: Experiments on the Proton and the Observation of Scaling". In: *A Distant Light*. Springer, 2000, pp. 94–126.

[257] Gregg Jaeger. "Are virtual particles less real?" In: *Entropy* 21.2 (2019), p. 141.

[258] C. Adloff and H1 Collaboration. "Measurement of Neutral and Charged Current Cross-Sections in Positron-Proton Collisions at Large Momentum Transfer". In: (1999). DOI: 10.1007/s100520050721. eprint: arXiv:hep-ex/9908059.

[259] H1 Collaboration and C. Adloff. "Measurement of Neutral and Charged Current Cross Sections in Electron-Proton Collisions at High Q^2". In: (2000). DOI: 10.1007/s100520100607. eprint: arXiv:hep-ex/0012052.

[260] H1 Collaboration and C. Adloff. "Deep-Inelastic Inclusive ep Scattering at Low x and a Determination of α_s". In: (2000). DOI: 10.1007/s100520100720. eprint: arXiv:hep-ex/0012053.

[261] ZEUS Collaboration. "Measurement of the neutral current cross section and F_2 structure function for deep inelastic $e+p$ scattering at HERA". In: (2001). DOI: 10.1007/s100520100749. eprint: arXiv:hep-ex/0105090.

[262] A. Cooper-Sarkar. *ZEUS NLO QCD fits*. 2001. eprint: arXiv:hep-ph/0110386.

[263] Alberto C Benvenuti et al. "A high statistics measurement of the proton structure functions F2 (x, Q2) and R from deep inelastic muon scattering at high Q2". In: *Physics Letters B* 223.3-4 (1989), pp. 485–489.

[264] The New Muon Collaboration. "Measurement of the proton and deuteron structure functions, F2p and F2d, and of the ratio sigma(L)/sigma(T)". In: (1996). DOI: 10.1016/S0550-3213(96)00538-X. eprint: arXiv:hep-ph/9610231.

[265] The New Muon Collaboration. "Accurate Measurement of F2d/F2p and Rd-Rp". In: (1996). DOI: 10.1016/S0550-3213(96)00673-6. eprint: arXiv:hep-ex/9611022.

[266] D0 Collaboration and B. Abbott. "Inclusive Jet Production in $\overline{p}p$ Collisions". In: (2000). DOI: 10.1103/PhysRevLett.86.1707. eprint: arXiv:hep-ex/0011036.

[267] D0 collaboration and B. Abbott. "High-p_T Jets in pbarp Collisions at $\sqrt{s}$ = 630 and 1800 GeV". In: (2000). DOI: 10.1103/PhysRevD.64.032003. eprint: arXiv:hep-ex/0012046.

[268] T. Affolder. "Measurement of the Inclusive Jet Cross Section in $\bar{p}p$ collisions at $\sqrt{s}$ = 1.8 TeV". In: (2001). DOI: 10.1103/PhysRevD.64.03200110.1103/PhysRevD.65.039903. eprint: arXiv:hep-ph/0102074.

[269] FNAL E866/NuSea Collaboration et al. "Improved Measurement of the $\bar{d}/\bar{u}$ Asymmetry in the Nucleon Sea". In: (2001). DOI: 10.1103/PhysRevD.64.052002. eprint: arXiv:hep-ex/0103030.

[270] G Moreno et al. "Dimuon production in proton-copper collisions at $\sqrt{s}$ = 38.8 GeV". In: *Physical Review D* 43.9 (1991), p. 2815.

[271] CCFR/NuTeV Collaboration, : and U. K. Yang. "Measurements of F_2 and $xF_3(\nu) - xF_3(\overline{\nu})$ from CCFR ν_μ-Fe and $\overline{\nu_\mu}$-Fe data in a physics model independent way". In: (2000). DOI: 10.1103/PhysRevLett.86.2742. eprint: arXiv:hep-ex/0009041.

[272] WG Seligman et al. "Improved Determination of α s From Neutrino-Nucleon Scattering". In: *Physical Review Letters* 79.7 (1997), p. 1213.

[273] F. Abe et. al and The CDF Collaboration. "Measurement of the lepton charge asymmetry in W-boson decays produced in p-pbar collisions". In: (1998). DOI: 10.1103/PhysRevLett.81.5754. eprint: arXiv:hep-ex/9809001.

[274] J. Pumplin et al. "New Generation of Parton Distributions with Uncertainties from Global QCD Analysis". In: (2002). DOI: 10.1088/1126-6708/2002/07/012. eprint: arXiv:hep-ph/0201195.

[275] Daniel Stump et al. "Inclusive Jet Production, Parton Distributions, and the Search for New Physics". In: (2003). DOI: 10.1088/1126-6708/2003/10/046. eprint: arXiv:hep-ph/0303013.

[276] K. J. Eskola, H. Paukkunen, and C. A. Salgado. "EPS09 - a New Generation of NLO and LO Nuclear Parton Distribution Functions". In: (2009). DOI: 10.1088/1126-6708/2009/04/065. eprint: arXiv:0902.4154.

[277] M. Hirai, S. Kumano, and T. -H. Nagai. "Determination of nuclear parton distribution functions and their uncertainties at next-to-leading order". In: (2007). DOI: 10.1103/PhysRevC.76.065207. eprint: arXiv:0709.3038.

[278] T. Sjöstrand and P. Skands. "Transverse-Momentum-Ordered Showers and Interleaved Multiple Interactions". In: (2004). DOI: 10.1140/epjc/s2004-02084-y. eprint: arXiv:hep-ph/0408302.

[279] Torbjörn Sjöstrand and Maria van Zijl. "A multiple-interaction model for the event structure in hadron collisions". In: *Physical Review D* 36.7 (1987), p. 2019.

[280] VV93350 Sudakov. "Vertex parts at very high energies in quantum electrodynamics". In: *Zh. Eksp. Teor. Fiz.* 3 (1956), pp. 65–71.

[281] Toichiro Kinoshita. "Mass singularities of Feynman amplitudes". In: *Journal of Mathematical Physics* 3.4 (1962), pp. 650–677.

[282] Tsung-Dao Lee and Michael Nauenberg. "Degenerate systems and mass singularities". In: *Physical Review* 133.6B (1964), B1549.

[283] Guido Altarelli and Giorgio Parisi. "Asymptotic freedom in parton language". In: *Nuclear Physics B* 126.2 (1977), pp. 298–318.

[284] Yu L Dokshitser. "Calculation of structure functions of deep-inelastic scattering and e+ e-annihilation by perturbation theory in quantum chromodynamics". In: *Soviet Journal of Experimental and Theoretical Physics* 46 (1977), p. 641.

[285] Vladimir Naumovich Gribov and Lev N Lipatov. *Deep inelastic e p-scattering in a perturbation theory.* Tech. rep. Inst. of Nuclear Physics, Leningrad, 1972.

[286] Shanshan Cao and Abhijit Majumder. "Nuclear modification of leading hadrons and jets within a virtuality ordered parton shower". In: (2017). DOI: 10.1103/PhysRevC.101.024903. eprint: arXiv:1712.10055.

[287] Stefan Höche. *Introduction to parton-shower event generators.* 2014. eprint: arXiv:1411.4085.

[288] Xin-Nian Wang and Xiaofeng Guo. "Multiple Parton Scattering in Nuclei: Parton Energy Loss". In: (2001). DOI: 10.1016/S0375-9474(01)01130-7. eprint: arXiv:hep-ph/0102230.

[289] A. Majumder. *The in-medium scale evolution in jet modification.* 2009. eprint: arXiv:0901.4516.

[290] Zhong-Bo Kang et al. "Jet quenching phenomenology from soft-collinear effective theory with Glauber gluons". In: (2014). DOI: 10.1103/PhysRevLett.114.092002. eprint: arXiv:1405.2612.

[291] Xiaofeng Guo and Xin-Nian Wang. "Multiple Scattering, Parton Energy Loss and Modified Fragmentation Functions in Deeply Inelastic eA Scattering". In: (2000). DOI: 10.1103/PhysRevLett.85.3591. eprint: arXiv:hep-ph/0005044.

[292] Abhijit Majumder. "Hard collinear gluon radiation and multiple scattering in a medium". In: (2009). DOI: 10.1103/PhysRevD.85.014023. eprint: arXiv:0912.2987.

[293] P. Aurenche, B. G. Zakharov, and H. Zaraket. "Failure of the collinear expansion in calculation of the induced gluon emission". In: (2008). DOI: 10.1134/S0021364008110039. eprint: arXiv:0804.4282.

[294] P. Aurenche, B. G. Zakharov, and H. Zaraket. *Comment on "Success of collinear expansion in the calculation of induced gluon emission"*. 2008. eprint: arXiv:0806.0160.

[295] Tan Luo et al. "Multiple jets and γ-jet correlation in high-energy heavy-ion collisions". In: (2018). DOI: 10.1016/j.physletb.2018.06.025. eprint: arXiv:1803.06785.

[296] Yayun He et al. "Interplaying mechanisms behind single inclusive jet suppression in heavy-ion collisions". In: (2018). DOI: 10.1103/PhysRevC.99.054911. eprint: arXiv:1809.02525.

[297] Wei Chen et al. "Effects of jet-induced medium excitation in γ-hadron correlation in A+A collisions". In: (2017). DOI: 10.1016/j.physletb.2017.12.015. eprint: arXiv:1704.03648.

[298] Ben-Wei Zhang, Enke Wang, and Xin-Nian Wang. "Heavy Quark Energy Loss in Nuclear Medium". In: (2003). DOI: 10.1103/PhysRevLett.93.072301. eprint: arXiv:nucl-th/0309040.

[299] Shanshan Cao et al. "Linearized Boltzmann transport model for jet propagation in the quark-gluon plasma: Heavy quark evolution". In: (2016). DOI: 10.1103/PhysRevC.94.014909. eprint: arXiv:1605.06447.

[300] RD Field and Richard Phillips Feynman. "A parametrization of the properties of quark jets". In: *Nuclear Physics B* 136.1 (1978), pp. 1–76.

[301] Bryan R Webber. "A QCD model for jet fragmentation including soft gluon interference". In: *Nuclear Physics B* 238.3 (1984), pp. 492–528.

[302] Bo Andersson et al. "Is there screwiness at the end of the QCD cascades?" In: *Journal of High Energy Physics* (July 1998), p. 014. DOI: 10.1088/1126-6708/1998/09/014.

[303] Bo Andersson et al. "Parton fragmentation and string dynamics". In: *Physics Reports* 97.2-3 (1983), pp. 31–145.

[304] Gunnar S Bali. "QCD forces and heavy quark bound states". In: *Physics Reports* 343.1-2 (2001), pp. 1–136.

[305] Gavin P. Salam. "Towards Jetography". In: (2009). DOI: 10.1140/epjc/s10052-010-1314-6. eprint: arXiv:0906.1833.

[306] Ryan Atkin. "Review of jet reconstruction algorithms". In: *Journal of Physics: Conference Series* 645.1 (Sept. 2015), p. 012008. DOI: 10.1088/1742-6596/645/1/012008. URL: https://dx.doi.org/10.1088/1742-6596/645/1/012008.

[307] G Arnison et al. "Hadronic jet production at the CERN proton-antiproton collider". In: *Physics Letters B* 132.1-3 (1983), pp. 214–222.

[308] Gerald C. Blazey et al. *Run II Jet Physics: Proceedings of the Run II QCD and Weak Boson Physics Workshop*. 2000. eprint: arXiv:hep-ex/0005012.

[309] Gavin P. Salam and Gregory Soyez. "A practical Seedless Infrared-Safe Cone jet algorithm". In: (2007). DOI: 10.1088/1126-6708/2007/05/086. eprint: arXiv:0704.0292.

[310] Matteo Cacciari, Gavin P. Salam, and Gregory Soyez. "FastJet user manual". In: (2011). DOI: 10.1140/epjc/s10052-012-1896-2. eprint: arXiv:1111.6097.

[311] Matteo Cacciari, Gavin P. Salam, and Gregory Soyez. "The anti-k_T jet clustering algorithm". In: (2008). DOI: 10.1088/1126-6708/2008/04/063. eprint: arXiv:0802.1189.

[312] Stefano Catani et al. "Longitudinally-invariant k_T-clustering algorithms for hadron-hadron collisions". In: *Nuclear Physics B* 406.1-2 (1993), pp. 187–224.

[313] CMS collaboration et al. *A Cambridge-Aachen (CA) based jet algorithm for boosted top-jet tagging*. Tech. rep. CMS-PAS-JME-09-001, 2009.

[314] Matteo Cacciari and Gavin P Salam. "Pileup subtraction using jet areas". In: *Physics Letters B* 659.1-2 (2008), pp. 119–126.

[315] Matteo Cacciari et al. "Jet reconstruction in heavy ion collisions". In: *The European Physical Journal C* 71.1 (2011), pp. 1–21.

[316] ALICE Collaboration. "Measurement of charged jet suppression in Pb-Pb collisions at $\sqrt{s_{\mathrm{NN}}}$ = 2.76 TeV". In: (2013). DOI: 10.1007/JHEP03(2014)013. eprint: arXiv:1311.0633.

[317] STAR Collaboration. "Measurement of inclusive charged-particle jet production in Au+Au collisions at $\sqrt{s_{NN}}$=200 GeV". In: (2020). DOI: 10.1103/PhysRevC.102.054913. eprint: arXiv:2006.00582.

[318] Bjoern Schenke, Prithwish Tribedy, and Raju Venugopalan. "Fluctuating Glasma initial conditions and flow in heavy ion collisions". In: (2012). DOI: 10.1103/PhysRevLett.108.252301. eprint: arXiv:1202.6646.

[319] Björn Schenke, Chun Shen, and Prithwish Tribedy. "Features of the IP-Glasma". In: *Nuclear Physics A* 982 (Feb. 2019), pp. 435–438. DOI: 10.1016/j.nuclphysa.2018.08.015.

[320] Jia Liu, Chun Shen, and Ulrich W. Heinz. *Pre-equilibrium evolution effects on heavy-ion collision observables*. 2015. eprint: arXiv:1504.02160.

[321] Victor Ambrus et al. "Fast kinetic simulator for relativistic matter". In: (2022). DOI: 10.1038/s43588-022-00333-x. eprint: arXiv:2201.09277.

[322] P. Batyuk et al. "Correlation femtoscopy study at energies available at the JINR Nuclotron-based Ion Collider fAcility and the BNL Relativistic Heavy Ion Collider within a viscous hydrodynamic plus cascade model". In: *Phys. Rev. C* 96 (2 Aug. 2017), p. 024911. DOI: 10.1103/PhysRevC.96.024911. URL: https://link.aps.org/doi/10.1103/PhysRevC.96.024911.

[323] ALICE Collaboration. "Multi-strange baryon production at mid-rapidity in Pb-Pb collisions at $\sqrt{s_{\mathrm{NN}}}$ = 2.76 TeV". In: (2013). DOI: 10.1016/j.physletb.2013.11.048. eprint: arXiv:1307.5543.

[324] ALICE Collaboration. "K*(892)^0 and Φ(1020) production in Pb-Pb collisions at $\sqrt{s_{\mathrm{NN}}}$ = 2.76 TeV". In: (2014). DOI: 10.1103/PhysRevC.91.024609. eprint: arXiv:1404.0495.

[325] Anton Andronic et al. "Decoding the phase structure of QCD via particle production at high energy". In: *Nature* 561.7723 (2018), pp. 321–330.

[326] ALICE Collaboration. "First measurement of jet mass in Pb-Pb and p-Pb collisions at the LHC". In: (2017). DOI: 10.1016/j.physletb.2017.11.044. eprint: arXiv:1702.00804.

[327] Yen-Jie Lee. "Jet quenching at RHIC and the LHC". In: *Journal of Physics Conference Series* 446 (Sept. 2013), pp. 2001–. DOI: 10.1088/1742-6596/446/1/012001.

[328] ATLAS Collaboration. "Measurements of the Nuclear Modification Factor for Jets in Pb+Pb Collisions at $\sqrt{s_{\mathrm{NN}}}$ = 2.76 TeV with the ATLAS Detector". In: (2014). DOI: 10.1103/PhysRevLett.114.072302. eprint: arXiv:1411.2357.

[329] ATLAS Collaboration. "Measurement of the nuclear modification factor for inclusive jets in Pb+Pb collisions at $\sqrt{s_{\mathrm{NN}}}$ = 5.02 TeV with the ATLAS detector". In: (2018). DOI: 10.1016/j.physletb.2018.10.076. eprint: arXiv:1805.05635.

[330] CMS Collaboration. "Measurement of inclusive jet cross sections in pp and PbPb collisions at sqrt(s[NN]) = 2.76 TeV". In: (2016). DOI: 10.1103/PhysRevC.96.015202. eprint: arXiv:1609.05383.

[331] ALICE Collaboration. "Measurements of inclusive jet spectra in pp and central Pb-Pb collisions at $\sqrt{s_{\mathrm{NN}}}$ = 5.02 TeV". In: (2019). DOI: 10.1103/PhysRevC.101.034911. eprint: arXiv:1909.09718.

[332] Iu Karpenko, Pasi Huovinen, and Marcus Bleicher. "A 3+1 dimensional viscous hydrodynamic code for relativistic heavy ion collisions". In: *Computer Physics Communications* 185.11 (2014), pp. 3016–3027.

Appendix A

Theoretical Part

A.1 Natural units

Natural units are a system of units based on universal physical constants in some way. The common way to construct a natural system of units is putting some universal constants equal to one (i.e., $c = \hbar = 1$). However, there are some relations between constants. For example, the fine structure constant,

$$\alpha = \frac{1}{4\pi\varepsilon_0}\frac{e^2}{\hbar c} = k_e\frac{e^2}{\hbar c},$$

is dependent on speed of light, c, reduced Planck constant, $\hbar = \frac{h}{2\pi}$, elementary electric charge, e, and Coulomb constant, $k_e = \frac{1}{4\pi\varepsilon_0}$, where ε_0 is the permittivity in vacuum. Those relations put constrains on the systems of natural units. For example, it is not possible to create a system where $c = \hbar = k_e = e = 1$ since it would mean that $\alpha = 1$ and as the fine structure constant $\alpha \approx \frac{1}{137}$ is a dimensionless constant that cannot be rescaled further.

The examples of the most known systems of natural units can be seen in Table A.1. This work is using the Planck system of natural units. However, the elementary charge e is referred as it is, without expressing it through the fine structure constant relation.

Table A.1: Values of some physical constants in different natural unit systems.

Quantity	Planck	Stoney	Schrödinger	Hartee	Dirac	Stille
c	1	1	$\frac{1}{\alpha}$	$\frac{1}{\alpha}$	1	1
$\hbar$	1	$\frac{1}{\alpha}$	1	1	$\frac{1}{\alpha}$	$\frac{1}{\alpha}$
G	1	1	1	G	G	G
k_B	1	1	1	1	1	1
k_e	1	1	1	1	1	1
e	$\sqrt{\alpha}$	1	1	1	1	1
m_e	m_e	m_e	m_e	1	1	m_e
m_p	m_p	m_p	m_p	m_p	m_p	1

When one puts certain constants equal to one, it has some interesting implications on the units of some quantities. For example, the familiar relativistic energy formula

$$E^2 = \vec{p}^2c^2 + m^2c^4,$$

is in natural units ($c = 1$) expressed as

$$E^2 = \vec{p}^2 + m^2,$$

where $\vec{p}$ is momentum and m is the mass. Since the squares of the units of those three quantities must be the same, the units of those quantities follow

$$[E] = [p] = [m],$$

where $[\cdot]$ gives the units of a given quantity. One has to express all three quantities with the same units. Those units are units of energy and the consensus is that they are expressed in electonvolts (eV). With a similar approach, one can continue and use the formulae to express physical quantities in consistent units.

Table A.2 represents the units of quantities in the International System of Units (SI) and in the system of Planck's natural units. Quantities are expressed as some integer power of energy units. Zeroth power is also included, since some quantities like velocity β or angular momentum L became dimensionless. Differences between this work and Table A.2 are that the time and length are expressed in femtometres (fm=$10^{-15}\times$m). This is because the femtometre is the most convenient scale of nuclear and particle physics. Furthermore, the cross section is expressed either as fm^{-2} or barn b.

Table A.2: Physical quantities, their SI units, their natural units, and their corresponding factor for dimensional analysis.

Quantity	SI	Natural	Factor
Energy E	kg m^2 s^{-2}	eV	1
Mass m	kg	eV	c^{-2}
Momentum p	kg m s^{-1}	eV	c^{-1}
Length l	m	eV^{-1}	$\hbar c$
Time t	s	eV^{-1}	$\hbar$
Velocity $v = \beta$	m s^{-1}	-	c
Angular momentum L	kg m^2 s^{-1}	-	$\hbar$
Cross section σ	m^2	eV^{-2}	$(\hbar c)^2$
Force F	kg m s^{-2}	eV^2	$(\hbar c)^{-1}$
Charge Q	C = A s	-	1
Temperature T	K	eV	k_B^{-1}

It is possible to reverse the process and put the universal constants back into the equations, so there can be done some quantitative calculations. One can simply use the factors that are displayed in the Table A.2 or use dimensional analysis. The dimensional analysis is a powerful tool that can be also used to derive the exact expression of some formulae. For example, Bekenstein-Hawking law describes that the entropy of the black hole is proportional to Schwarzschild area of the black hole. With dimensional analysis, the exact expression can be simply derived as

$$S_{\mathrm{BH}} = \frac{c^3}{4G\hbar} A_s.$$

A.2 Special relativity

The Minkowski metric in this work reads as

$$\eta = \begin{pmatrix} 1 & 0 & 0 & 0 \\ 0 & -1 & 0 & 0 \\ 0 & 0 & -1 & 0 \\ 0 & 0 & 0 & -1 \end{pmatrix}.$$

In the special relativity there are covariant vectors X_μ and contravariant vectors denoted as X^μ. It is possible to use Minkowski metric $\eta^{\mu\nu} = \eta_{\mu\nu}$ to chnge covariant vector to contravariant

$$X^\mu = \eta^{\mu\nu} X_\mu$$

and vice versa

$$X_\mu = \eta_{\mu\nu} X^\nu,$$

where this implies $\eta^{\mu\gamma}\eta_{\gamma\nu} = \mathbb{I}_4$ as a simple property of Minkowski metric. There can be covariant and contravariant tensors with arbitrary rank ($Y_{\mu\nu\gamma\ldots}$ and $Y^{\mu\nu\gamma\cdots}$). However, in special relativity, the most common tensors are of rank 1 or 2. Rank 1 tensors are called four-vectors.

Lorentz tensors from special relativity are transformed via Lorentz transformation Λ. Every Lorentz transformation can be expressed as a square 4×4 matrix $\Lambda_{\mu\nu}$. Lorentz transformations form a group called Lorentz group. Lorentz transformations keep quadratic form

$$\left(X^\mu\right)\cdot\left(X^\nu\right) = X^\mu \eta_{\mu\nu} X^\nu$$

invariant. The signature of this quadratic form is (1,3) and it is often incorrectly referred as an inner product. However, since the axiom $\left(X^\mu\right)\cdot\left(X^\nu\right) \geq 0$ is not fulfilled, it cannot be called an inner product. Quadratic form can be referred as a pseudo-inner product. If the quadratic form $\left(X^\mu\right)\cdot\left(X^\nu\right) > 0$, the four-vector X^μ is called a timelike vector since its time component (X^0) is dominant. If the pseudo-inner product $\left(X^\mu\right)\cdot\left(X^\nu\right) < 0$, the four-vector X^μ is called a spacelike vector since its space components (X^1, X^2, X^3) are dominant. In the case of nonzero vectors X^μ, if $\left(X^\mu\right)\cdot\left(X^\nu\right) = 0$ the vectors are referred as null vectors that are parallel to the light cone. That is why null vectors are also called light vectors.

From the invariance of the spacetime interval, one can obtain the condition for Lorentz transformation as

$$\eta = \Lambda^T \eta \Lambda.$$

Then one can proceed and transform the vector $\left(X^\nu\right)$ as

$$X'_\mu = \Lambda_{\mu\nu} X^\nu$$

or make a reverse transformation of vector $\left(X'^\nu\right)$

$$X_\mu = \Lambda^{-1}_{\nu\mu} X'^\nu.$$

Part of the Lorentz group are 3D rotations that are solely represented by SO(3) group. The next part of the Lorentz group is the boost. Boost is a relative motion with constant velocity transformation without rotation. The Lorentz boost transformation with velocity $\vec{v}$ parallel to the

$x-$axis is

$$\Lambda_{\text{boost}} = \begin{pmatrix} \gamma & -\gamma\beta & 0 & 0 \\ -\gamma\beta & \gamma & 0 & 0 \\ 0 & 0 & 1 & 0 \\ 0 & 0 & 0 & 1 \end{pmatrix},$$

where

$$\gamma = \frac{1}{\sqrt{1-\beta^2}}, \qquad \beta = ||\vec{v}||.$$

Equivalently, the Lorentz boost transformation can be expressed with rapidity $\mathscr{Y} = \operatorname{arctanh}\beta$ as follows

$$\Lambda_{\text{boost}} = \begin{pmatrix} \cosh\mathscr{Y} & -\sinh\mathscr{Y} & 0 & 0 \\ -\sinh\mathscr{Y} & \cosh\mathscr{Y} & 0 & 0 \\ 0 & 0 & 1 & 0 \\ 0 & 0 & 0 & 1 \end{pmatrix}.$$

The final two components are time reversal and parity transformation

$$\Lambda_{\text{time}} = \left(T^{\mu}{}_{\nu}\right) = \begin{pmatrix} -1 & 0 & 0 & 0 \\ 0 & 1 & 0 & 0 \\ 0 & 0 & 1 & 0 \\ 0 & 0 & 0 & 1 \end{pmatrix}, \qquad \Lambda_{\text{parity}} = \left(P^{\mu}{}_{\nu}\right) = \begin{pmatrix} 1 & 0 & 0 & 0 \\ 0 & -1 & 0 & 0 \\ 0 & 0 & -1 & 0 \\ 0 & 0 & 0 & -1 \end{pmatrix}.$$

One can use multiple transformations from a given transformation group and the final transformation will be an element of the transformation group. Combination of rotation and boost is called a proper orthochronous Lorentz transformation. The combination of a proper orthochronous Lorentz transformation and time reversal is called a proper antichronous Lorentz transformation. The combination of a proper orthochronous Lorentz transformation and parity transformation is called an improper orthochronous Lorentz transformation. Finally, the combination of proper orthochronous Lorentz transformation, time reversal, and parity transformation is called an improper antichronous Lorentz transformation. If one adds translation transformations to the Lorentz group, then the resulting group is called the Poincaré group.

Four-vector, also called Lorentz vectors, are an essential part of the special theory of relativity. The most basic four-vector is called an event and it represents a point in the Minkowski space

$$\left(x^{\mu}\right) \equiv x = (t, x, y, z).$$

Four-velocity is event under the derivative with respect to the proper time τ

$$\left(u^{\mu}\right) = \left(\frac{\mathrm{d}x^{\mu}}{\mathrm{d}\tau}\right) = (\gamma, \gamma\vec{v}),$$

since the $\frac{\mathrm{d}t}{\mathrm{d}\tau} = \gamma$. Four-momentum is defined as four-velocity multiplied by the invariant mass

$$\left(p^{\mu}\right) \equiv m\left(u^{\mu}\right) = (E, \vec{p}),$$

since $\gamma m = E$. One can analogically derive four-force or four-acceleration. However, they are not necessary to introduce in this work. Furthermore, one can find the conserved charges like baryon number or electric charge and define their four-vector. The four-baryon number flux is defined as

$$N^{\mu} = n u^{\mu},$$

where n is the baryon density. Similarly, the four-current is

$$(J^\mu) = \rho\,(u^\mu) = (\rho, \vec{j}),$$

where ρ is charge density and $\vec{j}$ is the current density. Furthermore, in electromagnetism, it is important to also define the four-potential

$$(A^\mu) = (\phi, \vec{A}),$$

where ϕ is a scalar electromagnetic potential and $\vec{A}$ is the vector electromagnetic potential. Electromagnetic potential generates the electric and magnetic field

$$\vec{E} = -\vec{\nabla}\phi - \frac{\partial \vec{A}}{\partial t}, \qquad \vec{B} = \vec{\nabla}\vec{A},$$

where $\nabla = \left(\frac{\partial}{\partial x}, \frac{\partial}{\partial y}, \frac{\partial}{\partial z},\right)$ is a vector operator called nabla. In the special theory of relativity, the electric and magnetic fields are together represented via the electromagnetic rank 2 tensor F, also called Faraday tensor. Faraday tensor is the exterior derivative of the electromagnetic four-potential

$$F \equiv \mathrm{d}A.$$

This can be rewritten in component form as

$$F_{\mu\nu} = \partial_\mu A_\nu - \partial_\nu A_\mu,$$

where

$$\left(\partial_\mu\right) \equiv \left(\frac{\partial}{\partial x^\mu}\right) = \left(\frac{\partial}{\partial t}, \vec{\nabla}\right)$$

is called the four-gradient. The pseudo-inner product of the four-gradient is called D'Alembert operator

$$\Box \equiv \partial_\mu \partial^\mu.$$

A.3 Clifford algebra $\mathrm{Cl}_{1,3}(\mathbb{R})$

The Clifford algebra $\mathrm{Cl}_{1,3}(\mathbb{R})$ is constructed from γ-matrices that must obey relations

$$\{\gamma^\mu, \gamma^\nu\} = \gamma^\mu\gamma^\nu + \gamma^\nu\gamma^\mu = 2\eta^{\mu\nu}\mathbb{I}_4, \qquad \left(\gamma^\mu\right)^\dagger = \gamma^0\gamma^\mu\gamma^0.$$

Those conditions satisfy the Dirac representation

$$\gamma^0 = \sigma^3 \otimes \mathbb{I}_2 = \begin{pmatrix} 1 & 0 & 0 & 0 \\ 0 & 1 & 0 & 0 \\ 0 & 0 & -1 & 0 \\ 0 & 0 & 0 & -1 \end{pmatrix}, \quad \gamma^1 = i\sigma^2 \otimes \sigma^1 = \begin{pmatrix} 0 & 0 & 0 & 1 \\ 0 & 0 & 1 & 0 \\ 0 & -1 & 0 & 0 \\ -1 & 0 & 0 & 0 \end{pmatrix},$$

$$\gamma^2 = i\sigma^2 \otimes \sigma^2 = \begin{pmatrix} 0 & 0 & 0 & -i \\ 0 & 0 & i & 0 \\ 0 & i & 0 & 0 \\ -i & 0 & 0 & 0 \end{pmatrix}, \quad \gamma^3 = i\sigma^2 \otimes \sigma^3 = \begin{pmatrix} 0 & 0 & 1 & 0 \\ 0 & 0 & 0 & -1 \\ -1 & 0 & 0 & 0 \\ 0 & 1 & 0 & 0 \end{pmatrix},$$

where σ^i are Pauli matrices (see Appendix A.4) and $\otimes$ is the tensor product. There are other representations that are also important, like the chiral representation called the Weyl representation of γ-matrices. However, they are not essential for this work.

It is also convenient to denote the product of γ-matrices that is also considered as a γ-matrix that in Dirac representation reads as

$$\gamma^5 = i\gamma^0\gamma^1\gamma^2\gamma^3 = \sigma^1 \mathbb{I}_2 = \begin{pmatrix} 0 & 0 & 0 & 1 \\ 0 & 0 & 1 & 0 \\ 0 & 1 & 0 & 0 \\ 1 & 0 & 0 & 0 \end{pmatrix}$$

The essential notation from the Clifford algebra is the Feynman slash notation

$$\not{A} \equiv \gamma^\mu A_\mu,$$

where A^μ is arbitrary four-vector or four-operator.

The Clifford algebra in Euclidean space (i.e., with metric $\delta_{\mu\nu} = \mathrm{diag}(1,1,1,1)$) the $\gamma-$matrices are usually defined as

$$\left(\gamma^\mu\right)_{\mathrm{E}} = \left(\gamma^4 \equiv i\gamma^0, \vec{\gamma}\right).$$

Matrices defined like that satisfy the relation

$$\{\gamma^\mu_{\mathrm{E}}, \gamma^\nu_{\mathrm{E}}\} = -2\delta^{\mu\nu}\mathbb{I}_4.$$

A.4 Lie algebra SU(2) and SU(3)

The (N^2-1) elements of SU(N) group must satisfy the Lie algebra

$$[\mathscr{A}, \mathscr{B}] = if_{\mathscr{A}\mathscr{B}\mathscr{C}}\mathscr{C},$$

where $f_{\mathscr{A}\mathscr{B}\mathscr{C}}$ is the structure constant.

Essential for this work is SU(2) and SU(3) Lie algebra. In the case of SU(2) the $(N^2-1) = 3$ elements are called Pauli matrices and they are 2×2 complex matrices defined as

$$\sigma_1 = \sigma_{\mathrm{x}} = \begin{pmatrix} 0 & 1 \\ 1 & 0 \end{pmatrix}, \qquad \sigma_2 = \sigma_{\mathrm{y}} = \begin{pmatrix} 0 & -i \\ i & 0 \end{pmatrix}, \qquad \sigma_3 = \sigma_{\mathrm{z}} = \begin{pmatrix} 1 & 0 \\ 0 & -1 \end{pmatrix}.$$

They satisfy the Lie algebra

$$\left[\sigma^i, \sigma^j\right] = if_{ijk}\sigma^k,$$

where the structure constant $f_{ijk} = 2\varepsilon_{ijk}$ and ε_{ijk} is called Levi-Civita symbol. Furthermore, the Pauli matrices also satisfy anticommutation relations

$$\left\{\sigma^i, \sigma^j\right\} = 2\delta_{ij}\mathbb{I}_2.$$

Elements of the SU(3) Lie algebra are called Gell-Mann matrices. They satisfy the Lie algebra

$$[\lambda_{\mathrm{з}}, \lambda_{\mathrm{щ}}] = 2if^{\mathrm{зщд}}\lambda_{\mathrm{д}},$$

where Cyrillic indices goes from 1 to 8 since $N^2-1 = 3^2-1 = 8$. Matrices from Gell-Mann matrix representation are defined as

$$\lambda_1 = \begin{pmatrix} 0 & 1 & 0 \\ 1 & 0 & 0 \\ 0 & 0 & 0 \end{pmatrix}, \quad \lambda_2 = \begin{pmatrix} 0 & -i & 0 \\ i & 0 & 0 \\ 0 & 0 & 0 \end{pmatrix}, \lambda_3 = \begin{pmatrix} 1 & 0 & 0 \\ 0 & -1 & 0 \\ 0 & 0 & 0 \end{pmatrix}, \lambda_4 = \begin{pmatrix} 0 & 0 & 1 \\ 0 & 0 & 0 \\ 1 & 0 & 0 \end{pmatrix},$$
$$\lambda_5 = \begin{pmatrix} 0 & 0 & -i \\ 0 & 0 & 0 \\ i & 0 & 0 \end{pmatrix}, \lambda_6 = \begin{pmatrix} 0 & 0 & 0 \\ 0 & 0 & 1 \\ 0 & 1 & 0 \end{pmatrix}, \quad \lambda_7 = \begin{pmatrix} 0 & 0 & 0 \\ 0 & 0 & -i \\ 0 & i & 0 \end{pmatrix}, \lambda_8 = \frac{1}{\sqrt{3}} \begin{pmatrix} 1 & 0 & 0 \\ 0 & 1 & 0 \\ 0 & 0 & -2 \end{pmatrix}.$$

Finally, the structure constant of SU(3), $f^{\text{зщд}}$, that is consistent with the mentioned Gell-Mann matrices is defined as

$$f^{123} = 1,$$
$$f^{147} = f^{165} = f^{246} = f^{257} = f^{345} = f^{376} = \frac{1}{2},$$
$$f^{458} = f^{678} = \frac{\sqrt{3}}{2}.$$

The rest of the structure constant can be deduced from its antisymmetric properties.

A.5 Mandelstam variables

Mandelstam variables are Lorentz-invariant quantities that are composed of four four-momenta. They describe three different channels of $2 \to 2$ scattering processes that can be seen in Figure A.1.

Mandelstam variables are defined as

$$s = (p_1 + p_2)^2 = (p_3 + p_4)^2$$
$$t = (p_1 - p_3)^2 = (p_4 - p_2)^2$$
$$u = (p_1 - p_4)^2 = (p_3 - p_2)^2,$$

where p_1 and p_2 are four-momenta of incoming particles and p_3 and p_4 are four-momenta of outgoing particles. The square root of s is the center-of-mass energy $E_{\text{CoM}} = \sqrt{s}$. This is important for high energy physics since the energy of the collision is expressed in $\sqrt{s}$. Furthermore, t is known as four-momentum transfer. The sum of the Mandelstam variables is the sum of the squared masses of participating particles

$$s + t + u = m_1^2 + m_2^2 + m_3^2 + m_4^2.$$

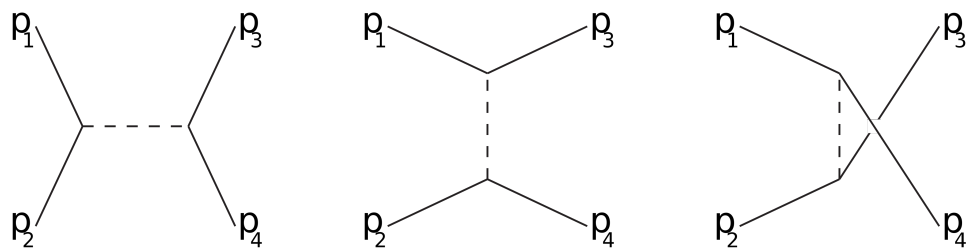

(a) s-channel (space-channel) (b) t-channel (time-channel) (c) u-channel (u-channel)

Figure A.1: Channels for Mandelstam variables.

In the ultrarelativistic limit ($E = p$), that neglect the masses of participating particles, the Mandelstam variables reads as

$$\begin{aligned} s &\approx \quad 2p_1p_2 \approx 2p_3p_4, \\ t &\approx -2p_1p_3 \approx 2p_2p_4, \\ u &\approx -2p_1p_4 \approx 2p_3p_2. \end{aligned}$$

Appendix B

Additional simulation results

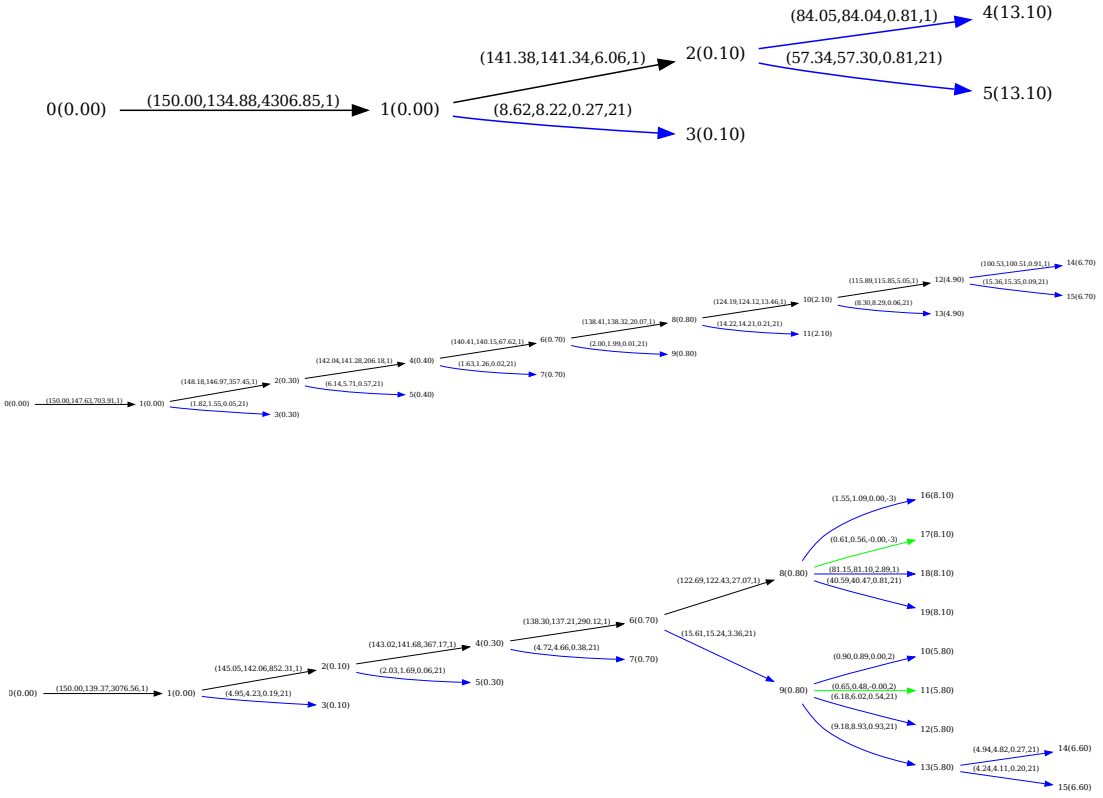

Figure B.1: Parton splittings obtained from MATTER for vacuum evolution (upper), evolution with medium-modified Sudakov form factor (middle), evolution with medium-modified Sudakov form factor and recoils with medium (lower). Blue arrows are low virtuality partons, green arrows are holes.

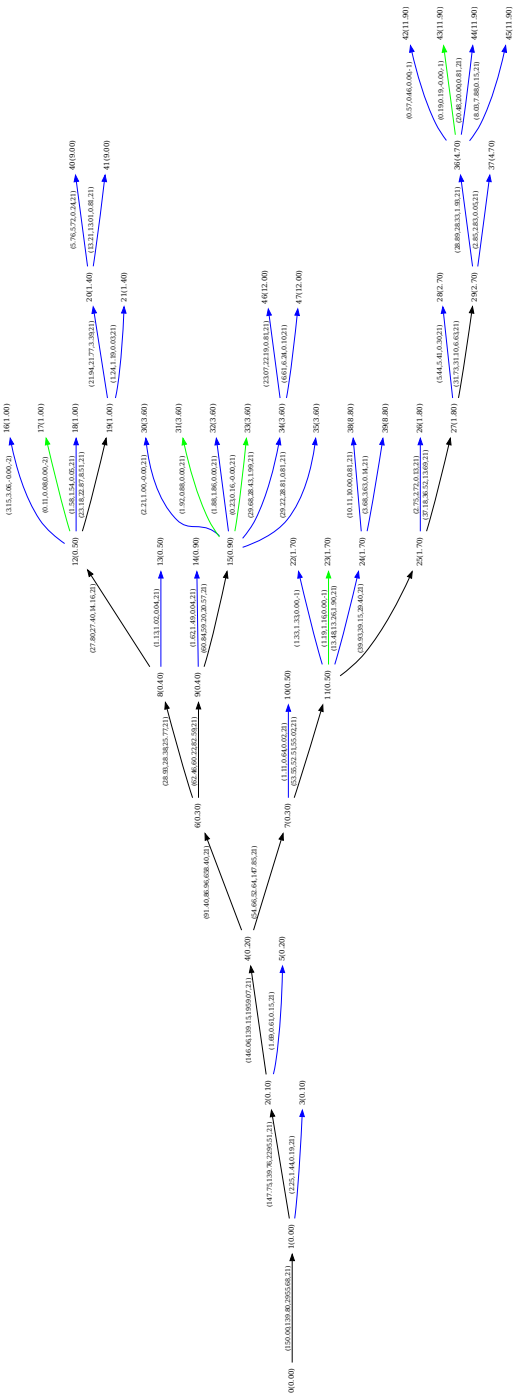

Figure B.2: Parton splittings obtained from MATTER + LBT with leading only option for LBT and vacuum option for MATTER. Blue arrows are low virtuality partons, green arrows are holes.

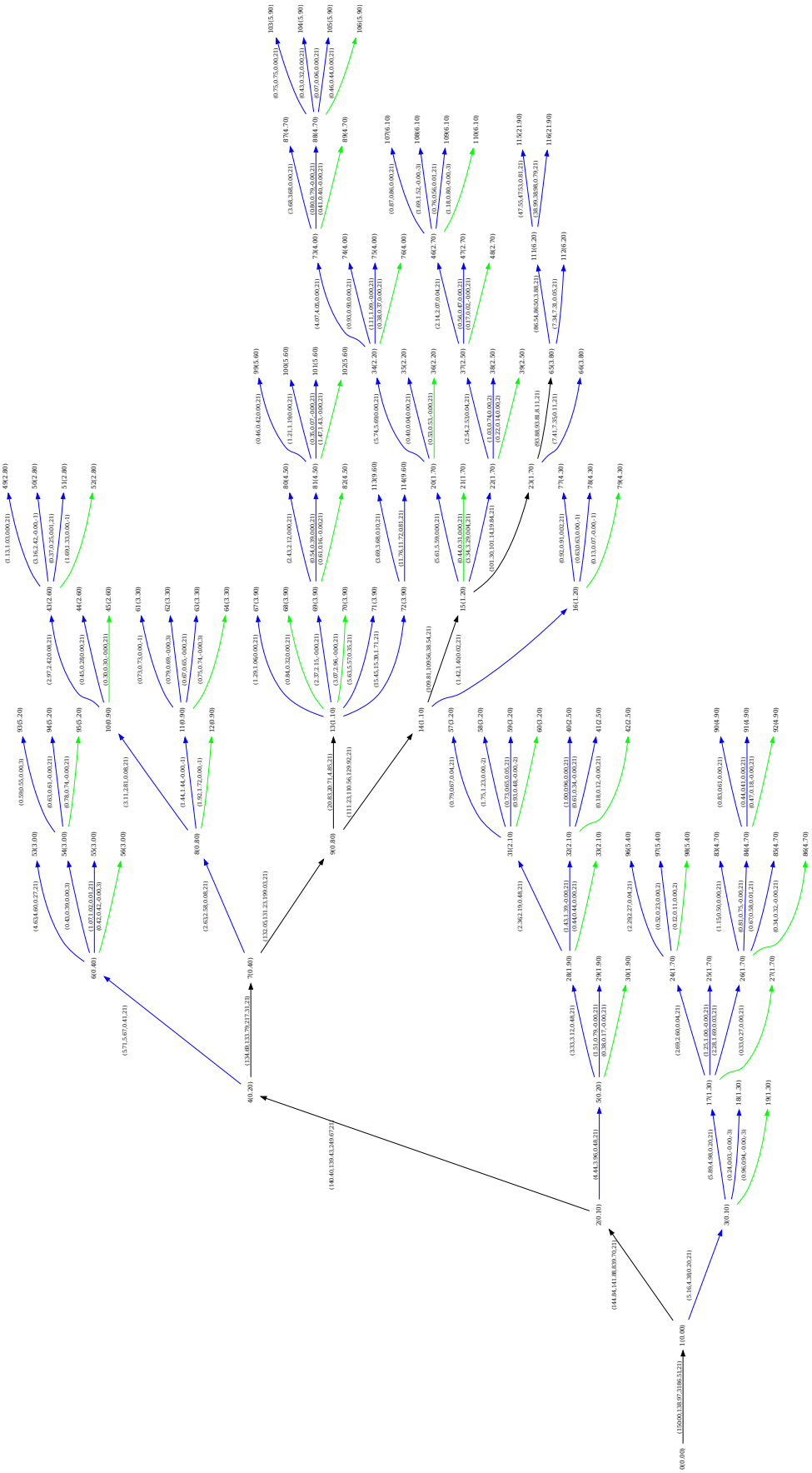

Figure B.3: Parton splittings obtained from MATTER + LBT with vacuum evolution for MATTER and full evolution for LBT. Blue arrows are low virtuality partons, green arrows are holes.

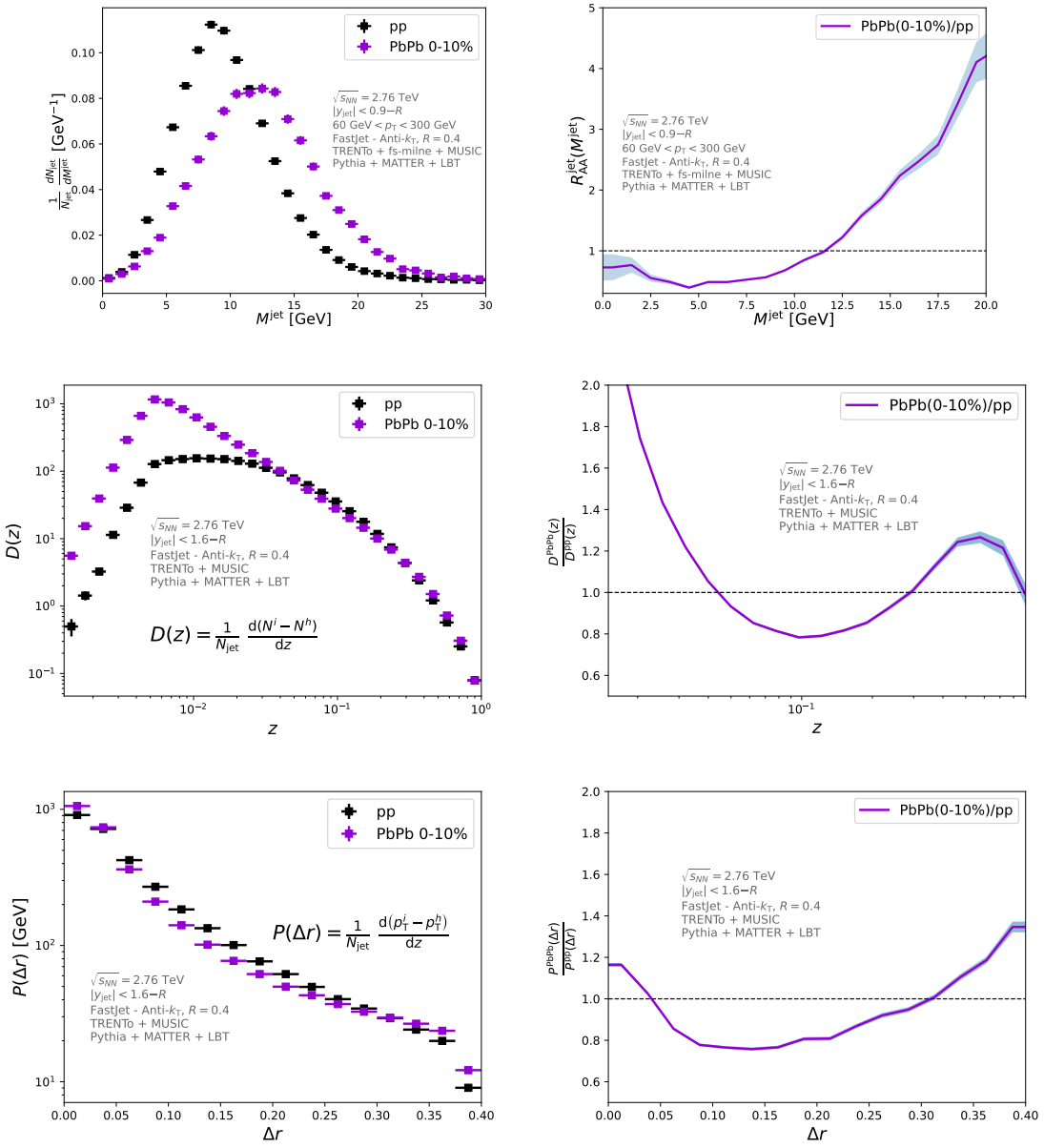

Figure B.4: Jet mass M^{jet} spectra (top left), mass-dependent jet nuclear modification factor (top right), jet fragmentation function $D(z)$ (middle left), ratio $D^{\text{PbPb}}(z)/D^{pp}(z)$ (middle right), Jet shape $P(\Delta r)$ (bottom left), and ratio $P^{\text{PbPb}}(\Delta r)/P^{pp}(\Delta r)$ (bottom right) for pp collisions (black squares) and 0-10% PbPb (magenta squares) at $\sqrt{s_{\text{NN}}}$ = 2.67 TeV obtained from T$_{\text{R}}$ENTo [1] + `freestream-milne` [2] + `MUSIC` [3] + `Pythia` [6] + `MATTER` [7] + `LBT` [8] implemented in `Jetscape` [9].

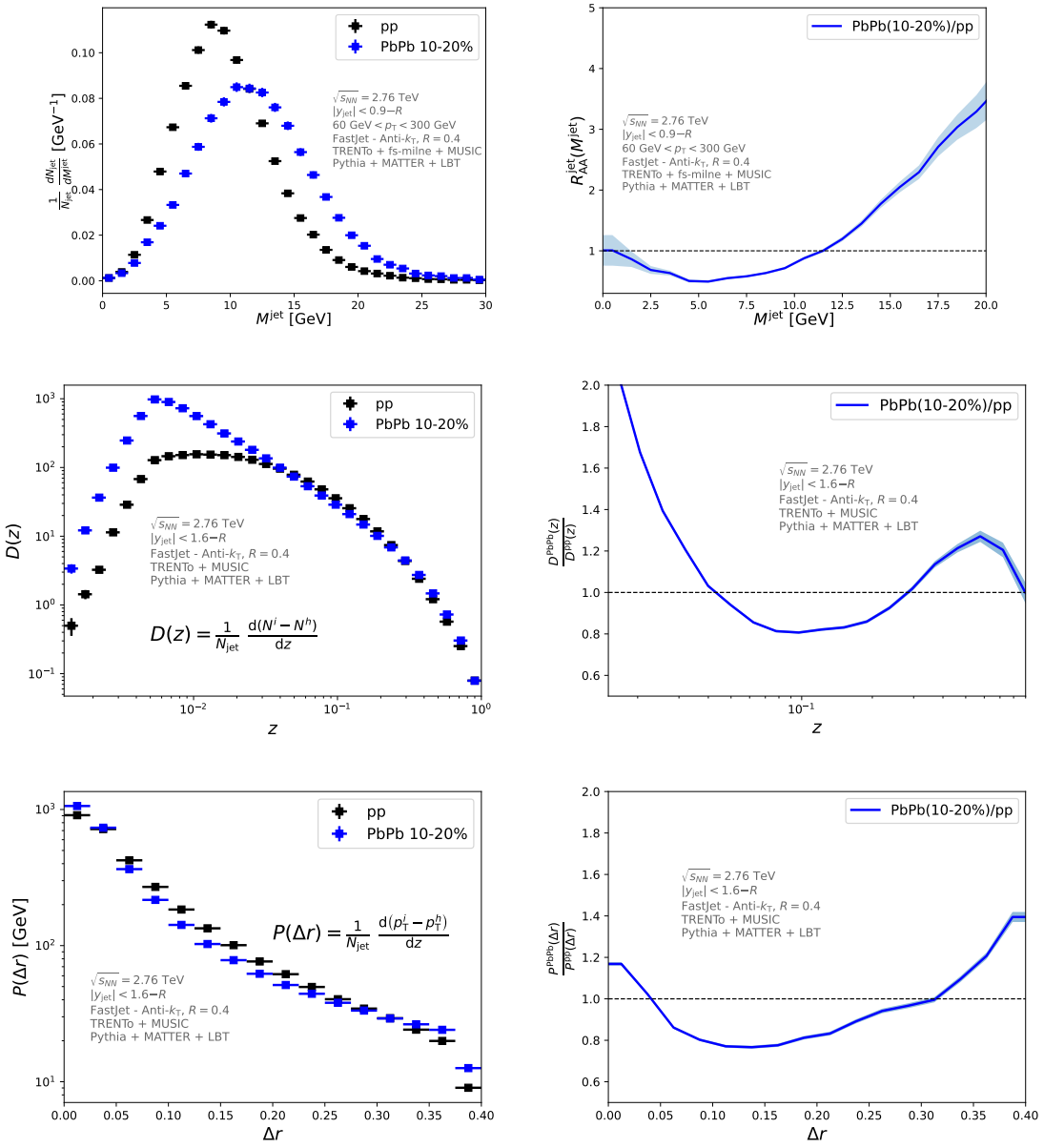

Figure B.5: Jet mass M^{jet} spectra (top left), mass-dependent jet nuclear modification factor (top right), jet fragmentation function $D(z)$ (middle left), ratio $D^{\text{PbPb}}(z)/D^{pp}(z)$ (middle right), Jet shape $P(\Delta r)$ (bottom left), and ratio $P^{\text{PbPb}}(\Delta r)/P^{pp}(\Delta r)$ (bottom right) for pp collisions (black squares) and 10-20% PbPb (blue squares) at $\sqrt{s_{\text{NN}}} = 2.67$ TeV obtained from TRENTo [1] + `freestream-milne` [2] + `MUSIC` [3] + `Pythia` [6] + `MATTER` [7] + `LBT` [8] implemented in `Jetscape` [9].

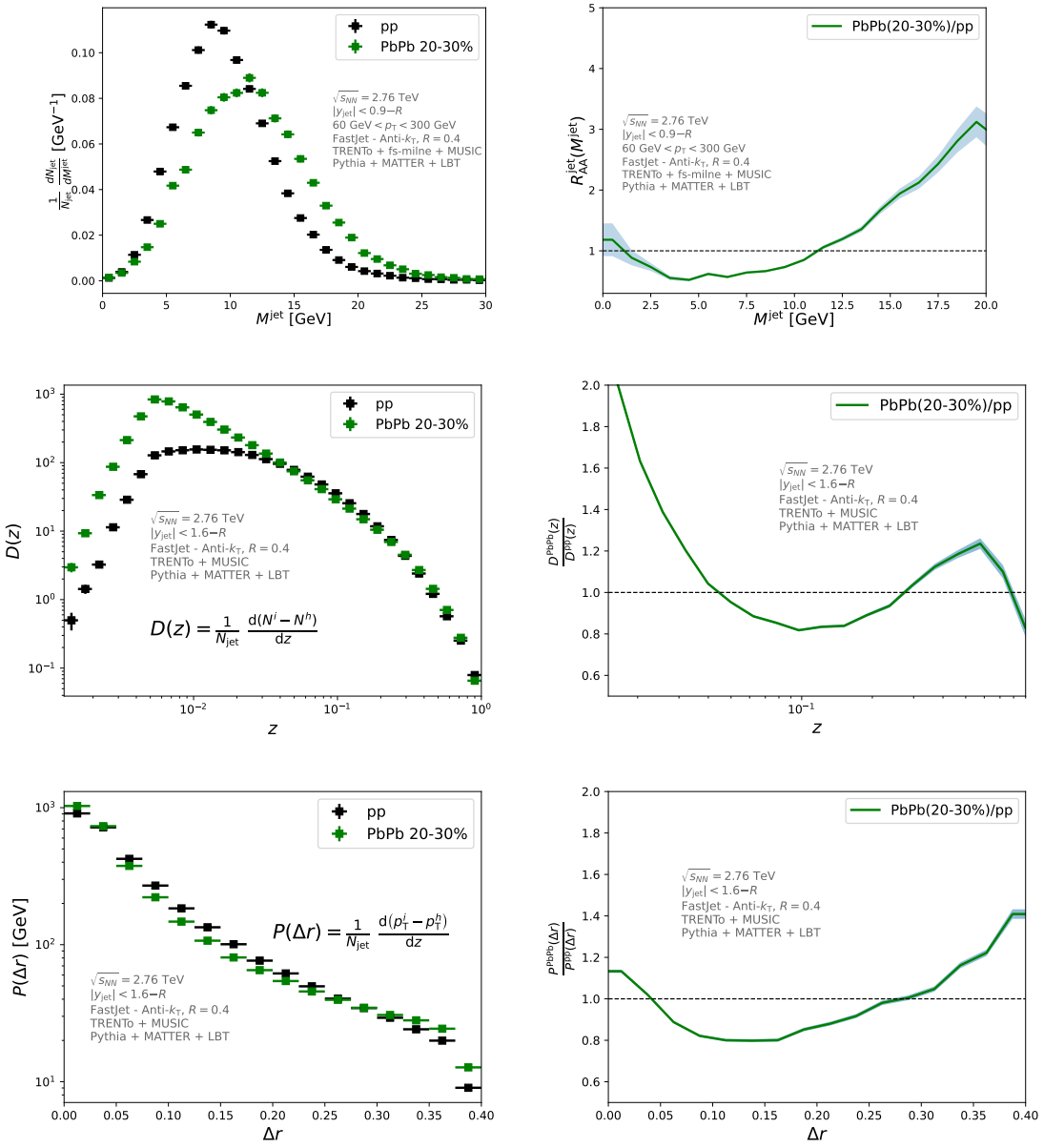

Figure B.6: Jet mass M^{jet} spectra (top left), mass-dependent jet nuclear modification factor (top right), jet fragmentation function $D(z)$ (middle left), ratio $D^{\text{PbPb}}(z)/D^{pp}(z)$ (middle right), Jet shape $P(\Delta r)$ (bottom left), and ratio $P^{\text{PbPb}}(\Delta r)/P^{pp}(\Delta r)$ (bottom right) for pp collisions (black squares) and 40-50% PbPb (green squares) at $\sqrt{s_{\text{NN}}}$ = 2.67 TeV obtained from TRENTo [1] + `freestream-milne` [2] + `MUSIC` [3] + `Pythia` [6] + `MATTER` [7] + `LBT` [8] implemented in `Jetscape` [9].

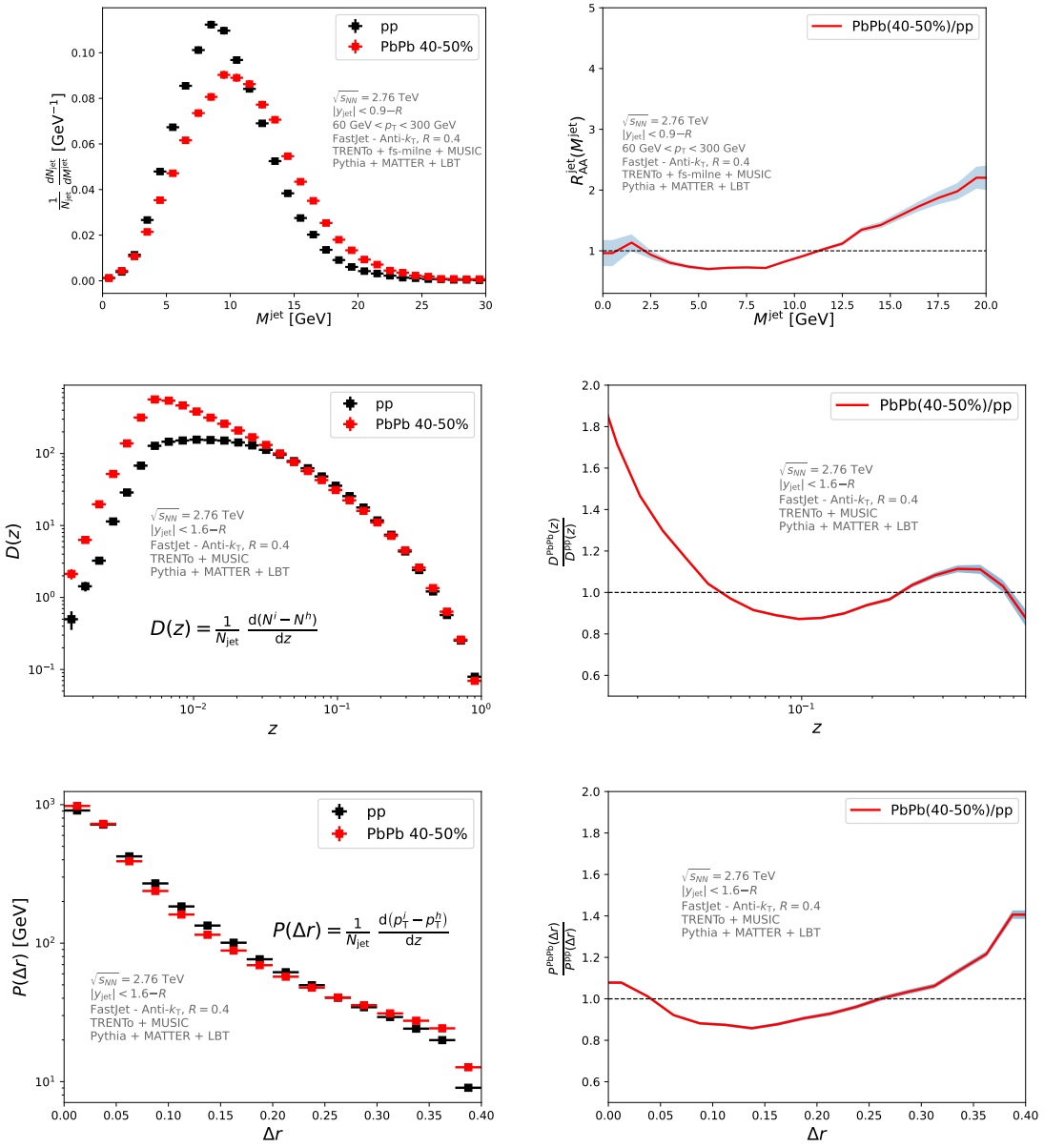

Figure B.7: Jet mass M^{jet} spectra (top left), mass-dependent jet nuclear modification factor (top right), jet fragmentation function $D(z)$ (middle left), ratio $D^{\text{PbPb}}(z)/D^{pp}(z)$ (middle right), Jet shape $P(\Delta r)$ (bottom left), and ratio $P^{\text{PbPb}}(\Delta r)/P^{pp}(\Delta r)$ (bottom right) for pp collisions (black squares) and 40-50% PbPb (red squares) at $\sqrt{s_{\text{NN}}} = 2.67$ TeV obtained from T$_{\text{R}}$ENTo [1] + `freestream-milne` [2] + `MUSIC` [3] + `Pythia` [6] + `MATTER` [7] + `LBT` [8] implemented in `Jetscape` [9].

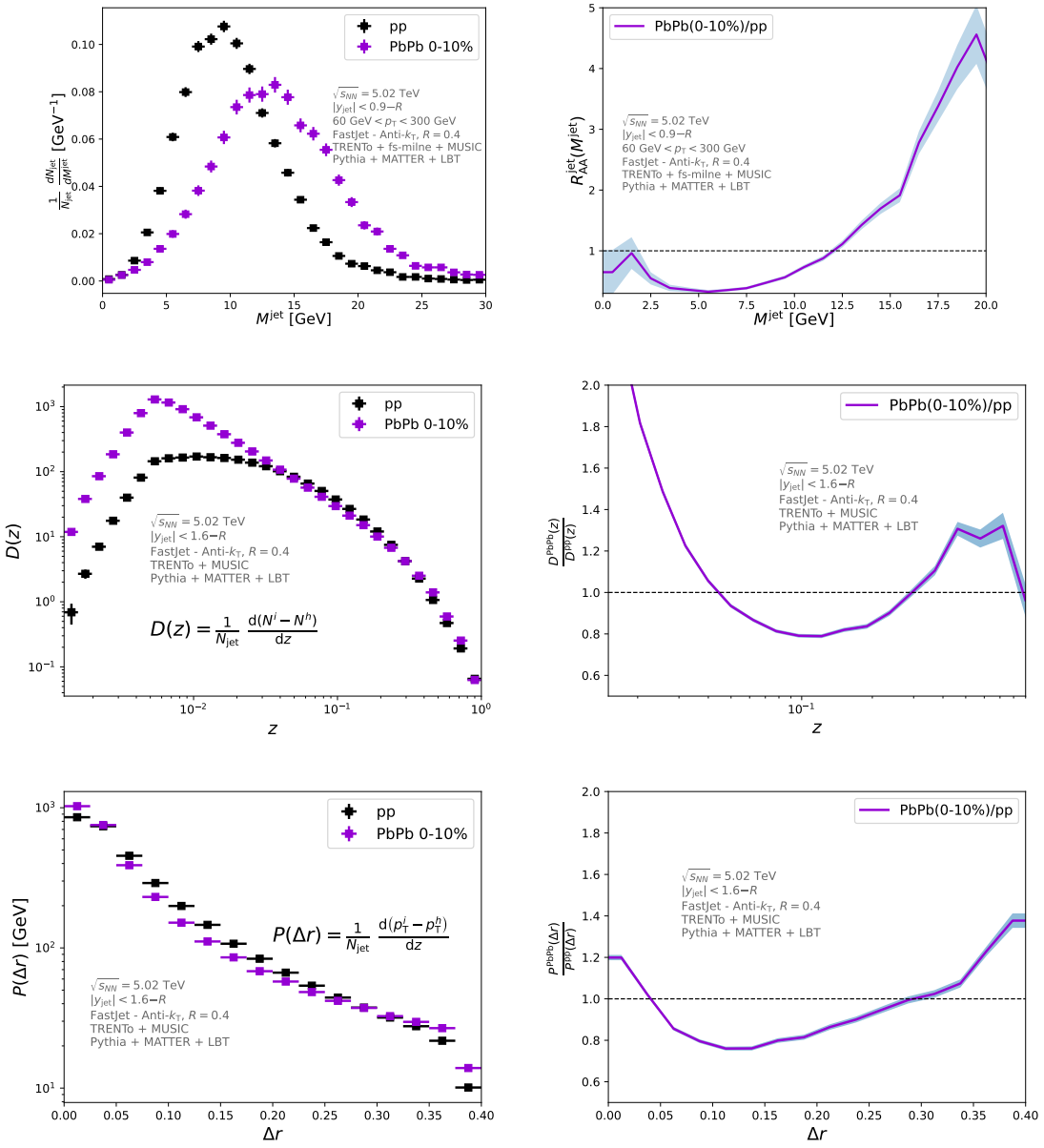

Figure B.8: Jet mass M^{jet} spectra (top left), mass-dependent jet nuclear modification factor (top right), jet fragmentation function $D(z)$ (middle left), ratio $D^{\text{PbPb}}(z)/D^{pp}(z)$ (middle right), Jet shape $P(\Delta r)$ (bottom left), and ratio $P^{\text{PbPb}}(\Delta r)/P^{pp}(\Delta r)$ (bottom right) for pp collisions (black squares) and 0-10% PbPb (magenta squares) at $\sqrt{s_{\text{NN}}} = 5.02$ TeV obtained from TRENTo [1] + `freestream-milne` [2] + `MUSIC` [3] + `Pythia` [6] + `MATTER` [7] + `LBT` [8] implemented in `Jetscape` [9].

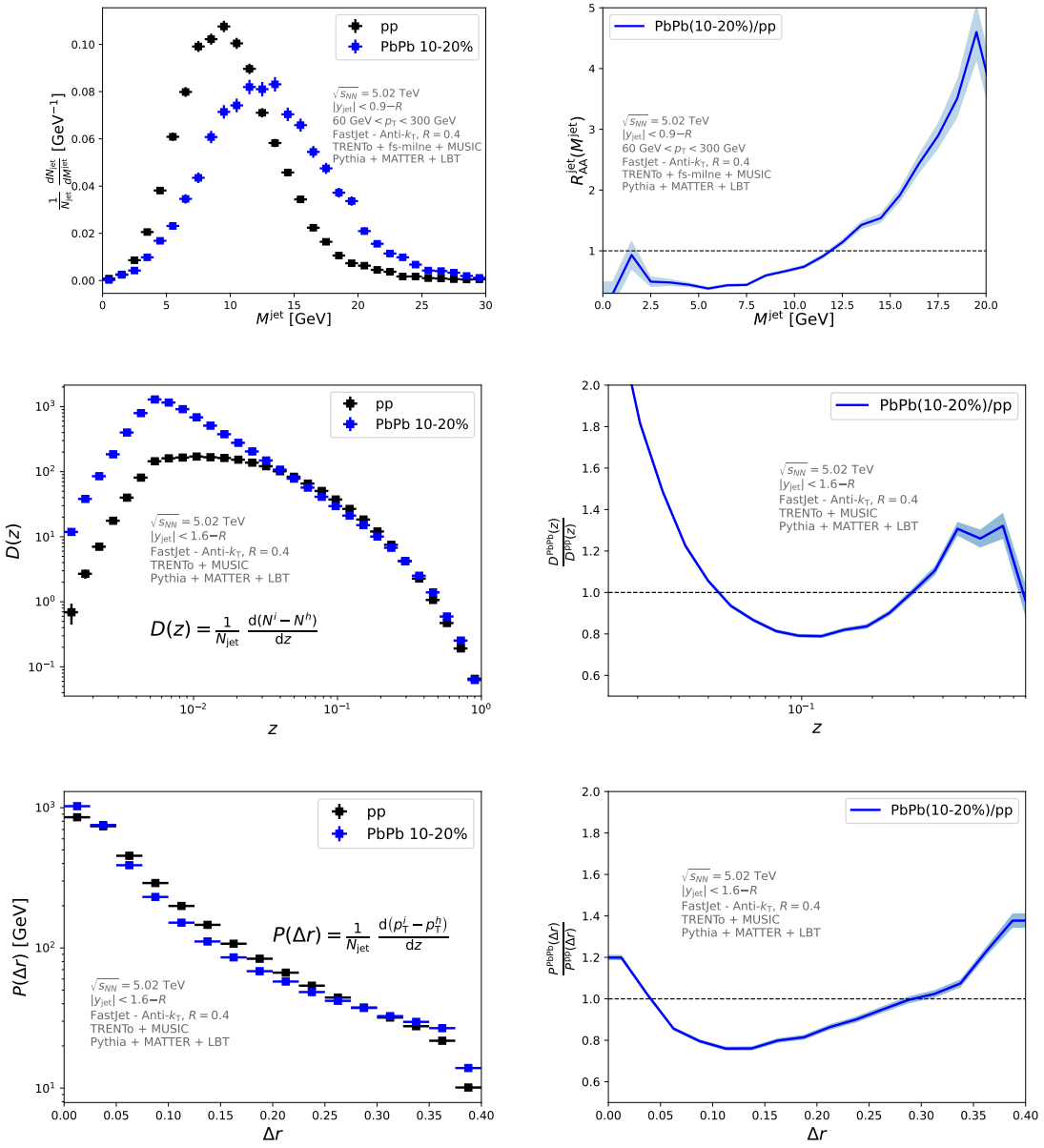

Figure B.9: Jet mass M^{jet} spectra (top left), mass-dependent jet nuclear modification factor (top right), jet fragmentation function $D(z)$ (middle left), ratio $D^{\text{PbPb}}(z)/D^{pp}(z)$ (middle right), Jet shape $P(\Delta r)$ (bottom left), and ratio $P^{\text{PbPb}}(\Delta r)/P^{pp}(\Delta r)$ (bottom right) for pp collisions (black squares) and 10-20% PbPb (blue squares) at $\sqrt{s_{\text{NN}}} = 5.02$ TeV obtained from TRENTo [1] + `freestream-milne` [2] + `MUSIC` [3] + `Pythia` [6] + `MATTER` [7] + `LBT` [8] implemented in `Jetscape` [9].

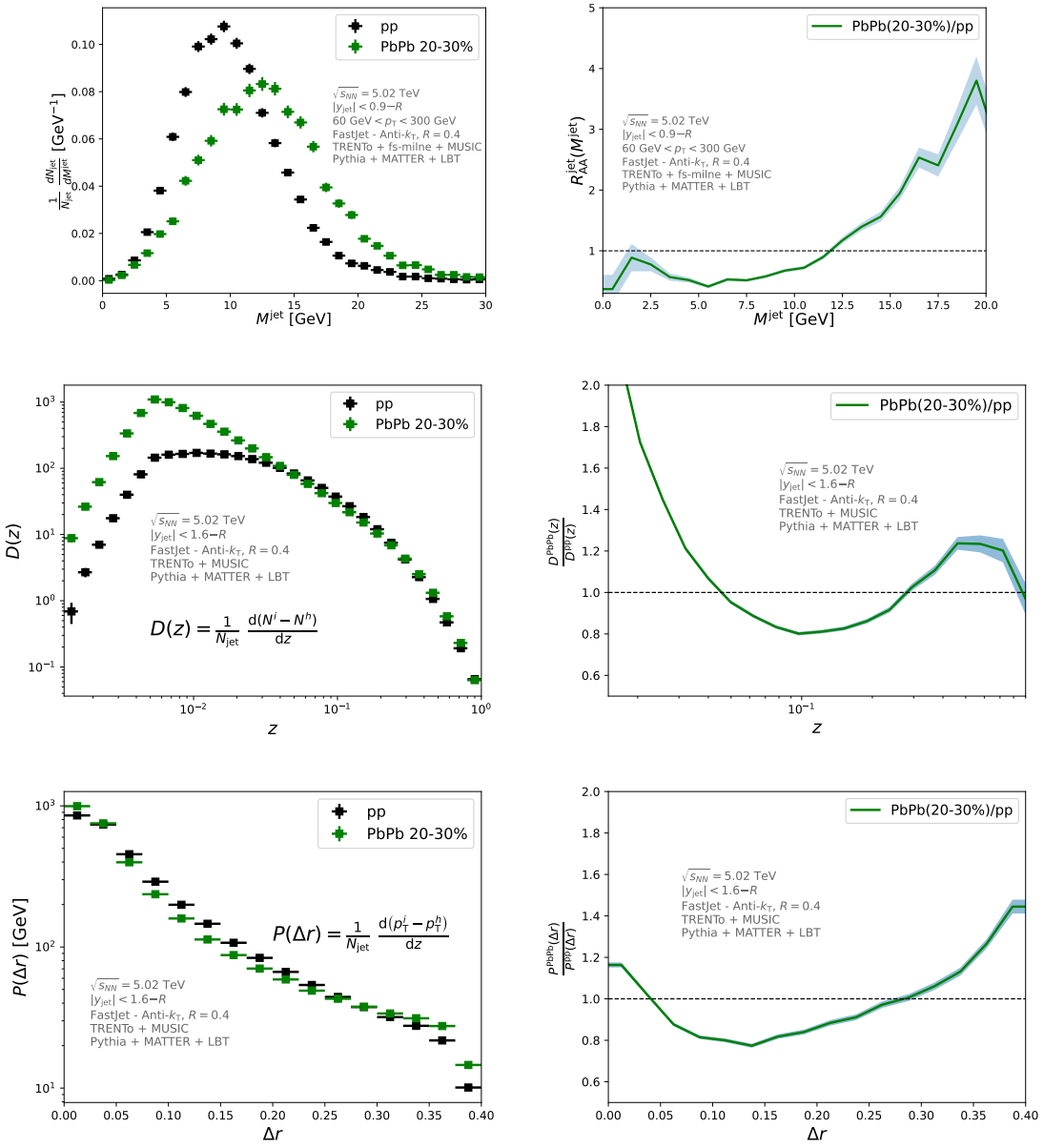

Figure B.10: Jet mass M^{jet} spectra (top left), mass-dependent jet nuclear modification factor (top right), jet fragmentation function $D(z)$ (middle left), ratio $D^{\text{PbPb}}(z)/D^{pp}(z)$ (middle right), Jet shape $P(\Delta r)$ (bottom left), and ratio $P^{\text{PbPb}}(\Delta r)/P^{pp}(\Delta r)$ (bottom right) for pp collisions (black squares) and 20-30% PbPb (green squares) at $\sqrt{s_{\text{NN}}}$ = 5.02 TeV obtained from T_RENTo [1] + `freestream-milne` [2] + `MUSIC` [3] + `Pythia` [6] + `MATTER` [7] + `LBT` [8] implemented in `Jetscape` [9].

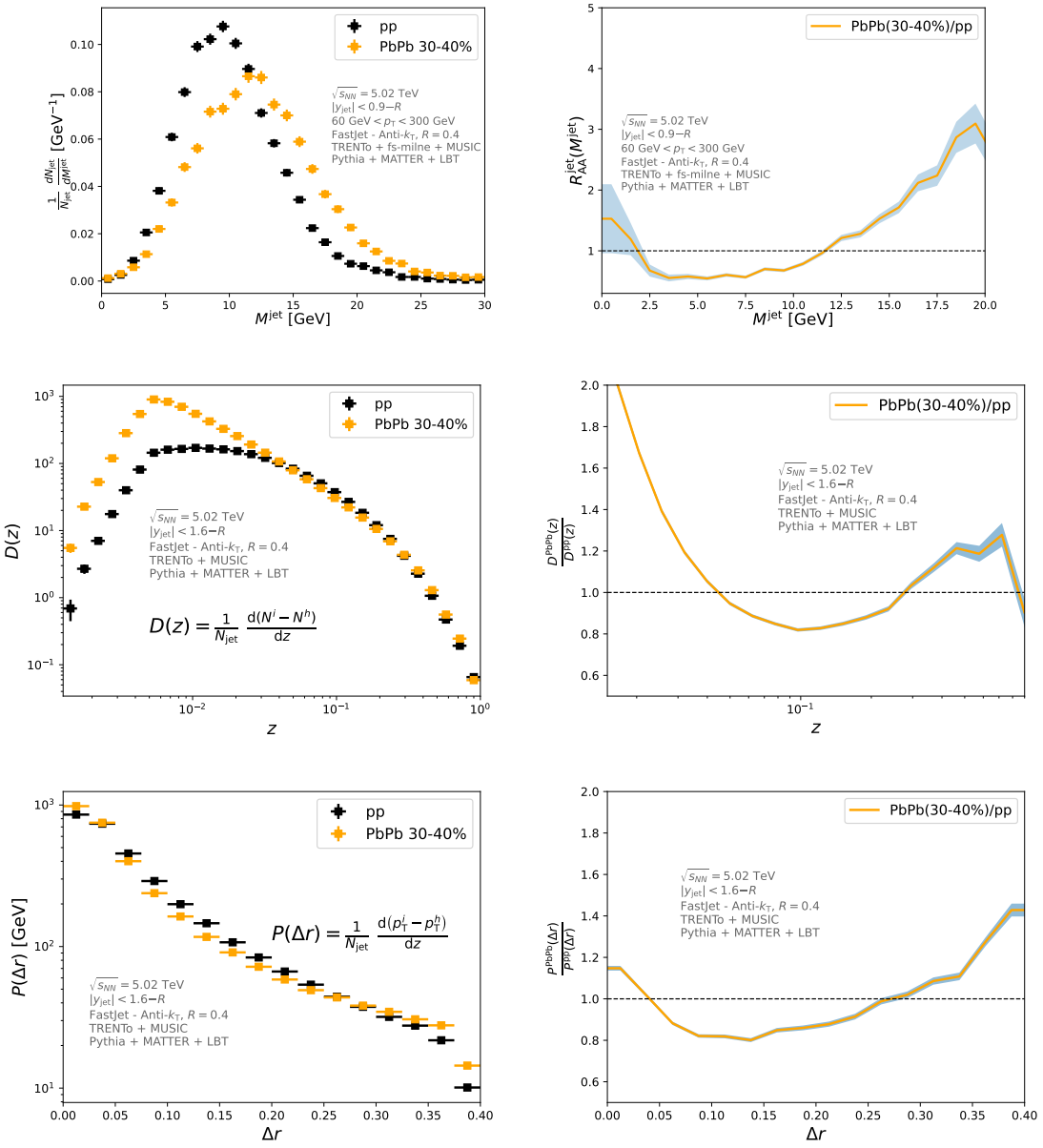

Figure B.11: Jet mass M^{jet} spectra (top left), mass-dependent jet nuclear modification factor (top right), jet fragmentation function $D(z)$ (middle left), ratio $D^{\text{PbPb}}(z)/D^{pp}(z)$ (middle right), Jet shape $P(\Delta r)$ (bottom left), and ratio $P^{\text{PbPb}}(\Delta r)/P^{pp}(\Delta r)$ (bottom right) for pp collisions (black squares) and 30-40% PbPb (orange squares) at $\sqrt{s_{\text{NN}}} = 5.02$ TeV obtained from TRENTo [1] + `freestream-milne` [2] + `MUSIC` [3] + `Pythia` [6] + `MATTER` [7] + `LBT` [8] implemented in `Jetscape` [9].

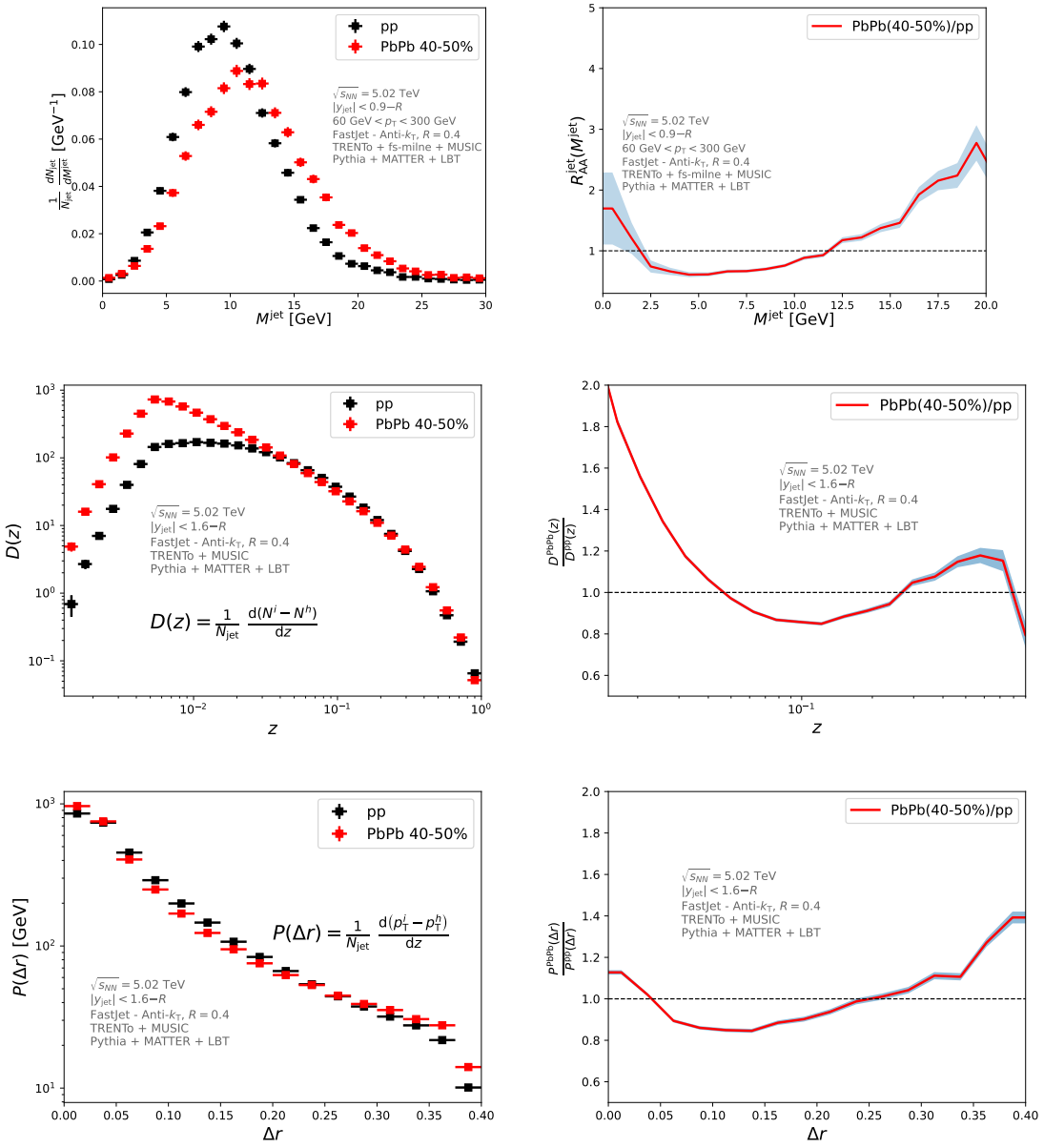

Figure B.12: Jet mass M^{jet} spectra (top left), mass-dependent jet nuclear modification factor (top right), jet fragmentation function $D(z)$ (middle left), ratio $D^{\text{PbPb}}(z)/D^{pp}(z)$ (middle right), Jet shape $P(\Delta r)$ (bottom left), and ratio $P^{\text{PbPb}}(\Delta r)/P^{pp}(\Delta r)$ (bottom right) for pp collisions (black squares) and 40-50% PbPb (red squares) at $\sqrt{s_{\text{NN}}} = 5.02$ TeV obtained from T$_{\text{R}}$ENTo [1] + `freestream-milne` [2] + `MUSIC` [3] + `Pythia` [6] + `MATTER` [7] + `LBT` [8] implemented in `Jetscape` [9].

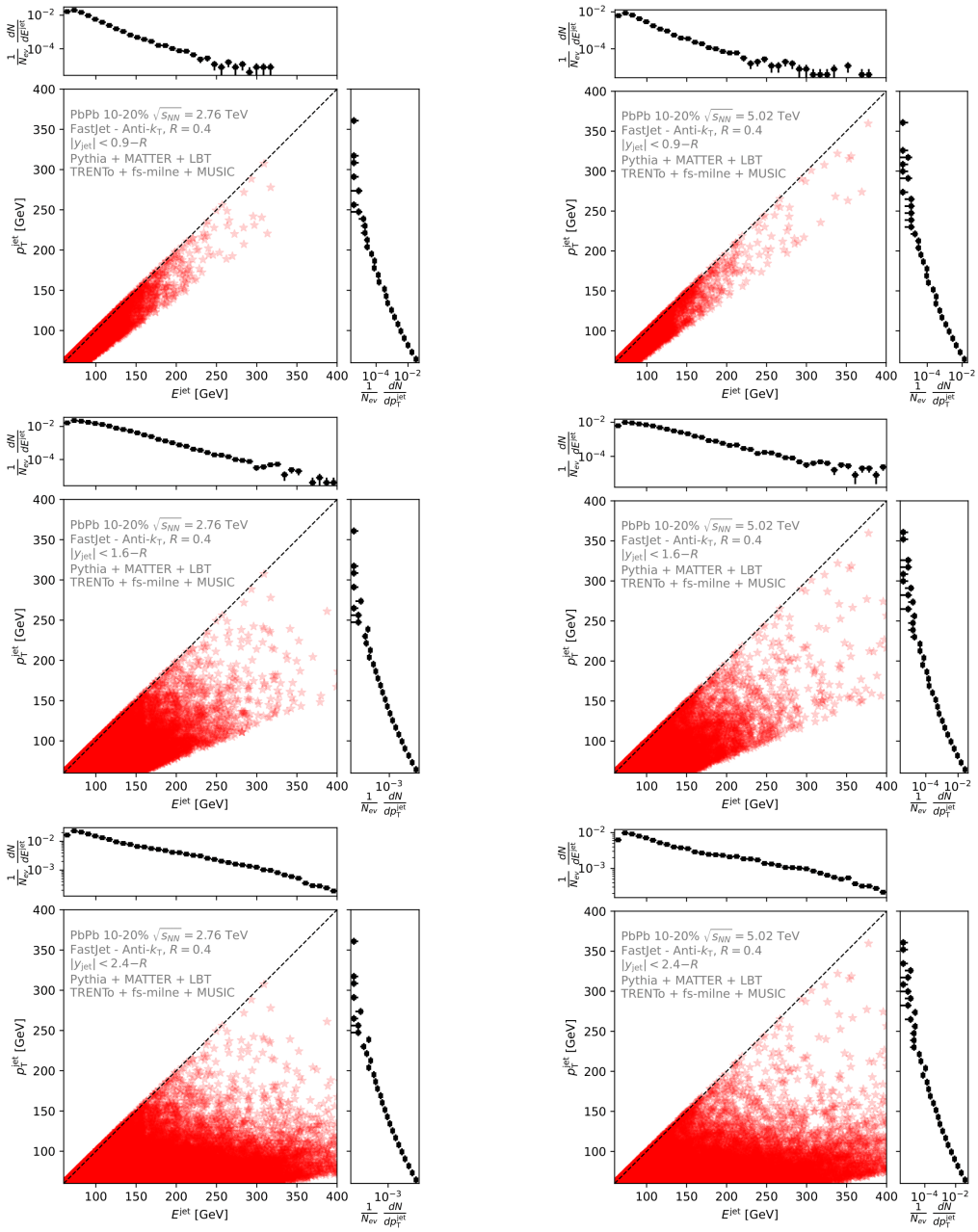

Figure B.13: Jet scatter plot in the $(p_{\mathrm{T}}^{\mathrm{jet}}, E^{\mathrm{jet}})$ space for different rapidity intervals $|y_{\mathrm{jet}}| \leq 0.9 - R$ (upper row), $|y_{\mathrm{jet}}| \leq 1.6 - R$ (middle row), and $|y_{\mathrm{jet}}| \leq 2.4 - R$ (lower row) for 10-20% PbPb collisions at $\sqrt{s_{\mathrm{NN}}} = 2.67$ TeV (left column) and $\sqrt{s_{\mathrm{NN}}} = 5.02$ TeV (right column) obtained from TRENTo [1] + `freestream-milne` [2] + `MUSIC` [3] + `Pythia` [6] + `MATTER` [7] + `LBT` [8] implemented in `Jetscape` [9].

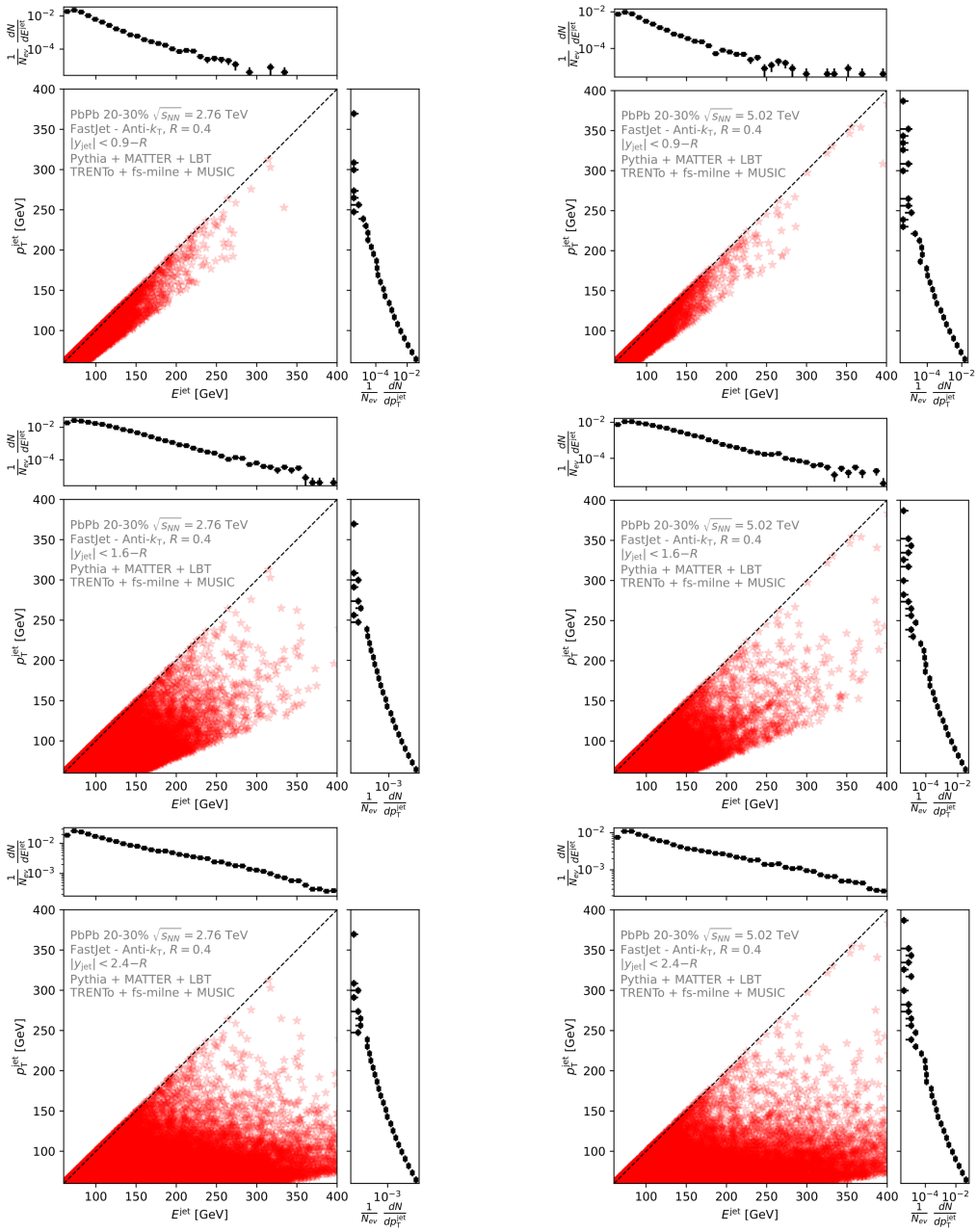

Figure B.14: Jet scatter plot in the $(p_{\mathrm{T}}^{\mathrm{jet}}, E^{\mathrm{jet}})$ space for different rapidity intervals $|y_{\mathrm{jet}}| \leq 0.9 - R$ (upper row), $|y_{\mathrm{jet}}| \leq 1.6 - R$ (middle row), and $|y_{\mathrm{jet}}| \leq 2.4 - R$ (lower row) for 20-30% PbPb collisions at $\sqrt{s_{\mathrm{NN}}} = 2.67$ TeV (left column) and $\sqrt{s_{\mathrm{NN}}} = 5.02$ TeV (right column) obtained from TRENTo [1] + `freestream-milne` [2] + `MUSIC` [3] + `Pythia` [6] + `MATTER` [7] + `LBT` [8] implemented in `Jetscape` [9].

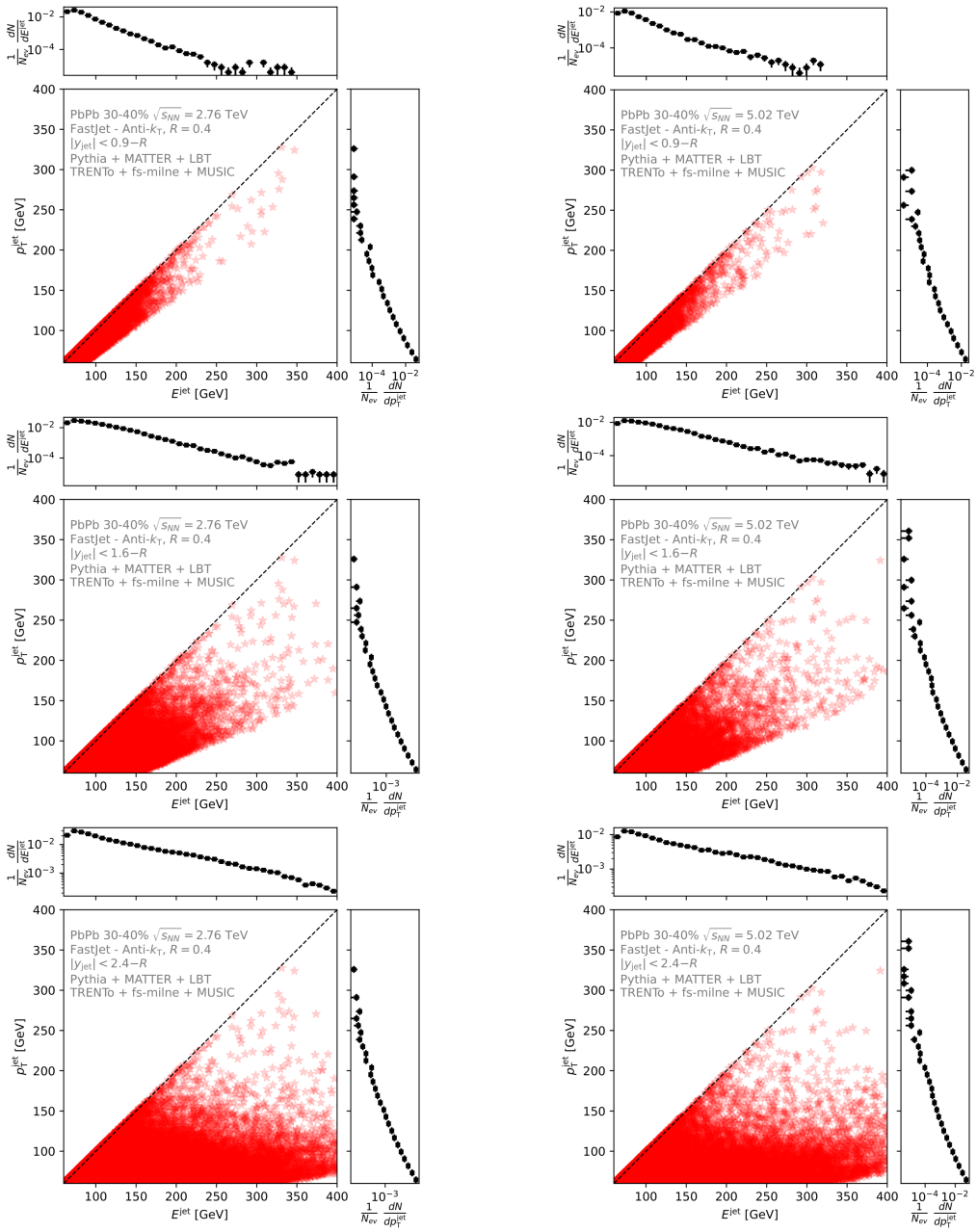

Figure B.15: Jet scatter plot in the $(p_{\mathrm{T}}^{\mathrm{jet}}, E^{\mathrm{jet}})$ space for different rapidity intervals $|y_{\mathrm{jet}}| \leq 0.9 - R$ (upper row), $|y_{\mathrm{jet}}| \leq 1.6 - R$ (middle row), and $|y_{\mathrm{jet}}| \leq 2.4 - R$ (lower row) for 30-40% PbPb collisions at $\sqrt{s_{\mathrm{NN}}} = 2.67$ TeV (left column) and $\sqrt{s_{\mathrm{NN}}} = 5.02$ TeV (right column) obtained from TRENTo [1] + `freestream-milne` [2] + `MUSIC` [3] + `Pythia` [6] + `MATTER` [7] + `LBT` [8] implemented in `Jetscape` [9].

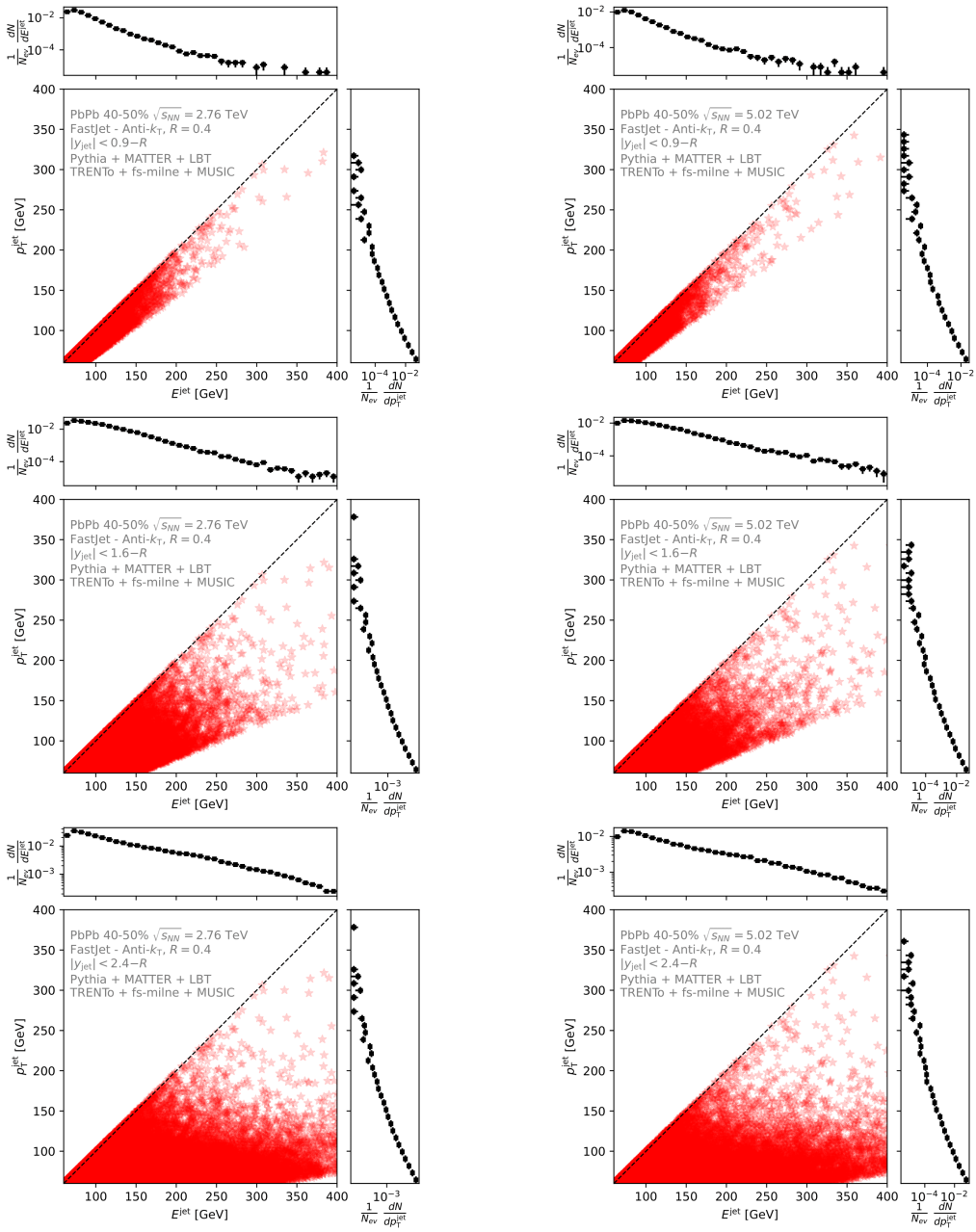

Figure B.16: Jet scatter plot in the $(p_{\mathrm{T}}^{\mathrm{jet}}, E^{\mathrm{jet}})$ space for different rapidity intervals $|y_{\mathrm{jet}}| \leq 0.9 - R$ (upper row), $|y_{\mathrm{jet}}| \leq 1.6 - R$ (middle row), and $|y_{\mathrm{jet}}| \leq 2.4 - R$ (lower row) for 40-50% PbPb collisions at $\sqrt{s_{\mathrm{NN}}} = 2.67$ TeV (left column) and $\sqrt{s_{\mathrm{NN}}} = 5.02$ TeV (right column) obtained from TRENTo [1] + `freestream-milne` [2] + `MUSIC` [3] + `Pythia` [6] + `MATTER` [7] + `LBT` [8] implemented in `Jetscape` [9].

Appendix C

Parameter space setup

Parameters used for all simulation results presented in Capter 5. Left column corresponds to centre-of-mass nucleon-nucleon pair energy $\sqrt{s_{\mathrm{NN}}}$ = 2.67 TeV, right column corresponds to centre-of-mass nucleon-nucleon pair energy $\sqrt{s_{\mathrm{NN}}}$ = 5.02 TeV. If there is only left column, it means that parameters for that specific module are symmetric.

C.1 Soft sector parameters for heavy-ion simulation

C.1.1 TRENTo parameters

```
<Trento>
  <PhysicsInputs
    projectile='Pb'
    target='Pb'
    sqrts='2670'
    cross-section='6.18'
    normalization='13.94'
  </PhysicsInputs>
  <CutInputs
    centrality-low='0'
    centrality-high='10'>
  </CutInputs>
  <TransInputs
    reduced-thickness='0.0'
    fluctuation="1.044"
    nucleon-width="0.956"
    nucleon-min-dist="1.27">
  </TransInputs>
</Trento>
```

```
<Trento>
  <PhysicsInputs
    projectile='Pb'
    target='Pb'
    sqrts='5020'
    cross-section='6.76'
    normalization='18.38'
  </PhysicsInputs>
  <CutInputs
    centrality-low='0'
    centrality-high='10'>
  </CutInputs>
  <TransInputs
    reduced-thickness='0.0'
    fluctuation="1.044"
    nucleon-width="0.956"
    nucleon-min-dist="1.27">
  </TransInputs>
</Trento>
```

C.1.2 Preequilibrium parameters

```
<Preequilibrium>
  <tau0>0.01</tau0>
  <taus>1.16</taus>
  <FreestreamMilne>
    <name>FreestreamMilne</name>
    <freestream_input_file>freestream_input</freestream_input_file>
  </FreestreamMilne>
</Preequilibrium>
```

C.1.3 Hydrodynamics parameters

```
<Hydro>
  <MUSIC>
    <name>MUSIC</name>
    <Initial_time_tau_0>1.16</Initial_time_tau_0>
    <T_dependent_Shear_to_S_ratio>3</T_dependent_Shear_to_S_ratio>
      <eta_over_s_T_kink_in_GeV>0.21</eta_over_s_T_kink_in_GeV>
      <eta_over_s_low_T_slope_in_GeV>-0.38</eta_over_s_low_T_slope_in_GeV>
      <eta_over_s_high_T_slope_in_GeV>0.38</eta_over_s_high_T_slope_in_GeV>
      <eta_over_s_at_kink>0.11</eta_over_s_at_kink>
    <temperature_dependent_bulk_viscosity>1</temperature_dependent_bulk_viscosity>
    <freezeout_temperature>0.160</freezeout_temperature>
  </MUSIC>
</Hydro>
```

C.1.4 iSS parameters

```
 <iSS>
  <Perform_resonance_decays>0</Perform_resonance_decays>
  <hydro_mode>1</hydro_mode>
  <iSS_table_path>../external_packages/iSS/iSS_tables</iSS_table_path>
  <iSS_particle_table_path>
    ../external_packages/iSS/iSS_tables
  </iSS_particle_table_path>
  <afterburner_type>2</afterburner_type>
  <number_of_repeated_sampling>1</number_of_repeated_sampling>
</iSS>
```

C.1.5 Afterburner parameters

```
<Afterburner>
  <SMASH>
    <name>SMASH</name>
    <SMASH_config_file>
      ../external_packages/smash/smash_config.yaml
    </SMASH_config_file>
    <SMASH_particles_file>
      ../external_packages/smash/smash_code/input/particles.txt
    </SMASH_particles_file>
    <SMASH_decaymodes_file>
      ../external_packages/smash/smash_code/input/decaymodes.txt
    </SMASH_decaymodes_file>
    <end_time>300.0</end_time>
  </SMASH>
</Afterburner>
```

C.2 Hard sector parameters for heavy-ion simulation

C.2.1 Parton initial state parameters

```
<Hard>
  <PythiaGun>
    <pTHatMin>60</pTHatMin>
    <pTHatMax>1000</pTHatMax>
    <LinesToRead>
      HardQCD:all = on
      PDF:useHardNPDFA=on
      PDF:useHardNPDFB=on
      PDF:nPDFSetA=1
      PDF:nPDFSetB=1
      PDF:nPDFBeamA = 100822080
      PDF:nPDFBeamB = 100822080
    </LinesToRead>
    <eCM>2760</eCM>
  </PythiaGun>
</Hard>
```

```
<Hard>
  <PythiaGun>
    <pTHatMin>60</pTHatMin>
    <pTHatMax>1000</pTHatMax>
    <LinesToRead>
      HardQCD:all = on
      PDF:useHardNPDFA=on
      PDF:useHardNPDFB=on
      PDF:nPDFSetA=1
      PDF:nPDFSetB=1
      PDF:nPDFBeamA = 100822080
      PDF:nPDFBeamB = 100822080
    </LinesToRead>
    <eCM>5020</eCM>
  </PythiaGun>
</Hard>
```

C.2.2 MATTER parameters

```
<tStart>1.16</tStart>
<Matter>
   <name>Matter</name>
   <useHybridHad>0</useHybridHad>
   <broadening_on>0</broadening_on>
   <brick_med>0</brick_med>
   <in_vac>0</in_vac>
   <matter_on>1</matter_on>
   <recoil_on>1</recoil_on>
   <Q0>2.0</Q0>
   <vir_factor>0.25</vir_factor>
   <T0>0.16</T0>
   <hydro_Tc>0.16</hydro_Tc>
   <qhat0>-2.0</qhat0>
   <alphas>0.25</alphas>
</Matter>
```

C.2.3 LBT parameters

```
<Lbt>
   <name>Lbt</name>
   <Q0>2.0</Q0>
   <in_vac>0</in_vac>
   <only_leading>0</only_leading>
   <hydro_Tc>0.16</hydro_Tc>
   <alphas>0.25</alphas>
</Lbt>
```

C.2.4 Jet hadronisation parameters for brick medium simulation

```
<JetHadronization>
   <name>colorless</name>
   <take_recoil>1</take_recoil>
   <eCMforHadronization>
      1380
   </eCMforHadronization>
</JetHadronization>
```

```
<JetHadronization>
   <name>colorless</name>
   <take_recoil>1</take_recoil>
   <eCMforHadronization>
      2510
   </eCMforHadronization>
</JetHadronization>
```

C.3 Parameters for brick simulation

C.3.1 Static brick medium parameters

```
<Hydro>
  <Brick
    bjorken_expansion_on="false"
    start_time="0.5">
    <T> 0.195 </T>
  </Brick>
</Hydro>
```

```
<Hydro>
  <Brick
    bjorken_expansion_on="false"
    start_time="0.5">
    <T> 0.198 </T>
  </Brick>
</Hydro>
```

C.3.2 Parton initial state parameters for brick medium simulation

```
<Hard>
  <PythiaGun>
    <pTHatMin>60</pTHatMin>
    <pTHatMax>1000</pTHatMax>
    <LinesToRead>
      HardQCD:all = on
      PDF:useHardNPDFA=on
      PDF:useHardNPDFB=on
      PDF:nPDFSetA=1
      PDF:nPDFSetB=1
      PDF:nPDFBeamA = 100822080
      PDF:nPDFBeamB = 100822080
    </LinesToRead>
    <eCM>2760</eCM>
  </PythiaGun>
</Hard>
```

```
<Hard>
  <PythiaGun>
    <pTHatMin>60</pTHatMin>
    <pTHatMax>1000</pTHatMax>
    <LinesToRead>
      HardQCD:all = on
      PDF:useHardNPDFA=on
      PDF:useHardNPDFB=on
      PDF:nPDFSetA=1
      PDF:nPDFSetB=1
      PDF:nPDFBeamA = 100822080
      PDF:nPDFBeamB = 100822080
    </LinesToRead>
    <eCM>5020</eCM>
  </PythiaGun>
</Hard>
```

C.3.3 MATTER parameters for brick medium simulation

```
<tStart>0.0</tStart>
<Matter>
   <name>Matter</name>
   <brick_lenght> 6.098 </brick_lenght>
   <useHybridHad>0</useHybridHad>
   <broadening_on>0</broadening_on>
   <in_vac>0</in_vac>
   <brick_med>1</brick_med>
   <matter_on>1</matter_on>
   <recoil_on>1</recoil_on>
   <Q0>2.0</Q0>
   <vir_factor>0.25</vir_factor>
   <T0>0.16</T0>
   <hydro_Tc>0.16</hydro_Tc>
   <qhat0>-2.0</qhat0>
   <alphas>0.25</alphas>
</Matter>
```

C.3.4 LBT parameters for brick medium simulation

```
<Lbt>
   <name>Lbt</name>
   <Q0>2.0</Q0>
   <in_vac>0</in_vac>
   <only_leading>0</only_leading>
   <hydro_Tc>0.16</hydro_Tc>
   <alphas>0.25</alphas>
</Lbt>
```

C.3.5 Jet hadronisation parameters for brick medium simulation

```
<JetHadronization>
   <name>colorless</name>
   <take_recoil>1</take_recoil>
   <eCMforHadronization>
      1380
   </eCMforHadronization>
</JetHadronization>
```

```
<JetHadronization>
   <name>colorless</name>
   <take_recoil>1</take_recoil>
   <eCMforHadronization>
      2510
   </eCMforHadronization>
</JetHadronization>
```

C.4 Parameters for proton-proton collisions

C.4.1 Parton initial state parameters for proton-proton collisions

```
<Hard>
  <PythiaGun>
    <pTHatMin>60</pTHatMin>
    <pTHatMax>1000</pTHatMax>
    <LinesToRead>
      HardQCD:all = on
    </LinesToRead>
    <eCM>2760</eCM>
  </PythiaGun>
</Hard>
```

```
<Hard>
  <PythiaGun>
    <pTHatMin>60</pTHatMin>
    <pTHatMax>1000</pTHatMax>
    <LinesToRead>
      HardQCD:all = on
    </LinesToRead>
    <eCM>5020</eCM>
  </PythiaGun>
</Hard>
```

```
<Matter>
  <Q0> 1.0 </Q0>
  <recoil_on> 0 </recoil_on>
  <broadening_on> 0 </broadening_on>
  <brick_med> 0 </brick_med>
  <in_vac> 1 </in_vac>
  <vir_factor> 0.25 </vir_factor>
 </Matter>
```

C.4.2 Jet hadronisation parameters for proton-proton collisions

```
<JetHadronization>
  <name>colorless</name>
  <take_recoil>1</take_recoil>
  <eCMforHadronization>
    1380
  </eCMforHadronization>
</JetHadronization>
```

```
<JetHadronization>
  <name>colorless</name>
  <take_recoil>1</take_recoil>
  <eCMforHadronization>
    2510
  </eCMforHadronization>
</JetHadronization>
```

Appendix D

List of Constants

$h = 6.626\,070 \cdot 10^{-34}$ JHz^{-1}	Planck constant
$\hbar = 1.054\,571 \cdot 10^{-34}$ JHz^{-1}	Reduced Planck constant
$c = 299\,792\,458$ ms^{-1}	Speed of light in vacuum
$\sqrt{\hbar c^5/G} = 1.220 \cdot 10^{19}$ GeV	Planck energy
$\sqrt{\hbar G/c^3} = 1.616 \cdot 10^{-35}$ GeV	Plack lenght
$\hbar c = 197.32$ MeVfm	
$k_B = 1.380\,649 \cdot 10^{-23}$ JK^{-1}	Boltzmann constant
$e = 1.602\,176 \cdot 10^{-19}$ C	Elementary charge
$\mu_0 = 1.256\,637 \cdot 10^{-6}$ NA^{-2}	Magnetic permeability in vacuum
$\varepsilon_0 = 8.854\,187 \cdot 10^{-12}$ Fm^{-1}	Electric permittivity in vacuum
$\alpha = 7.297\,352 \cdot 10^{-3}$	Fine structure constant
$G_F = 1.166\,378 \cdot 10^{-5}$ GcV^{-2}	Fermi's coupling constant
$m_p = 1.672\,621 \cdot 10^{-27}$ kg	Proton mass
$m_p c^2 = 938.272$ MeV	Proton rest energy
$m_n = 1.674\,927 \cdot 10^{-27}$ kg	Neutron mass
$m_n c^2 = 939.565$ MeV	Neutron rest energy
$m_e = 9.109\,383 \cdot 10^{-31}$ kg	Electron mass
$m_e c^2 = 0.510\,998$ MeV	Electron rest energy
$M_W c^2 = 80.4335 \pm 0.0094$ GeV	$W^{\pm}$ rest energy
$M_Z c^2 = 91.19$ GeV	Z rest energy
$M_H c^2 = 125$ GeV	Higgs boson rest energy
$\sin^2 \theta_W = 0.222$	Sinus squared of Weinberg angle
$\Lambda_{\mathrm{QCD}}^{N_f=3} = 332 \pm 17$ MeV	QCD scale with five flavours
$\Lambda_{\mathrm{QCD}}^{N_f=5} = 210 \pm 14$ MeV	QCD scale with three flavours
$\tau_\mu = 2.197 \cdot 10^{-6}$ s	Muon mean lifetime
$\tau_\tau = 2.906 \cdot 10^{-19}$ s	Tauon mean lifetime
$\tau_{WZ} = 3 \cdot 10^{-25}$ s	W and Z mean lifetime
$\rho_0 = 0.16$ fm^{-3}	Nuclear matter density

Appendix E

List of Acronyms

AdS/CFT	anti-de Sitter/conformal field theory
ALFA	Absolute Luminosity for ATLAS
ALICE	a Large Ion Collider Experiment
ATLAS	a Toroidal LHC Apparatus
BES	Beam Energy Scan
BNL	Brookhaven National Laboratory
BSM	Beyond the Standard Model
CDF	Collider Detector at Fermilab
CERN	*Conseil européen pour la recherche nucléaire*
CMS	Compact Muon Solenoid
DGLAP	Dokshitzer-Gribov-Lipatov-Alterelli-Parisi
DIS	Deep Inelastic Scattering
EoS	Equation of State
EWT	Electroweak Theory
HIC	Infrared
IR	Infrared and Collinear
IRC	Heavy Ion Collision
KATRIN	Karlsruhe Tritium Neutrino Experiment
LBT	Linear Boltzmann Transport
LHC	Large Hadron Collider
LRF	Local Rest Frame
$\overline{\text{MS}}$	Modified Minimal Subtraction scheme
MPI	Multiple Parton Interactions
NLO	Next-to-Leading Order
PDF	Parton Distribution Function
QCD	Quantum Chromodynamics
QED	Quantum Electrodynamics
QFD	Quantum Flavourdynamics
QFT	Quantum Field Theory
QGP	Quark-Gluon Plasma
QMD	Quantum Molecular Dynamics
RHIC	Relativistic Heavy Ion Collider
RTA	Relaxation Time Approximation
SI	*Système international d'unités*

SLAC	Stanford Linear Accelerator Center
STAR	Solenoidal Tracker at RHIC
TOTEM	Total Elastic and Diffractive Cross Section Measurement
UV	Ultraviolet